

**New Insights into the Cellular Lipid
Cascade Using Infrared
Microspectroscopy**

A thesis submitted to the University of Manchester for the degree
of Doctor of Philosophy in the Faculty of Chemical Engineering
and Analytical Science

October 2018

Thomas A Gladwell

Contents

List of Abbreviations	6
Abstract	7
Declaration	8
Copyright Statement	9
Acknowledgements	11
Chapter 1	13
1.1 Cancer Statistics	14
1.2 Prostate Cancer Risk Factors	14
1.2.1 Age	14
1.2.2 Ethnicity	14
1.2.3 Diet	15
1.3 Current Treatments and Prognosis	16
1.3.1 Localised or Locally Advanced Prostate Cancer Treatment Options	16
1.3.2 Advanced Prostate Cancer Treatment Options	18
1.4 Anatomy of the Prostate	19
1.5 Cancer Metastasis Mechanisms	20
1.5.1 Androgen Receptors	20
1.5.2 Interleukin-6 Signalling	21
1.5.3 The Metastatic Process	21
1.5.4 Invasion and Degradation of the Local Stroma	23
1.5.5 Tight Cell Junctions	25
1.5.6 Bone Invasion	26
1.6 Arachidonic Acid	28
1.6.1 Arachidonic Acid to Prostaglandin COX Pathways	30
1.7 Studies Assessing the Role of COX-2 in Prostate Cancer	32
1.7.1 Celecoxib as an Inhibitor for the COX-2 Pathway	40
1.8 The Role of Adipocytes in Tumour Metastasis to the Bone	41
1.9 Cell Cycle	42
1.10 Aims of Study	43
Chapter 2	52

2.1 Fundamental Culture Concepts	53
2.1.1 Cell Fixation	54
2.1.2 Formalin Fixation Chemical Mechanisms	57
2.1.2.1 The Reaction of Formalin	58
2.1.3 Cell Confluency.....	60
2.1.4 Cyclodextrin	61
2.2 Cell lines.....	62
2.2.1 PC-3	62
2.2.2 PC-3M.....	63
2.2.3 LNCaP	63
2.2.4 LNCaP C4-2	63
2.2.5 LNCaP C4-2B.....	63
2.2.6 DU145.....	64
2.2.7 PNT2.....	64
2.3 Fourier Transform Infrared (FT-IR) Spectroscopy	64
2.3.1 Electromagnetic Radiation (EMR).....	64
2.3.2 Quantization of Energy	65
2.3.3 Infrared Radiation	66
2.3.4 Vibrations of Molecules	67
2.3.5 Molecular Vibrations.....	69
2.3.5.1 Skeletal Vibrations.....	69
2.3.5.2 Group Frequencies.....	69
2.3.6 Biological structural information Using FT-IR	69
2.4 FT-IR Instrumentation.....	70
2.4.1 Michelson Interferometer	70
2.5 FT-IR Microscopy	72
2.5.1 Signal to Noise Ratio	73
2.5.2 The Use of FT-IR Microscopy in Monitoring Lipid Uptake and Metabolism in Prostate Cancer.....	73
2.6 Experimental Methodology.....	76
2.6.1 Materials	76
2.6.2 Cell Line Culture	77

2.6.3 Cell Treatment of Arachidonic Acid	77
2.6.4 COX-2 inhabitation	77
2.6.5 Fluorescence Microscopy	77
2.6.6 Fourier Transform Infrared Microscopy.....	78
2.7 Data Processing	78
2.7.1 Cell Finder Algorithm.....	78
2.7.2 RMieS Correction	79
2.7.3 Noise Reduction.....	82
2.7.4 Vector Normalisation.....	84
2.7.5 Spectral Derivatives.....	85
2.7.6 Multivariate Analysis	85
2.7.6.1 Principal Component Analysis	85
2.7.6.2 Seeded Principal Component Analysis.....	87
2.7.6.3 PCA Methodology and Median Positional Plots	88
Chapter 3.....	93
3.1 Invasive Prostate Cancer Cell Lines.....	95
3.1.1 PC-3M Spectral Comparison.....	95
3.1.2 PCA of the C=O Fatty Acid Carbonyl Stretch for PC-3M Cells.....	100
3.1.3 PCA of the C=O Fatty Acid Carbonyl Stretch for PC-3 Cells	104
3.1.4 PCA of the C=O Fatty Acid Carbonyl Stretch for DU145 Cells.....	106
3.1.5 PCA of the C=O Fatty Acid Carbonyl Stretch for LNCaP C4-2B Cells.....	108
3.1.6 PCA of the C=O Fatty Acid Carbonyl Stretch for LNCaP C4-2 Cells	110
3.2 Non-Invasive Cell Lines.....	112
3.2.1 PCA of the C=O Fatty Acid Carbonyl Stretch for LNCaP Cells	112
3.2.2 PCA of the C=O Fatty Acid Carbonyl Stretch for PNT2 Cells	113
3.3 Discussion	114
3.4 The Invasion Assays of PC-3 and PNT2 Cell Lines	116
3.5 PC-3 Cyclodextrin Control.....	120
3.7 Chemical Differences.....	128
3.8 Chapter Conclusion	137
Chapter 4.....	139
4.1 COX-2 Inhibitor Selection	140

4.1.1 The Action of NS398.....	141
4.2 Comparing the uptake of AA with Active and Inhibited Cellular COX-2 Enzymes	142
4.3 Discussion	153
4.4 Invasion Assay	155
4.5 A Control Study Analyzing the Biochemical Effect of Cyclodextrin and NS398 on the Global Lipid Chemistry.....	159
4.6 Seeded PCA Investigating the Effect of COX-2 Inhibition on AA uptake and Prostaglandin E2 Synthesis	161
4.7 AA Seeded PCA.....	162
4.8 PGE ₂ Seeded PCA.....	164
4.8 Conclusion.....	168
Chapter 5	171
5.1 Molecular d ₈ -AA and Spectral Vibration.....	172
5.2 Investigating the Effect of d ₈ -AA Uptake and COX-2 Inhibition on Prostate Cancer Cell Lines Using FT-IRM and Seeded PCA	173
5.2.1 Seeded PCA of d ₈ -AA Treated Prostate Cancer Cell Lines	175
5.2.2 Seeded PCA of d ₈ -AA Treated Prostate Cancer Cell Lines COX-2 inhibited	178
5.3 Investigating COX-2 Inhibition via DHA and AA Competition	179
5.3.1 PCA of Prostate Cancer Cell Lines Treated With DHA	180
5.3.2 Seeded PCA of Prostate Cancer Cell Lines Treated with DHA and AA	181
5.4 Conclusion.....	183
Chapter 6.....	185
6.1 Studying the Effect of AA on PC-3 Cells through Fluorescence Microscopy	186
6.2 Studying the Effect COX-2 inhibition on AA Uptake in PC-3 Cells through Fluorescence Microscopy.....	193
6.3 Investigating the Cellular Distribution of AA Using Low Magnification FT-IRM Imaging For COX-2 Active and Inactive PC-3 Cells Treated with AA.	198
6.4 Investigating AA Distribution within PC-3 Cells Using High Magnification FT-IRM	203
6.4.1 Condenser Alignment	204
6.4.2 High Magnification FT-IR Parameter Optimisation.....	206
6.4.3 High Magnification FT-IR False Colour Images	207
6.5 PC-3 Motility and Morphological Cellular Changes	214

6.6 Conclusion.....	219
Chapter 7	221
7.1 Conclusion.....	222
7.2 Future Work	225

List of Abbreviations

AA	Arachidonic Acid	LO	Linseed Oil
AR	Androgen Receptor	LOX	Lipoxygenase
BMS	Bone Marrow Stroma	LT	leukotriene
BPH	Benign Prostatic Hyperplasia	MCT	Mercury Cadmium Telluride
CAM	Cell Adhesion Molecule	MO	Menhaden Oil
		MS	Mass Spectrometry
CDP	Critical Drying Point	MVD	Microvessel Density
CO	Corn Oil	NBA	Northern Blot Analysis
COX	Cyclooxygenase	NSAID	Non-Steroidal Anti-inflammatory Drug
		OOR	Out of Range
COX-1	Cyclooxygenase-1	PBS	Phosphate Buffer Solution
COX-2	Cyclooxygenase-2	PCA	Principal Component Analysis
CTC	Circulating Tumour Cell		
		PC	Principal Component
DD	Double Distilled	PG	Prostaglandin
DHA	Docosahexaenoic Acid	PGD₂	Prostaglandin D ₂
DHT	Dihydrotestosterone	PGE₂	Prostaglandin E ₂
DMSO	Dimethyl Sulfoxide	PIN	Prostatic Intraepithelial Neoplasia
d8-AA	Deuterated Arachidonic Acid	PLA2	Phospholipase A2
		PSA	Prostate Specific Antigen
ECM	Extracellular Matrix	RMieS	Resonant Mie Scattering
EMR	Electromagnetic Radiation		
EMSC	Extended Multiplicative Signal Correction	SNR	Signal to Noise Ratio
FM	Fluorescence Microscopy	TB	Thromboxane
FPA	Focal-Plane Array	TCJ	Tight Cell Junction
FT-IRM	Fourier Transform Infrared Microspectroscopy		
HBBS	Hanks Bovine Buffer Solution	TURP	Transurethral Resection of the Prostate
		WN	Wavenumber
HIFU	High Intensity Frequency Ultrasound	ZPD	Zero Path Difference
HT	Hormone Therapy	ω-3	Omega-3
IL-6	Interleukin-6	ω-6	Omega-6
IMD	Intracellular Microvessel Density		
IR	Infrared		

Abstract

Although prostate cancer is the most diagnosed cancer in men worldwide, there is geographical variance in both incidence and morbidity, with higher trends in Westernised developed countries. In particular, the high levels of the omega-6 polyunsaturated fatty acid arachidonic acid (AA) in Western diets has been shown to promote aggressive prostate cancer *in vitro*. However, the exact mechanism through which AA induces the aggressive phenotype has not been fully characterised. Here Fourier transform infrared microspectroscopy (FT-IRM) coupled with fluorescence microscopy (FM) was used to follow AA metabolism in prostate cancer cell lines. Using partially deuterated AA, (d₈-AA), with a distinctive C-D stretch seen at 2251 cm⁻¹ providing molecular specificity, coupled with Nile Red Fluorescence imaging, it has been shown that, unlike the non-invasive prostate cancer cell lines PNT2 and LNCaP, invasive prostate cancer lines PC-3M, PC-3, LNCaP C4-2B and DU145 readily uptake and metabolise AA, producing prostaglandin E₂ (PGE₂) via the cyclooxygenase-2 (COX-2) pathway. Inhibition of the COX-2 pathway with NS938 reduces the invasive stimulus of AA and blocks the uptake of AA. Similarly, the addition of the omega-3 poly unsaturated fatty acid Docosahexaenoic acid (DHA), previously shown to inhibit AA induced invasion, inhibited cellular AA uptake in invasive cell line PC-3. In conclusion, it has been demonstrated that FT-IRM can be utilised to follow metabolomics processes within a prostate model and provide an insight to the molecular pathways underlying the metabolome. This could play a pivotal role in understanding the chemistry and behaviour of the initiation of metastatic prostate cancer.

Declaration

No portion of the work referred to in this thesis has been submitted in support of an application for another degree or qualification of this or any other university or other institute of learning.

Thomas Alexander Gladwell

Copyright Statement

(i) The author of this thesis (including any appendices and/or schedules to this thesis) owns certain copyright or related rights in it (the “Copyright”) and he has given The University of Manchester certain rights to use such Copyright, including for administrative purposes.

(ii) Copies of this thesis, either in full or in extracts and whether in hard or electronic copy, may be made only in accordance with the Copyright, Designs and Patents Act 1988 (as amended) and regulations issued under it or, where appropriate, in accordance with licensing agreements which the University has from time to time. This page must form part of any such copies made.

(iii) The ownership of certain Copyright, patents, designs, trademarks and other intellectual property (the “Intellectual Property”) and any reproductions of copyright works in the thesis, for example graphs and tables (“Reproductions”), which may be described in this thesis, may not be owned by the author and may be owned by third parties. Such Intellectual Property and Reproductions cannot and must not be made available for use without the prior written permission of the owner(s) of the relevant Intellectual Property and/or Reproductions.

(iv) Further information on the conditions under which disclosure, publication and commercialisation of this thesis, the Copyright and any Intellectual Property and/or Reproductions described in it may take place is available in the University IP Policy (see <http://documents.manchester.ac.uk/DocuInfo.aspx?DocID=487>), in any relevant Thesis restriction declarations deposited in the University Library, The University

Library's regulations (see <http://www.manchester.ac.uk/library/aboutus/regulations>)
and in The University's policy on Presentation of Theses.

Acknowledgements

I would like to thank my supervisor Professor Peter Gardner and co-supervisor Dr. Michael Brown for their scientific guidance and support throughout this PhD. I would also like to thank Dr. Alex Henderson for his statistical and computational knowledge, which was of great help throughout my project. I would like to thank Dr. Claire Hart for her knowledge of cellular systems and culture and guidance in the training I received. Finally, I would like to thank my partner, close family and friends for their support and encouragement throughout this project. Without the help and support of the mentioned people, this project would not have been able to happen.

[Blank Page]

Chapter 1

Introduction

1.1 Cancer Statistics

In the last 20 years, the global trend of mortality and morbidity of prostate cancer has significantly increased (1). In 2000, there were 543,000 new cases diagnosed and it was the third most diagnosed cancer in men worldwide (2). By 2002, 679,000 men were diagnosed worldwide, increasing in 2012 to over 1,000,000 diagnoses and 300,000 mortalities (3,4,5). Finally, in 2018 there were 1,600,000 men diagnosed and 366,000 mortalities from prostate cancer worldwide (6). The figures indicate that the morbidity of prostate cancer has tripled between 2000 and 2018, putting a huge strain on oncological medicine. The growing average age of global populations will only exacerbate the problem (7), with the global population expected to grow to 8.3 billion by 2030 (8).

1.2 Prostate Cancer Risk Factors

1.2.1 Age

It is well documented that typically prostate cancer incidence increases with age (9). The overall prognosis is poorer for younger men diagnosed with prostate cancer, typically with a more aggressive phenotype of the disease (10,11,12). The median age of prostate cancer diagnosis has decreased from 72 to 68 years old between the years 1988 and 2003 (13). The median age of men with prostate cancer diagnoses appears to have plateaued between 2003 and 2015 (14).

1.2.2 Ethnicity

It is well recognised and accepted that the risk of prostate cancer is much higher in black men than in white men globally (15). The difference in prostate cancer incidence

between race maybe skewed by the fact that different countries have different health care tests available and hence detection pathways between countries. It is consistent through all communities that black men are at a higher risk of developing prostate cancer younger (16,17). The PROCESS study carried out by Ben-Shlomo *et al.* discovered that the age-adjusted incidence rate in black Caribbean men was over triple that of white men, with black African men just under triple the age-adjusted incidence rate (18).

1.2.3 Diet

Evidence suggests that dietary fats may play an important role in the aetiology of prostate cancer, although the extent is currently unknown (19,20,21). The composition of dietary fats could influence the risk of prostate cancer (22). There are three main types of dietary fats: saturated, monounsaturated and polyunsaturated (23). A saturated fatty acid contains no double bonds in its carbon backbone, a monounsaturated fatty acid contains 1 double bond in its carbon backbone and a polyunsaturated fatty acid contains more than 1 double bond in its carbon backbone. Two common polyunsaturated fatty acids which are said to play a pivotal role in the progression of cancer are omega-6 (ω -6) and omega-3 (ω -3) fatty acids.

There has been a major shift in the dietary balance in developed countries between ω -6: ω -3 fatty acids through industrialisation and changing diets, with parts of America consuming a dietary ratio of ω -6: ω -3 fatty acids as high as 20:1 (24), these trends directly couple with incidence rates of prostate cancer, suggesting that ω -6 fatty acids play a role in the development of the disease.

1.3 Current Treatments and Prognosis

The treatment, management and prognosis of prostate cancer is thought to be improved if caught early, although the literature surrounding this is currently unclear (25). Age, co-morbidities, type, size and grade of the cancer (whether the cancer has metastasised) dictate the management of prostate cancer, both increasing the complexities regarding treatment management and developing patients care plans (26). These factors greatly influence the direction in which patient's treatment options are aimed, ultimately with the decision to treat the disease aggressively usually by chemo/radio-therapy or manage the condition via hormone therapy (cure or control). For many men, there will be no need for treatment but each individual case is different (27).

The stage of prostate cancer is determined through the results of the patient's prostate examination, biopsy and scans determining if the cancer is localised or if the patient has secondary cancer sites (28).

1.3.1 Localised or Locally Advanced Prostate Cancer Treatment Options

If the cancer is localised and the patient is relatively young, there is the potential to cure the disease surgically by a radical prostatectomy. This surgery carries risks, the most common being urinary incontinence and impotence (29). There is a rare and potentially fatal risk associated with the treatment; there is a possibility to displace tumour cells into the circulating blood, which could lead to secondary tumour sites (30). After a radical prostatectomy, ejaculation is no longer possible, meaning infertility is inevitable (31). Radiotherapy can be coupled with the surgical procedure or used as an individual treatment option, killing, slowing down or alleviating symptoms depending on the stage of the disease (32).

A treatment option which has become common more recently is brachytherapy, where radioactive seeds are planted within the prostate (33). This treatment option is effective and offered when the disease is localised and contained within the prostate. Depending on the patient, a low, medium or high dose can be delivered (34). The dose can either be permanent or fixed meaning the treatment can be varied depending on the patient's condition and needs. The advantage of this treatment is a dramatic increase to quality of life with the patient often returning to daily life reasonably quickly. The radiation is also short acting meaning the likelihood of damaging the surrounding healthy tissue is low. A disadvantage to long term use is damage or interference to adjacent organs (35).

Another treatment option for localised or sometimes locally advanced prostate cancer is high-intensity focused ultrasound (HIFU). This technique requires an ultrasound probe to be inserted into the rectum in close proximity to the prostate using high frequency ultrasound energy to destroy cancerous prostate tissue (36). This treatment is in the infancy stage of development with the long-term side effects yet to be known, therefore it is only available as part of clinical trials (37).

Cryotherapy is an alternative treatment for localised prostate cancer. Needles are inserted into the prostate and a low temperature gas is passed down the needle to freeze the target area in the prostate (38). There are two main forms of this technique, whole-prostate cryotherapy where the entire prostate is frozen and focal cryotherapy, where only part of the prostate is frozen, in turn freezing less healthy tissue (39). The advantage to this treatment is the technique is relatively less invasive than other techniques with a fast recovery time. The disadvantages mainly arise from the lack of knowledge associated with the long-term risks with possible urinary and erection issues (40).

Transurethral resection of the prostate (TURP) is a surgical procedure that removes sections of the prostate. A thin metal tube is used with a camera and metal loop. The metal loop is heated with a current and used to cut away the cancerous region. A catheter is then inserted flushing the bladder with fluid, washing away any pieces of removed prostate (41). The risks for TURP are low with the potential to lose the ability to ejaculate (42).

Hormone therapy (HT) is a treatment that can be used in all stages of prostate cancer. Testosterone is a key hormone in the development and proliferation of prostate cancer. Depriving prostate cancer cells of testosterone limits and suppresses the growth of the disease. HT either stops your body from producing testosterone or blocks testosterone from reaching prostate cancer cells (43). Prostate cancer eventually becomes resistant to the hormone with the length of time differing for each patient. Once the prostate cancer has become resistant (43), there are secondary hormones which can be used to limit the growth of the disease (44).

1.3.2 Advanced Prostate Cancer Treatment Options

The term advanced is given when the disease is no longer localised and spread to a secondary site through metastasis, usually to organs surrounding the prostate or the bone. This means treatment options are much more limited, with a primary focus on pain management and quality of life (45). HT will be used to control the growth of the prostate cancer outside the primary site, but this has a limited effectiveness. Bisphosphates are used when the patient is symptomatic of bone pain (45). When the patient stops responding to hormone therapy there is a potential to carry out clinical trials using radium-223. Active bone cells uptake radium-223, as cancer cells are more active than bone cells, the probability of cancer cells up taking the radium-223 is much

higher than healthy bone cells, making the treatment ideal to target bone metastasis in advanced stages of the disease (46). Steroids also may be taken by the patient with advanced stages of the disease. Steroids act by limiting the cancers invasive ability for a limited time, as well as reduce symptoms such as inflammation and edema (47). Beyond these treatments, resources are exhausted and the mode of care is switched to palliative.

1.4 Anatomy of the Prostate

The prostate is anatomically separated into three main glandular zones, the peripheral, transition and central zones. The structure of the prostate gland secretory duct consists of prostate epithelium which is comprised of basal, intermediate, neuroendocrine and luminal cells (48) which can be seen in a prostate gland cross section in Figure 1.

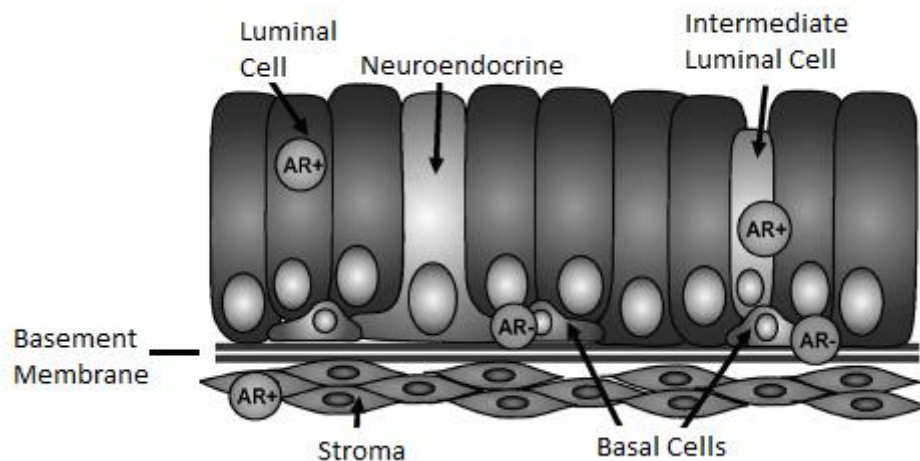


Figure 1 – Structural diagram of the cellular arrangement in the prostate gland secretory duct (49)

It has been said that only the basal and luminal cells are the cancer-causing cells by origin according to work carried out on both basal and luminal cells by Wilson and Moscatelli *et al.* (50). Because tumour tissue consists of luminal cells with no basal cells, the train of thought amongst pathologists is that luminal cells must be the origin of the disease. On the other hand, cell biologists believe basal cells have a greater regenerative potential leading to the argument that basal cells are the true origin. A key finding by Goldstein *et al.* was that a mutation can occur in a basal cell but still end up with a luminal tumour (51), which is a nice indication that both cells can lead to tumour formation. Work carried out by Wang *et al.* found that luminal cells were consistently the tumour causing cells (52), with luminal cells favoured as the tumour origin. It was also said that basal cells only give rise to tumour after differentiation into luminal cells. The study suggested that the origin was still unclear to whether luminal, basal or both was the cause of prostate cancer.

1.5 Cancer Metastasis Mechanisms

1.5.1 Androgen Receptors

Initial work carried out by Huggins and Hodges highlighted the dependence of prostate cancer cells on androgen. Androgens are essential steroid hormones which regulate male sexual development and differentiation (53). The major androgens in males are testosterone dihydrotestosterone (DHT) and androstenedione. It was seen that androgen binds to the androgen receptor (AR), translocating to the nucleus, the binding of androgen to androgen responsive regions influences the transcription of androgen-regulated genes (Prostate-specific antigen (PSA)). This in turn stimulates the proliferation of prostate cancer cells and inhibits apoptosis of the foreign cancer cell (54). Current treatments controlling early metastatic prostate cancer such as HT aim to

reduce the androgen levels within the body by essentially castrating the patient stopping the production of testosterone (55). All patients at some point will progress as the tumour becomes resistant to the treatment, by adapting to the androgen-deprived environment becoming castrate-resistant. There are several mechanisms which lead to castrate-resistant prostate cancer which plays a huge role in leading to bone metastasis. Firstly, prostate cancer cells become “hypersensitive” to androgen stimulation by upregulating the AR expression. Secondly the paracrine and autocrine production of androgen is upregulated. Steroids such as oestrogens also have the ability to activate the AR. By-pathways have been found to contribute to the AR growth of prostate cancer cells using interleukin-6 signalling described below (56).

1.5.2 Interleukin-6 Signalling

Interleukin-6 (IL-6) is a glycoprotein related to progressive castrate-resistant prostate cancer and is expressed in prostate cancer cells as early as benign hyperplasia (57). As the cancer progresses and becomes more advanced with metastatic characteristics, there is an increased expression of IL-6 (58).

1.5.3 The Metastatic Process

In 1889 Paget *et al.* proposed that the metastasis of a solid tumour can be described by a “seed and soil” hypothesis (59). In this model, the tumour is the seed and the soil describes the organ. The soil is very fertile, aiding the growth and development of the seed (tumour). The model also states that the seed can only metastasise to the soil. This is still classed as an excellent description of tumour metastasis but the description lacks the detail on a molecular level for organ specific metastasis.

There are multiple steps which lead to the growth of a metastatic tumour, namely: angiogenesis, local migration, invasion, intravasation, circulation, extravasation leading to angiogenesis and colonisation in the new site (60). These events are fundamental in allowing discrimination of the tumour cells from the primary to secondary or tertiary foci. A statistic released by health organisations show that over half of the patient diagnosed with cancer also have detectable metastatic progression with a higher level of patients showing micro-metastatic progression beyond the standard diagnostics used by health care professionals (61).

The formation of a tumour begins with the initial development of a neoplasm (a foreign tissue to its environment) through various cell signalling mechanisms coupled with the introduction of specific growth factors. Studies have shown that, for a neoplasm to exceed 1 mm in diameter within the primary site, angiogenesis must occur (62). It is noted that oxygen can only diffuse across a capillary into a depth of roughly 150 μm , therefore it is essential to create new blood vessels around and within the tumour to supply the oxygen needed to avoid cell induced death from hypoxia. The steps involved in neovascularisation are epithelial cell formation, the migration and proliferation of these cells so they are located in the correct area, then finally the formation of the vascular loop and basement membrane where the basement membrane is a thin, fibrous extracellular matrix which separates epithelium, endothelium and connective tissues. Cellular instructions are used and activated, similar to that of wound healing to lyse the nearest environment allowing the new blood vessel to reach the required tumour location. The need for tumour angiogenesis has been shown in studies carried out by Vartanian *et al.* highlighting the correlation of intracellular microvessel density (IMD) and poor prognosis in prostate cancer tumours (63), showing a much greater IMD in

prostate cancer tissue than in healthy tissue. Hence indicating the importance of angiogenesis in neoplastic growth.

For cancerous cells to spread, they need to be able to break away from neighbouring cells. Loss of cell adhesion is vital for cells to have the ability to metastasise and travel to nearby lymphatic and blood vessels. Within a normal prostate gland, epithelial cells are strongly bound to one another, so initially the cancerous cell phenotype has to change from a stationary to a migratory phenotype. It must be noted, that when the tumour cell reaches a secondary site and has successfully metastasised, there is an upregulation to the cell adhesive mechanism to reattach the cell to a secondary metastatic site. When this occurs, there is a lower promotion of the cell adhesion molecules (CAM) (64). CAM is a calcium-dependent transmembrane surface protein which enables the binding to either same or different cell types (65). Coman *et al.* first displayed the adhesive nature of malignant cells (66). One interesting area which needs to be elucidated is the influence of calcium concentration within a cell's environment. Changing calcium concentration would influence the ability for CAM's to bind to other surface molecules consequently effecting the adhesive ability as the protein requires calcium ions to function. The CAM which is of most interest is E-cadherin (CDH1) which is specific for the binding of epithelial cells. The binding of two epithelial cells via E-cadherin within the prostate forms an adherens junction. The E-cadherins repeat on the extra-cellular membrane and are the calcium binding domains (67).

1.5.4 Invasion and Degradation of the Local Stroma

The extracellular matrix (ECM) plays an important role in the stromal invasion process. This is a group of molecules secreted by the cell providing biochemical and structural support to the neighbouring cells. Integrins are another type of CAM involved in

stromal invasion, these are used to mediate interactions between the ECM and tumour cells during the first metastatic invasion. By regulating these interactions between the different CAM's, the tumour cell is able to move out its native environment amongst the stromal cells been capable of staying and penetrating other regions by upregulating the second CAM integrin. This was shown by Edlund *et al.* where they used the prostate cancer cell line LNCaP to show the binding of the cancer cell matrix components on laminin (fibrous protein located on the basal lamina of the epithelia) and vitronectin (ECM protein) (68). It is important and pivotal that the cancer cells break down the tissue barriers to escape and metastasise, this process involves the basement membrane and interstitial connective tissue (main components of the EMC). The ECM is broken down by several different proteases namely: matrix metalloproteinases, serine proteinases, cysteine proteinases and aspartyl proteinases. Once the tumour cell escapes its primary site, it needs to breach the basement membrane entering and exiting the blood vessels or lymphatic system in intra- and extra- vasation.

Once the tumour cell has penetrated the basement membrane, entering the lymphatic of vascular system, there are two potential outcomes. The tumour cell can either seed and multiply at the site or break away as either a single cell or a group of tumour cells. For the tumour cells to survive within the blood, they have to overcome the immune responses within the blood and be able to cope with the turbulent shear forces exerted on the cells by the blood flow. It is evident that when the tumour cells use the lymphatic system for mobilisation avoiding the intense immune response within the blood stream. When tumour cells are within the blood stream, immune recognition should create a response to the tumour cell antigens and handled by the antigen presenting cells. Often the tumour cells down-regulate the antigen expression which initiates the cytotoxic T-

lymphocyte destruction [69]. Tumour cells also overcome the shear forces within the turbulent blood flow by adhering to platelets by expressing the receptors on the tumour cells surface and allow the tumour cells to stay within the small micro-blood vessels [70]. Once the tumour cell reaches its metastatic site, the same processes are undergone with extravasation out of the blood or lymphatic vessels, cellular adhesion to the new environment and angiogenesis supplying the secondary tumour with the oxygen needed to survive and grow. Before the epithelial cancer cells enter the blood vessels, they must breach the endothelial vascular wall penetrating through tight cell junctions in the endothelial lining.

1.5.5 Tight Cell Junctions

Over the years, cancer research invested a large amount of time looking at tumour progression and development. More recently, research groups and institutions are investing a significant amount of time looking at the roll of tight cell junctions (TCJ) in cancer metastasis, as secondary tumours are responsible for most cancer related deaths due to malignancy (71). To truly take advantage and exploit the potential discovery of the roll of TCJ in cancer metastasis, the architecture, structure and biochemical behaviour between endothelial cells needs to be explored and understood.

TCJ are discrete sites of fusion between the adjacent epithelial cells outer plasma membrane joined by a number of fibrils in a series of kissing points (72). The TCJ is thought of as the first impeding structure when a tumour cell begins its metastasis (73). There are a number of directly related studies carried out mentioned previously showing the loss of the TCJ is through the up and down regulation of joining proteins. Recent studies have shown that, depending on the organ site, there are different degrees of

permeability of the TCJ (74). The TCJ contains three regional constituents: Integral transmembrane proteins, plaque anchoring proteins and regulatory proteins (75). The integral transmembrane proteins are adhesion proteins which ensures the correct assembly of the TCJ structure and controls the function of the TCJ via homotypic and heterotypic interactions. Concurrent functions are seen for the Plaque anchoring and regulatory proteins, enabling successful assembly and maintenance of the TCJ. These proteins provide a link, acting as a scaffold between neighbouring endothelial cells. This link provides access between the neighbouring actin cytoskeleton and also enables cell to cell signalling (75). The TCJ has four fundamental roles, the first of which provides the separation and sealing of intercellular space between the apical and basolateral fluid compartments of endothelia and epithelia. Secondly, provides a reservoir for TCJ molecules, which act as intermediates and transducers in cell signalling mechanisms, highlighting the importance of TCJ in the role of cell differentiation, proliferation, growth and polarisation. Thirdly, the TCJ provides the mediation of adhesion. Finally, the TCJ provides the separation of different tissues acting as a barrier to cell migration and motility (76). The development of human cancer is frequently associated with the failure of epithelial and endothelial cells to form TCJ's allowing an insufficient balance in apicobasal polarity (76).

1.5.6 Bone Invasion

Once the circulating tumour cells (CTC's) are within the vascular system, they have the potential to locate and attach to different areas in the body. There is overwhelming statistics relating cancer metastasis to the bone, with studies showing 90% of prostate cancer patients die with bone metastasis (77). Currently the mechanisms involving cancer metastasis to the bone are poorly understood so there is little information

available regarding why prostate cancer spreads to the bone so often. Prostate cells bind to human bone marrow endothelial cells, there is a greater binding affinity to these cells compared to other endothelial cells and a proposed “dock and lock” mechanism has been suggested (78). This model suggests that the epithelial cells in the bone regularly express adhesion molecules such as P-selectin and the Sialyl-Lewis(X) carbohydrate on the surface of the prostate cancer is attracted and associates through a docking mechanism (79). The mechanism following this to lock the prostate cancer cells to the epithelial cells is mediated by integrins as mentioned above.

Not only are integrins essential for the early steps in prostate cancer metastasis, they could also play an important role in colonisation. It is said that the integrins which are expressed by the prostate cancer cells are also expressed in osteoclasts (a large multinucleate bone cell which absorbs bone tissue during growth and healing) facilitate tumour spreading within the bone. A study carried out by Cooper *et al.* shows that integrin $\alpha v \beta 3$ is expressed in metastatic PC-3 cells and mediates migration on tissue culture plates coated with vitronectin and osteopontin to resemble the environment within the bone (80).

1.6 Arachidonic Acid

AA is a polyunsaturated ω -6 fatty acid. The fatty acid is a 20-carbon chain, containing 4 *cis*-double bonds. The first double bond is located 6 carbons back from the opposite end to the carboxylic acid group [81]. The structure can be seen in Figure 2.

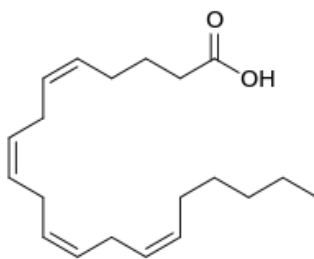


Figure 2 - Skeletal Structure of Arachidonic Acid

Studies show that ω -6 fatty acids such as linoleic and AA promote cell proliferation in prostate cancer cell lines (82,83,84), whereas the reverse is true of long chain polyunsaturated ω -3 fatty acids which exhibit inhibitory effect on cellular proliferation (85).

Fatty acids are seen to influence a wide range of diseases such as inflammation, heart disease and the aggression of cancers. Diet has a great influence on prostate cancer with rates of prostate cancer varying with geographic location, yet the influence on risk factors are still widely controversial (86). Omega-6 fatty acids such as AA and linoleic acid promote cell proliferation in cancer cell lines whilst omega-3 fatty acids inhibit cell proliferation. Fish derived ω -3 fatty acids, more specifically docosahexaenoic acid (DHA) and their role in prostate cancer treatment and prevention are currently a controversial topic. (87). A study carried out by Chaudry *et al.* examined tissues from radical prostatectomy and found that there was 10 times as much AA in tumour tissue

than healthy prostate tissue (88). It is seen that the tumour cells use AA to fuel the development and progression of the disease but the pathway is not fully understood.

There are multiple pathways thought to be responsible for AA induced cell proliferation in prostate cancer tissue. It is thought that the pathway which produces specific eicosanoids (signal molecules, most classified as hormones derived from ω -3 and ω -6 fatty acids where the ω -6 fatty acid are generally known for pro-inflammation and ω -3 known to influence inflammation less) which mediate the inflammatory response. The eicosanoids are produced by leukocytes which invade the tumour and tissue cells. Autocrine (cell signalling which produces hormones/ chemical messengers which bind to their complementary receptors on the same cell leading to a change in the cell) Paracrine (cell to cell communication which produces signals inducing changes in cells in the region close by and changing the differentiation and behaviour of the cells) the molecules produced by the signal pathways autocrine and paracrine are called autocrine factors and paracrine factors respectively. The eicosanoids act as autocrine and/ or paracrine factors which have essential biological roles such as blood clotting, immune response and cell proliferation (89). The eicosanoids fall into 3 major groups: prostaglandins (PGs), leukotrienes (LTs) and thromboxanes (TBs).

Eicosanoids have also been found to be involved in enzymatic pathways of the isoenzymes cyclooxygenases (COXs) (90). COX enzymes (1 and 2) catalyses the omega-3 and omega-6 fatty acids to produce prostanoids (a sub category of eicosanoids). Eicosanoids can also be associated with lipoxygenases (LOXs) which are a group of iron containing enzymes that break down the dioxygenation of fatty acids in lipids. The last enzymatic pathway being cytochrome p450.

1.6.1 Arachidonic Acid to Prostaglandin COX Pathways

The work carried out by Masferrer *et al* provides evidence that COX-2 derived prostaglandins influence tumour growth via metabolic mechanisms and angiogenesis promotion within the tumour (91). It is well documented that COX-2 catalyses the rate limiting step in the biosynthesis of prostaglandin (PG) (92). Therefore, it is of the upmost interest to understand and gain a deeper knowledge into metabolic pathways between AA and the prostanoids. The first stage of the AA to PG pathway involves the COX-1/2 enzyme converting AA into the unstable PGG₂ and further into PGH₂ via the oxygenase and the peroxidase functions respectively (93). The metabolism of PGH₂ is very much environment and cell specific. There are three possible pathways the in which the PGH₂ metabolises, firstly thromboxane (TB) synthesis specific to macrophages and platelets, secondly prostacyclin synthesis found in endothelial cells and finally the PGs which are present in many cell signalling pathways (94) all of which can be seen in the COX pathways of the AA cascade shown in Figure 3. Two metabolites within the prostaglandin sub category are of deep interest in current prostate cancer research, PGD₂ and E₂.

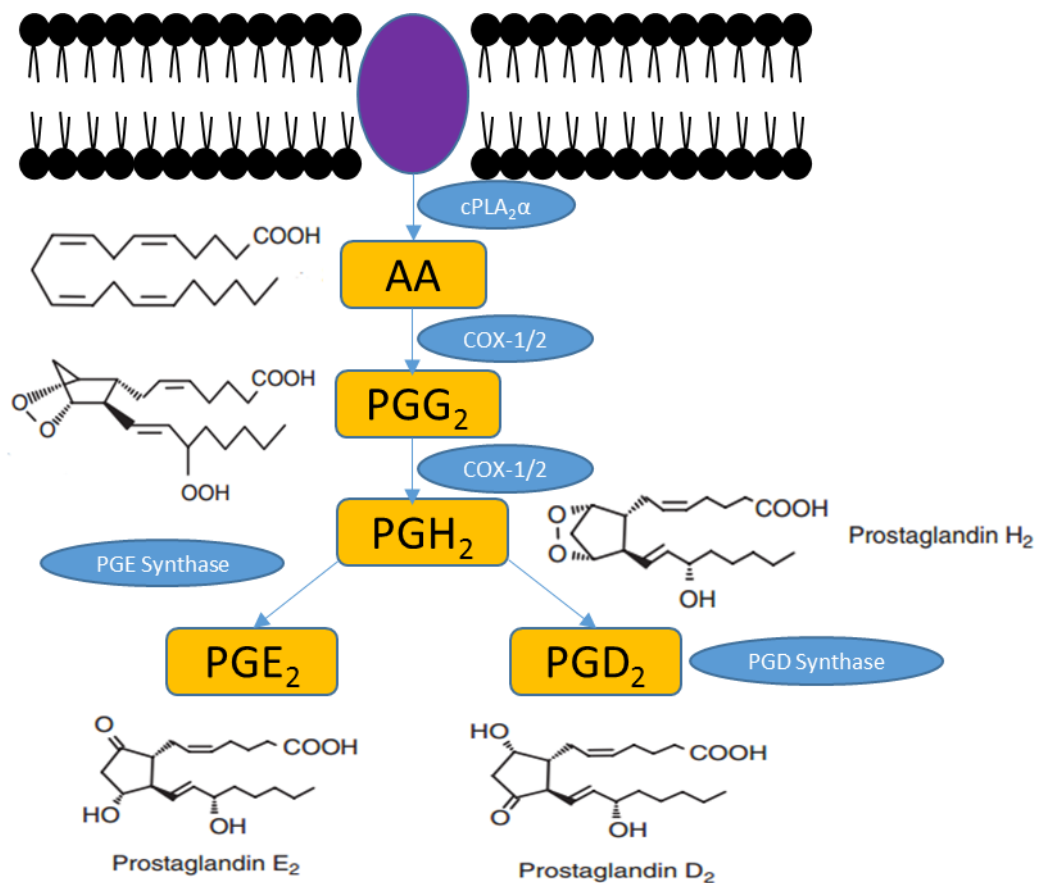


Figure 3 – The AA metabolic Pathway through COX-1 and COX-2 action specific to PGs E₂ and D₂ accompanied with their chemical structures.

1.7 Studies Assessing the Role of COX-2 in Prostate Cancer

The cellular AA metabolic pathways are well documented (84), but the metabolism of AA in the development of prostate cancer is currently poorly understood. A pathway which is of great interest is the COX pathway, where AA undergoes enzymatic transformation to the prostaglandins via the enzyme isoforms COX-1 and COX-2. It is said that the COX-1 enzyme is present in nearly all human cells (constitutively) without regard to cellular environment in contrast to its COX-2 isoform which is more inducible with its concentration noticeably increasing in tissues with incidences of inflammation (95). Another interesting point is that the v_{\max} (the enzymes optimum rate) and the k_m (concentration of substrate which allows half of v_{\max}) are very similar for both COX isoforms (96). It is seen that both enzymes are integral membrane glycoproteins located on the luminal surface of nuclear envelope and the endoplasmic reticulum (97).

It is stated in many studies that the COX-2 expression increased in cancerous tissues such as gastrointestinal, pancreatic, lung, prostate and breast with the most noticeable colon malignant tissue with the suggestion that COX-2 inhibitors which are anti-inflammatory drugs may decrease the risk of malignant tissues (98). Fradet *et al.* state that many sources (bacterial and viral infections, diet, and intraprostatic urine reflux) can lead to and develop inflammation which in turn influences the risk of prostate cancer (99). This hypothesis is strengthened further by Patel *et al.*, who carried out an in-depth review of literature, stating that epidemiological evidence that nonsteroidal anti-inflammatory drugs potentially decrease the risk of prostate cancer by the inhibition of the COX-2 enzyme which has been validated in pre-clinical studies (100).

Another study highlighting the importance of inflammation in cancer development is work by Wang *et al.*, looking at COX-2 expressions with respect to areas of inflammation (101). Immunohistochemical analysis was carried out on 43 human prostate cancer sets for the COX-2 correlation with T-lymphocytes, macrophage densities and CD31 marked micro-vessel density (MVD) *in situ*. The study showed that 40 of the 43 samples showed a range of COX-2 expression levels with a greater intensity linked with higher Gleason graded tissue and areas of chronic inflammation. Areas of positive expressions of COX-2 showed to have high levels of T-lymphocytes and macrophages in contrast to the negatively expressed COX-2 regions. The study hypothesises that COX-2 could be a potential therapeutic target for prostate cancer treatment showing regions of inflammation linked with strong positive expressions of COX-2 linked to tumorigenesis and angiogenesis in the surrounding stromal tissue.

Liu *et al.* investigated the effects of inhibiting the COX-2 enzyme on tumour development and progression (102). The study uses 28 nude mice which were each subcutaneously inoculated with 10^6 PC3 cells in which all tumours in mice were palpable. Half the set of mice were randomised and administered a control drug over 9 weeks with 3 weekly doses, and the remaining mice administered NS398, which is a COX-2 inhibitor on the same dose regime. After the 9-weeks, all mice were euthanised and histochemically analysed for proliferation, apoptosis and MVD. The mice which received the control drug showed a substantially increased tumour surface area at 285 mm^2 compared to those who received the COX-2 inhibitor at 22 mm^2 . Immunohistochemistry revealed that there was no change in cellular proliferation between the control and COX-2 inhibited populations, but there was increased apoptosis and decrease micro-vessel density (MVD) in the mice who received the COX-2

inhibition. Overall the NS398 COX-2 inhibitor showed dramatic signs of PC-3 suppression with decreased angiogenesis potentially achieved by tumour cell apoptosis induction.

A study carried out by Kirschenbaum *et al.* aimed to define and determine COX-1 and COX-2 expressions in prostate tissue ranging from healthy to diseased (98). There was 31 paraffin embedded prostate carcinoma samples obtained from a radical prostatectomy, each of the tumour specimens were analysed with respect to the samples 2 highest Gleason grades leading to 62 cancerous samples. After further analysis 28 of the 31 samples were determined to be prostatic intraepithelial neoplasia (PIN) accompanied by 10 samples with benign prostatic hyperplasia (BPH) were analysed from transurethral resections of the prostate. The samples were stained with mouse anti-human COX-1 and COX-2 antibodies where the comparison was made between the histologic tissue types (luminal and basal BPH, different Gleason cancerous tissue and PIN). The study was semi-quantitative giving an immuno-reactive average intensity score for each histological group. It was seen that both COX-1 and COX-2 expressions increase in prostate cancer tissue with COX-2 increasing alone in both luminal and basal PIN. There was no sign of change in the BPH tissues, overall showing that the COX-1 and COX-2 expressions may play a significant role in the progression of prostate cancer. A point to be noted is that neither age nor race was mentioned, both of which change morbidity and alter the aggression of the disease. Also, an average intensity was taken when looking at the immuno-reactive sections of the tissue samples, this could lead to a distortion where key features of the tissue may be overlooked when obtaining a global representation of the tissue samples.

A study by Otto *et al.* is also in agreement with the findings of Kirschenbaum *et al.* where the expression of COX-2 was monitored in various animal models. It is found that the overexpression of COX-2 causes noticeable tumorigenesis. When the COX-2 pathway is inhibited, a reduction of the progression and incidence was seen. These findings are reinforced by the work conducted by Prescott *et al.*, where genetic and clinical studies were examined and analysed, the result suggested that COX-2 upregulation is a key step in the development and proliferation in carcinogenesis (103).

Hughes-Fulford *et al.* was able to demonstrate the uptake of exogenous AA by PC-3 cells using Nile red fluorescence which ultimately triggered RNA induction within minutes followed by protein and PGE₂ synthesis within 2 hours (104). It is said that the AA stimulates the phospholipase A₂ which was described as dose dependant along with the COX-2 gene expression where COX-1 had no increase. Further to this, Hughes-Fulford was able to show phospholipase and COX-2 inhibition by flurbiprofen (COX inhibitor) which reduced tumorigenesis, highlighting AA and PGE₂ play a critical role in the stimulation of prostate tumour growth by altering the gene expressions in PC-3 cells.

Experiments carried out by Connolly *et al.* aimed to examine the effects of dietary fatty acids on the human prostate cell line DU145 (105). They carried out 2 experiments, the first of which 25 mice were fed 23% (wt/wt) fat diets looking at 3 different diets: 18% corn oil (CO) with 5% linseed oil (LO), 18% LO with 5% CO and finally 18% menhaden oil (MO) with 5% CO, 7 days later 1 million DU145 cells were subcutaneously injected into the nude mice with the rich fat diets carrying on for 6 weeks. The mice that were fed 18% CO with 5% LO and 18% LO with 5% CO showed very similar tumour growth rates compared to the 18% MO with 5% CO where the

tumour growth rate fell by 30%. The hypothesis made was the 18% MO compared to the CO or LO had reduced the amount of AA available limiting the production of PGE₂ reducing the tumour growth rate. The second experiment 25 mice were injected with first 5x10⁵ cells and 25 more with 1x10⁶ cells directly into the prostate. The mice were fed high or low-fat linoleic acid diet for 10 weeks. On autopsy, macroscopic cancers and microscopic intraprostatic tumours were assessed. It was found that the mice with the higher load (1x10⁶ DU145 cells) 43 of the 50 mice developed large macroscopic tumours the average tumour mass in the high fat treated cells was twice that in the low-fat diet. This could be an indication of the AA acid metabolised to PGE₂ plays a critical role in the proliferation and tumorigenesis of prostate cancer.

A study by Hussain *et al.* displays further evidence that COX-2 is over expressed in human prostate cancer (106). The study uses 12 matchless pairs of benign and prostate carcinoma tissue from the same patient analysing the COX-2 mRNA expressions. The investigation proved very interesting, showing clear indication towards an increased COX-2 mRNA expression in the prostate carcinoma tissue compared to that of the benign tissue. Further analysis was carried out looking at the COX-2 protein expression, which again was significantly higher in the prostate carcinoma tissue than in the benign tissue.

Coupled with the study carried out by Hussain *et al.* was the work by Yoshimura *et al.* which investigated the effects of COX-2 within prostate carcinoma tissue compared to that of benign (107). The experiment uses an assortment of tissues including: 28 prostate adenocarcinoma (PAC), 8 BPH, 1 PIN and 8 healthy. It was found that very low expressions of COX-1 expressions were found in prostate tumour cells with the immuno-reactive expression clearly marked for COX-2. Both COX-1 and COX-2

expressions were weak in BPH and healthy tissues. Overall, the most intense COX-2 expression was seen in the prostate adenocarcinoma tissue. Further mRNA analysis was carried out concluding the same outcomes as what was seen initially in the protein analysis. In conclusion the findings showed that the COX-2 expression had great effects on the regulation and proliferation of prostate carcinoma cells. The study by Yoshimura *et al.* ties in with work carried out by Kirchenbaum *et al.* both concluding increased COX-2 expressions in prostate carcinoma tissue with an effect on the cellular regulation and proliferation of prostate carcinoma cells (98,107). Although both studies are initially promising, there are limitations present in both studies regarding low sample size and patient count and lack of patient details regarding the patients current age, race, prescribed medication and stage of the cancer.

Another study backing the evidence behind the COX-2 expression in prostate carcinoma tissue was undertaken by Madaan *et al.*, the results showed a positivity for COX-2 expressions in 72.1 % of PIN tissue and 44.7 % of prostate carcinoma tissue (108). It was seen than there was an overexpression of COX-2 within prostate carcinoma and PIN tissue compared to that of BPH.

A study carried out by Tjandrawinata and Dahiva *et al.* which look at the cellular downstream consequence of arachidonic acid metabolism specifically the effect of PGE₂ on cellular proliferation and COX-2 regulation (109). It was found that adding dimethyl prostaglandin E₂ to the human prostate cell lines PC-3 and LNCaP increased cellular proliferation, DNA content and endogenous PGE₂. With the PC-3 cells, it was also found that the regulation of the COX-2 mRNA levels was both time and dose dependent with the greatest stimulation seen at 2 hours and 5 µg ml⁻¹. Tjandrawinata and Dahiva *et al.* hypothesise that PGE₂ has a significant effect on cellular growth, with

the activation of the COX-2 expression depending predominantly on newly synthesised PGE₂. This study does not only give insight to the potential of blocking the AA cascade via suppressing the COX-2 activity but also highlights that the metabolite PGE₂ could play a key role in preventing the proliferation and development of prostate cancer.

An investigation carried out by Zha *et al.* used the prostate cell lines LNCaP, PC-3 and DU145 and TSU to investigate the COX-2 expression in protein and mRNA in the prostate as well as tumour samples taken fresh from radical prostatectomy (110). All the cell lines were found to have an undetectable COX-2 protein expression under basal conditions and when induced by a phorbol ester treatment expressed COX-2 protein expressions in the PC-3 and TSU cell lines with undetectable expressions again in the DU145 and LNCaP cell lines. Immunohistochemically analysis was carried out on 144 human prostate carcinoma samples with the findings showing that no consistent pattern emerged when looking for the overexpression of COX-2 proteins in prostate carcinoma tissue compared to that of healthy prostate tissue. This finding contradicts most publications regarding COX-2 expression in prostate carcinoma tissues.

To further support the contradicting study of Zha *et al.* is the work carried out by Subbarayan *et al.* where normal prostate cells (epithelial, smooth muscle and stromal) were compared to the prostate cancer cell lines PC-3, LNCaP and DU145 investigating the expression levels and sub-cellular distribution of COX-1 and COX-2 (111). The results highlighted high levels of basal protein and mRNA COX-2 levels within the normal prostate epithelial cells but low levels in the prostate cancer cell lines PC-3, DU145, LNCaP and the normal prostate cell types smooth muscle and stromal. The hypothesis was proposed that the COX-1 and COX-2 gene expression was increased as a response to the tumour necrosis factor- α (TNF- α) which is said to be a potent inducer

of the COX-2 expression. Using northern blot analysis (NBA) and reverse transcription-PCR identified differing kinetics between the two COX isoforms in normal and cancerous prostate cells in response to TNF- α . In normal cells, it was seen that the COX-2 expression increased with a much-organized sub-cellular distribution establishing a perinuclear ring after roughly 4-hour exposure to TNF- α . There was a subtle change in the cancerous cells, with the COX-2 expression indicated to be elevated which a significantly reduced sub-cellular structured distribution. The diffusion of COX-2 protein was also seen in cancerous cells to specific regions of other cancerous cells cytoplasm. This study suggests that the COX-2 expression is not shown in cancerous tissue with the expression only elevated within endothelial cells which contrasts most literature reinforcing the work carried out by Zha *et al.*

Work carried out by Sung *et al.* suggested that COX-1 was universally expressed in all epithelial cancer cell lines derived from human colon, lung, breast and prostate carcinoma (DU145, LNCaP and PC-3) whereas COX-2 expression was varied between cell lines showing negative expressions in the LNCaP and PC-3 cell lines and a positive expression in the DU145 cell line, both enzymes were expressed in main cancer histology's (112). This indicates that COX-2 expressions are not present in all cancerous cell lines. Overall there are strong opposing arguments regarding the expression of COX-2 in cancerous cells which highlights that there is little understood regarding the action of COX-2 in the development of cancer itself and its potential as a therapeutic target. There are conflicting arguments within the field that require elucidation and further investigation.

1.7.1 Celecoxib as an Inhibitor for the COX-2 Pathway

Celecoxib is an extremely selective reversible inhibitor of the COX-2 enzyme, impeding the AA to PG metabolism (113). Celecoxib is a readily prescribed nonsteroidal anti-inflammatory drug (NSAID) to treat a range of conditions such as pain relief in arthritis in clinical practice (114). Non-selective NSAIDs such as aspirin inhibit both COX-1 and COX-2 activity, as mentioned previously COX-1 is vital in many fundamental cellular processes compared to COX-2 which is predominantly found in incidents of tissue inflammation (114). With celecoxib an inhibitor selective to only COX-2, it provides the increased benefit when administered by not interfering with the common “housekeeping” tasks COX-1 needs to perform, whilst minimising inflammation and prevent such side effects gastrointestinal drug reactions (stomach ulcers) (115). There has been much speculation to whether celecoxib should be used in the clinical treatment of prostate cancer with literature showing some insight that celecoxib has the potential to influence the COX-2 pathway in AA metabolism.

An investigation carried out by Patel *et al.* aimed to identify whether celecoxib possesses anti-tumor properties (116). The human prostate cell lines PC-3 and LNCaP were used and subjected to a clinically achievable dose at $2.5 - 5 \mu\text{mol L}^{-1}$ throughout a 31-day course. The drug treated cells were compared against a control set treated with dimethyl sulfoxide (DMSO) only. COX-1 but not COX-2 was seen in both cell lines treated with celecoxib. It was suggested that celecoxib inhibited the cell growth of the PC-3 and LNCaP cell lines, blocking the G1 cell cycle reducing DNA synthesis. A follow up experiment was carried out using PC-3 xenografts. The celecoxib had a dose dependent effect on the PC-3 xenografts with respect to tumor volume and there was

no effect on intratumor PGE₂. The highest dose yielded the greatest tumor volume reduction of 52% also reducing cellular proliferation and MVD by 50%.

1.8 The Role of Adipocytes in Tumour Metastasis to the Bone

Once the tumour has invaded the bone, treatment becomes very limited and directed towards palliative care. Many different models have been studied over the years to show a prostate cancer cells migratory potential within the bone marrow stroma (BMS). Brown *et al.* carried out a particularly interesting study highlighting the importance of lipids in the mechanism of BMS invasion of the prostate cancer cells (117). Adipocytes are specialised cells which stores and produces fatty acids and triacylglycerides (118) as well as the mobilisation of fatty acids through lipolysis (119) which is a response to the energy metabolism of hormones, cytokines and many other factors (120). Brown *et al.* showed that when adipocyte formation was not stimulated in BMS grown in the absence of hydrocortisone there were dramatically reduced levels of BMS invasion. There is elevated excitement and interest over the mechanism and metabolism of the molecular species present within the adipocytes and how this influences the development and progression of prostate cancer. The interaction between the adipocyte and the prostate cancer cell is a key piece of information regarding the metastasis of prostate cancer. Tokuda *et al.* showed that when PC-3 cells were co-cultured with adipocytes both the proliferative rate increased and the differential growth pattern was altered (121). Oil Red O staining was used to show up neutral lipids, and the findings showed an elevated level of lipid droplets within the PC-3 cells cytoplasm showing an uptake of lipids from the adipocytes compared to a standard monoculture control of PC-3 cells.

1.9 Cell Cycle

The cell cycle is the mechanism by which cells divide and duplicate themselves to form genetically identical doubles. There are a number of checkpoints within the cell cycle by which the cell checks if the mechanism has been followed correctly, if the process has been incorrectly followed the checkpoint triggers apoptosis (122).

The process begins after the nuclear division of the previous cycle, the initial stage is termed G₁, whereby the cell readies itself for the beginning of DNA synthesis. The second stage of the of the cell cycle is the S-phase, where the cell undergoes DNA synthesis. The third stage of the cycle is the G₂ phase, this is the gap between DNA replication and nuclear division. Once the G₂ phase has finished, mitosis begins, which is the starting point of the cell division, whereby chromosomes in the nucleus are separate followed by the final stage of mitosis cytokinesis. This is where the cell splits into two daughter cells by cytoplasmic cleavage. After the cell has physically divided into two, the stage G₀ commences, where the cell is in growth arrest until signalled to commence the G₁ Phase once again. During the G₁ stage, there is a checkpoint which is a restriction point R, by which once the cell reaches this point in the cell cycle, the cell is fully committed in undergoing DNA synthesis. The R restriction point is found to be bypassed in malignant cells continuing the cell cycle allowing incorrect copies of cells to be permitted (122). The overall cell cycle is depicted in Figure 4.

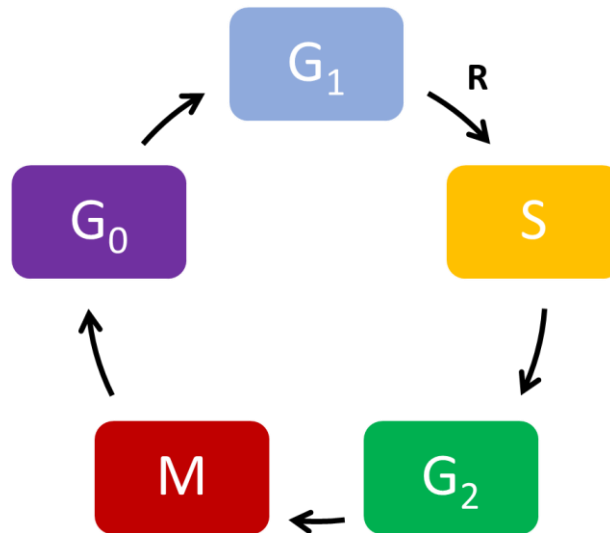


Figure 4 – Flow diagram of the cell cycle

1.10 Aims of Study

An evaluation has been presented on the current treatment options for prostate cancer in the United Kingdom. The treatment options are limited once prostate cancer has invaded and broken away from the localised prostate. The NHS currently takes a watchful approach if possible; meaning treatment is carried out only when the disease is worsening based on misleading PSA tests, biopsies and scans. There is a therapeutic need to assess the biochemical processes and changes the disease undertakes when it begins its metastatic journey. Currently, the metastatic chemical process is unclear in the progression of the disease. If the potential or potency of the invasiveness of prostate cancer can be limited or suppressed then the time taken for prostate cancer to metastasise will increase, hence making the watchful approach more effective as there will be smaller changes in disease progression which can be monitored incrementally over time. Patients with the disease will in turn have a sustained quality of life for a longer period of time, albeit limited to the stage in which the disease is detected.

There are clear geographical trends in prostate cancer incidence and mortality and westernised diets. There is an interest surrounding the role of AA in the progression of prostate cancer. The application of FT-IRM to biochemical metabolic processes has rarely been used, with little literature surrounding the use of FT-IRM on single cell analysis of prostate cancer. The first aim of the research is:

- To investigate the initial chemical effects of AA on invasive and non-invasive cell lines and determine whether FT-IRM is a sensitive enough tool in the biochemical evaluation of lipid metabolism.

The role of the COX-2 enzyme in prostate cancer progression is unclear, with the role controversial in literature. Many studies are suggestive that COX-2 plays a role in the progression of the disease. Although there are studies implying COX-2 has no effect on tumour progression. The second aim of this study is:

- To determine the chemical effect COX-2 has on AA uptake, metabolism and invasiveness by using the specific COX-2 inhibitor NS398.

The global lipid chemistry requires specificity. The tracking of AA requires unique vibrational signatures. Applying a deuterated tag could potentially provide a specific vibration around the C-D stretch. The omega-3 fatty acid DHA is known to have anti-inflammatory properties. The cellular uptake mechanisms for DHA and AA are similar. There is molecular competition between DHA and AA for the COX-2 enzyme. The third and fourth aims of this study are to:

- To investigate the cellular uptake of AA and COX-2 inhibition using a deuterated label
- To compare the COX-2 inhibitor NS398 to a competitive uptake mechanism using DHA

There are a few FT-IRM studies carried out at high magnification with a pixel size of $0.7 \times 0.7 \mu\text{m}$. A limitation to using high magnification is the low signal to noise ratio, making the identification of specific spectral features problematic. There is a need to identify the cellular lipid distribution. Nile-red is a fluorescent dye used to identify cellular lipids. The cellular motility is an essential feature for the invasion and metastatic process. The arrangement of highly proteinous actin filaments play a critical role in cellular motility and therefore invasion. The final aims of this study are to:

- To determine whether lipid distributions and cellular structure can be seen using high magnification FT-IR
- To use FM as a complementary technique to the FT-IRM chemical images to track lipid uptake and metabolism
- To investigate the protein structure in motile invasive prostate cancer cells through FT-IRM high magnification chemical imaging

References

- ¹ G. P. Haas, N. Delongchamps, O. W. Brawley, C. Y. Wang, G. D. L. Roza. The Worldwide Epidemiology of Prostate Cancer: Perspectives from Autopsy Studies. *Can J Urol.* 15 (2008) 2866-3871.
- ² D. M. Parkin. Global Cancer Statistics in the Year 2000. *Lancet Oncol.* 2 (2001) 533-543.
- ³ J. Ferlay, F. Bray, P. Pisani, D. M. Parkin. Global Cancer Statistics, 2002. *Ca Cancer J Clin.* 55 (2005) 74-108.
- ⁴ L. A. Torre, F. Bray, R. L. Siegel, J. Ferlay, J. Lortet-Tieulent, A. Jemal. Global cancer statistics, 2012 *CA Cancer J Clin.* 65(2015) 87-108.
- ⁵ L. A. Torre, F. Bray, R. L. Siegel, J. Ferlay, J. Lortet-Tieulent, A. Jemal. Global cancer statistics, 2012 *CA Cancer J Clin.* 65(2015) 87-108.
- ⁶ C. H. Pernar, E. M. Ebot, K. M. Wilson, L. A. Mucci. The Epidemiology of Prostate Cancer. *Cold Spring Harb Perspect Med.* 10 (2018) 69-87.
- ⁷ A. Jemal, F. Bray, M. M. Center, J. Ferlay, E. Ward, D. Forman. Global Cancer Statistics. *CA Cancer J Clin.* 61 (2011) 69-90
- ⁸ United Nations Population Division (2007). *World Population Prospects: The 2008 Revision.* New York: United Nations.
- ⁹ Prostate Cancer UK. 2017 *Are you at risk?* [ONLINE] available at: <https://prostatecanceruk.org/prostate-information/are-you-at-risk>. [Accessed 11 August 2018].
- ¹⁰ S. Siddiqui, S. Sengupta, J. Slezak, E. Bergstral. Impact of Patient Age at Treatment on Outcome Following Radical Retropubic Prostatectomy for Prostate Cancer. *J Urol.* 175 (2006) 952-957.
- ¹¹ R. Merrill, J. Bird. Effect of Young Age on Prostate Cancer Survival: A Population-Based Assessment United States. *Cancer Causes Control.* 13 (2002) 435-443.
- ¹² A. Ugnat, L. Xie, R. Semenciw, C. Waters, Y. Mao. Survival Patterns for the Top Four Cancers in Canada: The Effects of Age, Region and Period. *European J. of Cancer Prevention.* 14 (2005) 91-100.
- ¹³ D. W. Lin, M. Porter, B. Montgomery. Treatment and Survival Outcomes in Young Men Diagnosed with Prostate Cancer: A Population Based Cohort Study. *Cancer.* 115 (2009) 2863-2871.
- ¹⁴ Cancer Research UK. 2018. *Incidence of Prostate Cancer.* [ONLINE] Available at: <https://www.cancerresearchuk.org/health-professional/cancer-statistics/statistics-by-cancer-type/prostate-cancer/incidence#heading-One>. [Accessed 27 July 2018].
- ¹⁵ P. Kheirandish, F. Chingwundoh. Ethnic Differences in Prostate Cancer. *Br J Cancer.* 105 (2011) 481-485.
- ¹⁶ G. Aus, C. C. Abbou, M. Bolla, A. Heidenreich, H. P. Schmid, H. V. Poppel, J. Wolff, F. Zattoni. EAU Guidelines on Prostate Cancer. *Eur Urol.* 48 (2005) 546-551.
- ¹⁷ B. K. Edwards, M. L. Brown, P. A. Wingo, H. L. Howe, E. Ward, L. A. Ries, D. Schrag, P. M. Jamison, A. Jemal, X. C. Wu, C. Friedman, L. Harlan, J. Warren, R. N. Anderson, L. W. Pickle. Annual Report to the Nation on the Status of Cancer. *J Natl Cancer Inst.* 97 (2005) 1407-1427.
- ¹⁸ Y. Ben-Shlomo, S. Ekan, F. Ibrahim, B. Patel, K. Anson, F. Chingwundoh, C. Corbishley, D. Doring, B. Thomas, D. Gullatt, R. Kirby, G. Muir, V. Nargund, R. Popert, C. Metcalfe, R. Persad. The Risk of Prostate Cancer Amongst Black Men in the United Kingdom: The PROCESS Cohort Study. *Eur Urol.* 53 (2008) 99-105.
- ¹⁹ N. K. Khankari, H. J. Murff, C. Zeng, W. Wen, R. A. Eeles, D. F. Easton, Z. Kote-Jarai, A. A. Olama, S. Benlloch, K. Muir, G. G. Giles, F. Wiklund, H. Gronberg, C. A. Haiman, J. Schleutker, B. G. Nordestgaard, R. C. Travis, J. L. Donovan, N. Pashayan, K. T. Khaw, J. L. Stanford, W. J. Blot, S. N. Thibodeau, C. Maier, A. S. Kibel, C. Cybulski, L. Cannon-Albright, H. Brenner, J. Park, R. Kaneva, J. Batra, M. R. Teixeira, H. Pandha, W. Zheng. Polyunsaturated Fatty Acids and Prostate Cancer Risk: A Mendelian Randomisation Analysis from the PRACTICAL Consortium. *Br J Cancer.* 115 (2016) 624-631.
- ²⁰ D. D. Alexander, J. K. Bassett, D. L. Weed, E. Cernkovich, B. H. Watson, W. Harris. Meta-Analysis of Long-Chain Omega-3 Polyunsaturated Fatty Acids (LCω-3PUFA) and Prostate Cancer. *Nutr Cancer.* 67 (2015) 543-554.
- ²¹ C. Sobolewski, C. Cerella, M. Dicato, L. Ghibelli, M. Diederich. The Role of Cyclooxygenase-2 in Cell Proliferation and Cell Death in Human Malignancies. *Int J Cell Biol.* 215 (2010) 8-17.
- ²² E. Bidoli, R. Talamini, C. Bosetti, E. Negri, D. Maruzzi, M. Montella, S. Franceschi. *La Vecchia* (2005) *C Ann Oncol.* 16 (2005) 152-157.

- ²³ Y. Li, A. Hruby, A. M. Bernstein, S. H. Ley, D. Dong, S. E. Chiuve, L. Sampson, K. M. Rexrode, R. B. Rimm, W. C. Willett, F. B. Hu. Saturated Fats Compared With Unsaturated Fats and Sources of Carbohydrates in Relation to Risk of Coronary Heart Disease: A Prospective Cohort Study. *J. Amer Col Cardio.* 66 (2015) 1538-1548.
- ²⁴ A. P. Simopoulos. An Increase in the Omega-6/Omega-3 Fatty Acid Ratio Increases the Risk for Obesity. *Nutrients.* 8 (2016) 128-132.
- ²⁵ D. Mazhar, J. Waxman. Prostate Cancer. *Post med Journal.* 78 (2002) 590-595.
- ²⁶ J. T. Helgstrand, M. A. Roder, N. Klemann, B. G. Toft, K. Brasso, B. Vainer, P. Iversen. Diagnostic Characteristics of Lethal Prostate Cancer. *Eur J Can.* 84 (2017) 18-26.
- ²⁷ G. W. Chodak, The Role of Watchful Waiting in the Management of Localized Prostate Cancer. *J Urol.* 152 (1994) 1766-1768.
- ²⁸ C. W. Tsao, M. H. Lin, S. T. Wu, E. Meng, S. H. Tang, H. I. Chen, G. H. Sun, D. S. Yu, S. Y. Chang, T. L. Cha. Combining Prostate-Specific Antigen and Gleason Score Increases the Diagnostic Power of Endorectal Coil magnetic Resonance Imaging in Prostate Cancer Pathological Stage. *J Chin Med Ass.* 76 (2013) 20-24.
- ²⁹ P. C. Walsh, Anatomic Radical Prostatectomy: Evolution of the Surgical Technique. *J Urol.* 160 (1998) 2418-2424.
- ³⁰ J. R. Marshall, M. R. King. Surgical Intervention and Circulating Tumour Cell Count: A commentary. *Trans Can Res.* 5 (2016) 1-6.
- ³¹ L. R. Schover, M. V. D. Kaaij, R. V. Dorst, C. Creutzberg, E. Huyghe, C. E. Kiserud. Sexual Dysfunction and Infertility as Late Effects of Cancer Treatment. *Eur J Can Supp.* 12 (2014) 41-53.
- ³² M. Bolla, H. V. Poppel, L. Collette, P. V. Cangel, K. Vekemans, L. D. Pozzo, T. M. Reijke, A. Verbaeys, J. F. Bosset, R. V. Velthoven, J. M. Marechal, P. Scalliet, K. Haustermans, M. Pierart. Postoperative Radiotherapy After Radical Prostatectomy: A Randomised Controlled Trial (EORTC Trial). *Lancet.* 336 (2005) 572-578.
- ³³ N. N. Stone, R. G. Stock. Prostate Brachytherapy: Treatment Strategies. *J Urol.* 162 (1999) 421-426.
- ³⁴ C. L. Deufel, K. M. Furutani, R. A. Dahl, M. P. Grans, L. B. McLemore, C. L. Hallemeier, M. N. Wittich, J. A. Martenson, M. G. Haddock. Technique for the Administration of High-Dose-Rate Brachytherapy to the Bile Duct Using a Nasobiliary Catheter. *Brachytherapy.* 17 (2018) 718-725.
- ³⁵ D. M. Marcus, A. B. Jani, K. Godette, P. J. Rossi. A Review of Low-Dose-Rate Prostate Brachytherapy – Techniques and Outcomes. *J Nat Med Ass.* 102 (2010) 500-510.
- ³⁶ A. D. Rivera, A. M. Garcia, J. J. Escudero, P. G. Abad, M. F. Arjona, E. L. Alcina. High-Intensity Focused Ultrasound Therapy for the Treatment of Prostate Cancer: Medium-Term Experience. *Actas Urol Esp.* 18 (2017) 1-7.
- ³⁷ L. Mearini, L. D’Urso, D. Collura, E. Nunzi, G. Muto, M. Porena. High-Intensity Focused Ultrasound for the Treatment of Prostate Cancer: A Prospective Trial with Long-Term Follow-Up. *Scand J Urol.* 49 (2015) 267-274.
- ³⁸ F. D. Canet, F. S. Gallego, G. A. Funez, I. D. Ruiz, J. Laso, J. B. Burgos, V. L. Alvaro, R. G. D. Santos, F. R. Patron, J. B. Revilla. Cryotherapy Versus High-Intensity Focused Ultrasound for Treating Prostate Cancer: Oncological and Functional Results. *Actas Urol Esp.* 42 (2018) 355-364.
- ³⁹ A. S. M. Ali, H. Smith, D. Greene. Current Status of Cryotherapy in Prostate Cancer. *Brit J Med Surgical Urol.* 5 (2012) 35-38.
- ⁴⁰ R. F. Wolff, S. Ryder, A. Bossi, A. Briganti, J. Crook, A. Henry, J. Karnes, L. Potters, T. D. Reike, N. Stone, M. Burckhardt, S. Duffy, G. Worthy, J. Kleijnen. A Systematic Review of Randomised Controlled Trials of Radiotherapy for Localised Prostate Cancer. *Eur J Can.* 51 (2015) 2345-2367.
- ⁴¹ L. F. Kluskens. *Comprehensive Cytopathology* 3rd Edition. Philadelphia: Saunders.
- ⁴² Prostate Cancer UK. 2018. *Transurethral resection of the prostate (TURP)*. [ONLINE] Available at: <https://prostatecanceruk.org/media/758948/turp-fact-sheet.pdf>. [Accessed 20 August 2018].
- ⁴³ M. B. Garnick. Hormonal Therapy in the Management of Prostate Cancer: From Huggins to the Present. *Urol.* 49 (1997) 5-15.
- ⁴⁴ J. S. Lam, J. T. Leppert, S. N. Vemulapalli, O. Shvarts, A. S. Belldegrun. Secondary Hormonal Therapy for Advanced Prostate Cancer. *J Urol.* 175 (2006) 27-34.
- ⁴⁵ J. A. Smith, M. S. Soloway, M. J. Young. Complications of Advanced Prostate Cancer. *Urol.* 54 (1999) 8-14.
- ⁴⁶ S. Nilsson. Radium-223 Therapy of Bone Metastases in Prostate Cancer. *Seminars in Nuc Med.* 46 (2016) 544-556.

- ⁴⁷ M. D. Santis, F. Saad. Practical Guidance on the Role of Corticosteroids in the Treatment of Metastatic Castration-Resistant Prostate Cancer. *Urol.* 96 (2016) 156-164.
- ⁴⁸ M. Wahab, O. Silva. *Prostate Cancer*, 1st Edition. Philadelphia: Saunders.
- ⁴⁹ K. Garber. A Tale of Two Cells: Discovering the Origin of Prostate Cancer. *J. of the National Cancer Institute.* 102 (2010) 1528-1529.
- ⁵⁰ D. Moscatelli, E. L. Wilson. Pining Down the Origin of Prostate Cancer. *Sci Transl. Med.* 2 (2010) 38-48.
- ⁵¹ A. S. Goldstein, J. Huang, C. Guo, I. P. Garraway, O. N. Witte. Identification of a Cell of Origin for Human Prostate Cancer. *Sci.* 329 (2010) 568-571.
- ⁵² Z. Wang, R. Toivanen, S. Bergren P. Chambon, M. Shen Luminal Cells are Favoured as the Cell of Origin for Prostate Cancer. *J. of cellrep.* 8 (2014) 1339-1346.
- ⁵³ C. Huggins, C. V. Hodges. Studies on Prostatic Cancer: I. the Effect of Castration, of Estrogen, and of Androgen Injection on Serum Phosphates in Metastatic Carcinoma of the Prostate. *Cancer Res.* 1 (1941) 293-297.
- ⁵⁴ B. Kahn, J. Callazo, N. Kyprinanou. Androgen Receptor as a Driver of Therapeutic Resistance in Advanced Prostate Cancer. *J. of Biology.* 10 (2014) 588-595.
- ⁵⁵ M. Bolla. Long-Term Results with Immediate Androgen Suppression and External Irradiation in Patients with Locally Advanced Prostate Cancer (an EORTC Study): A Phase III Randomised Trial. *J. of Oncology.* 360 (2002) 103-108.
- ⁵⁶ P. Msaouel, N. Pissimissis, A. Halapas, M. Koutsilieris. Mechanisms of Bone Metastasis in Prostate Cancer: Clinical Implications. *J. of Endocrinology & Metabolism.* 22 (2008) 341-355.
- ⁵⁷ S. Dutt, A. Gao. Molecular mechanisms of castration-resistant prostate cancer progression. *Future Oncol.* 5 (2009) 1403-1413.
- ⁵⁸ A. Hobisch, H. Rogatsch, A. Hittmair, D. Fuchs, G. Bartsch, H. Klocker, G. Bartsch, Z. Culig. Immunohistochemical localization of interleukin-6 and its receptor in benign, premalignant and malignant prostate tissue. *J Pathol.* 191 (2000) 239-244.
- ⁵⁹ I. J. Fidler. The Pathogenesis of Cancer Metastasis: The 'Seed and Soil' Hypothesis Revisited. *Nat Rev Can.* 3 (2003) 453-458.
- ⁶⁰ M. Arya, S. Bott, I. Shergill. H. Ahmed, M. Williamson, H. Patel. The Metastatic Cascade in Prostate Cancer. *J. of Androl.* 11 (2006) 117-128.
- ⁶¹ T. Devita, R. Young, G. Canellos. Combination Versus Single Agent Chemotherapy, A Review of the Basis for Selection of the Drug Treatment of Cancer. *J. of Cancer.* 35 (1975) 98-110.
- ⁶² L. Foulds. The Experimental Study of Tumour Progression. *J. of Cancer Res.* 14 (1964) 327-339.
- ⁶³ R. Vartanian, N. Weidner. Endothelial Cell Proliferation in Prostatic Carcinoma and Prostatic Hyperplasia: Correlation with Gleason's Score, Microvessel Density and Epithelial Cell Proliferation. *J. of Lab Invest.* 73 (1995) 844-850.
- ⁶⁴ S. H. Lin, Y. S. Pu. Function and Therapeutic Implication of C-CAM Cell-Adhesion Molecule in Prostate Cancer. *Semin Oncol.* 26 (1999) 227-233.
- ⁶⁵ S. Brady, G. Siegel, R. W. Albers, D. Price (2011). *Basic Neurochemistry (Eighth Edition) – Principles of Molecular, Cellular, and Neurobiology.* Academic Press: Cambridge.
- ⁶⁶ D. Coman. Decreased Mutual Adhesiveness, A Property of Cells from Squamous Carcinomas. *J. of Cancer Res.* 20 (1944) 1202-1204.
- ⁶⁷ J. Behrens, M. Mareel, F. Roy. Dissecting Tumour Cell Invasion: epithelial Cells Acquire Invasive Properties After Loss of Uvomorulin-Mediated Cell Adhesion. *J. of Cell Biology.* 108 (1989) 2435-2437.
- ⁶⁸ M. Edlund, T. Miyamoto, R. Sikes, R. Ogle, G. Laurie, M. Farach-Carson, C. Otey, H. Zhau, L. Chung. Integrin Expression and Usage by Prostate Cancer Cell Lines on Laminin Substrata. *Cell Growth Differ.* 12 (2001) 99-107.
- ⁶⁹ M. Sanda, N. Restifo, J. Walsh, Y. Kawakami, W. Nelson, D. Pardol, J. Simons. Molecular Characterization of Defective Antigen Processing in Human Prostate Cancer. *J Natl Cancer Inst.* 87 (1995) 280-285.
- ⁷⁰ M. Trikha, E. Raso, Y. Cai, Z. Fazakas, S. Paku, A. Porter, J. Timar, K. Honn. Role of $\alpha\text{IIb}\beta\text{3}$ Integrin in Prostate Cancer Metastasis. *The Prostate.* 35 (1998) 185-192.
- ⁷¹ C. Coghlin, G. Murray. Current and Emerging Concepts in Tumour Metastasis. *J. of Pathol.* 1 (2010) 1-15.
- ⁷² A. Fanning, L. Mitic, J. Anderson. Transmembrane Proteins in the Tight Junction Barrier. *J Biol.* 6 (1999) 1337-1345.

- ⁷³ T. Martin, W. Jiang. Loss of Tight Junction Barrier Function and its Role in Cancer Metastasis. *J Biochem.* 6 (2009) 872-891.
- ⁷⁴ N. Utoguchi, H. Mizuguchi, A. Dantakean, H. Makimoto, Y. Wakai, Y. Tsutsumi. Effect of Tumour Cell-Conditioned Medium on Endothelial Macromolecular Permeability and its correlation with Collagen. *J Can.* 1 (1996) 24-28.
- ⁷⁵ L. Shen, C. Weber, D. Rayleigh, D. Yu, J. Turner. Tight Junction Pore and Leak Pathways: A Dynamic Duo. *Annual Review Physiology.* 73 (2011) 283-309.
- ⁷⁶ T. Martin. The Role of Tight Junctions in Cancer Metastasis. *Seminars in Cell and Developmental Biology.* 26 (2014) 244-231.
- ⁷⁷ L. Bubendorf, A. Schopfer, U. Wagner, G. Sauter, H. Moch, N. Willi, T. C. Gasser, M. J. Mihatsch. Metastatic Patterns of Prostate Cancer: An Autopsy Study of 1,589 Patients. *Human Pathol.* 31(2000) 578-583.
- ⁷⁸ K. Honn, D. Tang. Adhesion molecules and tumour cell interaction with endothelium and subendothelial matrix. *Cancer Metastasis Rev.* 11 (1992) 353-375
- ⁷⁹ S. Martensson, S. Bigler, M. Brown, P. Lange, M. Brawler, S. Hakomori. Sialyl-Lewis(X) and Related Carbohydrate Antigens in the Prostate. *J. of Human Pathology.* 26 (1995) 735-739.
- ⁸⁰ C. Cooper, C. Chay, K. Pienta. The role of alpha(v)beta(3) in prostate cancer progression. *Neoplasia.* 4 (2002) 191-194.
- ⁸¹ A. Rachlin, N. Wasylim. M. Goldberg. Synthesis of Arachidonic Acid. *J. of Organic Chemistry.* 26 (1961) 2688 – 2693.
- ⁸² P. K. Pandalai, M. J. Pilat, K. Yamazaki, H. Naik, K. J. Pienta. The Effects of Omega-3 and Omega-6 Fatty Acids on *in vitro* Prostate Cancer Growth. *Anticancer Res.* 16 (1996) 815-820.
- ⁸³ J. Ghosh, C. E. Myers. Arachidonic Acid Stimulates Prostate Cancer Cell Growth: Critical Role of 5-Lipoxygenase. *Biochem Biophys Res Commun.* 235 (1997) 418–423.
- ⁸⁴ D. P. Rose, J. M. Connolly. Effects of Fatty Acids and Eicosanoid Synthesis Inhibitors on the Growth of Two Human Prostate Cancer Cell Lines. *Prostate.* 18 (1991) 243–254.
- ⁸⁵ I. M. Berquin, Y. Min, R. Wu, J. Wu, D. Perry, J. M. Cline, M. J. Thomas, T. Thornburg, G. Kulik, A. Smith, I. J. Edwards, H. Zhang, H. Wu, J. X. Kang, Y. Q. Chen. Modulation of Prostate Cancer Genetic Risk by Omega-3 and Omega-6 Fatty Acids. *J Clin Invest.* 117 (2005) 1866–1875.
- ⁸⁶ P. Yang, C. Cartwright, J. Li, S. Wen, I. Prokhorova, I. Shureiqi, P. Troncoso, N. Navone, R. Newman, J. Kim. Arachidonic Acid Metabolism in Human Prostate Cancer. *International J. of Oncology.* 41 (2012) 1495-1503.
- ⁸⁷ M. Aucoin, K. Cooley, C. Knee, H. Fritz, L. G. Balneaves, R. Breau, D. Fergusson, B. Skidmore, R. Wong, D. Seely. Fish-Derived Omega-3 Fatty Acids and Prostate Cancer: A Systematic Review. *integr Cancer Ther.* 16 (2017) 32-62.
- ⁸⁸ A. Chaudry, K. Wahle, S. M. Clinton, L. Moffat. Arachidonic Acid Metabolism in Benign and Malignant Prostatic Tissue in Vitro: Effects of Fatty Acids and Cyclooxygenase Inhibitors. *Int J. of Cancer.* 57 (1994) 176-180.
- ⁸⁹ H. Higgs, S. Moncada, J. Vane. Eicosanoids in Inflammation. *Anne Clin Res.* 16 (1984) 287-299.
- ⁹⁰ I. I. Peleg, M. Wilcox. The Role of Eicosanoids, Cyclooxygenases, and Nonsteroidal Anti-Inflammatory Drugs in Colorectal Tumorigenesis and Chemoprevention. *J. of Clin Gastro.* 2002 (34) 117-125.
- ⁹¹ J. L. Masferrer, K.M. Leahy, A. T. Koki, B. S. Zweifel, S. L. Settle, B. M. Woerner, D. A. Edwards, A. G. Flickinger, R. J. Moore, K. Seibert. Antiangiogenic and Antitumor Activities of Cyclooxygenase-2 Inhibitors. *Cancer Research.* 60 (2000) 1306-1311.
- ⁹² C. Sobolewski, C. Cerella, M. Dicato, L. Ghibelli, M. Diederich, The Role of Cyclooxygenase-2 in Cell Proliferation and Cell Death in Human Malignancies. *Int. J of Cell Bio.* 2010 (2010) 0-21.
- ⁹³ N. V. Chandrasekharan, D. L. Simmons. The Cyclooxygenases. *J. of Genome Biology.* 5 (2004) 241.
- ⁹⁴ P. J. Jakobsson, W. L. Smith, Y. Urade. Enzymes of the Cyclooxygenase Pathways of Prostanoid Biosynthesis. *Chem Review.* 111 (2011) 5821-5865.
- ⁹⁵ J. R. Vane, Y. S. Bakhle, R. M. Botting. Cyclooxygenases 1 and 2. *Annu Rev Pharmacol Toxicol.* 38 (1998) 97-120.
- ⁹⁶ M. Pairet, G. Engelhardt, Distinct isoforms (COX-1 and COX-2) of cyclooxygenase: possible physiological and therapeutic implications, *Fundam. Clin. Pharmacol.* 10 (1996) 1–17.
- ⁹⁷ J. C. Otto, W. L. Smith. Prostaglandin Endoperoxide Synthases-1 and -2, *J. Lipid Mediat. Cell Signal.* 12 (1995) 139–156.

- ⁹⁸ A. Kirschenbaum, X. H. Liu, P. Adam, R. Lee, P. Unger, A. C. Levine, S. Yao . NS398, A Selective Cyclooxygenase-2 Inhibitor, Induces Apoptosis and Downregulates bcl-2 Expression in LNCaP cells. *Cancer Res.* 58 (1998) 4245–4249.
- ⁹⁹ V. Fradet, L. Cheng, G. Casey, J. S. Witte. Dietary Omega-3 FattyAcids, Cyclooxygenase-2 GeneticVariation and Aggressive Prostate Cancer Risk. *Clinical Cancer Res.* 15 (2009) 2559-2566.
- ¹⁰⁰ N. I. Patel, C. Kurek, Q. Dong. The Arachidonic Acid Pathway and its Role in Prostate Cancer Development and Progression. *J. of Urology.* 179 (2008) 1668-1675.
- ¹⁰¹ W. Wang, A. Bergh, J. E. Damber. Cyclooxygenase-2 Expression Correlates with Local Chronic Inflammation and Tumor Neovascularization in Human Prostate Cancer. *Clin Cancer Res.* 11 (2005) 3250-3256.
- ¹⁰² X. H. Liu, A. Kirschenbaum, S. Yao, R. Lee, J. F. Holland, A. C. Levine. Inhibition of Cyclooxygenase-2 Supresses Angiogenesis and the Growth of Prostate Cancer in Vivo. *J. of Urology.* 164 (2000) 820-825
- ¹⁰³ S. M. Prescott, F. A. Fitzpatrick. Cyclooxygenase-2 and carcinogenesis, *Biochim. Biophys Acta.* 1470 (2000) 69–78.
- ¹⁰⁴ M. Hughes-Fulford, R. R. Tjandrawinata. Up-regulation of Cyclooxygenase-2 by Product-prostaglandin E2. *Adv Exp Med Biol.* 407 (1997) 163-170.
- ¹⁰⁵ J.M. Connolly, M. Coleman, D.P. Rose, Effects of dietary fatty acids on DU145 human prostate cancer cell growth in athymic nude mice, *Nutr. Cancer* 29 (1997) 114–119.
- ¹⁰⁶ T. Hussain, S. Gupta, H. Mukhtar. Cyclooxygenase-2 and Prostate Carcinogenesis. *Cancer Lett.* 191 (2003) 125-135.
- ¹⁰⁷ R. Yoshimura, H. Sano, C. Masuda, M. Kawamura, Y. Tsubouchi, J. Chargui, N. Yoshimura, T. Hla, S. Wada, Expression of Cyclooxygenase-2 in Prostate Carcinoma. *Cancer.* 89 (2000) 589–596.
- ¹⁰⁸ S. Madaan, P. D. Abel, K. S. Chaudhary, R. Hewitt, M. A. Stott, G. W. Stamp, E. N. Lalani, Cytoplasmic Induction and Overexpression of Cyclooxygenase-2 in Human Prostate Cancer: Implications for Prevention and Treatment, *BJU Int.* 86 (2000) 736–741.
- ¹⁰⁹ R. R. Tjandrawinata, R. Dahiya, M. Hughes-Fulford. Induction of Cyclooxygenase-2 mRNA by Prostaglandin E2 in Human Prostatic Carcinoma Cells. *Br J Cancer.* 75 (1997) 1111-1118.
- ¹¹⁰ S. Zha, W.R. Gage, J. Sauvageot, E.A. Saria, M.J. Putzi, C.M. Ewing, D.A. Faith, W.G. Nelson, A.M. De Marzo, W.B. Isaacs, Cyclooxygenase-2 is up-regulated in proliferative inflammatory atrophy of the prostate, but not in prostate carcinoma, *Cancer Res.* 61 (2001) 8617–8623.
- ¹¹¹ V. Subbarayan, A.L. Sabichi, N. Llansa, S.M. Lippman, D.G. Menter. Differential Expression of Cyclooxygenase-2 and its Regulation by Tumor Necrosis Factor-alpha in Normal and Malignant Prostate Cells. *Cancer Res.* 61 (2001) 2720–2726.
- ¹¹² S. H. Hong, I. Avis, M. D. Vos, A. Martinez, A. M. Treston, J. L. Mulshine. Relationship of Arachidonic Acid Metabolizing Enzyme Expression in Epithelial Cancer Cell Lines to the GrowthEffect of Selective Biochemical Inhibitors, *Cancer Res.* 59 (1999) 2223–2228.
- ¹¹³ I. G. E. Zarraga, E. R. Schwarz. Coxibs and Heart Disease: What We Have Learned and What Else We Need to Know. *J Am Coll Cardiol.* 49 (2007) 1-14.
- ¹¹⁴ J. R. Vane, R. M. Botting. Mechanism of Action of Aspirin-Like Drugs. *Semin Arthritis Rheum.* 26 (1997) 2-10.
- ¹¹⁵ P. L. McCormack. Celecoxib: A Review of its Use for Symptomatic Relief in the Treatment of Osteoarthritis, Rheumatoid Arthritis and Ankylosing Spondylitis. *Drugs.* 71 (2011) 2457-2489.
- ¹¹⁶ M. I. Patel, K. Subbaramaiah, B. Du, M. Chang, P. Yang, R. A. Newman, C. Cordon-Cardo, H. T. Thatcher, A. J. Dannenberg. Celecoxib Inhibits Prostate Cancer Growth: Evidence of a Cyclooxygenase-2 Independent Mechanism. *Clin Cancer Res.* 11 (2005) 1999-2007.
- ¹¹⁷ M. D. Brown, C. A. Hart, E. Gazi, S. Bagley, N. W. Clarke. Promotion of Prostatic Metastatic Migration Towards Human Bone Marrow Stroma by Omega 6 and its Inhibition by Omega 3 PUFAs. *Br J Cancer.* 94 (2006) 842-853.
- ¹¹⁸ M. Ooktens, D. Montisano, I. Lyon, N. Baker. Transport and Metabolism of Extracellular Free Fatty Acids in adipose Tissue of Fed and Fasted Mice, *J. of Lipid Res.* 28 (1997) 528-539.
- ¹¹⁹ J. Sethi, G. Hotamisligril, The role of TNF-Alpha in Adipocyte Metabolism. *J. of Cellular Biology.* 10 (1999) 19-29.
- ¹²⁰ P. Kopelman (2003). Effects of Obesity Fat Topography: Metabolic and Endocrine Determinants. Oxford: Blackwell Science.

-
- ¹²¹ Y. Tokuda, Y. Satoh, C. Fukiyama, S. Toda, H. Sugihara, Z. Masaki. Prostate Cancer Cell Growth is Modulated by Adipocyte-Cancer Cells Interaction. *J. of Cellular Biology*. 91 (2003) 716-720.
- ¹²² B. Alberts, A. Johnson. J. Lewis (2002). *Molecular Biology of the Cell* 4th Edition. New York: Garland Science

Chapter 2

Experimental Theory and Methodology

2.1 Fundamental Culture Concepts

Within a cell, there are macromolecules such as phospholipids and proteins which bind to water molecules, these water molecules exist mainly in the cell cytosol, contributing to the cell's signalling, functionality and structure (1). Therefore, the removal or input of water to a cell will alter the biochemical functionality of a cell, in turn placing great importance to the culturing and experimental technique when analysing biochemical cellular behaviour. There are contradicting arguments within literature regarding the best experimental culturing techniques, making it paramount to gain an understanding and establish the most suitable culturing procedure.

A classic protocol directly cultures the cells onto the FT-IRM substrate within the medium, eventually removing the culture medium and leaving the substrates to air dry (2,3). A large proportion of literature suggests that the air-drying process causes noticeable delocalisation of biological molecules (4). This effect is said to be due to the large surface tension created from the air-water interface. Other members of the research community have used techniques such as cytopinning, whereby the cells are removed from the culture medium and centrifuged to concentrate low cell populations onto the substrate (5,6). This technique is well used in the field, but its harshness is not suitable to analyse subtle mechanistic biochemical changes. With a large degree of cells rupturing when spun onto the substrate, changing the cells native biochemical structure and distribution. Another technique which is used for cell drying is with nitrogen gas (7). This is said to reduce oxidative and surface tension effects although is usually associated with snap freezing (8). Another potential drying technique involves drying the sample with a centrifuge, usually requiring the substrate to be placed on tissue paper within a centrifuge tube, followed by centrifugation, resulting in rapid removal of the

liquid film above the cell monolayer, reducing surface tension effects (9). This technique comes with drawbacks of high-energy consumption and centrifuge parts are prone to mechanical wear requiring maintenance frequently (10).

The osmotic potential between the cell and its environment also needs consideration when choosing the culture medium. A change in osmotic potential can result in cell rupturing from swelling or shrinking (1). Another important point is that once the cell is dry or is drying, adequate quenching needs to be implemented as the drying process can commence autolytic progressions within the cell, with enzymes potentially degrading important macromolecule metabolites (11) fundamental to the study attempting to elucidate mechanistic features of the mesenchymal to amoeboid structural phenotype of PC-3 cells. A way to solve quenching issues and the autolysis of the cell, fixation is pivotal.

2.1.1 Cell Fixation

Fixation is an essential step in preserving the biochemical characteristics of a cell. Gazi *et al.* studied three suitable fixation processes for cultured substrates FT-IR analysis (4). The study aimed to give clear differentiation between three fixative methods. First of which placed the sample in 4% formalin in phosphate buffer solution (PBS) for 20 minutes, then rinsed in double deionised water for 3 seconds and air dried. The water rinse step proved a critical step in the fixation, removing the residual PBS from the cell surface, allowing greater differentiation of the nuclear and cytoplasmic compartments, as well as reducing Mie Scattering. FT-IR spectroscopic analysis was carried out on the effect of formalin on the cell spectra where a neat formalin spectrum was subtracted from the cell spectra and minimal intensity difference was seen in the region of 1100

cm^{-1} to 3000 cm^{-1} . The second method entailed fixing the cells with formalin as mentioned above but critical point dried (CPD). The CPD procedure initially increased the ethanol concentration within the cell environment to gradually displace the intracellular water. The ethanol is further displaced by acetone (miscible with liquid CO_2), the acetone within the cell been finally displaced by liquid CO_2 within a sealed chamber. This chamber is heated, an increase in pressure causing the CO_2 to evaporate. At a given temperature and pressure, the density of the vapour equals that of the liquid water phase reducing the water-vapour film almost eliminating the surface tension effect. As alcohol is used for this method, it would not be suitable for use in a lipidomic study as lipid leaching reagents (ethanol and acetone) decrease the intensity in the lipid ester $\nu_s(\text{C}=\text{O})$ band in FT-IR analysis. The third fixation method involved using glutaraldehyde and osmium tetroxide as a replacement for formalin followed by CPD. The aldehyde group reacts with cellular proteins to form irreversible imines, followed by the post fixation using osmium tetroxide, which forms irreversible cyclic esters preserving unsaturated lipids. This technique would not be suitable for the analysis of lipids in the mesenchymal to amoeboid phenotype transition as this technique distorts the lipid ester $\nu_s(\text{C}=\text{O})$ band and reduces the intensity between $1000\text{-}1500\text{ cm}^{-1}$ (4).

Another study carried out by Gazi *et al.* directly relates to the study of interest (12). Fat storage adipocyte cells were chemical fixed and examined using synchrotron radiation FT-IR spectroscopy. A 20-minute fixation using 4% formalin in PBS followed by a double deionized water wash and then left to air drying was used in this analysis. It was said that the fixation process was appropriate for fixing a PC-3 cell line but there was an effect on the lipid arrangement within the adipocyte. A number of disadvantages were highlighted by using this fixation process. Firstly, the PBS contains 1% methanol,

which in turn permeates the cell membrane albeit allowing faster fixation, but the methanol extracts extracellular lipids. Secondly, the air-drying creates surface tension effects. The fixation process is seen to decrease the symmetric and anti-symmetric vibrational modes of the CH₂ and CH₃ modes which would be expected with the 1% methanol present in the PBS. From studies made from Gazi *et al.* and other literature in the field, a flow mechanism has been created to best highlight the options of fixation and drying, seen in Figure 5. It must be noted that, to date, no ideal fixative has been discovered, meaning the choice is a trade-off between preserving morphology and maintaining chemical composition (13).

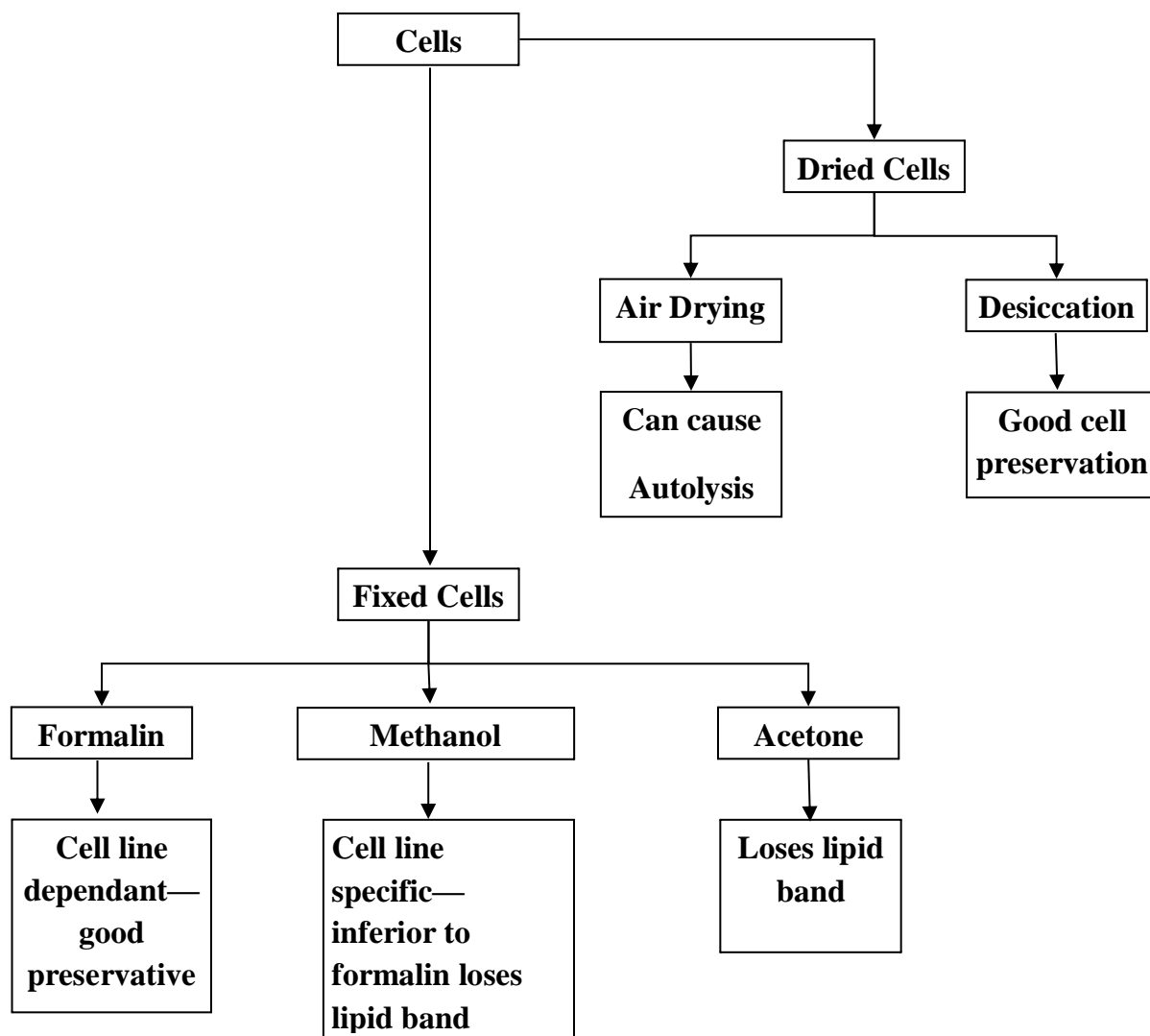


Figure 5 - Cell culturing methods decision diagram

2.1.2 Formalin Fixation Chemical Mechanisms

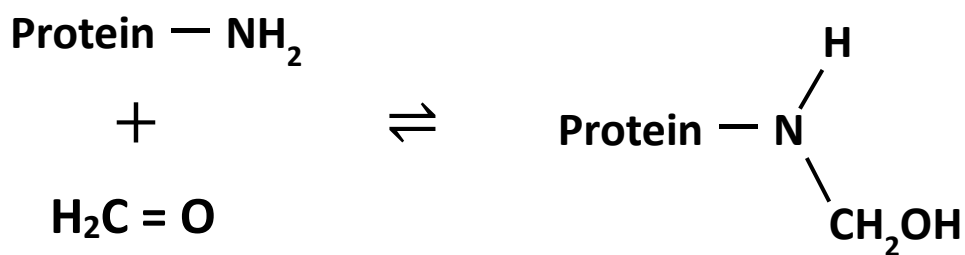
By examining the literature, formalin fixation appears to be the best fixation method for this study. Formalin fixation preserves the proteins, carbohydrates and any bio-active species, maintaining the spatial distribution of species within the cell (14), meaning the process is critical in examining molecular distributions through FT-IRM. In aqueous solution, formalin is hydrated to methylene glycol (15). Formalin simply acts as a

protein coagulative as a consequence of forming cross-links in the primary and secondary amine groups of proteins (16).

2.1.2.1 The Reaction of Formalin

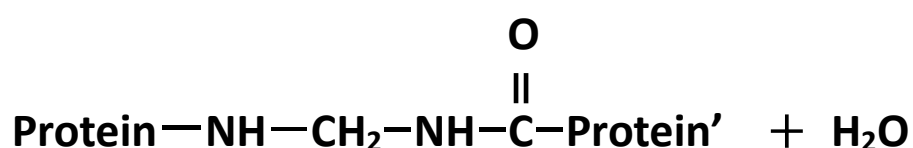
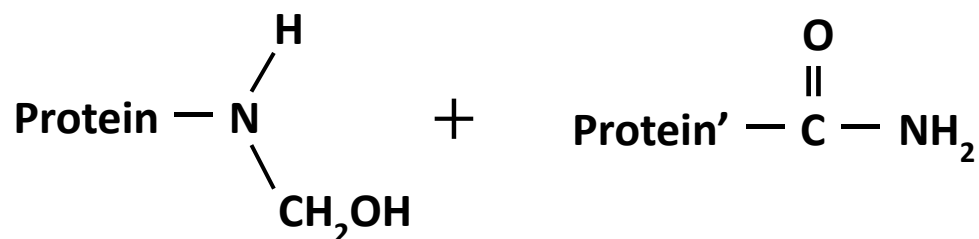
Formalin is a reactive electrophile which initially reacts with proteins to form a link, shown in reaction 1.

Reaction 1



The second reactive stage involves the cross linking of a protein by a CH₂ species through a condensation reaction, known as a methylene bridge (17). It must be noted that other functional groups can be involved in the methylene bridge such as amides and tyrosine carbon rings (18). The example reaction can be seen in reaction 2 below.

Reaction 2



There are a number of factors which influence the effectiveness of formalin fixation. Assuming that the concentration gradient is fixed, then diffusion of formalin can be described through Fick's first law of diffusion shown in equation 1.

$$J_i = \frac{DC_i \partial u_i}{RT \partial x} \quad \text{Equation 1}$$

Where J_i is the diffusion flux ($\text{mol m}^{-2} \text{s}^{-1}$), D is the diffusion coefficient ($\text{m}^2 \text{s}^{-1}$), C is the concentration (mol m^{-3}), R is the universal gas constant (J K^{-1}), T is absolute temperature (K), μ_i is the chemical potential (J mol^{-1}) and x is the length (m).

The diffusion coefficient is also a function of temperature, as described in equation 2.

$$D = K_B T \gamma \quad \text{Equation 2}$$

where K_B is the Boltzmann's constant (J K^{-1}) and γ is the terminal drift velocity ($\text{m}^2 \text{S}^{-1} \text{J}^{-1}$).

It can be seen that temperature directly influences the diffusion flux and the diffusion coefficient. Concentration directly influences the diffusion flux meaning an increase in formalin concentration results in an increase in formalin effectiveness, although this is very limited by the degradation of cellular content with high concentrations. Formalin fixation is also time dependant; the longer the fixation, the more effective the fixation, while left too long, sample degradation can also occur.

There are other factors which influence the effectiveness such as pressure and depth of penetration, but because single cells are analysed and the room pressure changes are insignificant these will not be discussed.

2.1.3 Cell Confluency

Cell confluency is problematic when culturing cells. The confluency rate is very difficult to control shown by Gasper and Goormaghtigh, when planning for an experiment, a level of sub-confluency is desired, due to the cells confluency increasing during an experiment (19). It is critical to keep similar cell coverages on substrates as biochemical changes occur with increased confluency. Once the cells become close to one another (greater level of confluency), cell signalling occurs changing the biochemical structure and distribution, altering the way PC-3 cells behave (20). Gasper and Goormaghtigh studied the effect of confluency rate on FT-IR spectrum, and

generally found that the greater the confluency, the greater the intensity of the FT-IR spectrum (19). It was also found that when a higher level of confluency was reached, significant shape changes of the FT-IR spectra occurred, quite possibly a result of biochemical modifications from the high confluency. The study showed spectral modifications to $950\text{ cm}^{-1} - 1200\text{ cm}^{-1}$ (region associated with nucleic acid vibrations), which could be down to DNA structure modifications at confluency above 80%. Additionally, there were clear modifications to the phospholipid carbonyl vibration at 1740 cm^{-1} .

2.1.4 Cyclodextrin

Cyclodextrins are cyclic oligosaccharides produced by enzymatic reactions from starch. The geometric properties of native cyclodextrins can be categorised into two groups, crystalline and aqueous solution (21). In the crystalline topology, either channel or cage types can exist. The cage or channel size is determined by several properties such as: molar mass, concentration and host to guest molecular ratio (22). The family of cyclodextrins can be subcategorised into α , β or γ – cyclodextrins, with 6, 7 and 8 sugar (glucose monomers) groups respectively, where γ – cyclodextrin are commonly used to solubilise drugs for delivery (23). The typical structure of cyclodextrins can be seen in Figure 6.

Cyclodextrin proves to be a very good biological solvent mainly due its low cost and toxicity (24). Arachidonic acid (AA) is a solid and requires a solvent acting as a vehicle to transport the AA into the PC-3 cell. The chemical properties (methyl and ethyl groups, long apolar chains and ester groups) make cyclodextrin a very good solvent as these chemical features are favourable for cyclodextrin and AA to form a guest: host

complex (25). The sugar encapsulation of AA by cyclodextrin relies on a successful docking of AA within the cyclodextrin structure to form interactions and hold the AA in place, forming a sugar cage around the AA (25). The transport of AA by sugar encapsulation is similar to the transport process in the body (25), providing a realistic transport mechanism into the cell allowing a more native evaluation of fatty acid uptake mechanisms.

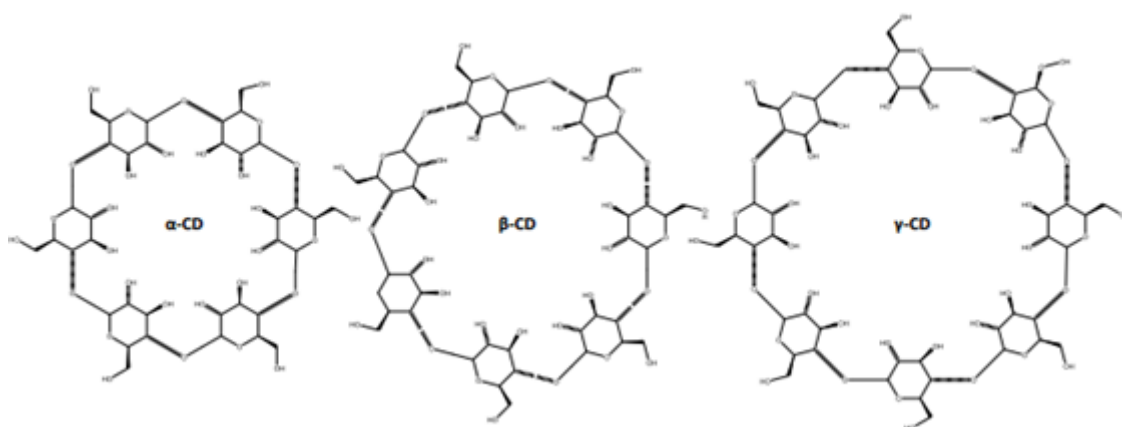


Figure 6 – α , β , γ – Cyclodextrin structures (26)

2.2 Cell lines

2.2.1 PC-3

Kaighn *et al.* established the cell line PC-3 from a human prostatic adenocarcinoma metastatic to the bone from a 62-year-old white Caucasian male. (27). PC-3 cells have a high tumorigenicity compared to DU145 cells with even greater tumorigenicity difference seen with LNCaP cell lines (28), the metastatic potentials are High, moderate and low respectively. PC-3 cells are androgen insensitive (28).

2.2.2 PC-3M

The cell line PC-3M, a sub-line of the cell line PC-3 was isolated from a PC-3 induced mouse tumour (29). Pettaway *et al.* showed the potential of PC-3M prostate carcinoma cell lines when a very high tumorigenicity model is required (30).

2.2.3 LNCaP

Horoszewicz *et al.* developed the cell line LNCaP by harvesting human prostate adenocarcinoma cells metastasised to the left supraclavicular lymph nodes from a 50-year-old white Caucasian male (31). It must be noted these cell lines are androgen sensitive.

2.2.4 LNCaP C4-2

Wu *et al.* produced the LNCaP subline LNCaP C4-2 by co-injecting the human cell lines LNCaP and a bone stromal cell line into an adult male mouse (32). The carcinomas produced had a clinical significance; they secreted prostate specific androgen (PSA), a clinical biomarker used for prostate cancer detection and management. When tumour cells interacted with the bone fibroblasts, a switch from androgen dependant to independent was observed in castrated mice. This cell lines are androgen insensitive.

2.2.5 LNCaP C4-2B

Thalmann *et al.* generated a bone metastatic subline by orthotopic injection of LNCaP C4-2 cell lines into castrated male mice (33). A primary tumour of the prostate was formed along with lymph node and bone metastasis, the cells that metastasised to the bone was isolated and harvested which resulted in the cell line LNCaP C4-2B. This cell line is androgen insensitive.

2.2.6 DU145

The cell line DU145 was harvested from a 69-year-old Caucasian male derived from a brain metastasis by Mickey *et al.* DU145 has a moderate tumorigenicity and metastatic potential and are also androgen sensitive (34).

2.2.7 PNT2

The Cell line PNT2 was obtained from the prostate of a 33-year-old white Caucasian male. The cell lines are non-tumorigenic in nude mice (35).

2.3 Fourier Transform Infrared (FT-IR) Spectroscopy

FT-IR spectroscopy is a highly versatile technique used in many applications of research. As an overview, FT-IR spectroscopy is the study of electromagnetic radiation in the IR and matter where photons interact with molecules resulting in an energy transfer to or from the molecule (vibrational excitation or de-excitation). These are considered to be discrete energy transfers which relate to vibrational quanta, and the analysis of these different energies can be exploited to determine the structure and functional groups of species of interest.

2.3.1 Electromagnetic Radiation (EMR)

EMR can be characterised as a simple harmonic wave propagating in a straight line free. Within the EMR there are two undulatory fields which are orthogonal to one another, both interacting with matter giving rise to a spectrum; these are electric and magnetic fields. A wave can be characterised by a number of different parameters, initially it is important to understand the term “*frequency*” (ν) which is defined as the number of oscillations a wave undergoes in 1 second, with the units coinciding with per second (s^{-1}) and the SI unit Hertz (Hz). Another property of the wave is the “*wavelength*” (λ),

defined as the distance a wave travels undergoing one full oscillation. The two parameters together give rise to the fundamental equation:

$$c = v\lambda \quad \text{Equation 3}$$

where c is the speed of light. Another way a wave can be characterised is through “*wavenumber*” ($\bar{\nu}$), defined as the reciprocal of the wave length. By subbing the reciprocal of the wave number in for wave length, the relationship between frequency and wave number is considered to be proportional, as described in equation 4:

$$v = c\bar{\nu} \quad \text{Equation 4}$$

2.3.2 Quantization of Energy

A given molecule in a given space can have numerous different energy levels. The existence in different discrete energy levels is defined as “*quantisation of energy*”. A discrete change in energy therefore results in a change in energy level (a change in quantum number). Energy level transitions can take place when there is an input or output of energy to or from a given molecule, resulting in excitation or de-excitation respectively. Early work done by Planck determined that the absorbed or desorbed energy can be in the form of EM radiation, leading to the fundamental energy difference between two energy levels in equation 5:

$$\Delta E = E_2 - E_1 \quad \text{Equation 5}$$

The energy difference (ΔE) between the energy at the state of greater excitation (E_2) and lower energy level (E_1) gives rise to the frequency of the radiation through the deduced equation 6:

$$\Delta E = h\nu \quad \text{Equation 6}$$

This Equation in spectroscopy is fundamental in the production of an absorbance spectrum. If a beam of monochromatic EMR hits a given molecule at an energy level E_1 , energy will be absorbed by the given molecule and its energy level will jump to E_2 . The absorbance of the monochromatic EMR by the molecule will result in a decreased intensity beam after the interaction with the molecule has taken place seen by the detector. The same can be done for a polychromatic beam containing several frequencies, the beam interacts with the given molecule and the decreased intensity beam will hit the detector, with the detector only showing the energy absorbed from a given frequency, the other frequencies remaining undiminished in intensity. This method produces an absorbance spectrum across the frequencies of EM radiation. It can be said the reverse is true with an energy change from E_2 to E_1 with an emission of energy, which produces an emission spectrum.

2.3.3 Infrared Radiation

When using IR EMR, it is important to know that the frequencies in the EM spectrum from IR radiation only induce a change in configuration of the molecule (vibration). The IR region in the EM spectrum is considered to have a wave number from 100 to 10^4 cm^{-1} with a frequency of 3×10^{12} to 3×10^{14} Hz. As the interaction of IR EMR with molecules induces a vibrational structural configuration, there must be a change in dipole. Initially looking solely at symmetric stretches, a molecule will not have a change in dipole (zero dipole moment) as the molecule remains in a symmetrical transition, therefore this molecule is known to be “*infrared in-active*”. Looking at an anti-symmetric stretch, the molecule has an uneven distribution of electrons as one bond shortens as the other extends, resulting in a periodical change in dipole moment, meaning the molecule is “*infrared active*”. There is another vibration of interest when

studying FT-IR spectroscopy, known as a bending vibration. This vibration can also be seen in carbon dioxide, with the oxygen atoms in the carbon dioxide moving in the y-axis around the central carbon atom, rather than with the symmetric or anti-symmetric stretches moving solely in the x-axis changing bond length. In the bending vibration, the bond lengths do not change, just the position on the oxygen atoms around the central carbon, this in turn results in another periodical dipole moment which produces an infrared active molecule.

Looking at any diatomic molecule, there will be a number of repulsive and attractive forces from the two atoms forming the molecule. There will be repulsive forces from the same electronically charged species such as electrons or protons, but there will be attractive forces between oppositely charged electronic species between electrons and protons. The molecule aims to minimise the force so the two atoms are at a distance (internuclear) where the attractive and repulsive forces are balanced, usually defined as the equilibrium bond length. If the distance between the atoms changes from the equilibrium bond length, then there is an imbalance in forces between the two atoms and one force will dominate. To do this, there needs to be an input of energy to overcome one of the forces. If the atoms get too close together, repulsive forces will dominate and rise almost exponentially, if the atoms are brought apart, then the repulsive forces reduce but the attractive forces become weaker with distance.

2.3.4 Vibrations of Molecules

A molecule is looked at in terms of Cartesian co-ordinates, with 3 main body axes describing the atoms position. A molecule with N atoms therefore has $3N$ co-ordinate values and therefore $3N$ degrees of freedom as once the positions are fixed, so are bond

lengths and angles. For non-linear molecules, translational movements of a molecule require 3 co-ordinates to describe its shape and position. The same goes for the rotational movements of a molecule requiring a total of 6 co-ordinate positions to describe both translational and rotational movements, leading to $3N - 6$ degrees of freedom and fundamental vibrations. Describing a linear molecule is slightly different, as there cannot be any rotation about a bond axis consequently requiring 2 co-ordinates to describe the rotational movements for a linear molecule, leaving $3N - 5$ degrees of freedom and fundamental vibrations.

Looking at the rotations and vibrations of a water molecule, there are $3N - 6$ fundamental vibrations and degrees of freedom, with $N = 3$ as the molecule is triatomic. The change in molecular shape is described by either bending or stretching. It is also important to think of the molecular symmetry within the molecule, and each bending or stretching mode can be either symmetric or antisymmetric. Symmetry about an axis is described by the symmetric or asymmetric movements around a particular axis. For a water molecule there is only one rotational symmetric axis, through the centre of the molecule bisecting the two O-H bonds equally spaced. This axis is termed the C_2 axis, as the molecule appears identical twice on a full 360° rotation. The bending and stretches can therefore be parallel or perpendicular to this axis. For a water molecule, there is a symmetric stretch at 3651.7 cm^{-1} (parallel) and this particular vibration is labelled ν_1 . There is also a symmetric bend (parallel) at 1595.0 cm^{-1} labelled ν_2 and finally an antisymmetric stretch (perpendicular) at 3755.8 cm^{-1} labelled ν_3 . The labelling is in terms of their decreasing frequency and symmetry type.

2.3.5 Molecular Vibrations

2.3.5.1 Skeletal Vibrations

Skeletal vibrations are a result of linear or branched chained structures within a molecule. Each of these structures result in several modes of vibration resulting in several infrared absorption bands. A change in a linear or branched structure changes the absorption band assignment. The region in which skeletal vibrations occur is defined as the “*fingerprint region*”, where the molecule or structure of the molecule can usually be defined alone by absorption bands in this region ($700 - 1400\text{ cm}^{-1}$).

2.3.5.2 Group Frequencies

Group frequencies are almost always independent of the molecule as a whole in contrast to skeletal vibrations. These vibrations are found well above and below that of skeletal vibrations. Atoms which are light in terminal groups are found to have high frequency with heavier atoms having a lower frequency (36).

2.3.6 Biological structural information Using FT-IR

Many biological structures and composition can be analysed in the mid IR region making FT-IR a very useful tool in obtaining biochemical information (37).

Protein structures have 4 prominent spectral features, the amide I band in the region of $1600\text{ cm}^{-1} - 1700\text{ cm}^{-1}$, the amide II band in the range $1500\text{ cm}^{-1} - 1560\text{ cm}^{-1}$, the amide A band in the region $3450\text{ cm}^{-1} - 3550\text{ cm}^{-1}$ and the amide III band in the range $1200\text{ cm}^{-1} - 1350\text{ cm}^{-1}$ (37). The amide I band contains contributions from the C=O stretching vibration of the amide group (~80%), a smaller contribution from the C-N stretching (~10%) and N-H bending (~10%). The amide II band having contributions from N-H bending (~60%) and C-N stretching (~40%). The amide A band mainly arises from N-

H stretching (~95%). The amide III band is very complex and arises from various coordinate displacements. The amide I and II peaks are sensitive to secondary protein structure. A broadened amide I and II peak can occur as a result of different protein conformations. Different protein conformations have different band assignments. These band assignments can overlap, creating a broadened amide I or II peak (37).

FT-IR can also identify dominant absorption features of lipid bands in the range 2800 cm^{-1} - 3000 cm^{-1} . Lipids give rise to asymmetric and symmetric C-H stretching vibrations of CH_3 (2956 cm^{-1} and 2874 cm^{-1}) and asymmetric and symmetric C-H stretching vibrations of CH_2 (2922 cm^{-1} and 2852 cm^{-1}). A strong band also is evident in lipid structures as a result of the 1736 cm^{-1} arises from the ester C=O groups in lipids.

There are major band assignments associated with the antisymmetric and symmetric stretching vibration at 1224 and 1087 cm^{-1} respectively of PO_2^- (37).

2.4 FT-IR Instrumentation

2.4.1 Michelson Interferometer

A key feature to a modern FT-IR spectrometer is the Michelson interferometer. Whereas previously wavelengths of light had to be measured individually through a grating and a slit on a dispersive instrument (36), the Michelson interferometer allows the detection of polychromatic IR radiation, meaning all wavelengths of light are measured at the same time, providing a multiplex advantage on sample acquisition speed. The Michelson interferometer also offers a throughput advantage compared to the dispersive instrument (36). The slit on the dispersive instrument severely limits the amount of energy reaching the sample compared to a Michelson interferometer,

meaning the Michelson interferometer has a better signal to noise ratio and the ability to measure high resolution spectra.

The Michelson interferometer works by combining many frequencies of radiation emitted from the source. A beam splitter placed directly in the radiations path splits the sources IR radiation and directs half the radiation towards the stationary mirror and half the light to the moving mirror. The light is reflected off the moving and stationary mirrors, finally recombining the radiation, directing through the sample and to the detector. When the moving mirror path difference is equal to the stationary mirror, there is constructive interference for all wavelengths of radiation known as the zero-path difference (ZPD). When a path difference is introduced by moving the mirror, there are different degrees of constructive and destructive interference. The interference pattern created for the combined radiation as a function of the moving mirror is called an interferogram. This interferogram can be thought of as a coded representation of all frequencies of light emitted from the source. The beam of varying constructive and destructive interference patterns where each wavelength is passed through the sample, specific wavelengths of light are absorbed and appear as lost frequencies at the detector. From this, the combined intensities are subjected to a Fourier transform, finally producing an absorbance spectrum of absorbance vs frequency. The Michelson interferometer can be seen in Figure 7.

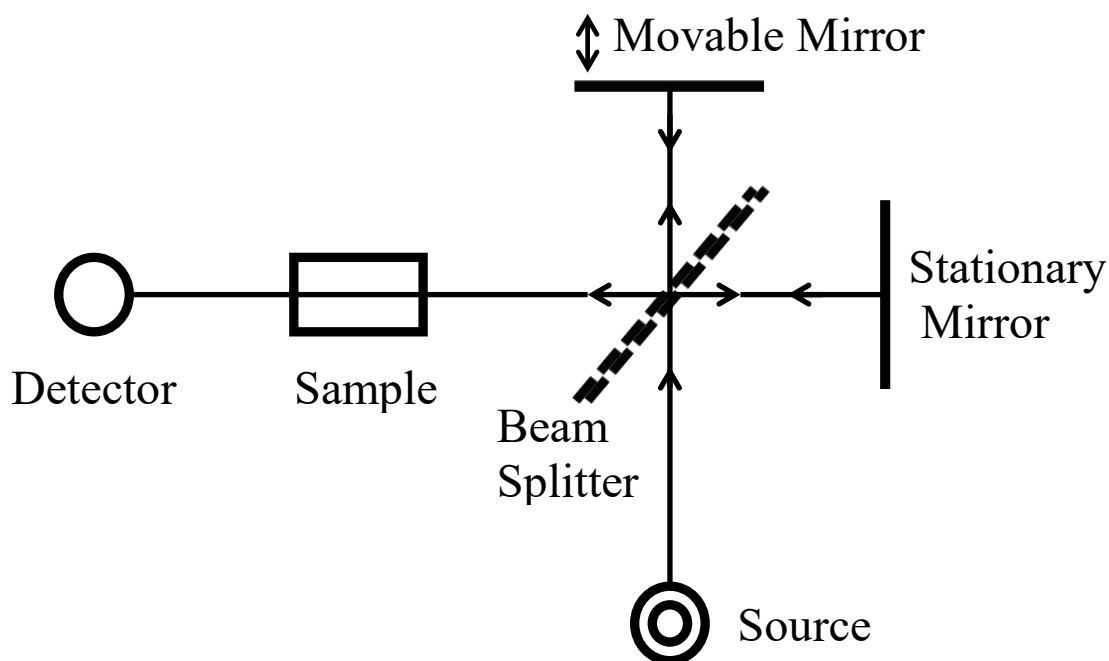


Figure 7 – Schematic diagram of the FT-IR Michelson interferometer

2.5 FT-IR Microscopy

FT-IR spectroscopy is very sensitive and can produce a full spectrum over a large range of frequencies in a short amount of time, which makes FT-IR spectroscopy a great tool for analysing biological samples. Biological samples such as cells, are too small to see with the human eye, so to focus the beam on the correct area of the sample is difficult. The cultured cells on the substrate are not always homogenous, with altering degrees of confluency. This ultimately leads to spectral variations depending on the degree of confluency. The use of an optical light microscope coupled with FT-IR spectroscopy allows the user to see where the beam is aiming, adding the advantage of the analysis been target specific.

2.5.1 Signal to Noise Ratio

Electronic amplification is used to increase and magnify the signal generated by the detector. Each signal produced will contain random fluctuations resulting from unauthentic electronic signals produced by the amplifier, detector, source or any electronic equipment involved in the data collection process. These unexpected fluctuations are generally called noise. Spectral peaks need to be distinguished from noise, therefore the peak intensity must be substantially larger than the noise intensity. The ratio between the real spectral peak intensity and the noise intensity is defined by “*signal to noise ratio*”.

2.5.2 The Use of FT-IR Microscopy in Monitoring Lipid Uptake and Metabolism in Prostate Cancer

The literature surrounding arachidonic acid and lipid uptake in prostate cancer cell lines is very limited due to the difficulty of the technique and the sensitivity to track molecules through the global cellular chemistry.

Brown *et al.* (2006) used reflection FT-IR to assess the lipid uptake of prostate cancer epithelial cells in bone marrow (38). By using the area under the CH₂ and CH₃ stretches, fatty acid uptake was highlighted in prostate epithelial cells and pools of fatty acid within the bone marrow were isolated. The images displayed were poorly defined, probably as a result of the spectral parameters used at 8 cm⁻¹ spectral resolution and 60 scans. No spectra were shown throughout the study, so speculation can only be drawn as to why the poorly defined chemical image was displayed. The areas under protein bands between 1485 cm⁻¹ – 1729 cm⁻¹ were used to define the boundaries between prostate cancer cells and the bone marrow. This range, which is described as the protein image, contains a lot of vibration features associated with the C=O lipid chemistry seen

between 1700 cm^{-1} – 1730 cm^{-1} , meaning the peak area is clearly influenced by the lipid chemistry. The data processing steps were poorly outlined throughout the paper, raising concerns surround the reproducibility of the FT-IR study.

Gazi *et al.* (2007) studied the cellular uptake and translocation of palmitic acid from an adipocyte loaded with the fatty acid (12). By following the CH_2 and CH_3 , C-D and C=O carbonyl stretches, the regions of lipids were isolated in PC-3 cells. The spectral resolution used was 4 cm^{-1} with over 700 scans. The spectra collected were of good quality and the C-D stretches were clearly defined. This study clearly indicates that FT-IR can track and follow specific vibrational features associated with lipid metabolism. The microscopy clearly identified lipid droplets within the PC-3 cells, with the FT-IR spectral features matching the translocation of the C-D stretches of the D_{31} -palmitic acid. Sub cellular locations of lipid accumulations were highlighted, strengthening the literature surrounding essential omega-6 fatty acids fuels metastasis. The data processing steps were poorly outlined throughout this investigation, raising questions surrounding the reproducibility of this study.

Gazi *et al.* were able to track both deuterated AA and palmitic acid in the uptake and metabolism of metastatic prostate cancer cell lines (39). This study claims to be able to the management of intracellular lipids when using a $6.6\text{ }\mu\text{m} \times 6.6\text{ }\mu\text{m}$ pixel size in high definition. This pixel size could only provide information on whether the cell has chemically changed and hence up taken any lipids, speculating the reorganisation of cellular lipids. Also, 64 sample scans were used, leading to a poor signal to noise in the spectra associated with AA, and the C-D stretch is unable to be identified through the noise, again further indication that more scans should have been used. All spectra related to palmitic acid uptake appear to clearly highlight the C-D stretches, probably

due to the significantly larger C-D bonds within the molecule compared to that of AA. The study demonstrated the effectiveness of mapping the lipid area, showing well defined lipid regions within the metastatic prostate cancer cell lines, another indication that FT-IR is a valuable technique when probing cellular lipids.

Brown *et al.* managed to demonstrate that deuterated tagging enabled arachidonic acid to be specifically tracked and mapped through the vibrational spectral characteristics of the C-D stretch (40). The C-D peaks in the study are undefined and mainly appear as spectral shoulders off the CO₂ peak at 2340 cm⁻¹. The spectral resolution used was 8 cm⁻¹, with 75 background and 64 sample scans. The C-D stretch is a specific but weak vibration. The number of scans used is rather low, with doubt regarding the signal to noise ratio needed to obtain spectral features associated with deuterated AA. In contrast, Gazi *et al.* were able to show well defined C-D peaks using over 700 scans (12), possibly further indication of the poor choice of spectral parameters. The spectra presented contain baseline distortions due to Mie scattering. It must be noted that there was no viable Mie correction method available and the scattering was not resolved in this study. It is debatable whether the spectral features presented are a result of the spectral distortions through Mie scattering rather than the chemistry of the C-D stretch. It must also be noted that the spectral processing steps are not highlighted throughout this study, making this very difficult to replicate.

A physiologically unrealistic concentration of d8-AA was also used, at concentrations of 25 and 100 µM, roughly 2.5 – 10 times greater than what would be seen of cells *in vivo* respectively. Large concentration of AA such as the level used by Brown *et al.* is said to be cytotoxic *in vitro*, inducing apoptosis (41). It could be scrutinised that the

chemical features seen in the cells are a result of the cell gearing up for apoptosis, with no further investigations carried out investigating cell apoptosis.

Literature strongly suggests that COX-2 plays a pivotal role in the carcinogenesis and development of prostate cancer (40). Regions of cancerous prostate tissue were found to contain higher levels of COX-2 expression compared to benign tissue. Tumour growth was noted to arrest or decrease when inhibiting cellular COX-2 in animal models.

Brown in 2014 noted that prostate cancer cells approached and penetrated tight cell junctions with a chemo-attraction towards AA (42). In order to penetrate the tight cell junction, a morphological change was required, switching from a mesenchymal to amoeboid phenotype, a key step in the penetration of tight cell junctions. The chemical changes are currently unknown to why AA induces a morphological transition in the progression of prostate cancer. Therefore, there is a need to investigate the effect of AA exposure on invasive and non-invasive prostate cancer cell lines and identify any chemical lipid changes which may be induced. Gaining insight to this simple morphological transition could pin point an essential chemical change which may induce intra or extra-vasation of prostate cancer cells and therefore lead to metastasis.

2.6 Experimental Methodology

2.6.1 Materials

All cell culture general reagents inhibitors and stains were purchased from Sigma-Aldrich (Poole, UK). Arachidonic acid was purchased from MP Biomedicals (London, UK) which was made up in methyl- β -cyclodextrin producing a 10 mg ml⁻¹ emulsion.

Foetal calf serum was provided by PAA Laboratories (Yoevil, UK). Calcium fluoride substrates were supplied by Crystran Limited (Poole, UK).

2.6.2 Cell Line Culture

All cell lines were verified by the Cancer Research UK Manchester Institute tissue typing service and cultured as previously described by Hart *et al.* and Brown *et al.* (43,44). All cell lines were cultured onto calcium fluoride substrates. The disks sterilised with 90% w/w ethanol for 1 hour and air dried before use following the protocol of Thomas (45). All cells were serum starved in RPMI 1640 for 24 hours before to induce cell cycle arrest and treated without antibiotics.

2.6.3 Cell Treatment of Arachidonic Acid

All AA and d₈-AA treatments were made up to a 20 µM concentration in RPMI 1640. The cell lines were cultured on CaF₂ substrates. All cells were washed in PBS after treatment and formalin fixed 4% for 20 minutes. Cultured substrates were then dipped in double distilled water following the protocol of Gazi *et al* and air dried (46).

2.6.4 COX-2 inhabitation

Cell lines were exposed to 10 µM NS398 in RPMI 1640 and culture in 37°C in 5% CO₂ for 30 minutes prior to treatment.

2.6.5 Fluorescence Microscopy

All cells were stained with 5µM Nile-red 5 minutes before treatment. The fluorescent cultures were carried out in Hank's Buffer Salt Solution (HBSS) without phenol red. All cultured substrates were washed in PBS and formalin fixed for 20 minutes, washed in double distilled (DD) water following the protocol of Gazi *et al.* and air dried.

Cultures were imaged on a Nikon Eclipse 90i Fluorescence microscope straight after drying.

2.6.6 Fourier Transform Infrared Microscopy

All measurements were taken in transmission mode and hyperspectral chemical images were obtained using an Agilent 670 FT-IR spectrometer coupled with an Agilent-620 IR microscope. The system was equipped with a 128×128 liquid nitrogen mercury cadmium telluride (MCT) focal plane array (FPA) detector, using 256 background scans with 128 sample scans at 4 cm⁻¹ resolution over a range 950 cm⁻¹ – 3800 cm⁻¹. A 15x magnification objective was used giving a pixel size of 5.5µm x 5.5 µm. For all High magnification images, a x25 objective and condenser was used providing a 0.7 µm x 0.7 µm pixel size carried out with 4000 scans and background scans and a wavenumber resolution of 10 cm⁻¹.

2.7 Data Processing

2.7.1 Cell Finder Algorithm

Initially, the cell finder threshold has to be decided. The lipid 2800 – 3000 cm⁻¹ was chosen because of the advantage in spatial resolution. The lipid range has a wavelength of 3.33 µm – 3.57 µm compared to that of the amide I band at 1600 cm⁻¹ having a wavelength of 6.25 µm. Hence the former should provide a sharper, more defined cellular edge.

Once the threshold range is decided, the area under the curve of the given range is calculated for each pixel spectra. These area values are then displayed as a lipid area value heat map displayed in Figure 8a. This lipid image is converted to a grey scale image, as shown in Figure 8b. The grey scale image is manually adjusted until it is a

good reflection of the lipid area value heat map. This is adjusted by choosing a threshold area value, whereby below a given value, the grey scale image is set as black and above the area value the pixels are set as white. This binary mask is then used to discard the pixel spectra of no biological interest. Single cells are highlighted and defined but the clumps of cells remain undefined until further processing is carried out.

To break the clumps into single cells, a watershed algorithm is employed. This converts the regional maxima into regional minima. The cell to cell boundaries were marked by a watershed algorithm. Conceptually, the image can be thought of as a landscape, and then water is poured into the landscape filling the lowest points. As the water begins to rise, the lowest threshold is filled and two wells become one. The points where two minima wells become one are named the watershed lines, which define the cell boundaries. This produces a number of pixels which represent each individual cell.

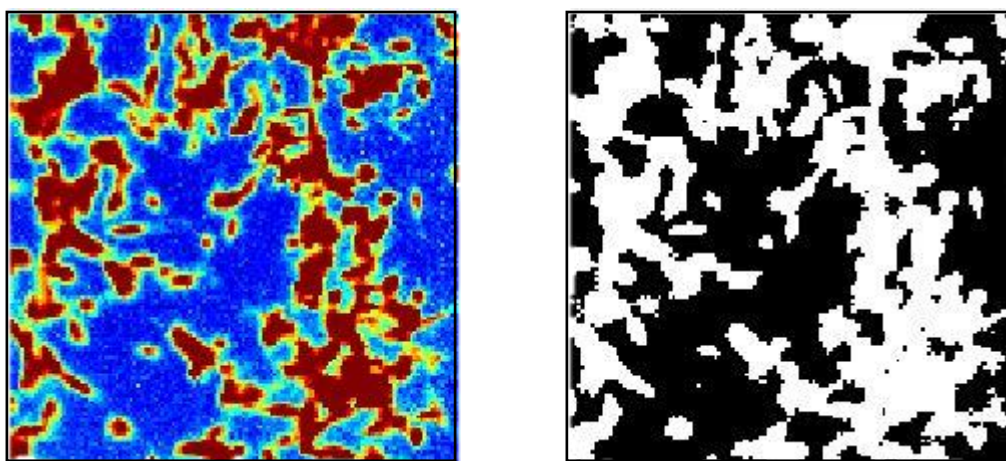


Figure 8 Cell finder lipid area images 704 μm x 704 μm (a) – Lipid area heat map (left) (b) – Grey scale lipid image (right)

2.7.2 RMieS Correction

FT-IR spectroscopy is a fantastic tool in determining biochemical behaviour within a cell. However, culture homogeneity and variability present many challenges in the

analysis and representation of cell spectra. The phenomena “*Mie Scattering*” occurs when a particle interacts with incident radiation of a similar wavelength of the particle size. When the radiation is incident on a particle, the discrete electric charges (electrons and protons) within the particle begin to oscillate resulting in a nett secondary emission of radiation. Additionally, some of the radiation could be absorbed by the particle, extinguishing some of the incident radiation; both scattering and absorption have the result of reducing the radiation intensity after traversing with a given particle.

Scattering from small particles is mostly Rayleigh scattering, occurring when the particle is roughly a tenth of the size radiation wavelength. This type of scattering is known to be elastic, with the photon energies of the scattered photons remaining unchanged. Mie scattering is predominantly wavelength dependant, when the wavelength of radiation is similar to that of the particle size the scattering pattern creates an antenna lobe in front of the particle in which the incident radiation struck, with the lobe becoming much sharper and focussed when the particle becomes larger than the wavelength of incident radiation shown below in Figure 9.

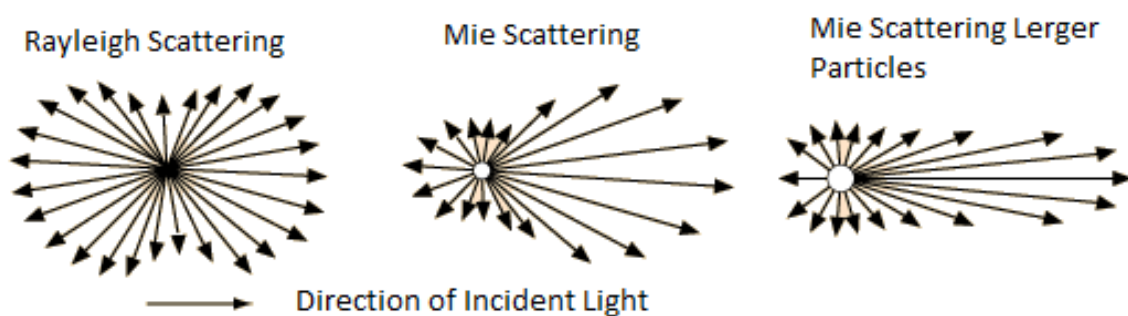


Figure 9 – Light scattering mechanisms for different particle sizes (47)

The factors that influence Mie scattering are particle geometry, particle refractive index in contrast to the surrounding environment and angle of incident radiation. The greatest scattering occurs when the wavelength of the incident radiation is approximately equal to that of the particle size.

Mie scattering proves very problematic when carrying out FT-IR studies on cellular systems, with large baseline distortions from scattering effects as cells as their size is similar to that of the wavelength used. Mie scattering also distorts peak shapes and apparent peak positions, making FT-IR interpretation skewed. Bassan *et al.* developed an algorithm named the resonant Mie scattering (RMieS) extended multiplicative signal correction (EMSC) to remove a recorded spectra of baseline distortions, shifts and peak width distortions (48). This algorithm takes a scatter free reference spectrum (Z_{ref}) allowing this to reconstruct the raw spectrum (Z_{raw}) correcting any distortion effects caused by RMieS (48). The assumption is made that the Z_{raw} is a superposition of Z_{ref} . With the greatest efficiency occurring when Z_{ref} is close to Z_{raw} . The user also needs to make a good choice of the reference spectrum, but when dealing with cells a very good representation is a Matrigel reference which contains all key spectral features similar to that of cells. To make the correction algorithm more effective and efficient, the iterative process replaces the reference spectrum with that of a corrected spectrum (Z_{corr}) removing any unwanted spectral features Z_{ref} may have, generally providing a more accurate representation of the true Z_{raw} . The RMieS algorithm is shown in Figure 10. It must be noted that the number of iterations is user specific and that each application may require a different number of iterations through varying levels of scattering.

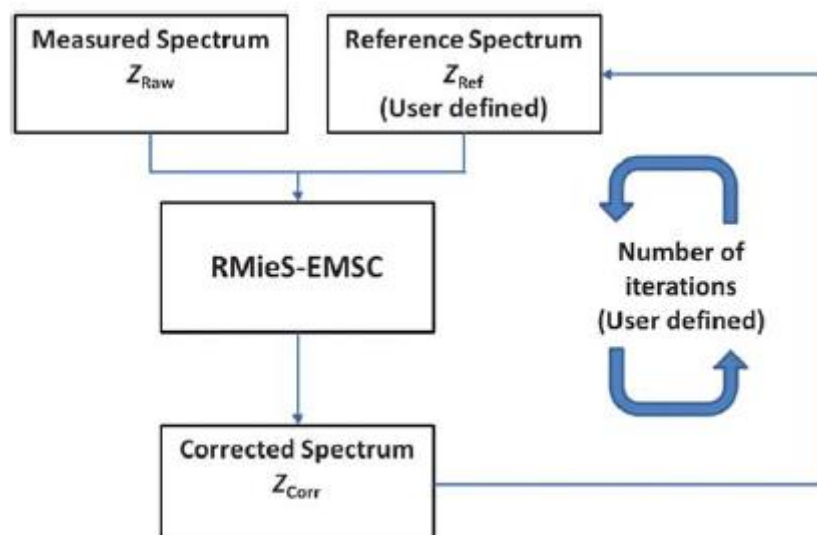


Figure 10 – RMieS iterative correction algorithm used to reduce scattering distortions in FT-IR investigations (48).

2.7.3 Noise Reduction

Cells usually have low absorption, due to their thickness and size. It is important to reduce the noise to enable subtle spectral features to be identified. A de-noise algorithm was used, by simply performing principal component analysis (PCA) on the data set. The principal components explaining the majority of the variance within the data set will contain significant biological information. As the principal component number increases, most of the percentage variance of the data set is accounted for; the remaining principal components explain the variance within the data set due to noise. Throughout this study the last 15 principal components were used to remove the noise within the data set, as all data collected had a reasonable signal to noise ratio and a good number of scans and background scans were used throughout the investigations. An example spectrum is displayed in Figure 11, showing the unprocessed spectrum in blue and the de-noised spectrum in red, translated 0.15 units in the positive Y direction for a comparison to be drawn. There is a small difference between the two spectra, but the

overall quality of the de-noised spectrum is better, with the majority of the noise removed, displaying a smooth spectrum with all significant biological features represented. This is important as, when carrying out multivariate analysis, biological differences are seen rather than differences as a result of noise. All de-noised spectra are assessed as to whether biological information has been removed by simply subtracting the pre-processed spectra from the de-noised spectra, obtaining difference spectra reflecting general noise. The difference spectrum of Figure 11 is shown in Figure 12, highlighting a general noise spectrum, indicating no significant biological information has been removed from the spectrum.

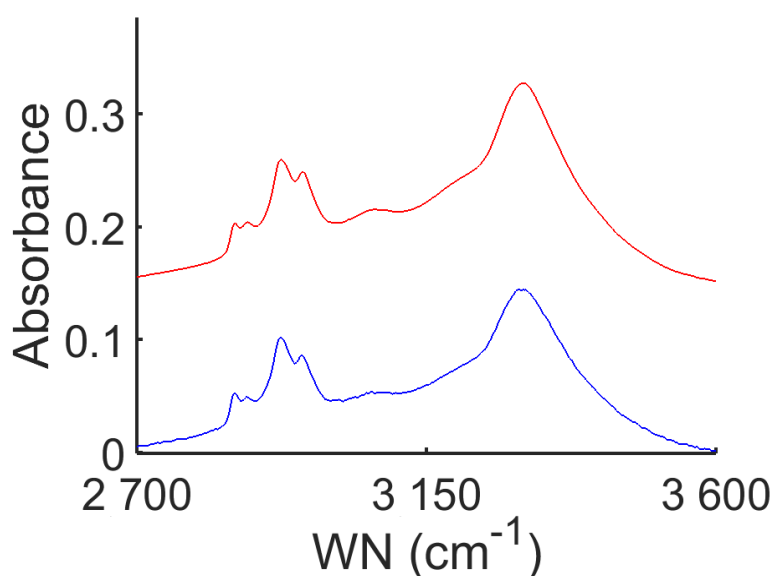


Figure 11 – A Comparison between an unprocessed spectrum (blue) and a noise reduced spectrum (red)

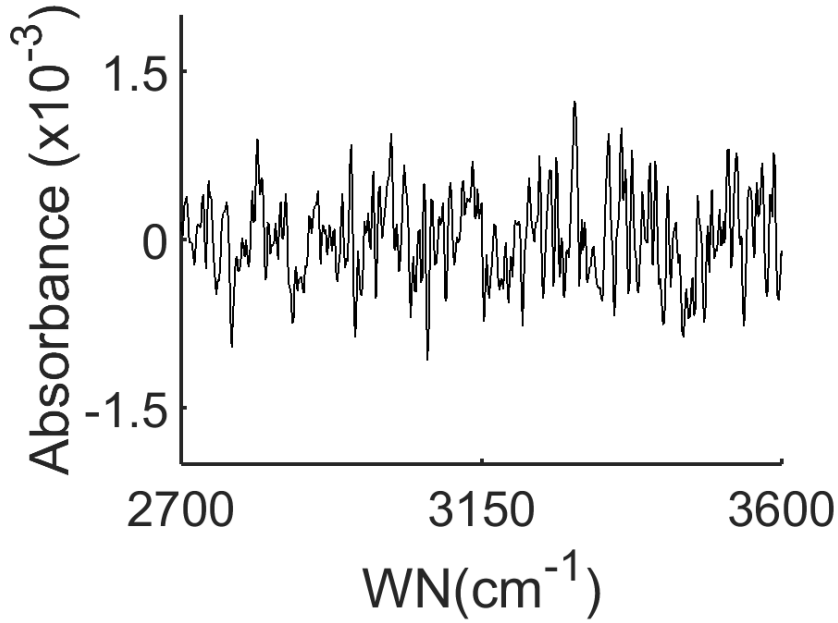


Figure 12 – A noise spectrum removed from the processed spectrum

2.7.4 Vector Normalisation

There is generally a large amount of variation in the thickness of biological samples; this causes great fluctuations in absorption intensity which can be explained by the Beer Lambert law. As the absorption peak intensities should be similar for each cell, it is necessary to find a commonality between the absorption peaks recorded so that biochemical information can be analysed with respect to biochemical change rather than varying sample thickness. This was carried out by calculating the normalising value T of the data set which can be seen in equation 8. Each wavenumber absorption variable is divided by the normalising value T vector normalising the data set, eliminating the majority of the spectral absorbance fluctuations due to sample thickness.

$$T = \sqrt{\sum_{i=1}^N x_i^2} \quad \text{Equation 8}$$

2.7.5 Spectral Derivatives

Spectral derivatives are taken as a way to identify subtle spectral features, particularly if a peak is convoluted amongst others or their changes in spectral gradients which indicate a change in peak what might have been overlooked. Throughout this study, the first derivate of spectra will be taken. First derivative has the advantage over second derivative in maintaining a relatively good signal to noise ratio.

2.7.6 Multivariate Analysis

2.7.6.1 Principal Component Analysis

PCA is used to simplify complex data sets reducing the dimensionality whilst retaining the trends within the data set (49). FT-IR biological data sets are often very large, with thousands of spectra with over a thousand data points per spectrum. Therefore, there is a need to simply the data set reducing the dimensions enable to find underlying biological patterns. PCA is an unsupervised learning method meaning the statistical tool finds patterns without any previous information around the data sets (50), for instance if cells are different cell types or if they have been treated with different drugs.

For a given FT-IR data set, the data is organised into a matrix of dimensions $I \times J$, I been the number of spectra and J being the number of data points (wavenumbers) for a given spectrum shown in Figure 13.

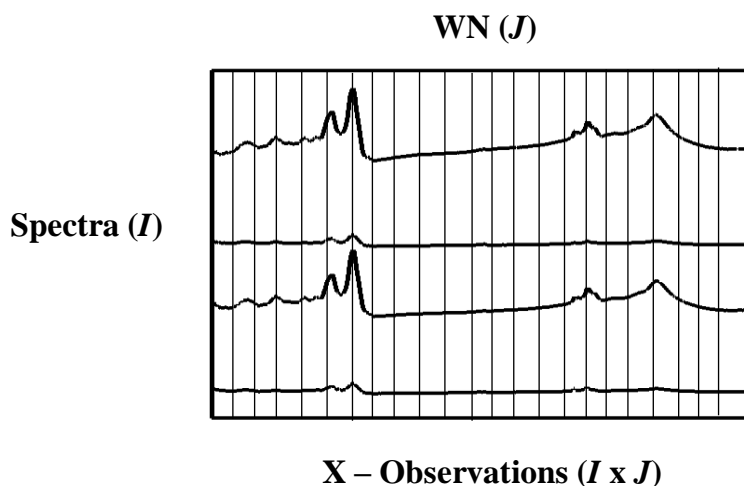


Figure 13 – Visual representation of the collected FT-IR data matrix, with spectra in rows and WN in columns

The spectra are all related and can be plotted in a space associating their data points and intensity. The mean of the data set is then calculated and subtracted from each data point, mean centring the data set, defining new axis scales with the mean effectively centred around (0,0), as displayed in Figure 14a. The direction of the data sets maximum variance is then defined, as shown in Figure 14b. This is found by calculating the covariance matrix of the data set, followed by Eigen decomposition exploiting the geometric properties of the Gaussian distribution. Geometrically, the Eigen vectors determine the axis of an ellipse surrounding the data, capturing the variance. A list of Eigen vectors and values are computed. The Eigen values determine the scale of the Eigen vectors, in other words the scale of variance in a given direction. The Eigen values are then ordered from largest to smallest with their related Eigen vectors. The largest Eigen value represents the vector direction with the largest spread of variance within the data set; this becomes principal component 1, with the second largest value becoming principal component 2. The variance of each principal component is the value of the Eigen value relating to a principal component's loading (principal components

co-efficient). The principal component score is how the dataset is spread for a given vector direction explaining a given variance within a dataset.

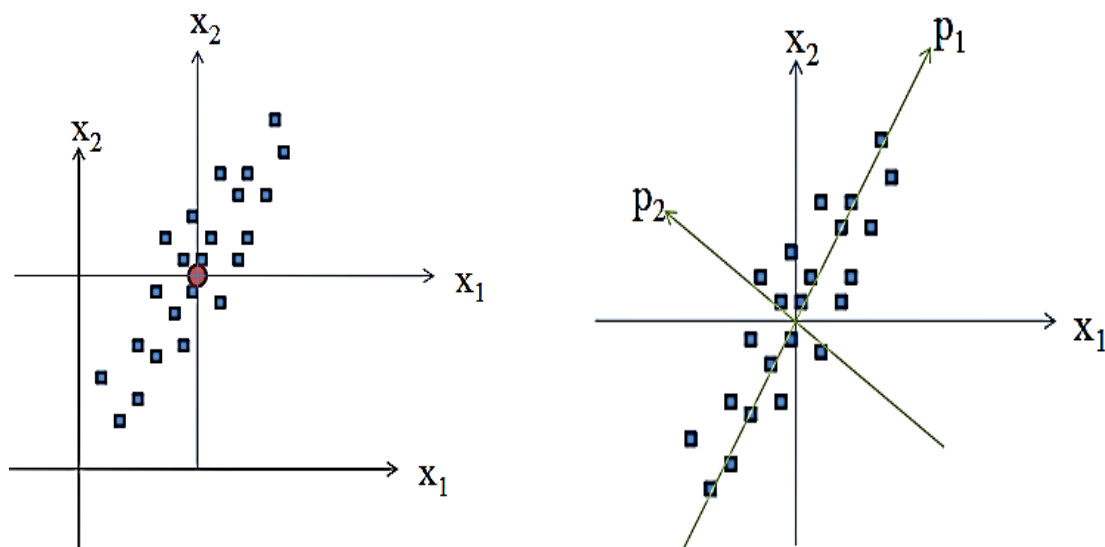


Figure 14 (a) – Mean centred dataset rescaling axes (b) – Direction of data sets maximum and second largest variance shown by p_1 and p_2 respectively

The principal component score plot is therefore a measure of how similar a given data set is to a specific variance, in terms of FT-IR spectra, how spectra differ due to different absorbencies. This can be exploited to show how given cells change over time with specific drug interactions, making this an ideal statistical tool for this study.

2.7.6.2 Seeded Principal Component Analysis

Seeded PCA or “spiked” chemometric PCA is carried out by simply biasing the non-supervised statistical technique PCA to force a particular outcome with respect to a specific molecule or vibrational signature. The exact protocol for seeded PCA can be seen in the work carried out by Keating (2016) (51). Keating’s technique forced the majority of the variance to be a specific spectrum in a given data set. This was achieved

by multiplying a given spectrum by a large order of magnitude ($>10^4$), and adding this data point to the data set on which PCA will be carried out. This data point multiplied by a large order of magnitude is known as the seed. When carrying out PCA analysis, the weighting of variance will be specifically related to seed, making the loadings for PC1 the pure seed spectrum, as the biggest difference in the data set is between the multiplied point and the rest of the data set points clustered very tightly together in comparison. Forcing a given loadings plot in PCA means any separation drawn throughout the data set is down to a specific molecule, if a pure molecule spectrum was used as the seed.

2.7.6.3 PCA Methodology and Median Positional Plots

All PCA was carried out pairwise, meaning that all spectra from all time points were placed into the same data matrix. PCA was performed on the full data matrix producing loadings representative of all time points for each individual experiment. PCA plots are shown throughout this study comparing $t=0$ min against 5, 15, 30 and 60 mins. It must be noted that when comparing $t=0$ min with $t=5$ min for example, the other time points $t=15$, 30 and 60 min have been blanked (whited) out for visual presentation and they are still contributing to the separation seen in the PCA plot.

Median positional plots are created by taking the median of the $t=0$ min cluster in PC1. This value is then subtracted from all median values for $t=0$, 5, 15, 30 and 60 mins. This is essentially centring the median, setting the $t=0$ min to zero. The difference between medians are then calculated between $t=0$ min and $t=5$, 15, 30 and 60 min and plotted. The relationship between the median positional plot and PCA score can be seen in Figure 15.

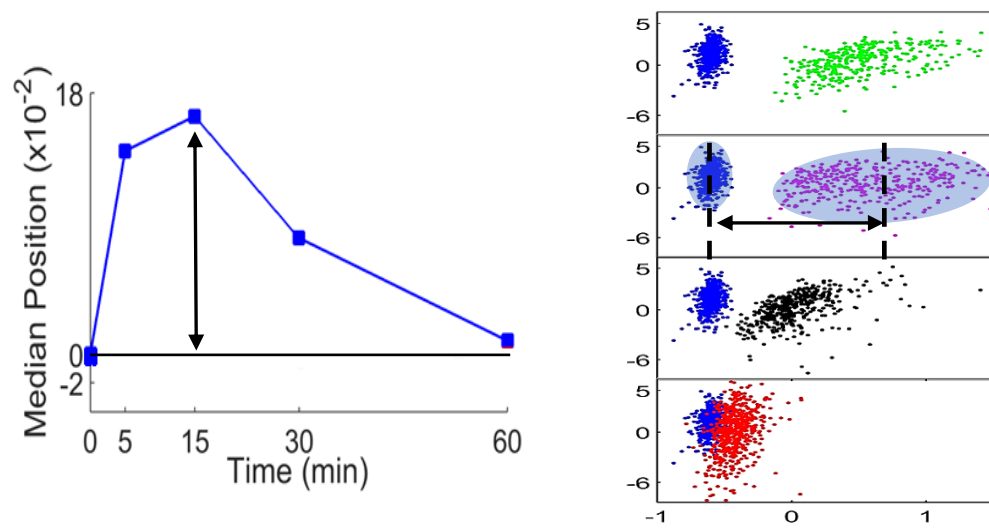


Figure 15 – An example of median positional plot accompanied by the PCA score plot.

References

- ¹ G. Pollack, I. Cameron, D. Wheatley (2008). *Water and the Cell*. Berlin: Springer Science + Business Media.
- ² P. Lasch, A. Pacifico, M. Diem. Spatially Resolved IR Microspectroscopy of Single Cells. *J. of Biopolymers*. 67 (2002) 335–338.
- ³ P. Lasch, M. Boese, A. Pacifico, M. Diem. FT-IR Spectroscopic Investigations of Single Cells on the Subcellular Level. *Vibrational Spectroscopy*. 28 (2002) 147–157.
- ⁴ E. Gazi, P. Gardner. Preparation of Tissues and Cells for Infrared and Raman Spectroscopy and Imaging. In: Srinivasan G, Editor. *Vibrational Spectroscopic Imaging for Biomedical Applications*. New York: McGraw-Hill
- ⁵ C. Koh. Preparation of Cells for Microscopy Using Cytospin. *Methods Enzymol*. 533 (2013) 235-240.
- ⁶ P. Pantelidis, G. Santilli, R. Knight. Sequential Identification of Apoptotic and Necrotic Cells on Individual Cytospin Preparations. *J. of Immunological Methods*. 214 (1998) 209-212.
- ⁷ A. Merrill, Y. Hannun (1999). *Sphingolipid Metabolism and Cell Signalling: Part A, Parts 1-2*. Cambridge: Academic Press.
- ⁸ C. Beleites, G. Steiner, M. G. Sowa, R. Baumgartner, S. Sobottka, G. Schackert, R. Salzer. Classification of Human Gliomas by Infrared Imaging Spectroscopy and Chemometric Image Processing. *Vibrational Spectroscopy*. 38 (2005) 143–149.
- ⁹ M. Tobin, M. Chesters, J. Chalmers, F. Rutten, S. Fisher, I. Symonds, A. Hitchcock, R. Allibone, S. Dias-Gunasekara. Infrared Microscopy of Epithelial Cancer Cells in Whole Tissues and in Tissue Culture, Using Synchrotron Radiation. *Royal Society of Chemistry*. 126 (2004) 27-39.
- ¹⁰ A. Acton (2013). *Cellular Structures – Advances in Research and Application: 2013 Edition*. Atlanta: Scholarlyeditions.
- ¹¹ A. Shukla (2009). *Industrial Enzymology: Encyclopedia of Enzymology-3*. New Delhi: Discovery Publishing House PVT.LTD.
- ¹² E. Gazi, P. Gardner, N. Lockyer, C. Hart, N. Clarke, M. Brown. Probing Lipid Translocation Between Adipocytes and Prostate Cancer Cells with Imaging FTIR Microspectroscopy. *J. of Lipid Research*. 48 (2007) 1846–1856.
- ¹³ S. M. Hewitt, F. A. Lewis, Y. Cao, R. C. Conrad. M. Cronin, K. D. Danenberg, T. J. Goralski, J. P. Langmore. R. G. Raja, P. M. Williams, J. F. Palma, J. A. Warrington. Tissue Handling and Specimen Preparation in Surgical Pathology: Issues Concerning the Recovery of Nucleic Acids from Formalin-Fixed, Paraffin-Embedded Tissue. *Arcj Pathol Lab Med*. 132 (2008) 1929-1935.
- ¹⁴ C. H. Fox, F. B. Johnson, J. Whitling, P. P. Roller. Formaldehyde Fixation. *J Histochem Cytochem*. 33 (1985) 845-753.
- ¹⁵ R. Golden, M. Valentini. Formaldehyde and Methylene Glycol Equivalence: Critical Assessment of Chemical and Toxicological Aspects. *Regulatory Toxicol and Pharmacol*. 69 (2014) 178-186.
- ¹⁶ J. A. Kieran (2016). Chapter 2 Fixation, In: *Histological and Histochemical Methods: Theory & Practice*. Oxford: Pergamon Press.
- ¹⁷ R. Thavarajah, V. K. Mudimbaimannar, J. Elizabeth, U. K. Rao, K. Ranganathan. Chemical and Physical Basics of Routine Formaldehyde Fixation. *J. Oral Maxillofac Pathol*. 16 (2012) 400-405.
- ¹⁸ J. T. Mason, T. J. O’Leary. Effects of Formaldehyde Fixation on Protein Secondary Structure: A Calorimetric and Infrared Spectroscopic Investigation. *J. Histochem Cytochem*. 39 (1991) 225-229.
- ¹⁹ R. Gasper, Erik Goormaghtigh. Effects of the Confluence Rate on the FT-IR Spectrum of PC-3 Prostate Cancer Cells in Culture. *Analyst*. 135 (2010) 3048-3051.
- ²⁰ A. Pacifico, L. Chiriboga, P. Lasch, M. Diem. Infrared Spectroscopy of Cultured Cells – II. Spectra of Exponentially growing serum-deprived and Confluent Cells. *Vibrational Spectroscopy*. 32 (2003) 107-115.
- ²¹ W. Saenger, J. Jacob, K. Gessler, T. Steiner, D. Hoffmann, H.Sanbe, K. Koizumi, S. Smith, T. Takaha. Structures of the common cyclodextrins and their larger analogues beyond the doughnut. *Chem Review*. 98 (1998) 1787-1802.
- ²² T. Loftsson, M. Masson, M. Brewster. Self-association of Cyclodextrins and Cyclodextrin Complexes. *J of Pharmaceuticals*. 93 (2004) 1091-1099.

- ²³ D. Pereira, P. Valentao, P. Andrade. Nano- and Microdelivery Systems for Marine Bioactive Lipids. *J. of Marine Drugs*. 12 (2014) 6014-6027.
- ²⁴ B. Gidwani, A. Vyas. A Comprehensive Review on Cyclodextrin-Based Carriers for Delivery of Chemotherapeutic Cytotoxic Anticancer Drugs. *Biomed Res Int*. 1 (2015) 1-12.
- ²⁵ L. Szenté, J. Szejtli, J. Szeman, L. Kato. Fatty Acid – Cyclodextrin Complexes, Properties and Applications. *J. of Lipids*. 16 (1993) 339-354.
- ²⁶ A. Harris, M. Welliver, R. Redfern, N. Kalynych, J. McDonough. Orthopaedic Surgery Implications of a Novel Encapsulation Process That Improves Neuromuscular Blockade and Reversal. *Int J Ortho Surgery*. 2006 (7) 1-9.
- ²⁷ M. Kaighn, K. S. Narayanm, Y. Ohnuki, J. F. Lechner, L.W. Jones. Establishment of a Human Prostate Cancer Cell Line (PC-3). *Inv Urology*. 17 (1979) 16-23.
- ²⁸ P. S. MulralliKrishna, C. S. Gondi, S. S. Lakka, A. Julta, N. Estes, M. Gujrati, J.S. Rao. RNA Interference-Directed Knockdown of Urokinase Plasminogen Activator and Urokinase Plasminogen Activator Receptor Inhibits Prostate Cancer Cell Invasion, Survival and Tumorigenicity *In vivo*. *J. Biol Chem*. 280 (2005) 36529-36540.
- ²⁹ Y. Ohnuki, M. M. Marnell, M. S. Babcock, J. F. Lechner, M. E. Kaighn. Chromosomal Analysis of Human Prostatic Adenocarcinoma Cell Lines. *Can Res*. 40 (1980) 524-534.
- ³⁰ A. A. Pettaway, S. Pathak, G. Greene, E. Ramirez, M. R. Wilson, J. J. Killion, I. J. Fidler. Selection of Highly Metastatic Variants of Different Human Prostatic Carcinomas Using Orthotopic Implantation in Nude Mice. *Clin Can Res*. 2 (1996) 1627-1636.
- ³¹ J. S. Horoszewicz, S. S. Leong, T. M. Chu, M. Friedman, L. Papsidero, U. Kim, L. S. Chai, S. Kakati, S. K. Arya, A. A. Sandberg. The LNCaP Cell Line – A New Model for Studies on Human Prostatic Carcinoma. *Prog Clin Biol Res*. 37 (1980) 115-132.
- ³² H. C. Wu, J. T. Hsieh, M. E. Gleave, N. M. Brown, S. Pathak, L. W. Chung. Derivation of Androgen-Independent Human LNCaP Prostatic Cancer Cell Sublines: Role of Bone Stromal Cells. *Int J. Cancer*. 57 (1994) 406-412.
- ³³ G. N. Thalmann, P. E. Anezinis, S. M. Chang, H. E. Zhau, E. E. Kim, V. L. Hopwood, S. Pathak, A. C. von Eschenbach, L. W. Chung. Androgen-Independent Cancer Progression and Bone Metastasis in the LNCaP Model of Human Prostate Cancer. *Cancer Res*. 54 (10) 2577-2581.
- ³⁴ D. D. Mickey, K. R. Stone, H. Wunderli, G. H. Mickey, R. T. Vollmer, D. F. Paulson. Heterotransplantation of a Human Prostatic Adenocarcinoma Cell Line in Nude Mice. *Can Res*. 37 (1977) 4049-4058.
- ³⁵ P. Berthon, O. Cussenot, L. Hopwood, A. Leduc, N. Maitland. Functional Expression of sv40 in Normal Human Prostatic Epithelial and Fibroblastic Cells – Differentiation Patterns of Nontumorigenic Cell Lines. *Int J Oncol*. 6 (1995) 333-343.
- ³⁶ C. Banwell, E. Mccash (1994). *Fundamentals for Molecular Spectroscopy*. McGraw Gill: New York.
- ³⁷ M. J. Baker, J. Trevisan, P. Bassan, R. Bhargava, H. J. Butler, K. M. Dorling, P. R. Fielden, S. W. Fogarty, N. J. Fullwood, K. A. Heys, C. Hughes, P. Lasch, P. L. Martin-Hirsch, B. Obinaju, G. D. Sockalingum, J. Sule-Suso, R. J. Strong, M. J. Walsh, B. R. Wood, P. Gardner, F. L. Martin. Using Fourier Transform IR Spectroscopy to Analyze Biological Materials. *Nat Protoc*. 8 (2014) 1771-1791.
- ³⁸ M. D. Brown, C. A. Hart, E. Gazi, S. Bagley, N. W. Clarke. Promotion of Prostatic Metastatic Migration Towards Human Bone Marrow Stroma by Omega 6 and its Inhibition by Omega 3 PUFAs. *Br J Cancer*. 94 (2006) 842-853.
- ³⁹ E. Gazi, T. J. Harvey, M. D. Brown, N. P. Lockyer, P. Gardner, N. W. Clarke. A FTIR Microspectroscopic Study of the Uptake and Metabolism of Isotopically Labelled Fatty Acids by Metastatic Prostate Cancer. *Vib Spec*. 50 (2009) 99-105.
- ⁴⁰ M. D. Brown, C. Hart, E. Gazi, P. Gardner, N. Lockyer, N. Clarke. Influence of Omega-6 PUFA Arachidonic Acid and Bone Marrow Adipocytes on Metastatic Spread from Prostate Cancer. *Br. J Can*. 102 (2010) 403-413.
- ⁴¹ C. Pompeia, T. Lima, R. Curi. Arachidonic Acid Cytotoxicity: Can Arachidonic Acid be a Physiological Mediator of Cell Death? *Cell Biochem Funct*. 21 (2003) 97-104.
- ⁴² M. Brown, J. A. Roulson, C. A. Hart, T. Tawadros, N. W. Clarke. Arachidonic Acid Induction of Rho-Mediated Transendothelial Migration in Prostate Cancer. *Br J Can*. 110 (2014) 2099-2108.
- ⁴³ M. D. Brown, C. A. Hart, E. Gazi, S. Bagley, N. W. Clarke. Promotion of Prostatic Metastatic Migration Towards Human Bone Marrow Stroma by Omega 6 and its Inhibition by Omega 3 PUFAs. *Br J Cancer*. 94 (2006) 842-853.

-
- ⁴⁴ C. A. Hart, M. Brown, S. Bagley, M. Sharrard, N. W. Clarke. Invasive Characteristics of Human Prostatic Epithelial Cells: Understanding the Metastatic Process. *Br J Cancer*. 92 (2005) 503-512.
- ⁴⁵ P. Thomas. Isolation of an Ethanol-Tolerant Endospore-Forming Gram-Negative *Brevibacillus* sp. As a Concert Contaminant in Grape Tissue Cultures. *J Appl Microbiol*. 101 (2006) 764-774.
- ⁴⁶ E. Gazi, T. J. Harvey, M. D. Brown, N. W. Clarke, N. P. Lockyer, P. Gardner. A FTIR Microspectroscopic Study of the Uptake and Metabolism of Isotopically Labelled Fatty Acids by Metastatic Prostate Cancer. *Vibrational Spectroscopy*. 50 (2009) 99-105.
- ⁴⁷ B. Castellani, E. Morini, M. Filippini, A. Nicolini, M. Palombo, F. Cotana, F. Rossi. Comparative Analysis of Monitoring Devices for Particulate Content in Exhaust Gases. *Sustainability*. 7 (2014) 4287-4307.
- ⁴⁸ P. Bassan, A. Sachdeva, A. Kohler, C. Huges. A. Henderson, J. Boyle, J. Shanks, M. Brown, N. Clarke, P. Gardner. FTIR Microscopy of Biological Cells and Tissue: Data Analysis Using Resonant Mie Scattering (RMieS) EMSC Algorithm. *Analyst*. 137 (2012) 1370-1377.
- ⁴⁹ J. Lever, M. Krzywinski, N. Altman. Points of Significance: Principal Component Analysis. *Nat Methods*. 14 (2017) 641-642.
- ⁵⁰ K. Rajan (2013). *Infomatics for Materials Science and Engineering: Data-Driven Discovery for Accelerated Experimentation and Application*. Butterworth-Heinemann: Oxford.
- ⁵¹ M. E. Keating. *Multivariate Statistical Methodologies Used in In-vitro Raman Spectroscopy: Simulations and Applications for Drug and Nonoparticle Interactions*. PhD Thesis Dublin Institute of Technology – Chapter 5. 107

Chapter 3

The Effect of Arachidonic Acid on Invasive and Non-Invasive Prostate Cancer Phenotypes

It is well documented that AA promotes prostate cancer invasion and proliferation (1), but the mechanisms and chemistry associated with the behaviour of the disease regarding invasion and metastasis is poorly understood. There is a need to understand and identify the initial process of exogenous exposure of AA to prostate cancer cell lines and whether the chemistry can be understood through FT-IRM. FT-IRM has been used in many biomedical applications but has rarely been used to track cellular metabolism (2). Understanding the initial cellular uptake behaviour could elucidate a potential key driver of metastasis within prostate cancer.

A structural change between a mesenchymal to amoeboid phenotype is an essential process an invasive cell must undertake to penetrate the endothelial tight cell junction during extravasation into the vessels and bone. AA has been seen by Brown *et al.* to induce this morphological change (2). But what is unknown is a cell's invasive ability dependant on AA uptake in turn limiting the cells ability to undergo morphological changes required to penetrate the vascular system.

In this chapter, FT-IRM will be used to investigate the chemical changes the invasive cell lines PC-3, DU145, LNCaP C4-2 and LNCaP C4-2B and non-invasive cell lines LNCaP and PNT2 undergo when exposed to exogenous AA. PCA will be used to track specific chemical changes throughout a 60-minute time course.

3.1 Invasive Prostate Cancer Cell Lines

All cell lines were cultured under standard protocol as described in section 2.6.2, serum starved overnight inducing cell cycle arrest, treated with 20 μ M AA in cyclodextrin for $t = 0, 5, 15, 30$, and 60 minutes and formalin fixed.

The acquired FT-IR raw spectra were put through an initial cell finder and RMieS correction algorithm. The RMieS corrected spectra were then put through a quality control, discarding any of the spectra with amide I peaks < 0.04 , denoised and vector normalised.

3.1.1 PC-3M Spectral Comparison

An initial investigation was carried out attempting to establish spectral signatures associated with the uptake of AA. PC-3M cells were used to initially identify key spectral positions, as the cell line is most invasive. The median spectra of PC-3M cells treated with AA for $t=0, 5, 15, 30$ and 60 min were compared, looking for spectral differences expressed by the cell line for different lengths of exposure to exogenous AA.

A spectrum of AA was collected and assessed between the spectral ranges $1000\text{ cm}^{-1} - 1800\text{ cm}^{-1}$ and $2600\text{ cm}^{-1} - 3500\text{ cm}^{-1}$ for a strong spectral feature than can be recognised within the highly complex cellular spectra, shown in Figure 16a and b respectively.

There was a peak present at 1732 cm^{-1} which has been enlarged and seen in Figure 17 which will be used as a spectral marker for the presence of AA.

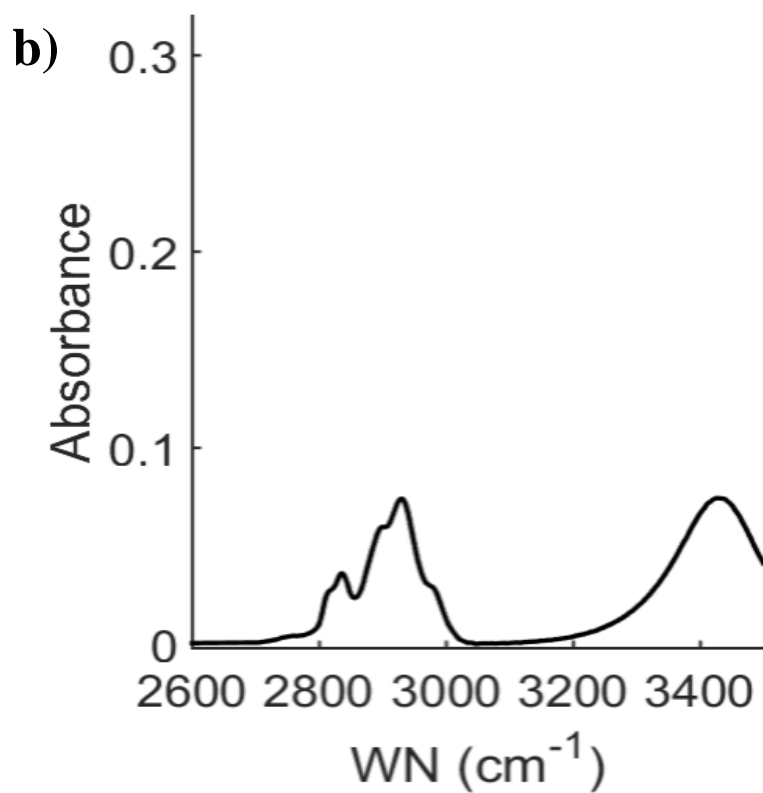
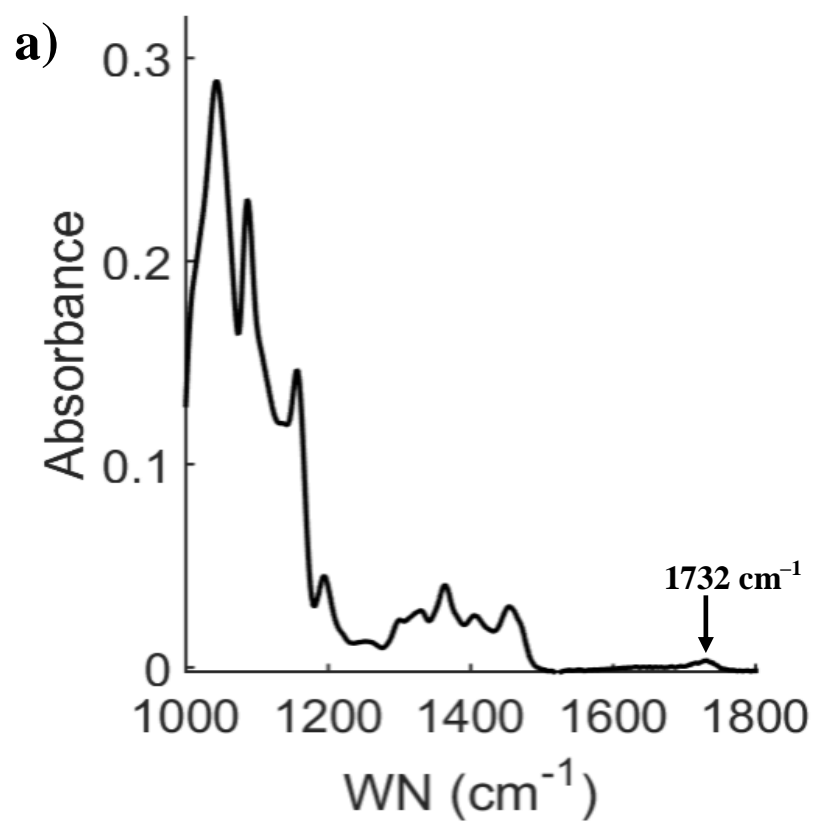


Figure 16 – AA spectrum between the spectral ranges (a) $1000\text{ cm}^{-1} - 1800\text{ cm}^{-1}$ and (b) $2600\text{ cm}^{-1} - 3500\text{ cm}^{-1}$.

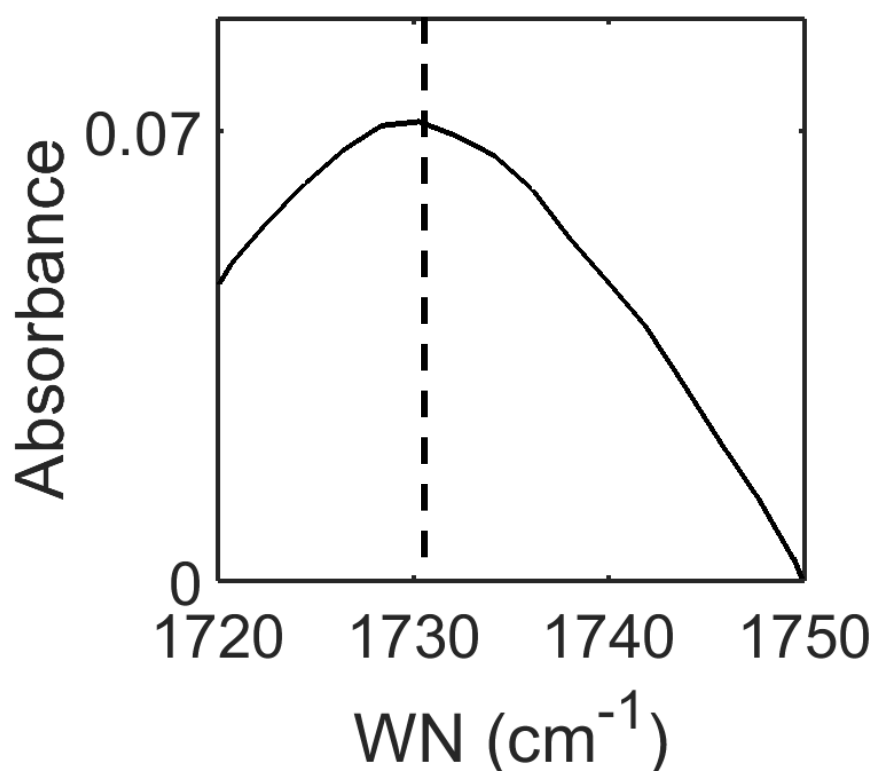


Figure 17 – Pure AA spectrum between 1720 cm^{-1} – 1750 cm^{-1} showing the specific C=O carbonyl stretch at 1732 cm^{-1} associated with AA with a dotted line

The median spectra for PC-3M cells treated with AA at time points $t=0$ (blue), 5 (green), 15 (magenta), 30 (black) and 60 (red) min can be seen in Figure 18. Firstly, significant changes in intensity between 1725 cm^{-1} – 1745 cm^{-1} can be seen, which is the C=O carbonyl stretch specific to fatty acid molecules. There appears to be a large increase in intensity at $t=5$ min followed by a larger increase by $t=15$ min. By $t=30$ and 60 min there are progressive decreases in intensity, probable indication of AA uptake and metabolic rejection. Secondly, there appears to be an emerging peak around 1732 cm^{-1} , specific to the uptake of AA.

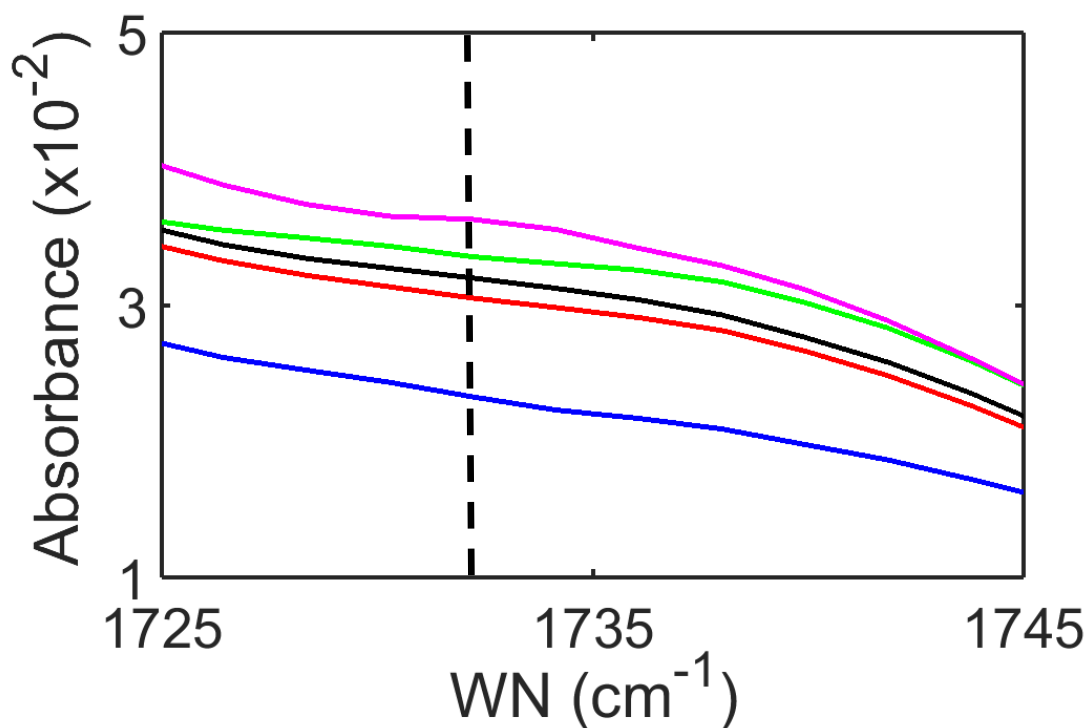


Figure 18 – A median spectral comparison of PC-3M cells at $t=0$ (blue), 5 (green), 15 (magenta), 30 (black) and 60 (red) min treated with AA, 1732 cm^{-1} C=O carbonyl peak shown with a black dotted line.

To further investigate the change in peak shape throughout the time course, the spectra were put through the first derivative to amplify small, subtle changes in peak shape, followed by the median. The first derivative function was preferred to the second derivative function as the spectra's SNR decreases through increasing differential order, maintaining a relatively high SNR in the first order. The median first derivative spectral comparisons of $t=0$ min (blue) versus $t=5$ (green), 15 (magenta), 30 (black) and 60 (red) min can be seen in Figure 19a, b, c and d respectively.

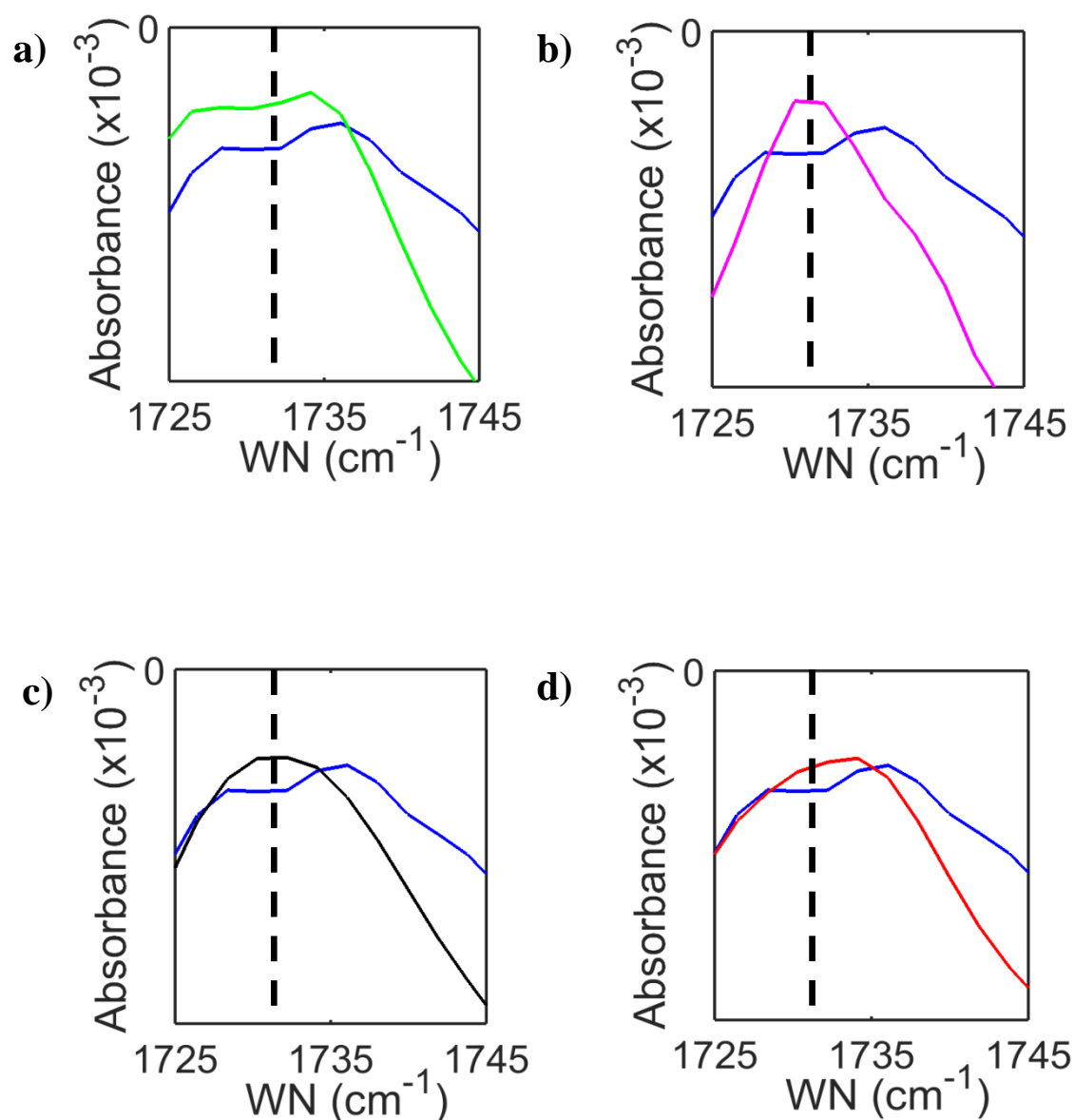


Figure 19 – The median first derivative spectral comparisons of PC-3M cells of $t=0$ min (blue) versus (a) $t=5$ (green), (b) 15 (magenta), (c) 30 (black) and (d) 60 (red) treated with AA. The 1732 cm^{-1} C=O carbonyl stretch is highlighted with a black dotted line.

The first derivative plots deconvolution the progression of a peak formation at 1732 cm^{-1} . Comparing $t=0$ and 5 min, $t=5$ min has a less negative value at 1732 cm^{-1} than $t=0$ min indicating that the gradient is becoming less steep with emergence of a peak shoulder. At 1740 cm^{-1} , the $t=5$ curve is becoming more negative than $t=0$ min, signifying the gradient steepening after the peak. At $t=15$ min, the same spectral behaviour is seen, to a more exaggerated effect with an even smaller negative gradient value at 1732 cm^{-1} and a greater negative value at 1740 cm^{-1} . Finally, $t=30$ and 60 min take the same spectral shapes, with $t=30$ min displaying a slightly less negative gradient value at 1732 cm^{-1} with similar gradient values at 1740 cm^{-1} . The pattern displayed clearly identifies the formation of a peak around 1732 cm^{-1} . This peak formation indicates AA uptake. The peak becomes less defined at $t=30$ and 60 min, probably good indication that the cellular system has broken down AA into its bioactive metabolites and rejected from the cell.

3.1.2 PCA of the C=O Fatty Acid Carbonyl Stretch for PC-3M Cells

PCA was used to investigate the biochemical changes throughout the 60-minute time course. The full spectra of PC-3M cells treated with AA for $t=0$ min can be seen in Figure 20a and b for spectral ranges $1000\text{ cm}^{-1} - 1800\text{ cm}^{-1}$ and $2600\text{ cm}^{-1} - 3500\text{ cm}^{-1}$ respectively. The cell spectra were put through a first derivative function. By placing the cellular first derivative spectra in the same PC score space allows the chemical variance between each time point to be compared relative to one another. The PCA analysis should further pick up and highlight the key spectral peak around 1732 cm^{-1} .

PCA was carried out on the cell line PC-3M between the spectral range $1720\text{ cm}^{-1} - 1750\text{ cm}^{-1}$ over the 60-minute time course which can be seen in Figure 21. The PCA

scores reveal a significant biochemical shift in PC-3M cells throughout the 60-minute time course when exposed to exogenous AA. At $t=0$ min (blue), the PC-3M cluster is relatively fitted with tight clustering representing no significant biochemical changes within the time point. At $t=0$ min, the cells are exposed to AA for a negligible amount of time as the substrate is washed of AA almost instantly then fixed. As all cells were serum starved overnight, variances in the cell cycle should be minimal, meaning the cells should be biochemically similar. As early as $t=5$ min, there is a significant shift in the negative direction of PC1 with respect to the initial $t=0$ min. The directional move indicates that the $t=5$ min cluster is becoming chemically similar to the negative PC1 loading plot displayed in Figure 22. The strong negative features displayed in the loading plot indicates the cell is attaining chemical features associated with the C=O carbonyl stretch of AA. At $t=15$ min, there is a further increase in negativity with respect to PC1. Again, further indicating an increase in cellular AA acquired from the endogenous pool. At $t=30$ min, there is a directional transition within the PCA plot, with the cellular spectra returning to a chemically similar state to the $t=0$ min cells. By $t=60$ min, there are no significant differences in the chemistry with respect to the initial $t=0$ min.

The PC-3M cell lines appeared to have an increased chemical similarity to AA, indicating uptake. The strong negative peak shown in the loading of PC1 is a marker of a peak shoulder forming, as the cells treated with AA move in the direction of this peak is a distinct marker that cells are taking on the spectral chemistry associated with AA uptake. By $t=30$ min the cells appeared to lose the chemistry associated with AA, implying either cellular rejection or metabolism.

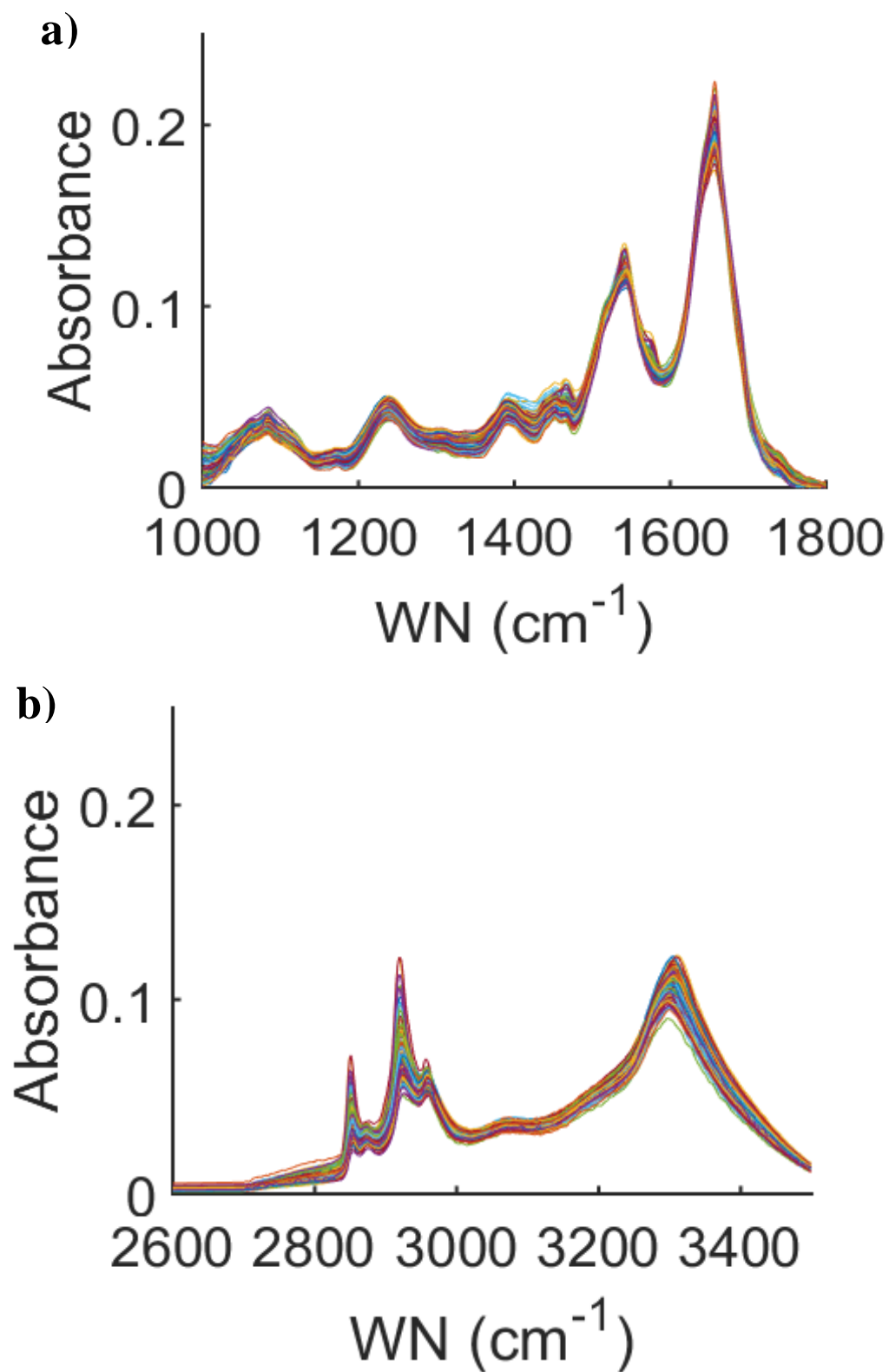


Figure 20 – FT-IR spectra of cell line PC-3M at $t=0$ min between the spectral ranges (a) 1000 cm^{-1} – 1800 cm^{-1} and (b) 2600 cm^{-1} – 3500 cm^{-1} .

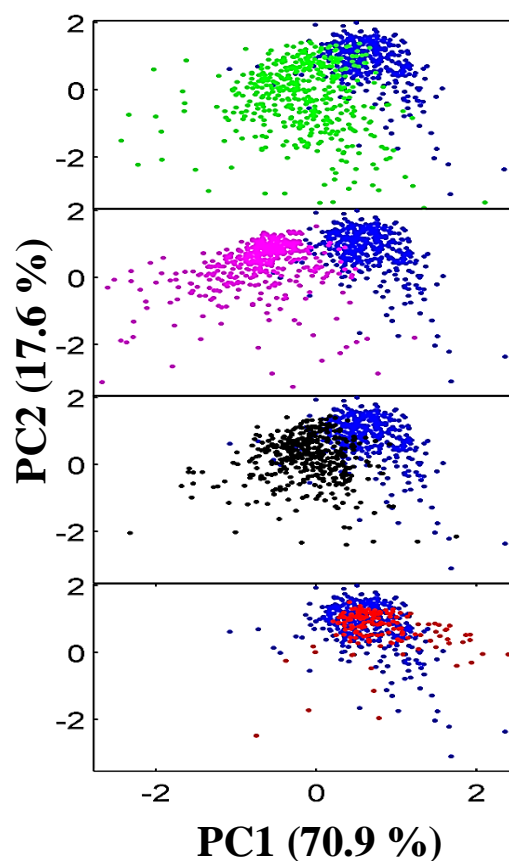


Figure 21 – PCA scores of FTIR spectra, examining the C=O stretch between 1720 cm^{-1} – 1750 cm^{-1} for the invasive cell line PC-3M treated with AA at time points (a) $t=0\text{ min}$ (blue) vs $t=5\text{ min}$ (green) and (b) $t=0\text{ min}$ (blue) vs $t=15\text{ min}$ (magenta) and (c) $t=0\text{ min}$ (blue) vs $t=30\text{ min}$ (black) and (d) $t=0\text{ min}$ (blue) vs $t=60\text{ min}$ (red).

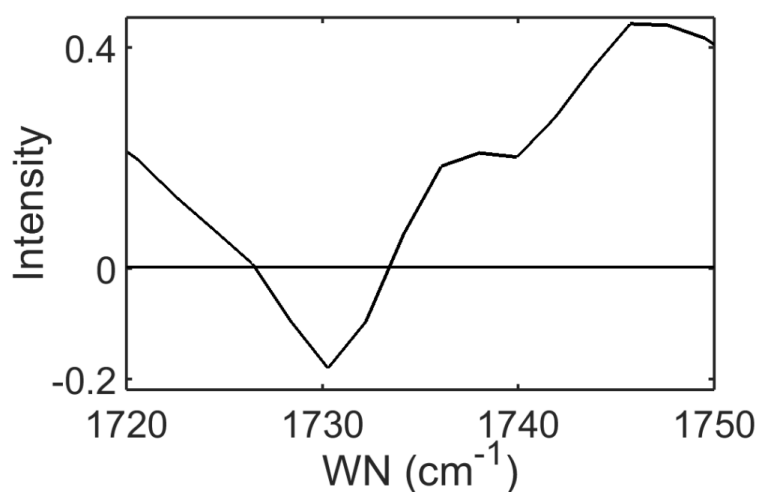


Figure 22 – PC1 loading plot for the cell line PC-3M

3.1.3 PCA of the C=O Fatty Acid Carbonyl Stretch for PC-3 Cells

The PCA scores of first derivative FTIR spectra for PC-3 cells treated with AA for $t=0$ min versus $t=5$, 15, 30, and 60 min can be seen in Figure 23. The cluster for $t=0$ min remains tight with the cells showing a chemical similarity. By $t=5$ min, there is a clear separation in the positive PC1 direction. The PC1 loading which can be seen in Figure 24 indicates that the $t=5$ min cell lines are becoming chemically similar to the carbonyl C=O chemistry associated with AA uptake represented in the positive PC1 loading, matching the direction of separation. By $t=15$ min, there is an even greater separation away from the $t=0$ min, indicating further AA uptake. Finally, $t=30$ and $t=60$ min progressively show less separation from $t=0$ min, the cells are more chemically similar to the initial time point containing no AA. This highlights the loss of cellular AA a possible indication of metabolism and cellular rejection.

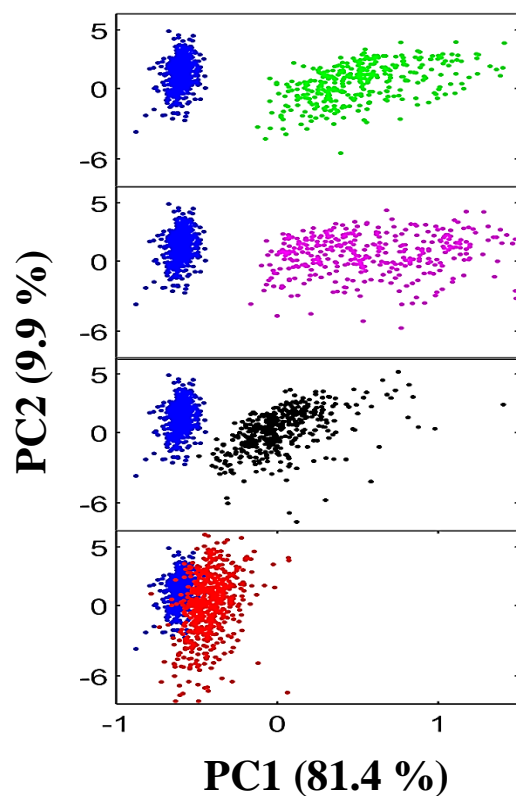


Figure 23 – PCA scores of FTIR spectra, examining the C=O stretch between 1720 cm^{-1} – 1750 cm^{-1} for the invasive cell line PC-3 treated with AA at time points (a) $t=0$ min (blue) vs $t=5$ min (green) and (b) $t=0$ min (blue) vs $t=15$ min (magenta) and (c) $t=0$ min (blue) vs $t=30$ min (black) and (d) $t=0$ min (blue) vs $t=60$ min (red).

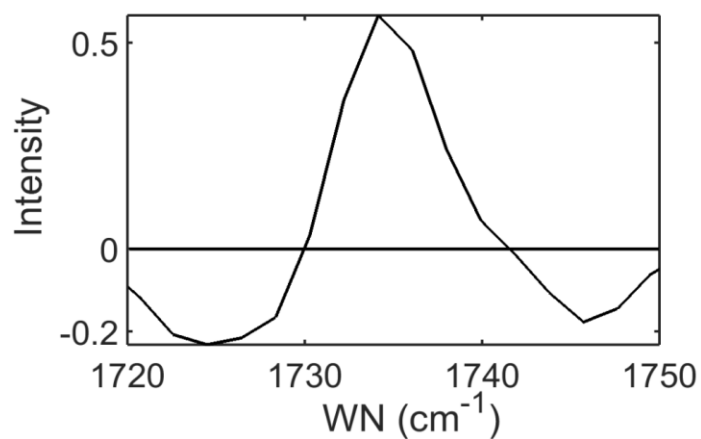


Figure 24 – PC1 loading plot for the cell line PC-3

3.1.4 PCA of the C=O Fatty Acid Carbonyl Stretch for DU145 Cells

The PCA scores of first derivative FTIR spectra for cell line DU145 cells treated with AA for $t=0$ min versus $t=5$, 15, 30, and 60 min can be seen in Figure 25. There is clear separation in the positive PC1 direction in the scores plot at $t=5$ and $t=15$ min from the initial $t=0$. The PC1 loading can be seen in Figure 26, with the positive PC1 loading representative of the C=O carbonyl stretch of AA, which is a good indication of uptake. The $t=5$ min appears much tighter than the $t=15$ min cluster, this is probably down to varying stages of the AA cascade. At $t=30$ min the cluster has become much tighter and have moved back in a negative direction towards the initial $t=0$ min time point losing the chemical features of the AA. At $t=60$ min the cells have moved to chemical spectral profile which matches the initial $t=0$ min, signifying a chemically similar state.

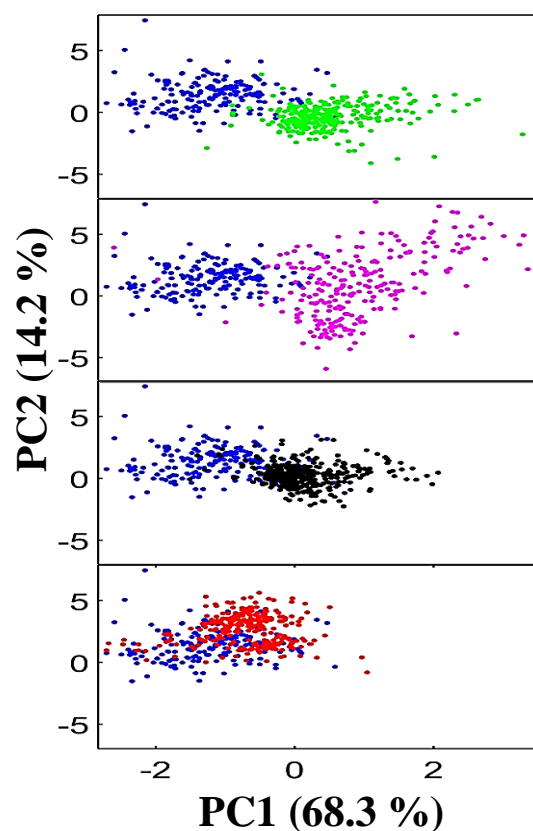


Figure 25 – PCA scores of FTIR spectra, examining the C=O stretch between 1720 cm^{-1} – 1750 cm^{-1} for the invasive cell line DU145 treated with AA at time points (a) $t=0\text{ min}$ (blue) vs $t=5\text{ min}$ (green) and (b) $t=0\text{ min}$ (blue) vs $t=15\text{ min}$ (magenta) and (c) $t=0\text{ min}$ (blue) vs $t=30\text{ min}$ (black) and (d) $t=0\text{ min}$ (blue) vs $t=60\text{ min}$ (red).

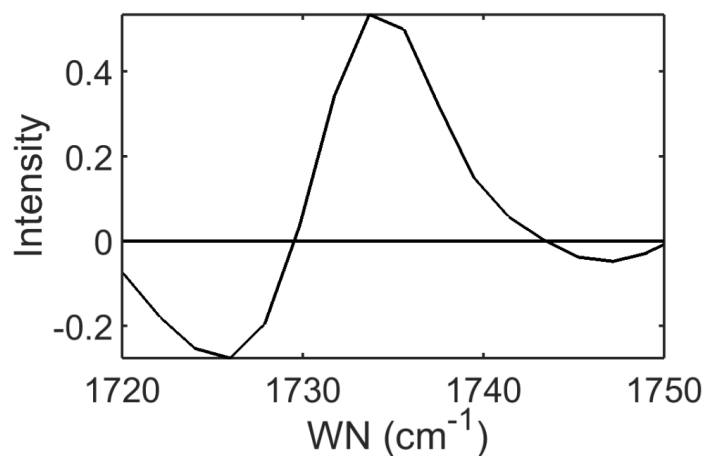


Figure 26 – PC1 loading plot for the cell line DU145

3.1.5 PCA of the C=O Fatty Acid Carbonyl Stretch for LNCaP C4-2B Cells

The PCA scores of first derivative FTIR spectra for LNCaP C4-2B cells treated with AA for $t=0$ min versus $t=5$, 15, 30, and 60 min can be seen in Figure 27. At $t=5$ min there is a defined separation in the positive PC1 direction away from the initial $t=0$ min cluster, with further separation seen by $t=15$ min. The dispersion is also more varied at $t=15$ min compared to that seen in $t=5$ min, this again is probably down to the cell experiencing different stages of the AA cascade. By $t=30$ min, the cluster is tight and moved in a more negative direction back towards $t=0$ min. At $t=60$ min there is no separation from the initial $t=0$ cluster. The PC1 loading can be seen in Figure 28 and again the positive loadings (direction of separation) indicate features of the 1732 cm^{-1} C=O AA carbonyl stretch. Again, there appears to be AA uptake and metabolism.

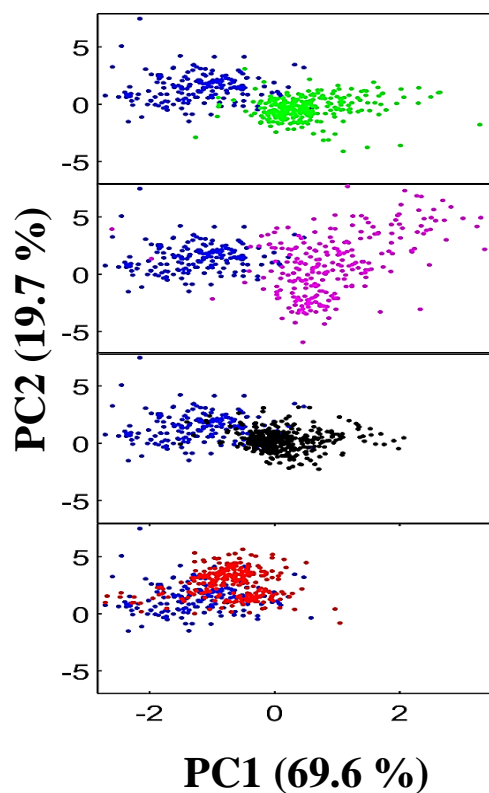


Figure 27 – PCA scores of FTIR spectra, examining the C=O stretch between 1720 cm^{-1} – 1750 cm^{-1} for the invasive cell line LNCaP C4-2B treated with AA at time points (a) $t=0\text{ min}$ (blue) vs $t=5\text{ min}$ (green) and (b) $t=0\text{ min}$ (blue) vs $t=15\text{ min}$ (magenta) and (c) $t=0\text{ min}$ (blue) vs $t=30\text{ min}$ (black) and (d) $t=0\text{ min}$ (blue) vs $t=60\text{ min}$ (red).

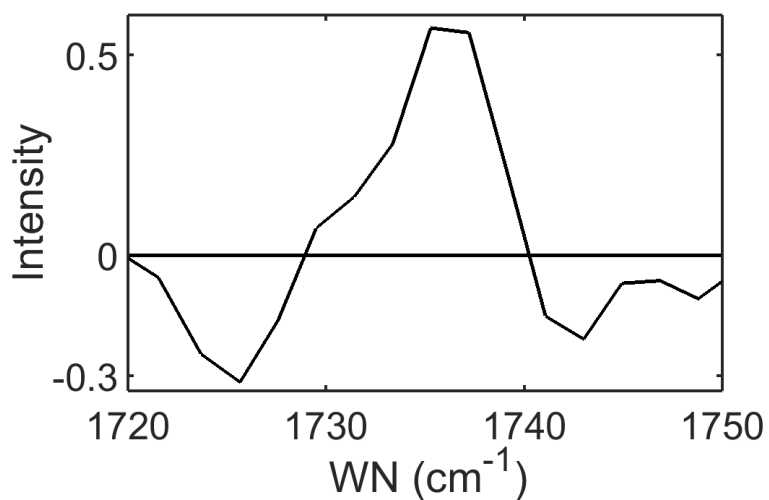


Figure 28 – PC1 loading plot for the cell line LNCaP C4-2B

3.1.6 PCA of the C=O Fatty Acid Carbonyl Stretch for LNCaP C4-2 Cells

The PCA scores of first derivative FTIR spectra for LNCaP C4-2 cells treated with AA for $t=0$ min versus $t=5$, 15, 30, and 60min can be seen in Figure 29. The $t=5$ min cluster has moved in the positive PC1 direction. The time points are still overlapping but there is indication that there are slight chemical variances between the two time points. The separation appears to have slightly increased by $t=15$ min with slight overlap still with the initial $t=0$ min cluster. At $t=30$ min the cluster is tighter with slight separation along PC1, with finally $t=60$ min showing no separation along PC1. The PC1 loading can be seen in Figure 30, showing the positive PC1 loadings showing chemistry associated with AA uptake with the C=O carbonyl stretch present at 1732 cm^{-1} . The separation does not appear as clear as the other invasive cell lines. The same trend is seen but to a less extent. The LNCaP C4-2 is the least invasive of the invasive cell lines used, which could be indication that the invasive phenotype could depend on the uptake and metabolism of AA.

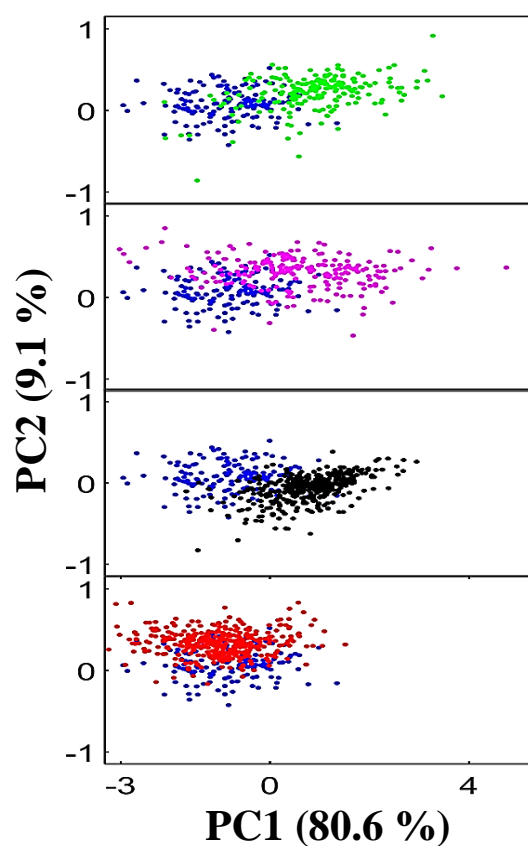


Figure 29 – PCA scores of FTIR spectra, examining the C=O stretch between 1720 cm^{-1} – 1750 cm^{-1} for the invasive cell line LNCaP C4-2 treated with AA at time points (a) $t=0\text{ min}$ (blue) vs $t=5\text{ min}$ (green) and (b) $t=0\text{ min}$ (blue) vs $t=15\text{ min}$ (magenta) and (c) $t=0\text{ min}$ (blue) vs $t=30\text{ min}$ (black) and (d) $t=0\text{ min}$ (blue) vs $t=60\text{ min}$ (red).

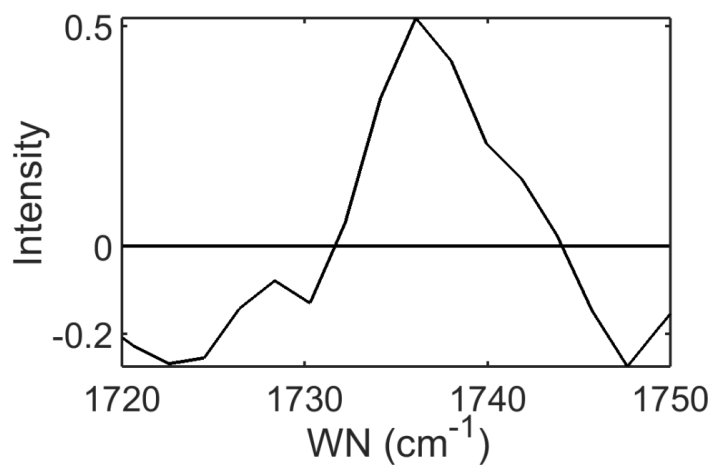


Figure 30 – PC1 loading plot for the cell line LNCaP C4-2

3.2 Non-Invasive Cell Lines

3.2.1 PCA of the C=O Fatty Acid Carbonyl Stretch for LNCaP Cells

The PCA scores of first derivative FTIR spectra for LNCaP cells treated with AA for $t=0$ min versus $t=5$, 15, 30, and 60 min can be seen in Figure 31. There appears to be no separation between any of the time points. All of the clusters remain on top of one another, displaying the lack of chemical variance throughout the 60-minute time course. It appears that the exogenous supply of AA has no detectable chemical effect on the non-invasive LNCaP cell line.

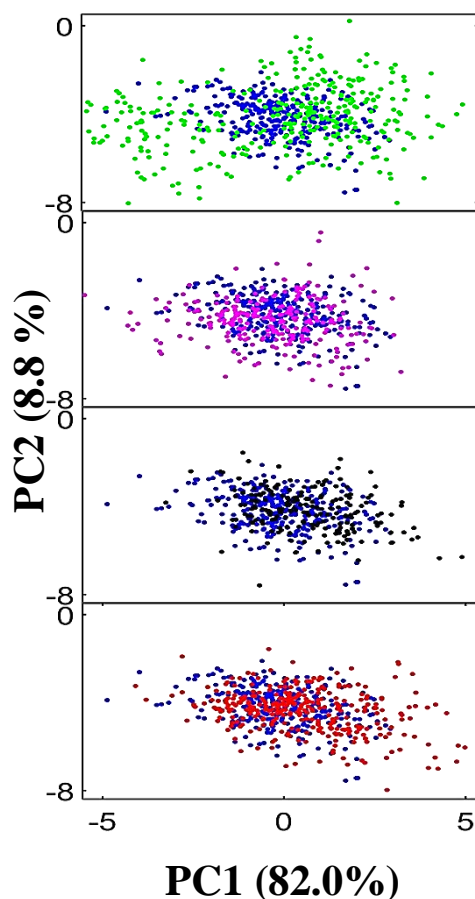


Figure 31 – PCA scores of FTIR spectra, examining the C=O stretch between 1720 cm^{-1} – 1750 cm^{-1} for the invasive cell line LNCaP treated with AA at time points (a) $t=0$ min (blue) vs $t=5$ min (green) and (b) $t=0$ min (blue) vs $t=15$ min (magenta) and (c) $t=0$ min (blue) vs $t=30$ min (black) and (d) $t=0$ min (blue) vs $t=60$ min (red).

3.2.2 PCA of the C=O Fatty Acid Carbonyl Stretch for PNT2 Cells

The PCA scores of first derivative FTIR spectra for PNT2 cells treated with AA for $t=0$ min versus $t=5$, 15, 30, and 60 min can be seen in Figure 32. Again, as seen with the other non-invasive cell line LNCaP, there is no PCA separation seen at any of the time points from the initial $t=0$ min. All of the cluster centres remain overlapped, expressing the chemical similarity between all of the time points. The cells appear to experience no chemical changes when exposed to exogenous AA.

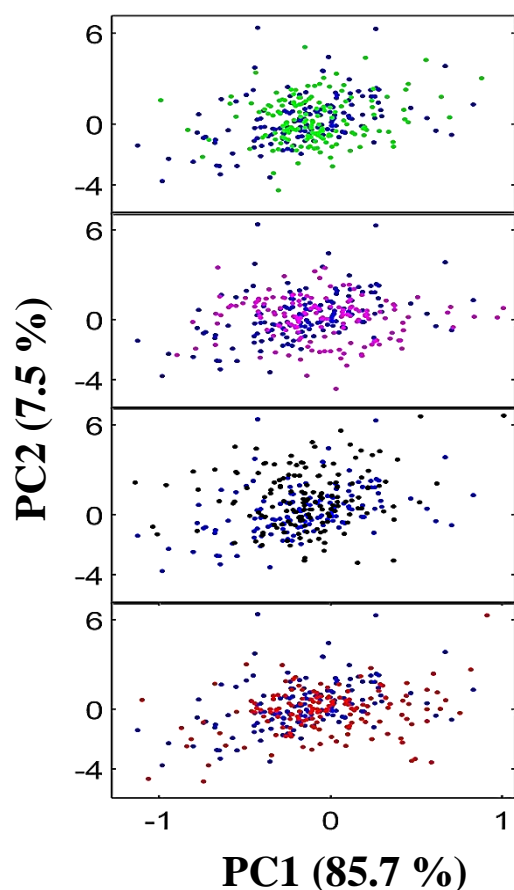


Figure 32 – PCA scores of FTIR spectra, examining the C=O stretch between 1720 cm^{-1} – 1750 cm^{-1} for the invasive cell line PNT2 treated with AA at time points (a) $t=0$ min (blue) vs $t=5$ min (green) and (b) $t=0$ min (blue) vs $t=15$ min (magenta) and (c) $t=0$ min (blue) vs $t=30$ min (black) and (d) $t=0$ min (blue) vs $t=60$ min (red).

3.3 Discussion

There is a very clear and distinct trend that has emerged when comparing the results of the PCA for all cell lines. The invasive cell lines PC-3M, PC-3, DU145, LNCaP C4-2B and LNCaP C4-2 display very similar chemical spectral profiles and trends throughout the 60-minute time course. The invasive cell lines all experience separation as early as 5 minutes with maximum separation seen by 15 minutes. By 30 minutes, the cells start to lose the chemical profile associated with AA uptake. It is clear, that by 60 minutes, all cell lines appear to return to their original pre-exposed spectral profile. The chemical behaviour highlighted by PCA implies that there is AA uptake in all invasive cell lines, albeit to different effects. The less aggressive cell line LNCaP C4-2 appears to show less separation compared to the highly invasive cell lines PC-3M and PC-3.

The separations in the PCA loadings are conclusive that the biochemical variances displayed throughout the 60-minute time course are a result of AA uptake and ejection. There are strong correlations in the loadings which indicate that the positive or negative direction of separation is a result of the 1732 cm^{-1} C=O stretch, which has been shown to be a signature of AA.

The time line of the chemistry displayed agrees with Brown et al. and is consistent with a physiologically realistic time scale (3). Throughout the first 15 minutes, there appears to be massive cellular biochemical change. Initially, there will be a massive cellular reaction to excess AA. The cell recognises that there is an abundance of AA available in the exogenous environment, triggers mass cellular uptake of AA. The cell regulates mass catalysis through the AA cascade, breaking AA through COX pathways into PGE₂. By $t=15\text{ min}$, if the AA cascade is underway, there will be a large amount of AA

converted to PGE₂. The PGE₂ is cytotoxic, so the bioactive metabolite is ejected from the cell, potentially the reason why clusters at $t=30$ and 60 min become more chemically similar to the initial $t=0$ min time point.

Brown *et al.* and Gazi *et al.* demonstrated the uptake of AA in invasive prostate cancer cell lines (4,5). These studies highlighted that invasive prostate cancer cells translocated AA from bone marrow adipocytes. Schumacher *et al.* further revealed that intraprostatic AA levels are significantly lower in cancer tissues compared that those of healthy tissue (6). This suggests that AA is preferentially metabolised into pro-tumour PGE₂ (7). These studies reinforce the spectral lipid changes seen in invasive prostate cancer cell lines. It appears that invasive cell lines uptake AA which directly effects their migratory potential, further implying that AA is an essential driver of prostate cancer metastasis.

When non-invasive cell lines are treated with AA, there appears to be no biochemical changes within the cellular system. This is significant, as all cellular systems would be expected to uptake AA as it is a key chemical component for cellular regulation. Non-invasive cell lines seem to have a limited ability to uptake AA. If the cellular systems fail to uptake AA, then the AA cascade will not commence. This potentially could be the reason why no biochemical change is seen throughout the 60-minute time course. The mechanism by which non-invasive cell lines have a suppressed uptake is currently unknown. There is no current literature surrounding this finding, which makes this question interesting. Is a key difference between an invasive and non-invasive cell line its ability to uptake and metabolise AA? It is already well documented in literature that AA causes an increase in prostate cancer cell proliferation and metastasis (2). Do the cells which invade need this AA as a fuel to increase the efficiency of its metastatic journey? Invasive cell lines must have a key chemical affinity to the AA, what drives

this affinity is unknown. It also must be noted that, if the key difference between an invasive and non-invasive phenotype is its fundamental ability to metabolise AA into key bioactive PGs, then what effect does PGE₂ have on prostate cancer metastasis?

3.4 The Invasion Assays of PC-3 and PNT2 Cell Lines

Furthering the PCA investigations, the invasive potentials of the invasive cell line PC-3 and non-invasive cell line PNT2 were investigated. A scratch assay was performed, where cells were grown in a well to 100% confluency. Once confluent, the cells were serum starved overnight. A set of 4 scratches were evenly scratched on the cultured substrate with a 1 ml Gilson tip, with 2 lines parallel to one another with the other 2 lines orthogonal to the initial two lines forming 4 crosses. Once scratched, the cells were washed twice with PBS, removing any of the loose cellular debris. The cells are treated with a 20 µM concentration of AA in cyclodextrin, with the 4 scratch interest points imaged and then incubated at 37 °C and 5% CO₂ v/v for 14 hours. After 14 hours of incubation, the scratch intersects are imaged again, allowing a comparison to be made on the cell's invasive potential on AA exposure.

The scratches for cell lines PC-3 before and after 14h exposure to AA can be seen in Figure 33a and b respectively. The scratches for PNT2 cells before and after 14h AA exposure can be seen in Figure 34a and b respectively.

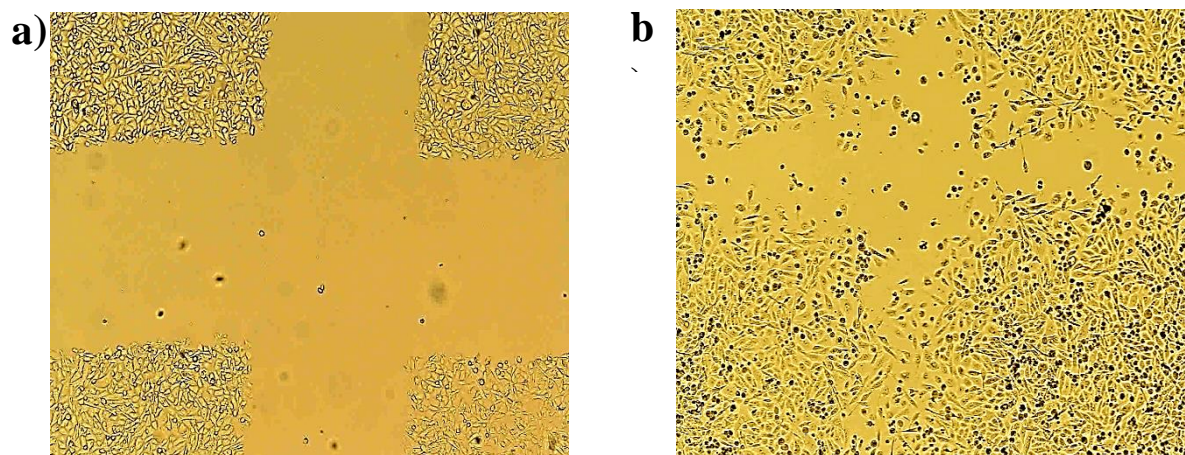


Figure 33 – Scratch invasion assay for PC-3 cells treated with AA for (a) 0 hours and (b) 14 hours imaged at x5 magnification 960 μm x 960 μm

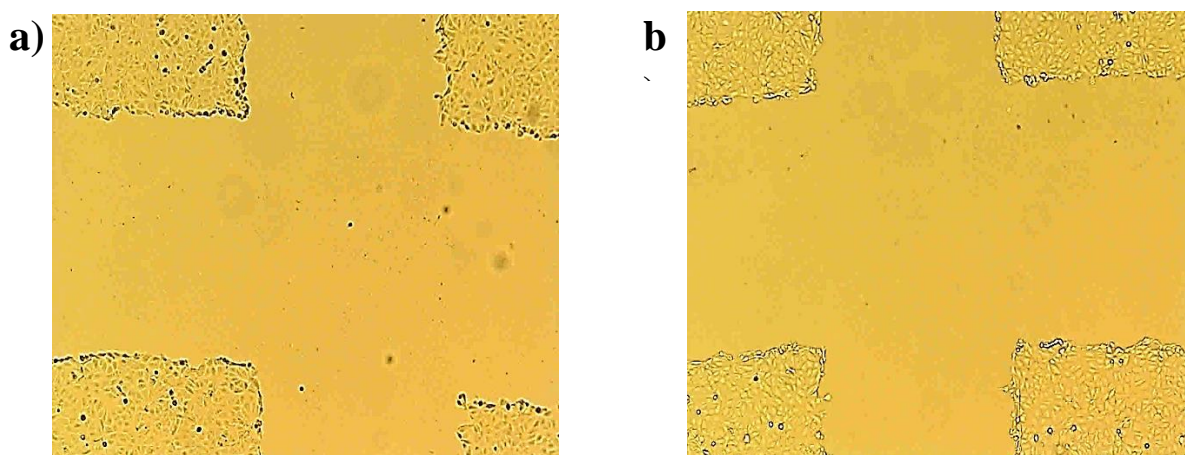


Figure 34 – Scratch invasion assay for PNT2 cells treated with AA for (a) 0 hours and (b) 14 hours imaged at x5 magnification 960 μm x 960 μm

Firstly, looking at the PC-3 cells at the initial 0-hour treatment, the scratch is evenly spaced and well defined. There is little cellular debris in the open scratch, with the wound clean. When the PC-3 cells have been exposed to AA for 14 hours, the cells had invaded the scratch, with a high degree of wound closure, which is consistent with the study carried out by Brown *et al.* demonstrating that AA influences PC-3 cells invasive potential (2).

The PNT2 cells at 0-hour exposure have a well-defined clear scratch. The wound is clean with no cellular debris. After 14-hour exposure to AA, the wound remained open with minimal wound closure. Brown *et al* was also able to display that the non-invasive cell line LNCaP were significantly less invasive than PC-3 cell lines when scratch assays were compared (2). This agrees with the result obtained with non-invasive PNT2 cell lines.

ImageJ was used to quantitate the degree of wound closure between the PC-3 and PNT2 cell lines, measuring the arbitrary scratch widths of each of the 4 crosses giving 16 measurements per well. These arbitrary lengths for each scratch were averaged, producing an average scratch width before and after 14 hours AA exposure. A migration index was calculated, which is essentially the distance of wound closure throughout the 14 hours. From this, the percentage wound closure was calculated for each of the 4 crosses in the well plate. The results for the cell lines PC-3 and PNT2 are displayed in Table 1 and Table 2 respectively. The comparison of wound closure for PC-3 and PNT2 cells are displayed in the bar plot in Figure 35.

PC-3				
Scratch	Before Treatment	After Treatment	Migration Index	Percentage Closure (%)
1	453.7	182.7	271.0	59.7
2	416.2	205.1	211.1	50.7
3	408.4	225.3	183.1	44.8
4	416.3	214.3	202.0	48.5

Table 1 – Invasion assay data for PC-3 cells treated with AA for 0 hours (before treatment) and 14 hours (after treatment) for all 4 scratches and 4 data points per scratch averaged, the.

PNT2				
Scratch	Before Treatment	After Treatment	Migration Index	Percentage Closure (%)
1	479.1	442.8	36.3	7.6
2	556.6	486.0	70.6	12.7
3	507.5	496.9	10.5	2.1
4	521.5	485.6	35.9	6.9

Table 2 – Invasion assay data for PNT2 cells treated with AA for 0 hours (before treatment) and 14 hours (after treatment) for all 4 scratches and 4 data points per scratch averaged.

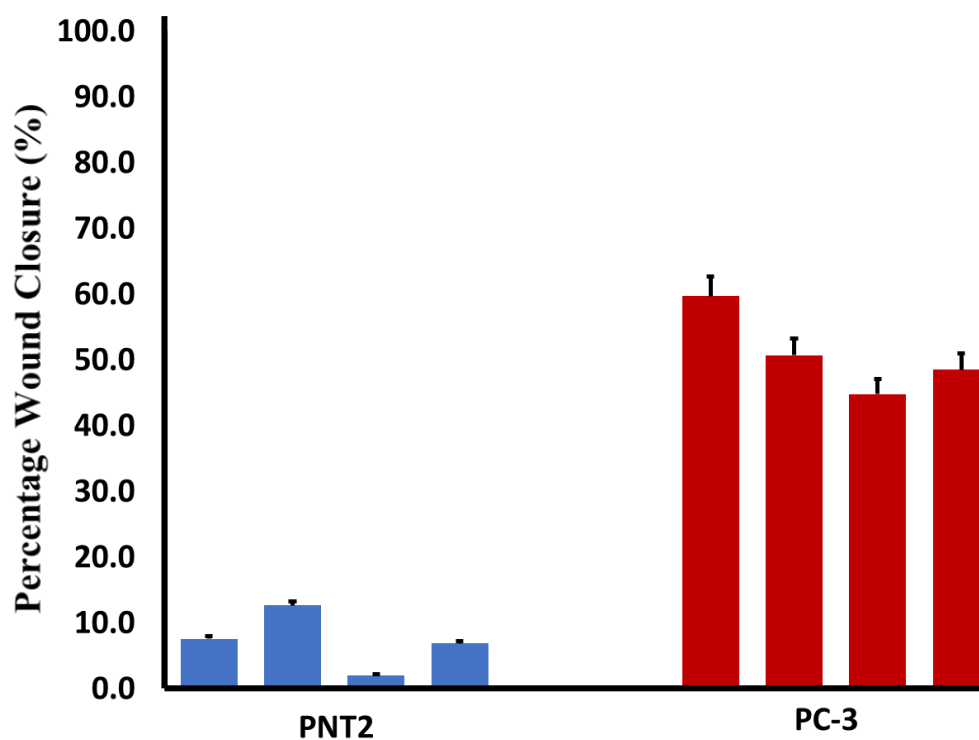


Figure 35 – Bar plot of the percentage wound closure after 14 hours exposure to AA for cell lines PNT2 (blue) and PC-3 cells (red)

There is a clear difference in the invasive ability of non-invasive PNT2 and invasive PC-3 cells with an approximate 40% difference in wound closure. The wound closure for each of the 4 crosses for both PNT2 and PC-3 cells show small margins of variability. This could be simply down to an uneven distribution of AA across the well or natural variation from complex mechanics of cellular systems.

There is a clear difference in cellular invasiveness when non-invasive and invasive cell lines are exposed to AA. It was seen that invasive cell lines readily uptake AA whereas non-invasive cell lines experienced no such behaviour in the PCA. This chemistry supports the degree of invasiveness witnessed, and supports the hypothesis that AA is the fundamental fuel required for prostate cancer cells to embark on their metastatic journey, with the non-invasive cells lacking a fundamental ability to uptake and metabolise AA.

3.5 PC-3 Cyclodextrin Control

Treating cells with pure AA is problematic, as it is insoluble. Therefore, cyclodextrin was chosen as a vehicle to deliver AA. The low toxicity and immunogenicity make cyclodextrin favourable to use (8). The disadvantage of using cyclodextrin is it disrupts the lipid structures within the cell membrane such as lipid rafts and cholesterol (9). Other solvents commonly used are DMSO and ethanol, but both are considered highly cytotoxic compared to the carbohydrate based cyclodextrin (10). It is essential to analyse the biochemical effect that cyclodextrin has on this study.

PC-3 cells were serum starved overnight before a 20 μ M treatment of AA was delivered followed by formalin fixation over a 60-minute time course. PCA was performed, with the scores can be seen in Figure 36. There is no separation displayed throughout the 60-

minute time course. All time point clusters overlap and show, displaying no significant biochemical variance throughout the time course.

It is known that the lipid membrane chemistry changes and is disrupted on exposure to cyclodextrin, one might expect to see a biochemical change. FT-IR examines the global cellular chemistry. Consequently, no overall biochemical change will be noticed for such small molecular changes within the membrane. Confidence can be drawn that the chemical changes witnessed are a result of the AA induced cellular mechanisms rather than cyclodextrin induced effects.

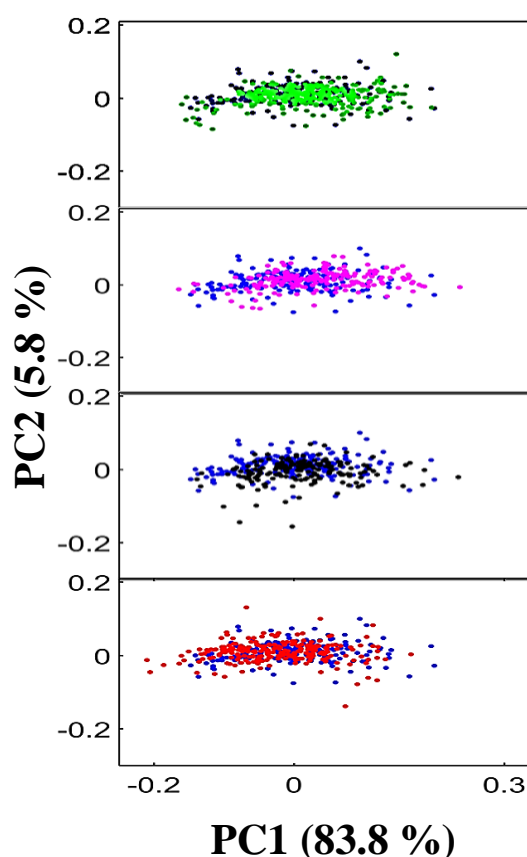


Figure 36 – PCA scores of FTIR spectra, examining the C=O stretch between 1720 cm^{-1} – 1750 cm^{-1} for the invasive cell line PC-3 treated with cyclodextrin at time points (a) $t=0$ min (blue) vs $t=5$ min (green) and (b) $t=0$ min (blue) vs $t=15$ min (magenta) and (c) $t=0$ min (blue) vs $t=30$ min (black) and (d) $t=0$ min (blue) vs $t=60$ min (red).

3.6 Cell Membrane Fluidity

The introduction of lipids to cancer cells effects numerous cellular processes such as cell growth, proliferation, differentiation and motility (11). Studies have already demonstrated that AA increases prostate cancer motility (12,13,14). Cellular motility is a key function in the progression and metastasis of prostate cancer. If the prostate cancer cells motility is limited, then the cellular invasiveness will be less potent. Los *et al.* identified a decrease in FT-IR CH_2/CH_3 ratio is indication of an increased membrane fluidity (15). Shorter chained fatty acids integrated within the membrane gives an increase in fluidity, as the fatty acid chains are shorter there are fewer CH_2 vibrations with the same number of terminal CH_3 vibrations, decreasing the ratio between the two. This is the case when cells are experiencing a shift from a mesenchymal to amoeboid phenotype, a key transition required to penetrate tight cell junctions and undergo intra and extra-vasation.

The CH_2/CH_3 lipid proportion will be monitored throughout the 60-minute time course for the 3 most invasive cell lines PC-3M, PC-3, LNCaP C42B and non-invasive cell lines PNT2 and LNCaP to further identify biochemical shifts with respect to AA induction.

The peak area will be used rather than the maximum peak intensity, as it provides a better overall representation of lipid quantity, as the area takes the peak shape into consideration. The asymmetric CH_2 and CH_3 peak areas have been examined, as they simply have a larger area compared to the symmetric stretches. A larger area should result in a smaller error within the ratio. The CH_2 asymmetric stretch peak falls at 2852 cm^{-1} taking the width of the peak between $2845\text{ cm}^{-1} - 2862\text{ cm}^{-1}$. The CH_3 asymmetric

stretch peak falls at 2922 cm^{-1} taking the width of the peak between $2915\text{ cm}^{-1} - 2947\text{ cm}^{-1}$

Rather than using a direct ratio of the CH_2 and CH_3 area values, a proportion will be used, where the area of the CH_2 asymmetric stretch will be divided by the sum of the areas of the CH_2 and CH_3 asymmetric stretches shown in equation 9.

$$R_{\text{CH}_2/\text{CH}_3} = \frac{A_{\text{CH}_2}}{A_{\text{CH}_2} + A_{\text{CH}_3}} \quad \text{Equation 9}$$

A proportion was used as to a simple ratio due to the scaling. A proportion will always give a value between 0 – 1. As $A_{\text{CH}_2} \rightarrow \infty$, $R_{\text{CH}_2/\text{CH}_3} \rightarrow 1$. Meaning sharp changes in spectral intensities will not result in a large value, simply a value between 0 – 1.

The median area proportion of CH_2/CH_3 asymmetric stretch vibrations for the invasive cell line PC-3M throughout the 60-minute time course can be seen in Figure 37. Overall, there is a decrease in the global CH_2/CH_3 proportion throughout the 60-minutes. This implies that the fluidity of the cell has shifted to a less rigid state, a key state a cell must reach to increase its motility. It appears that AA also induces a change in the fluidity as the cell gears up for its metastatic invasion. During the first 5-minutes, there is an increase in membrane fluidity, between 5 and 15 minutes there appears to be no change in fluidity. Finally, there is a sharp increase in cell fluidity between 15 and 30 minutes, with a progressively small increase to 60-minutes.

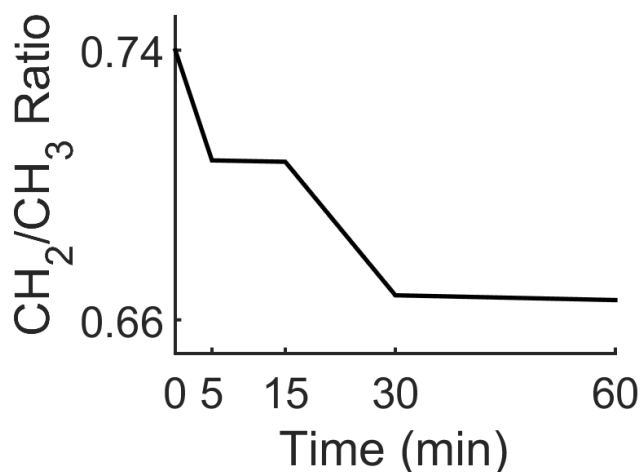


Figure 37 – Median CH₂ to CH₃ asymmetric proportion of PC-3M cells treated with AA at $t=0$, 5, 15, 30 and 60min.

The median area proportion of CH₂/CH₃ asymmetric stretch vibrations for the invasive cell line PC-3 throughout the 60-minute time course can be seen in Figure 38. Overall, there is a significant increase in cellular fluidity represented by a large decrease in the CH₂/CH₃ proportion. There is an increase in cell fluidity as early as 5 minutes, followed by a plateau until 30 minutes. Finally, there is a further increasing in cellular fluidity through the remainder of the time course until 60-minutes.

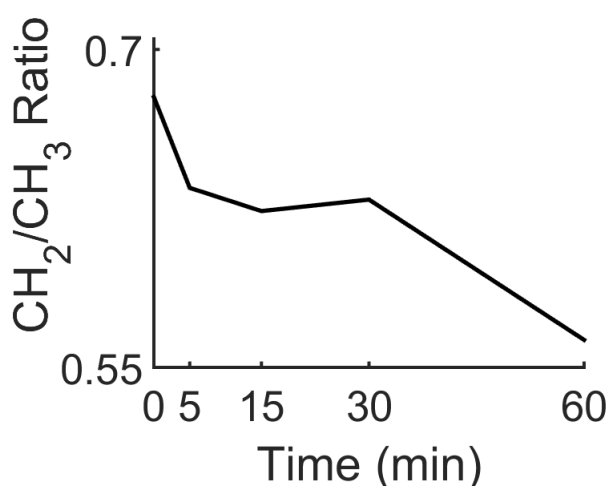


Figure 38 – Median CH₂ to CH₃ asymmetric proportion of PC-3 cells treated with AA at $t=0$, 5, 15, 30 and 60min

The median area proportion of CH_2/CH_3 asymmetric stretch vibrations for the invasive cell line LNCaP C4-2B throughout the 60-minute time course can be seen in Figure 39. There is a substantial increase in cell fluidity in the first 15-minutes. Between 15 and 30 minutes the fluidity plateaus with a further small increase for the remainder of the time course until 60-minutes.

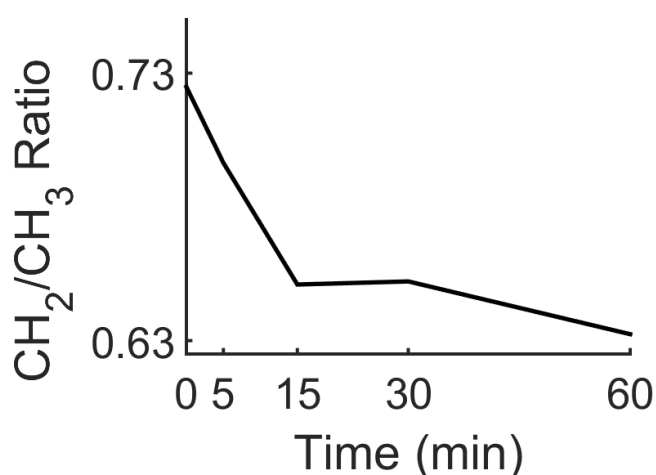


Figure 39 – Median CH_2 to CH_3 asymmetric proportion of LNCaP C4-2B cells treated with AA at $t=0$, 5, 15, 30 and 60min

The area proportion of CH_2/CH_3 asymmetric stretch vibrations for the non-invasive cell line PNT2 can be seen in Figure 40. There is no apparent trend or overall pattern seen with respect to the CH_2/CH_3 proportion. There appears to be no general shift in cell fluidity. There is an initial increase in CH_2/CH_3 proportion within the first 5-minutes, with the proportion returning to a similar proportion to the initial $t=0$ min for the remainder of the time course from 15-minutes onwards.

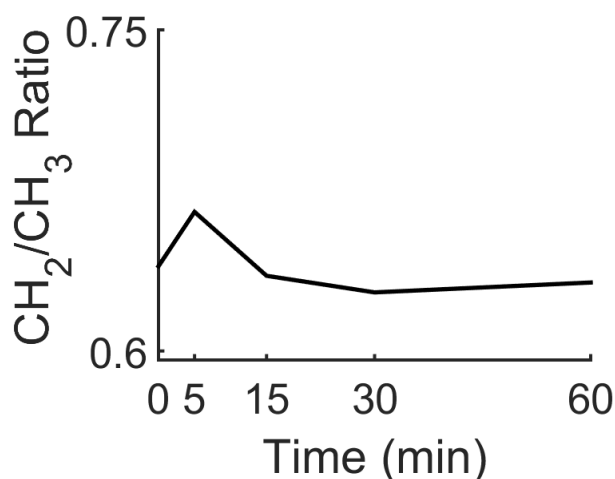


Figure 40 – Median CH₂ to CH₃ asymmetric proportion of PNT2 cells treated with AA at $t=0$, 5, 15, 30 and 60min

The area proportion of CH₂/CH₃ asymmetric stretch vibrations for the non-invasive cell line LNCaP can be seen in Figure 41. Throughout the first 15 minutes there appears to be a decrease in CH₂/CH₃ proportion followed by a gradual increase in proportion for the remainder of the time course. The overall change appears to be an increased cell rigidity with an increase in the CH₂/CH₃ proportion but it should be noted that the change is small.

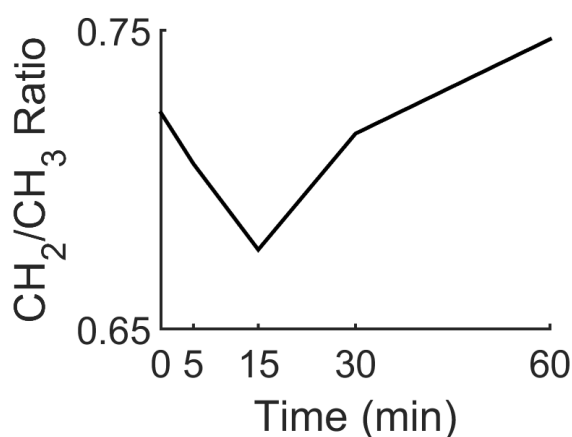


Figure 41 – Median CH₂ to CH₃ asymmetric proportion of LNCaP cells treated with AA at $t=0$, 5, 15, 30 and 60min.

There appears to be a distinct difference between cellular lipids in invasive and non-invasive cell lines when treated with AA over the 60-minute time course. The overall pattern seen throughout the invasive cell lines PC-3M, PC-3 and LNCaP C4-2B was a decrease in CH_2/CH_3 proportion indicating the increase of cellular fluidity. All cell lines appeared to have an initial decrease in proportion within the first 5-minutes, followed by a stabilisation period between 15-30 minutes where there appears to be little or no change with the CH_2/CH_3 proportion. This could be possible indication that AA is been incorporated in the lipid membrane on initial uptake, followed by PLA_2 action, cleaving the esterified AA from the lipid membrane. Once the AA is cleaved from the membrane it is metabolised. This period of metabolism could result in a period where there no further shift in membrane fluidity. After the stabilisation period, there appears to be a further decrease in CH_2/CH_3 proportion with an increase in cellular fluidity.

No such changes were seen in the non-invasive cell lines PNT2 and LNCaP. These cell lines showed no consistent trend with both increases or decreases in CH_2/CH_3 proportion. The magnitude of the overall nett change in CH_2/CH_3 proportion was small in comparison to the shifts seen with the invasive cell lines, this is suggestive of natural cellular variation rather than a significant change in cellular lipids from AA induction.

The results suggest that there is a difference in the AA induction mechanisms in invasive and non-invasive cell lines that lead to morphological cellular changes that increases cellular motility. The results were suggestive earlier that the non-invasive cell lines lacked a fundamental ability to uptake AA, whereas the invasive cell lines displayed spectral signatures of AA uptake and metabolism. The CH_2/CH_3 proportions also agree with the results initially displayed. If the key difference between invasive and non-invasive cell lines is the ability to uptake AA, then the cells motility will be

directly affected as a result of this. The non-invasive cell lines don't uptake AA, therefore cannot restructure the lipids in a way to increase the overall cellular fluidity essential for motility. This lack of fluidity then directly effects the cells ability to invade and metastasise.

3.7 Chemical Differences

It has been shown that the maximum chemical variance for all invasive cell lines is around 15-minutes. The maximum variance is reflective of the maximum chemical change a cell undergoes when exposed to AA. Therefore, the chemical difference between time point $t=0$ min and $t=15$ min needs to be assessed for the most invasive cell lines PC-3M, PC-3 and LNCaP C4-2B and the non-invasive cell lines PNT2 and LNCaP.

Difference spectra were produced by subtracting the median spectra of each cell line at $t=0$ min from the median spectra at $t=15$ min. The resulting spectrum displays positive values associated with a new chemical change at $t=15$ min, and a negative value associates lost chemical features whereby $t=0$ min displays more of a given spectral feature than that of the $t=15$ min time point. All difference spectra were placed on axes of the same order of magnitude, comparing the chemical changes of each cell line relatively. Two ranges are examined firstly between $1000\text{ cm}^{-1} - 1800\text{ cm}^{-1}$ and secondly between $2800\text{ cm}^{-1} - 3000\text{ cm}^{-1}$. The difference spectra for PC-3M cells between $1000\text{ cm}^{-1} - 1800\text{ cm}^{-1}$ and $2800\text{ cm}^{-1} - 3000\text{ cm}^{-1}$ can be seen in Figure 42a and b respectively. The difference spectra for PC-3 between $1000\text{ cm}^{-1} - 1800\text{ cm}^{-1}$ and $2800\text{ cm}^{-1} - 3000\text{ cm}^{-1}$ can be seen in Figure 43a and b respectively. The difference

spectra for LNCaP C4-2B between $1000\text{ cm}^{-1} - 1800\text{ cm}^{-1}$ and $2800\text{ cm}^{-1} - 3000\text{ cm}^{-1}$ can be seen in Figure 44 respectively.

PC-3M Median Difference Spectra

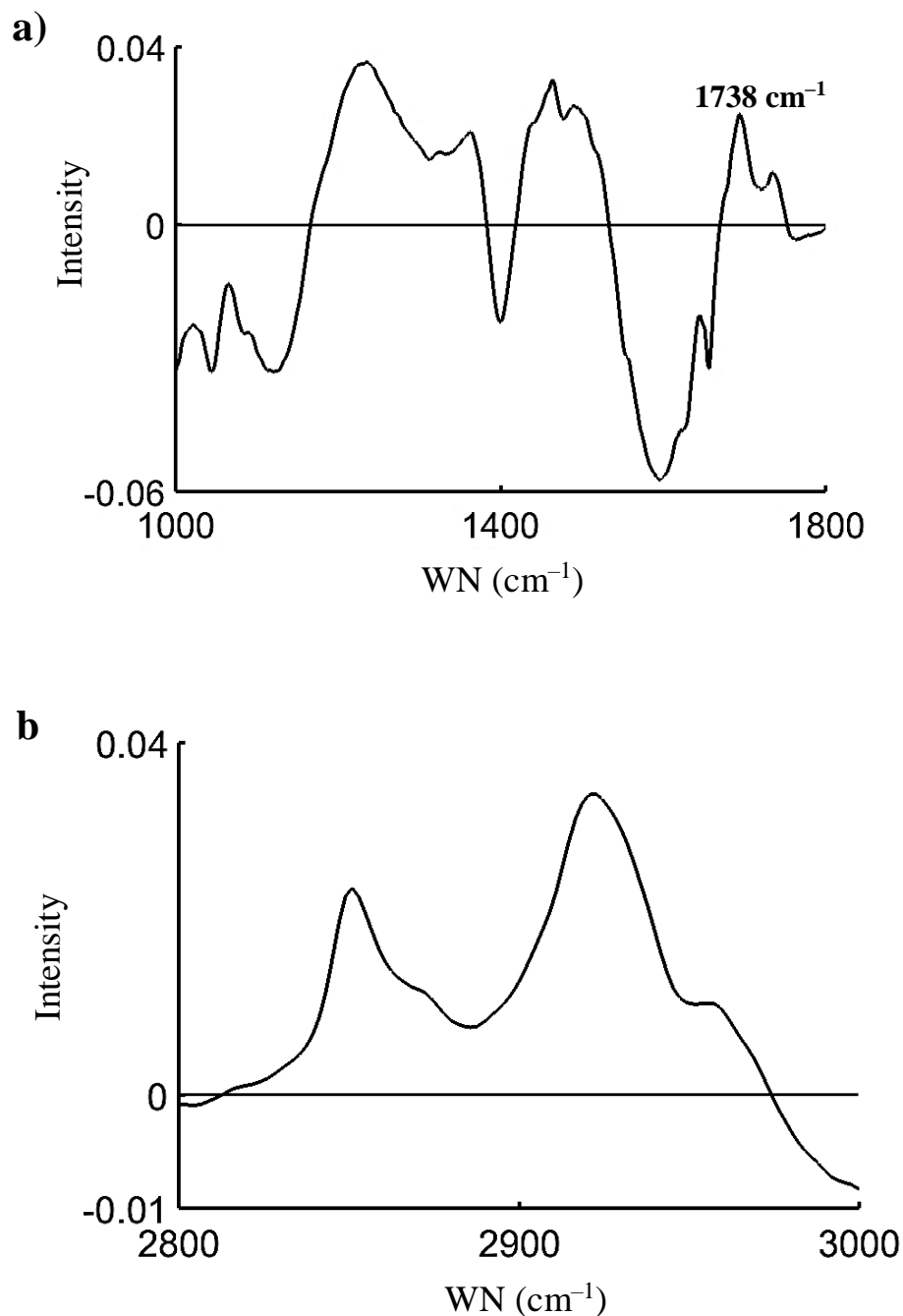


Figure 42 – Median difference spectra of PC-3M cells comparing $t=15\text{ min}$ with $t=0\text{ min}$ between (a) $1000\text{ cm}^{-1} - 1800\text{ cm}^{-1}$ and (b) $2800\text{ cm}^{-1} - 3000\text{ cm}^{-1}$ treated with AA.

PC-3 Median Difference Spectra

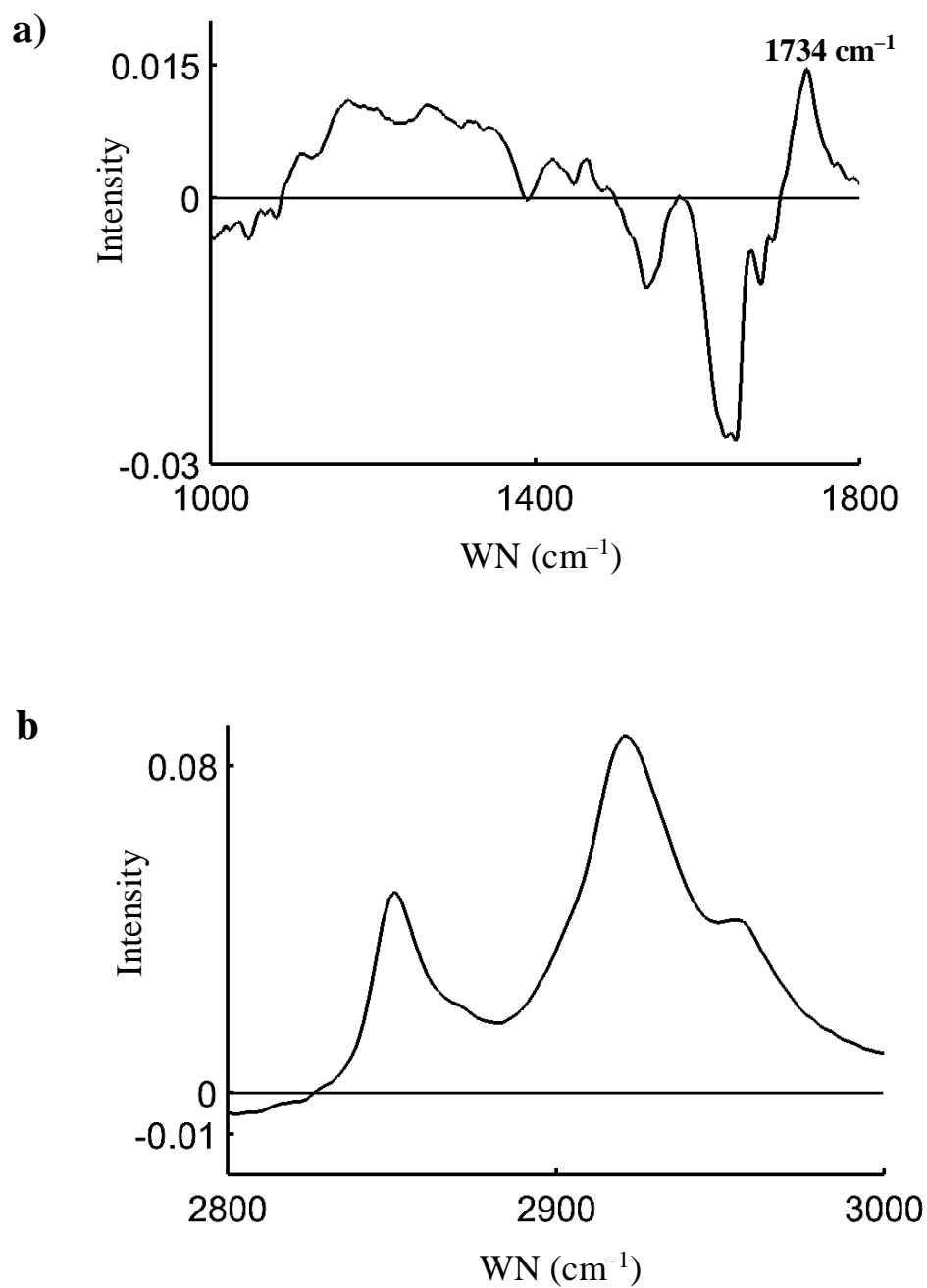


Figure 43 – Median difference spectra of PC-3 cells comparing $t=15$ min with $t=0$ min between (a) $1000\text{ cm}^{-1} - 1800\text{ cm}^{-1}$ and (b) $2800\text{ cm}^{-1} - 3000\text{ cm}^{-1}$ treated with AA.

LNCaP C4-2B Median Difference Spectra

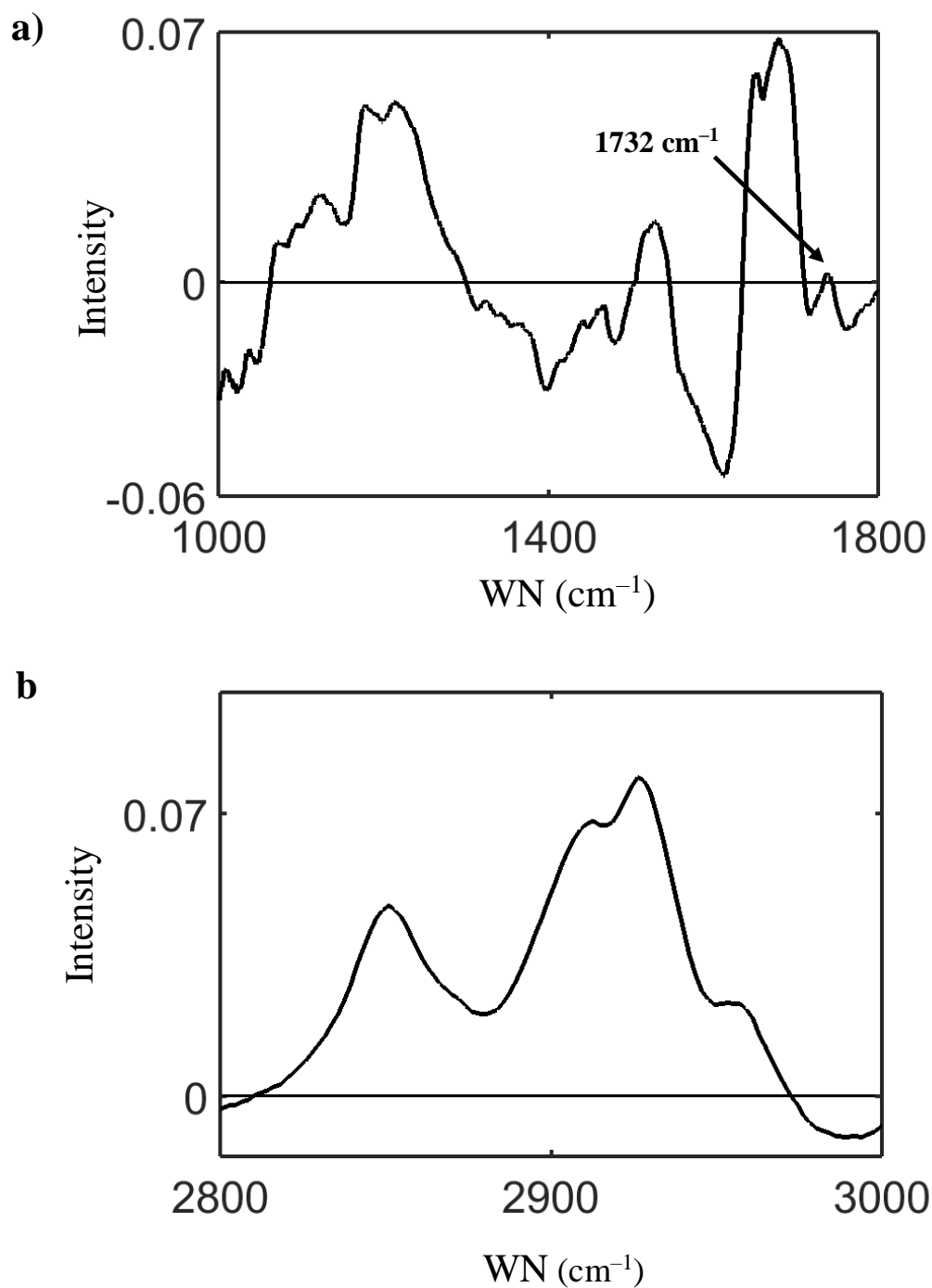


Figure 44 – Median difference spectra of LNCaP C4-2B cells comparing $t=15$ min with $t=0$ min between (a) $1000\text{ cm}^{-1} - 1800\text{ cm}^{-1}$ and (b) $2800\text{ cm}^{-1} - 3000\text{ cm}^{-1}$ treated with AA.

A list of spectral similarities for the invasive cell lines PC-3M, PC-3 and LNCaP C4-2B have been made for positive peak positions and negative peak positions shown in and Table 4 respectively. It is obvious that the positive changes in the difference spectra are solely down to the changes in cellular lipids which would be expected if the cell is taking up AA. There are distinct changes in the CH₂ and CH₃ vibrations, probably partly relating to the shifts displayed in membrane fluidity and the general uptake, storage and metabolism of the fatty acid. There is also the key marker for AA uptake displayed between 1730 cm⁻¹ and 1742 cm⁻¹ associated with the C=O carbonyl stretch of fatty acids. A 12 cm⁻¹ difference in wavenumber for the C=O carbonyl stretch appears rather large for a given vibration, it must be noted that AA is metabolised into PGE₂. There is a ketone C=O within a cyclic 5-carbon ring. This stretch is highly specific to 1742 cm⁻¹. One can speculate that the C=O peak displayed more towards the 1742 cm⁻¹ contains a significant amount of cellular PGE₂ with a peak towards 1732 cm⁻¹ is more associated with AA. The presence of cellular PGE₂ is again evidence of AA uptake and metabolism.

All 3 invasive cell lines have appeared to have less intensity associated with DNA and protein stretches from the C-O-C and PO₂⁻ stretches and the amide I stretch respectively at $t=15$ min compared to the initial $t=0$ min time point. A possible explanation to this is AA induces upregulation of COX-2 enzymes around the nuclear envelope and in the rough endoplasmic reticulum. To do this, transcription needs to be undertaken. Initially seeing a change in cellular mRNA inducing the transcription of COX-2 expressions.

Positive Spectral Positions (cm ⁻¹)			
Vibration	PC-3M	PC-3	LNCaP C4-2B
CH ₂ Bending Lipids	1466	1460	—
C=O Stretch Lipids	1738	1734	1742
Sym CH ₂ Stretch	2851	2851	2851
Asy CH ₂ Stretch	2922	2922	2926
Asy CH ₃ Stretch	2955	2957	2953

Table 3 – Positive common median difference spectral peaks between the cell lines PC-3M, PC-3 and LNCaP C4-2B.

Negative Spectral Positions (cm ⁻¹)			
Vibration	PC-3M	PC-3	LNCaP C4-2B
C-O-C Stretch Nucleic Acids	1049	1049	1049
PO ₂ - Stretch Nucleic Acids	1086	1086	—
Amide I	1657	1649	1615

Table 4 – Negative common median difference spectral peaks between the cell lines PC-3M, PC-3 and LNCaP C4-2B.

The difference spectra for PNT2 cell lines between $1000\text{ cm}^{-1} - 1800\text{ cm}^{-1}$ and $2800\text{ cm}^{-1} - 3000\text{ cm}^{-1}$ can be seen in Figure 45a and b respectively and the LNCaP cell lines in Figure 46a and b respectively. There appears to be no significant changes in cellular chemistry throughout the first 15 minutes for both non-invasive cell lines in both spectral ranges in contrast to the invasive cell lines. This again is indication that there is no significant uptake in AA for non-invasive cell lines. The median difference spectral analysis between the $t=0$ and $t=15$ min agrees with the PCA analysis carried out in sections 3.1 and 3.2 further indicating that the difference between a motile, metastatic cell is potentially its fundamental ability to uptake AA, which is a great fuel to provide cellular energy for metastatic endeavour.

PNT2 Median Difference Spectra

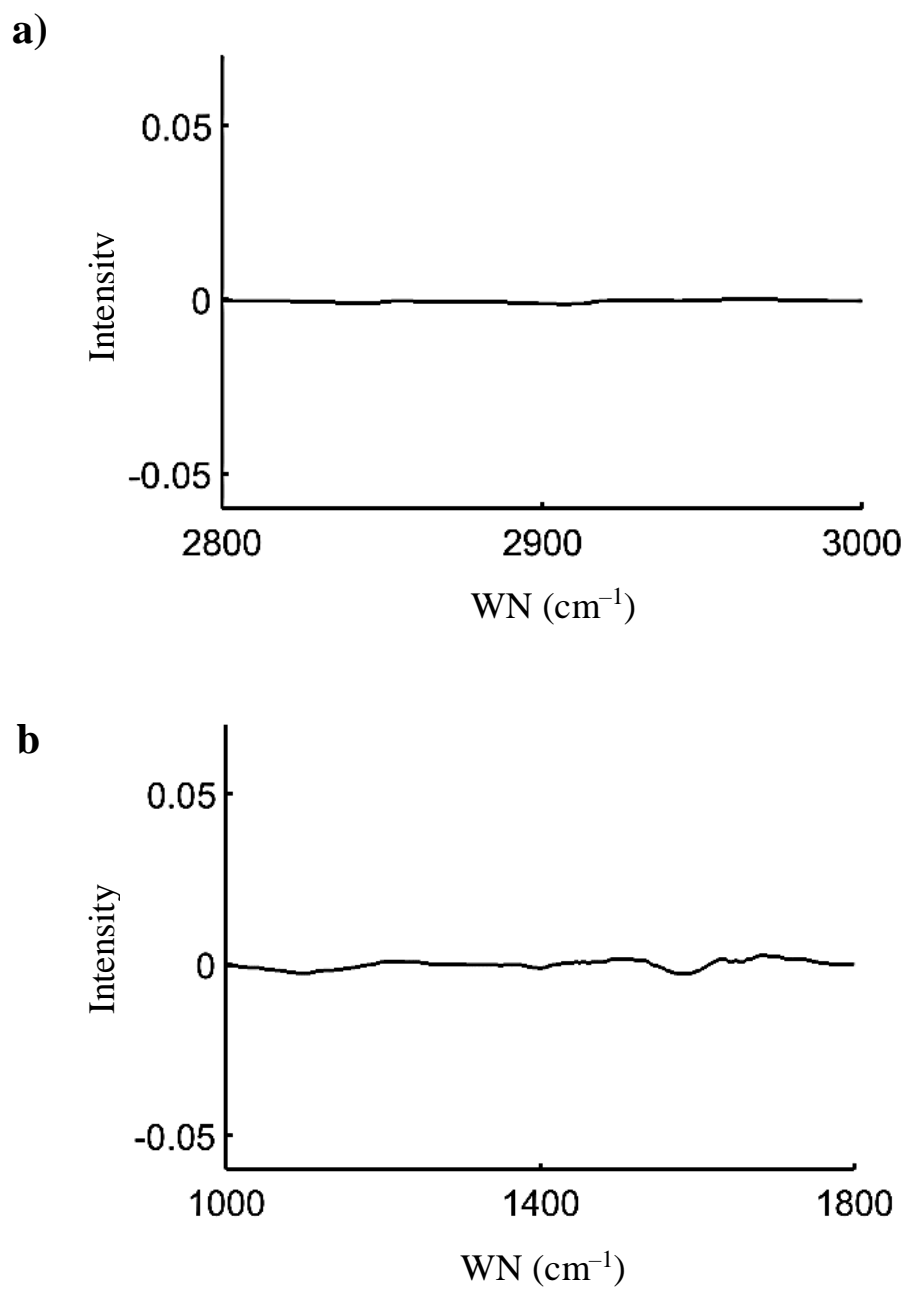


Figure 45 – Median difference spectra of PNT2 cells comparing $t=15$ min with $t=0$ min between (a) $1000\text{ cm}^{-1} - 1800\text{ cm}^{-1}$ and (b) $2800\text{ cm}^{-1} - 3000\text{ cm}^{-1}$ treated with AA.

LNCaP Median Difference Spectra

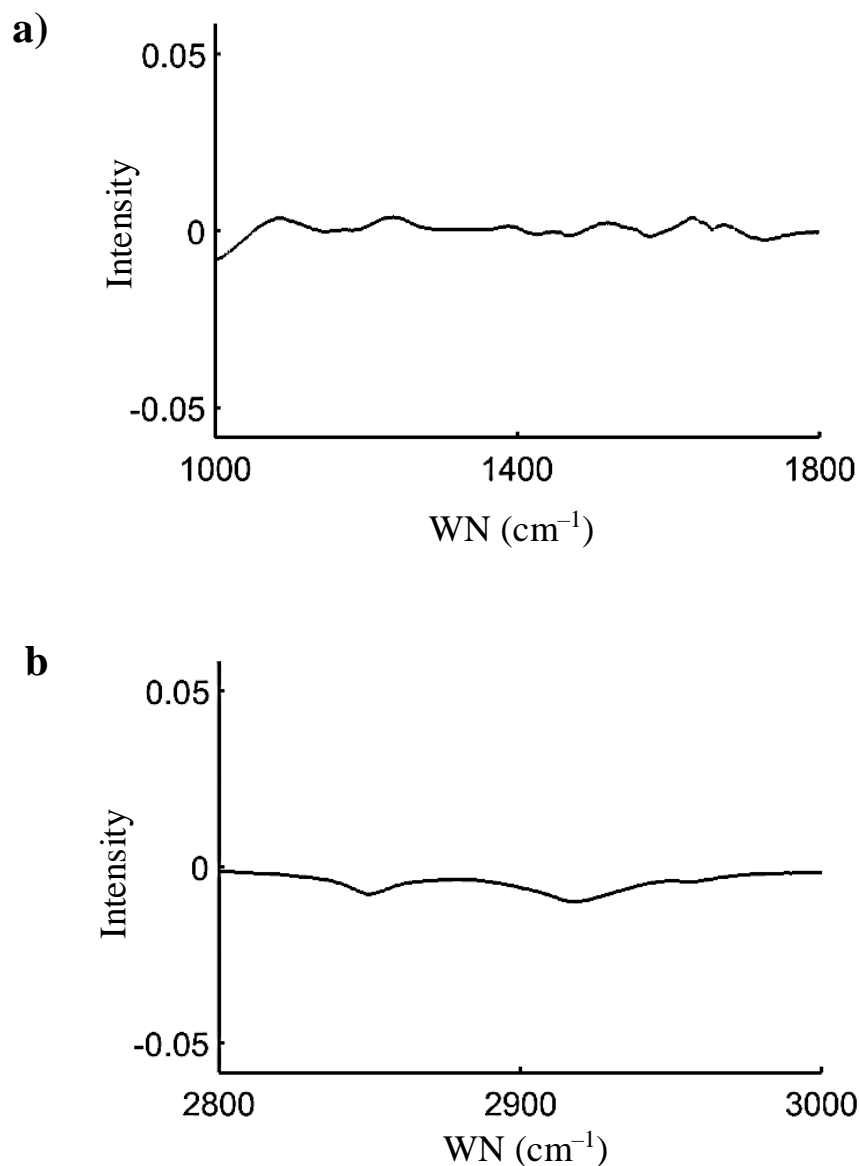


Figure 46 – Median difference spectra of LNCaP cells comparing $t=15$ min with $t=0$ min between (a) $1000\text{ cm}^{-1} - 1800\text{ cm}^{-1}$ and (b) $2800\text{ cm}^{-1} - 3000\text{ cm}^{-1}$ treated with AA.

3.8 Chapter Conclusion

Through FT-IRM PCA, there appears to be a difference in cellular AA uptake mechanisms. The invasive phenotype readily uptake AA, displaying the C=O carbonyl spectral features associated with AA. The maximum AA uptake occurred at 15-minutes for all invasive cell lines. After 15 minutes, the C=O carbonyl spectral features responsible for the separation in the PCA diminished throughout the remainder of the time course, possibly indicating AA metabolism. Throughout the time course, there is an apparent decrease in the CH₂/CH₃ area proportion, implying increased membrane fluidity, a key mechanism required to shift from a mesenchymal to amoeboid phenotype which is essential to penetrate endothelial tight cell junctions. The chemical differences were compared between $t=0$ min and $t=15$ min, with the main difference in invasive cell lines been an increase in spectral vibrations associated with the uptake of lipids.

Non-invasive cell lines showed no separation in PCA, no change in the proportion analysis of cellular fluidity or no difference in spectral chemistry throughout the first 15-minutes. It appears that the key difference between invasive and non-invasive cell lines is its ability to uptake AA. The invasive potential of non-invasive cell lines was basically non-existent compared to the invasive PC-3 cells in the invasion assays. The cells motility could be directly affected by the AA uptake mechanisms and possible indication that this shift in morphological phenotype could drive metastasis.

References

- ¹ Pandalai PK, Pilat MJ, Yamazaki K, Naik H, Pienta KJ (1996) The effects of omega-3 and omega-6 fatty acids on in vitro prostate cancer growth *Anticancer Res* 16(2):815-820.
- ² M. Brown, J. A. Roulson, C. A. Hart, T. Tawadros, N. W. Clarke. Arachidonic Acid Induction of Rho-Mediated Transendothelial Migration in Prostate Cancer. *Br J Can.* 110 (2014) 2099-2108.
- ³ M. D. Brown, C. A. Hart, E. Gazi, S. Bagley, N. W. Clarke. Promotion of Prostatic Metastatic Migration Towards Human Bone Marrow Stroma by Omega 6 and its Inhibition by Omega 3 PUFAs. *Br J Cancer.* 94 (2006) 842-853.
- ⁴ M. D. Brown, C. Hart, E. Gazi, P. Gardner, N. Lockyer, N. Clarke. Influence of Omega-6 PUFA Arachidonic Acid and Bone Marrow Adipocytes on Metastatic Spread from Prostate Cancer. *Br . J Can.* 102 (2010) 403-413.
- ⁵ E. Gazi, P. Gardner, N. Lockyer, C. Hart, N. Clarke, M. Brown. Probing Lipid Translocation Between Adipocytes and Prostate Cancer Cells with Imaging FTIR Microspectroscopy. *J. of Lipid Research.* 48 (2007) 1846–1856.
- ⁶ M. C. Schumacher, B. Laven, F. Petersson, T. Cederholm, E. Onelov, P. Ekman, C. Brendler. A Comparative Study of Tissue Omega-6 and Omega-3 Polyunsaturated Fatty Acids (PUFA) in Benign and Malignant Pathologic Stage pT2a Radical Prostatectomy Specimens. *Urol Oncol.* 31 (2013) 318-324.
- ⁷ D. Wang, R. N. DuBois. Eicosanoids and Cancer. *Nat Rev Cancer.* 10 (2011) 181-193.
- ⁸ M. L. Bruschi. Strategies to Modify the Drug Release from Pharmaceutical Systems. Cambridge: Woodhead Print, 2015.
- ⁹ Z. Huang, E. London. Effect of Cyclodextrin and Membrane Lipid Structure Upon Cyclodextrin–Lipid Interaction. *J. of Lipids.* 29 (2013): 14631-14638.
- ¹⁰ M. Timm, L. Saaby, L. Moesby, E. W. Hansen. Considerations Regarding use of Solvents in *in vitro* Cell Based Assays. *Cytotechnology.* 65 (2013):887-894.
- ¹¹ C. R. Santos, A. Schulze. Lipid Metabolism in Cancer. *FEBS J.* 279 (2012) 2610-2623.
- ¹² P. Yang, C. A. Cartwright, J. Li, S. Wen, I. N. Prokhorova, I. Shureiqi, P. Troncoso, N. M. Navone, R. A. Newman, J. Kim. Arachidonic Acid Metabolism in Human Prostate Cancer. *Int J Oncol.* 41 (2012) 1495-1503.
- ¹³ J. Ghosh, C. E. Myers. Arachidonic Acid Stimulates Prostate Cancer Cell Growth: Critical Role of 5-Lipoxygenase. *BBRC.* 235 (1997) 418-423.
- ¹⁴ K. Nithipatikom, W. Campbell. Roles of Eicosanoids in Prostate Cancer. *Future Lipidology.* 3 (2008) 453-467.
- ¹⁵ D. A. Los, N. Murata. Membrane Fluidity and its Roles in the Perception of Environmental Signals. *Biochimica et Biophysica Acta – Biomembranes.* 1 (2004) 142-157.

Chapter 4

The Effect of COX-2 Inhibition on Arachidonic Uptake and Metabolism on Prostate Cancer Cell Lines

It was shown in chapter 3 that the invasive cell lines PC-3M, PC-3, LNCaP C4-2, LNCaP C4-2B and DU145 readily uptake AA, whereas the non-invasive cell lines LNCaP and PNT2 demonstrated no such behaviour. An essential enzyme which is required in the catalysis of AA into its bioactive downstream metabolites is COX-2. In chapter 3, the results are suggestive that AA is a pivotal component in prostate cancer invasion and metastasis.

This chapter uses FT-IRM and PCA to further explore the effect of COX-2 inhibition on AA uptake and metabolism in invasive and non-invasive cell lines. If AA is the key driver of metastasis, then blocking the COX-2 pathway could prevent invasion and metastasis. This could give an indication of a potential therapeutic target for the control of localised prostate cancer. As prostate cancer only kills if it breaks from the localised site, then limiting prostate cancer cells invasive potential could limit the diseases ability to metastasise, making the watchful approach which is regularly implemented by oncologists more effective.

4.1 COX-2 Inhibitor Selection

COX-2 inhibitors are already widely used in medicine. They are a subclass of non-steroidal anti-inflammatory drugs (NSAIDs), their primary actions limiting the production of prostaglandins, mediating inflammation, pain and pyrexia (1). The older COX-2 inhibitors such as celecoxib and rofecoxib were shown to be broad with a reasonably good selectivity, but the drugs are also regarded as wide acting, effecting a wide range of physiological processes (2). A major limitation of celocoxib and rofecoxib is that they contain impurities (3). When carrying out a study looking at specific spectral changes, it is of upmost importance to know the chemical effect

observed is biological, rather than a cellular response to pharmaceutical impurities. N-[2-(Cyclohexyloxy)-4-nitrophenyl]methanesulfonamide (NS398) is regarded as a highly selective COX-2 inhibitor with a very high purity. Therefore, throughout this study NS398 will be used to block COX-2.

4.1.1 The Action of NS398

COX-2 inhibitors target the COX-2 rather than COX-1 because of the bulky methyl disulphide group on NS398. COX-2 enzymes have a larger and more accessible binding site which allows the bulky methyl disulphide group close enough to bind, whereas COX-1 has a binding site much smaller, with the molecule sterically hindered limiting the binding with the active site, increasing the molecular efficacy towards COX-2 (4). The molecular structure of NS398 can be seen in Figure 47.

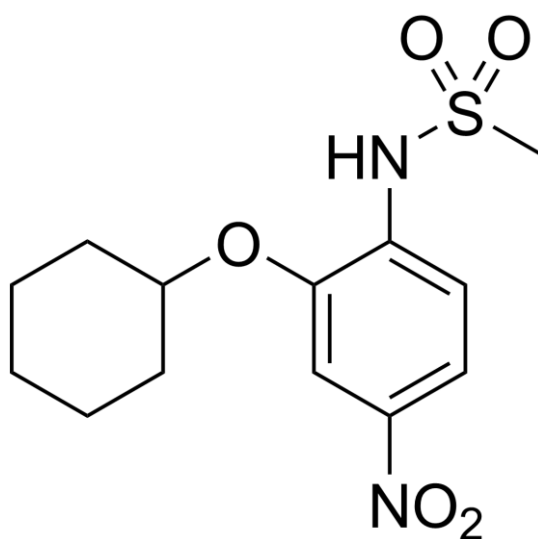


Figure 47 – Chemical structure of NS398

4.2 Comparing the uptake of AA with Active and Inhibited Cellular COX-2 Enzymes

The invasive cell lines PC-3M, PC-3, LNCaP C4-2B, LNCaP C4-2 and DU145 and non-invasive cell lines PNT2 and LNCaP were treated with AA for $t=0, 5, 15, 30$ and 60 min with an active COX-2 enzyme. A second experiment was carried out alongside the COX-2 active AA exposure whereby the COX-2 enzyme was inhibited. The cells are exposed to AA for the same time points $t=0, 5, 15, 30$ and 60 min. A side by side study between the COX-2 active and inhibited cell lines means the direct effect of blocking COX-2 on AA uptake can be monitored. Both studies monitoring AA uptake for the COX-2 active and inhibited enzymes were carried out from the same subculture of cell pool (same passage number) and treated under the same experimental conditions. This minimises biological variability from culturing as well as any variations due to experimental conditions such as temperature and incubation climate.

For the COX-2 inhibited study, all cell lines were treated with $10\text{ }\mu\text{M}$ NS398 prior to AA exposure. The AA treatment protocol for both COX-2 active and inhibited experiments remained the same as Chapter 3. The same FT-IR collection parameters were used as in Chapter 3 with a 4 cm^{-1} wavenumber resolution, 128 scans and 256 background scans. The data processing steps used was also the same, using the cell finder, RMieS correction, noise reduction and vector normalisation, example spectra can be seen for cell line PC-3M treated with AA for $t=0$ min between the spectral ranges $1000\text{ cm}^{-1} - 1800\text{ cm}^{-1}$ and $2600\text{ cm}^{-1} - 3500\text{ cm}^{-1}$ in Figure 48a and b respectively.

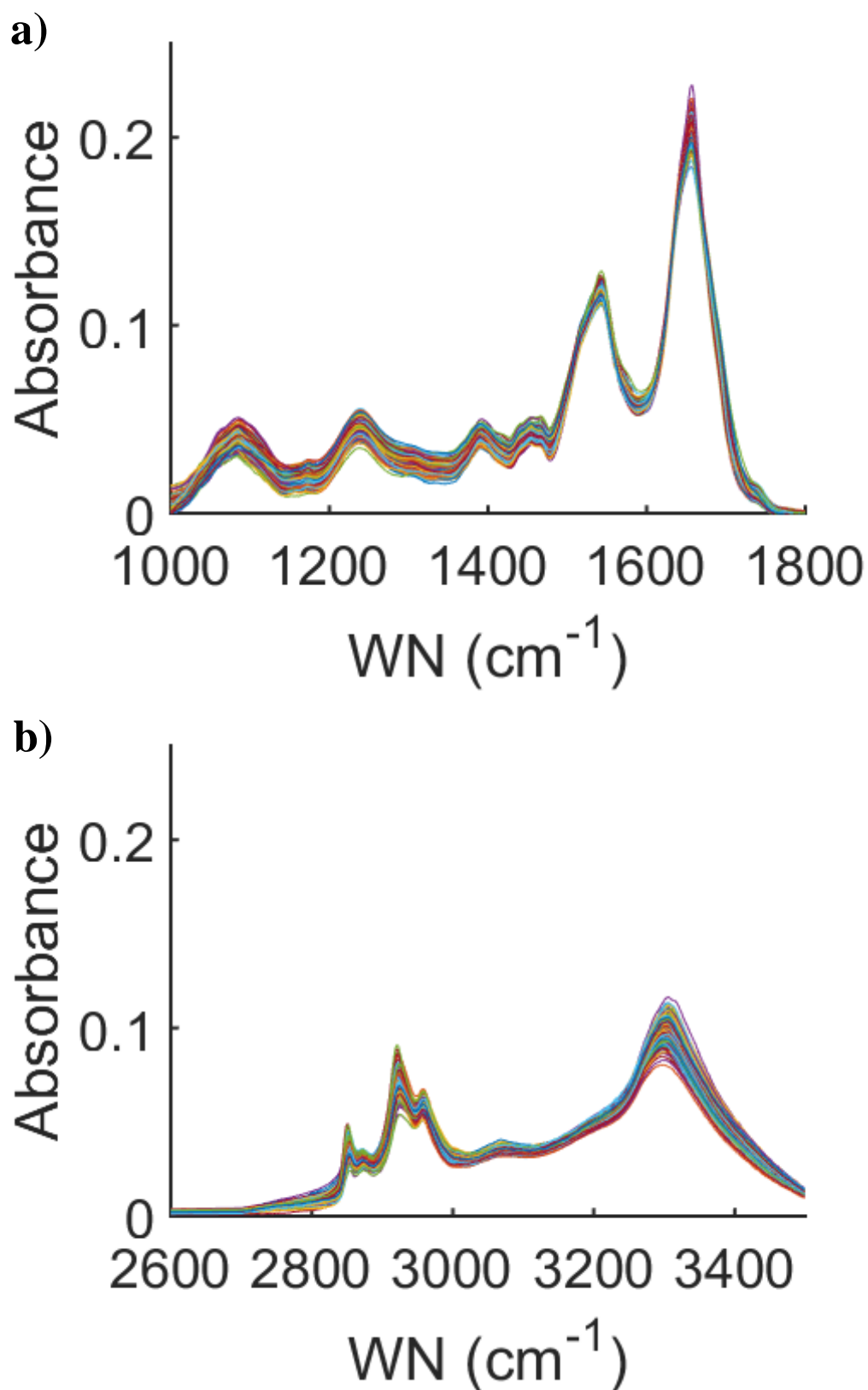


Figure 48 – FT-IR spectra of cell line PC-3M treated with AA for $t=0$ min between the spectral ranges (a) $1000\text{ cm}^{-1} - 1800\text{ cm}^{-1}$ and (b) $2600\text{ cm}^{-1} - 3500\text{ cm}^{-1}$.

First derivative PCA was used to assess the effect of AA exposure on cellular chemistry for the spectral range $1720\text{ cm}^{-1} - 1750\text{ cm}^{-1}$ for both invasive and non-invasive prostate cancer cell lines *in vitro*, specifically looking at cellular biochemical changes around the C=O carbonyl fatty acid stretch at 1732 cm^{-1} as a result of AA induction.

The median value was taken for each time point cluster within the principal component score space. The median value will only be taken from the axis of PC1 (x co-ordinate), meaning all chemical spectral changes are associated with PC1. Differences in this median value will therefore represent changes associated with chemical variance explained by PC1 between time points for a given time course. Therefore, a PCA plot can be presented in the form of a median position plot with respect to time. The median value of the initial $t=0$ min time point was subtracted from the median values of the remaining time points $t=5, 15, 30$ and 60 min, setting the value of $t=0$ min to 0, meaning the plot is relative to the initial $t=0$ min time point with directional transitions either side of the initial $t=0$ min cluster in the PCA score space represented simply by a positive or negative shift in the median positional plot.

The first derivative PCA median positional plot for PC-3M cells treated with AA and COX-2 active (blue) and COX-2 inhibited (red) can be seen in Figure 49. For the COX-2 active PC-3M cells treated with AA, there is a significant shift in the positive direction of PC1 in the PCA score space represented by a large positive increase in median positional value as early as $t=5$ min. Maximum PCA separation can be seen at $t=15$ min with the largest median positional value. The largest median position value is the time point with the most chemical variance compared to the initial $t=0$ min. The maximum separation is a result of increased cellular chemistry associated with the C=O AA carbonyl stretch at 1732 cm^{-1} , hence suggestive of AA uptake. At $t=30$ min, there

is a directional shift in PC1 within the PCA score space, shown by the decrease in the median positional plot. This highlights the loss of chemical variance compared that that of $t=15$ min, losing chemical characteristics associated with the C=O carbonyl stretch of AA. Finally, by $t=60$ min the median positional value overlaps with the initial $t=0$ min demonstrating the loss of all spectral features relating to the uptake of AA, potentially showing AA metabolism and cellular ejection.

When the COX-2 enzyme is inhibited, there appears to be no chemical change throughout the 60-minute time course. This is significant, as when the COX-2 enzyme is active there appears to be cellular uptake of AA and metabolism. There are minor fluctuations in the positive and negative direction relating to PCA separation, but the magnitude is insignificant, showing little biochemical variance throughout the time course.

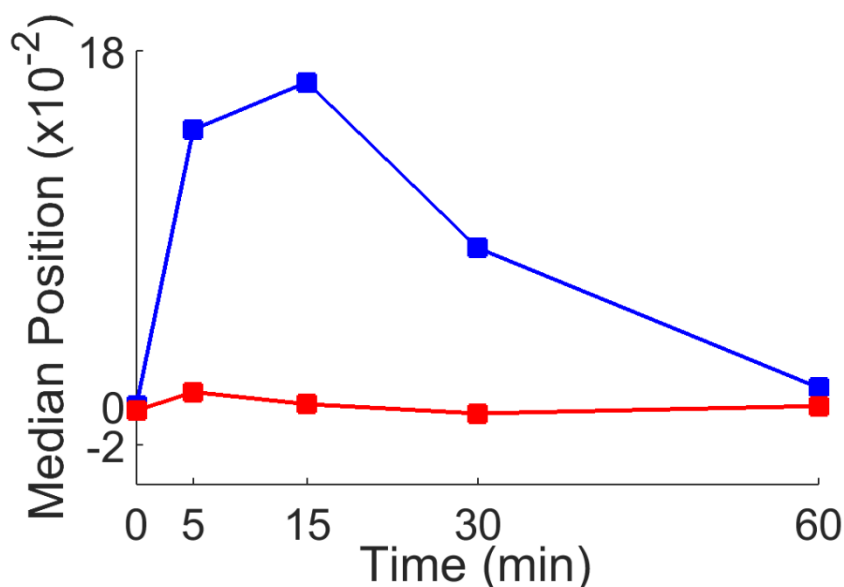


Figure 49 – PCA scores median cluster position plots of FTIR spectra, examining the C=O stretch between 1720 cm⁻¹ – 1750 cm⁻¹ for invasive cell line PC-3M treated with AA (blue) and COX-2 inhibited and treated with AA (red) for $t=0$, 5, 15, 30 and 60 min.

The first derivative PCA median positional plot for PC-3 cells treated with AA and COX-2 active (blue) and COX-2 inhibited (red) can be seen in Figure 50. When the COX-2 enzyme is active, there is a significant positive shift in the median positional plot within the first 5 minutes. There is a further increase in positive median position at $t=15$ min. At $t=30$ min, there is a significant decrease in median positional value representing the cluster moving in the negative direction, back towards the initial $t=0$ min cluster at 0. By $t=60$ min there is no difference between the initial $t=0$ min cluster, implying no chemical variance between the two time points. The initial shift in positive median value throughout the first 15 minutes represents a change in carbonyl C=O chemistry associated with the uptake of AA, the decrease in median positional value for $t=30$ and 60 min suggests that the cells are losing the chemistry associated with AA suggesting metabolic processes are underway, breaking down AA into its bioactive metabolites, eventually ejecting them from the cell.

When inhibiting the COX-2 enzyme, there appears to be no real change in median positional value in the PCA score space. This suggests that there is no change in chemistry associated with AA throughout the time course. The lack of chemical change indicates that when the COX-2 enzyme is inhibited the PC-3 cells fail to uptake AA, in contrast to COX-2 active PC-3 cells, where they appear to readily uptake AA.

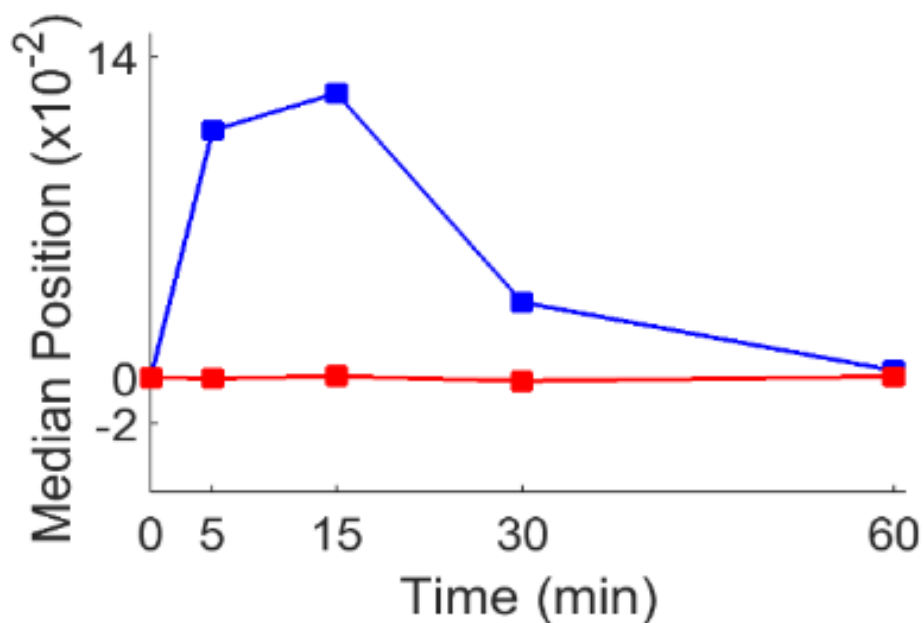


Figure 50 – PCA scores median cluster position plots of FTIR spectra, examining the C=O stretch between 1720 cm^{-1} – 1750 cm^{-1} for invasive cell line PC-3 treated with AA (blue) and COX-2 inhibited and treated with AA (red) for $t=0, 5, 15, 30$ and 60 min.

The first derivative PCA median positional plot for LNCaP C4-2B cells treated with AA and COX-2 active (blue) and COX-2 inhibited (red) can be seen in Figure 51. There is a major positive shift in median position in the PC1 direction within the PCA score from $t=0$ to $t=5$ min. There is a further increase in PCA separation in the positive PC1 direction by $t=15$ min shown by the further increase in median position. There is a directional transition at $t=30$ min returning back to the initial zero value at $t=0$ min, signifying less biochemical differences associated with lipid uptake than the $t=5$ and 15 min. At $t=60$ min, the median positional value becomes slightly negative, highlighting that that cells have lost all vibrational signatures of the AA and has returned to the initial chemical state, implying metabolism and metabolite ejection.

When the COX-2 enzyme is inhibited, there appears to be no real trend in median position throughout the time course when treated with AA. There are fluctuations in

both positive and negative median directions, with no significant order of magnitude. Throughout the time course there appears to be no changes in chemistry, indicating no AA uptake when COX-2 inhibition has been induced.

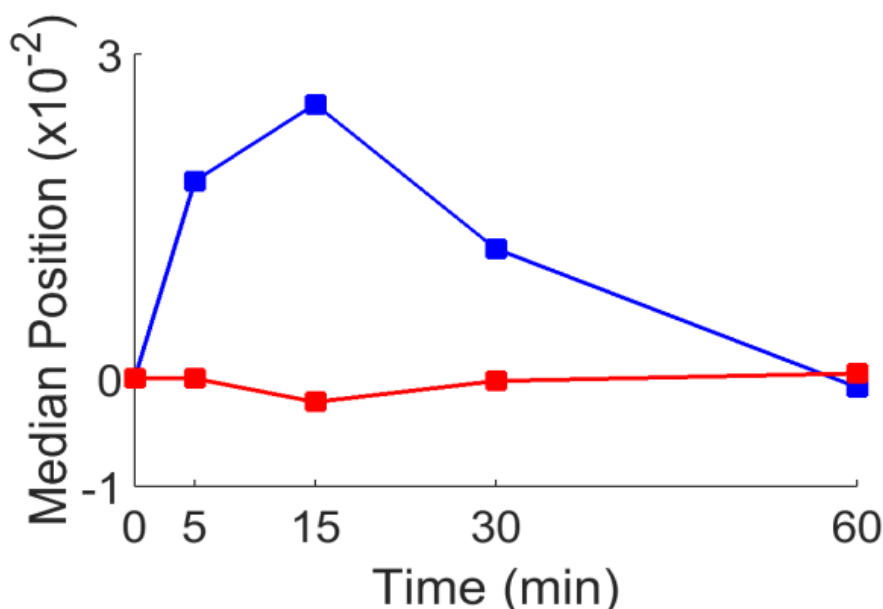


Figure 51 – PCA scores median cluster position plots of FTIR spectra, examining the C=O stretch between 1720 cm⁻¹ – 1750 cm⁻¹ for invasive cell line LNCaP C4-2B treated with AA (blue) and COX-2 inhibited and treated with AA (red) for $t=0, 5, 15, 30$ and 60 min.

The first derivative PCA median positional plot for DU145 cells treated with AA and COX-2 active (blue) and COX-2 inhibited (red) can be seen in Figure 52. There is an initial positive increase in median position in equal increments in $t=5$ and 15 min with maximum PCA separation (maximum median positional value) shown at $t=15$ min. This illustrates that the DU145 cells are becoming chemically different to the initial $t=0$ min as AA induces cellular changes. The cellular chemical changes are a result of AA uptake, with the spectral features indicative of the C=O carbonyl stretch specific to AA with the separation occurring between 1720 cm⁻¹ – 1750 cm⁻¹. There is a directional transition at $t=30$ min with the median positional value reducing similar to that of $t=5$

min. The median position value almost remains constant between $t=30$ and 60min. The results suggest that AA uptake occurred in the first 15 minutes. The lowered median value at $t=30$ min would suggest that the vibrational signatures associated with AA have reduced, possibly highlighting AA metabolism. There is a plateau of the median positional value between $t=30$ and 60 min, showing there is little biochemical change between the two time points. At $t=60$ min, there are chemical features associated with intracellular AA.

When blocking the COX-2 enzyme, there is no separation in the PCA score space throughout the 60-minute time course, with no common trend in time point median position. There are fluctuations in the negative and positive direction but insignificant compared to the COX-2 active median position values, implying no AA uptake.

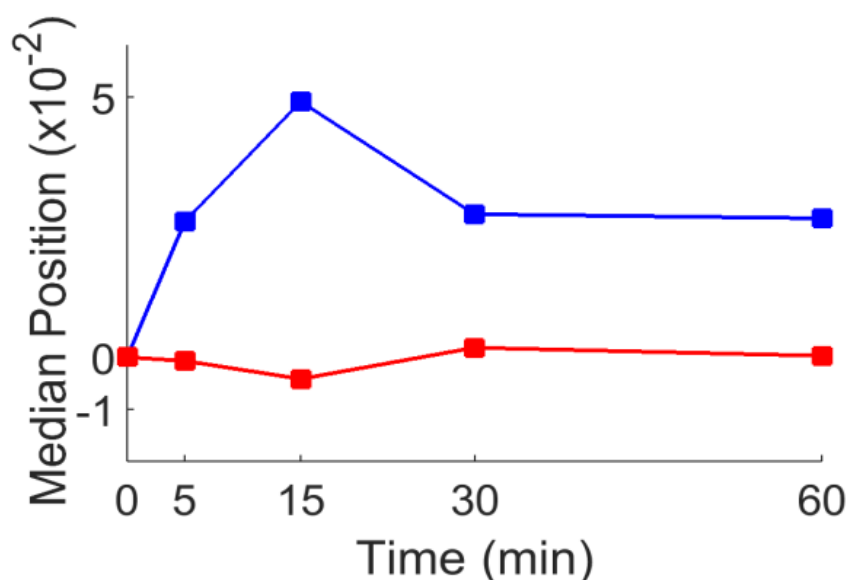


Figure 52 – PCA scores median cluster position plots of FTIR spectra, examining the C=O stretch between 1720 cm^{-1} – 1750 cm^{-1} for invasive cell line DU145 treated with AA (blue) and COX-2 inhibited and treated with AA (red) for $t=0$, 5, 15, 30 and 60 min.

The first derivative PCA median positional plot for LNCaP C4-2 cells treated with AA and COX-2 active (blue) and COX-2 inhibited (red) can be seen in Figure 53. At $t=5$ min there is already a significant shift in the positive direction of PC1, followed by a further shift to a maximum median position value at $t=15$ min. By $t=30$ min there is a directional shift in the PCA score, with $t=60$ min showing a similar PCA separation to $t=30$ min. The directional shift indicated the development of a chemical feature which is the C=O carbonyl stretch of AA, and the loss of the same feature, suggesting that the cell is using AA in cellular metabolism.

When inhibiting the COX-2 enzyme, there are no noticeable changes in fatty acid chemistry. The median positional values remain relatively constant with fluctuations in both the positive and negative direction of PC1 with no significant weighting. The results indicate that there is no AA uptake, from the minimal biochemical variance displayed throughout the time course in the PCA score space.

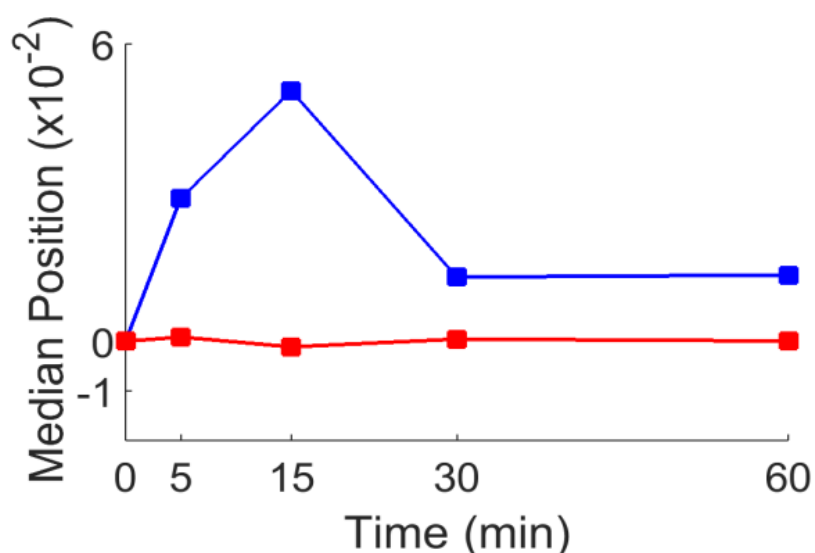


Figure 53 – PCA scores median cluster position plots of FTIR spectra, examining the C=O stretch between 1720 cm^{-1} – 1750 cm^{-1} for invasive cell line LNCaP C4-2 treated with AA (blue) and COX-2 inhibited and treated with AA (red) for $t=0, 5, 15, 30$ and 60 min.

The first derivative PCA median positional plot for PNT2 cells treated with AA and COX-2 active (blue) and COX-2 inhibited (red) can be seen in Figure 54. For both COX-2 active and inhibited studies, there appears to be no separation in the PCA throughout the 60-minute time course represented by no change in the median positional plots. There are minor fluctuations in median position value for both COX-2 active and inhibited, but no significant changes which would suggest no AA uptake in both studies. The COX-2 active and inhibited median position profiles match, implying that blocking the COX-2 enzyme has no change in outcome regarding cellular AA uptake.

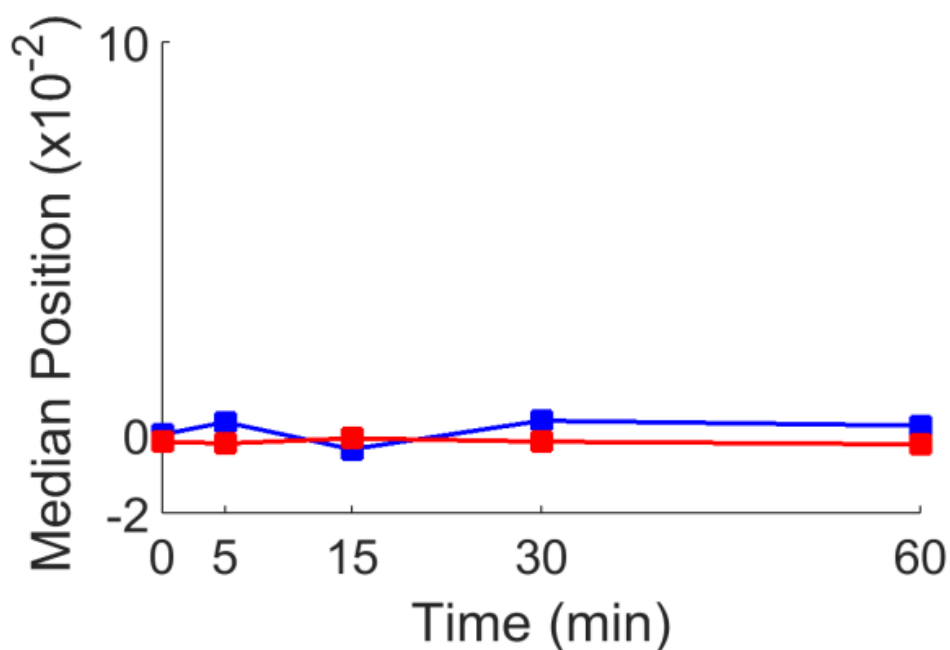


Figure 54 – PCA scores median cluster position plots of FTIR spectra, examining the C=O stretch between 1720 cm^{-1} – 1750 cm^{-1} for invasive cell line PNT2 treated with AA (blue) and COX-2 inhibited and treated with AA (red) for $t=0, 5, 15, 30$ and 60 min.

The first derivative PCA median positional plot for LNCaP cells treated with AA COX-2 active (blue) and COX-2 inhibited (red) can be seen in Figure 55. There is little difference between the median positional plots for both the COX-2 active and inhibited. There is no separation in the PCA plots for both studies. There are little fluctuations with insignificant magnitude in median positional, indicating that there are no cellular changes with respect to AA induction or uptake. Suppressing the COX-2 enzyme appears to have no effect on the AA uptake mechanisms of LNCaP, as the cell line seems to fail to uptake AA with the COX-2 enzyme active.

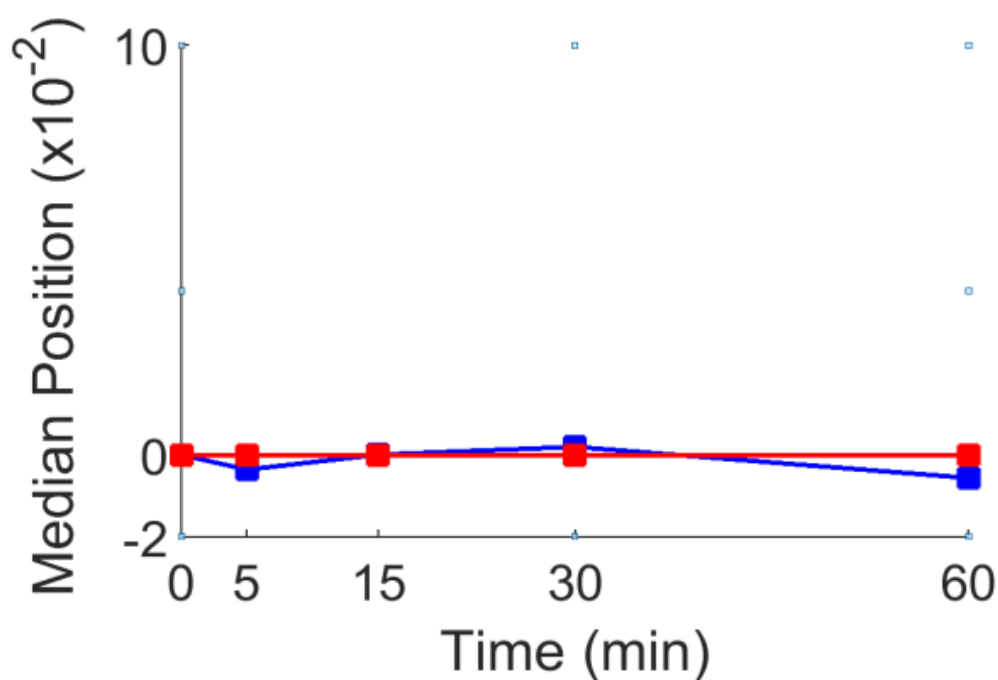


Figure 55 – – PCA scores median cluster position plots of FTIR spectra, examining the C=O stretch between 1720 cm^{-1} – 1750 cm^{-1} for invasive cell line LNCaP treated with AA (blue) and COX-2 inhibited and treated with AA (red) for $t=0, 5, 15, 30$ and 60 min.

4.3 Discussion

The invasive prostate cancer cell lines PC-3M, PC-3, LNCaP C4-2, DU145 and LNCaP C4-2 appear to readily uptake and metabolise AA with an active COX-2 enzyme, whereas non-invasive cell lines PNT2 and LNCaP exhibit no such behaviour. It is clear that all invasive cell lines uptake AA as early as 5 minutes, with a maximum uptake displayed at 15 minutes. This is represented by the maximum separation in the PCA score space and the maximum change in the median positional plot. By 30 minutes, all invasive cell lines appear to have a reduced spectral profile to that of AA, specific to the C=O carbonyl stretch at 1732 cm^{-1} . The non-invasive cell lines fail to display any biochemical variance within the 60-minute time course, with all time point clusters overlapping in the PCA score space and change in the median positional plots insignificant. This biological replicate study matches the findings in chapter 3, investigating AA uptake in invasive and non-invasive cell lines using PCA. The two studies are supportive of one another, resulting in the same conclusion. This demonstrates that the study is both reproducible and reliable. The results suggest that the difference in the invasive and non-invasive phenotype is the cells ability to uptake AA, and therefore metabolise the AA into its bioactive metabolites.

Inhibiting the COX-2 enzyme had a significant effect on the AA uptake behaviour of the invasive cell lines PC-3M, PC-3, LNCaP C4-2, DU145 and LNCaP C4-2. This is a very surprising result, blocking the COX-2 enzyme appears to mute or prevent cellular AA uptake in invasive cell lines, represented by the lack of change in the PCA scores. The COX-2 enzyme is within the cell around the nuclear envelope and the rough endoplasmic reticulum, meaning that AA needs to diffuse through the intracellular cytoplasm to reach the specific binding targets to be catalysed into PGE_2 through the

COX-2 pathway. Suppressing the COX-2 enzyme should in turn simply prevent the metabolism of AA, but the result suggests that the invasive cells fail to even uptake AA. When the COX-2 enzyme is blocked, the cell stops AA from being taken into the cell. It is proposed that there is an unknown upstream signalling mechanism which prevents the uptake of AA when the cellular COX-2 enzyme is inhibited. The specifics of this mechanism need to be elucidated but not tackled during this study. It appears that invasive prostate cancer cells are highly selective in what fatty acids enter and leave the cell. With a blocked COX-2 enzyme, the cell has no use for AA, as it can't be metabolised. It could be hypothesised that the cell realises it has no use for it, so simply does not allow the uptake of AA.

Blocking COX-2 for the non-invasive cell lines PNT2 and LNCaP has no effect on AA uptake. When the COX-2 enzyme is active, the cell fails to uptake AA, therefore it is expected that no chemical change would be seen throughout the COX-2 inhibition investigation.

AA stimulated mesenchymal to amoeboid transitions are already well documented, the results seen in this study suggest when the COX-2 enzyme is suppressed, invasive cells appear to lose their ability to not only metabolise AA but their ability to uptake AA in the first place. This in turn will have a knock on effect for the cellular regulation of membrane fluidity and structure: something key in the progression and metastasis of PCa. Prostate cancer cells require an amoeboid phenotype to penetrate endothelial tight cell junctions and metastasise into the bone marrow, the preferential PCa secondary site.

It is known that endogenous AA cell uptake is likely to be a driven effect by the heavily glycosylated integral membrane protein CD36 which is a binding site for fatty acids. Recent studies have predicted that the CD36 proteins contains a crystal structure cavity throughout the molecule, acting as a tunnel for fatty acid docking and transport (5). It is plausible that the CD36 membrane expression could influence the uptake of AA and there could be upstream signalling when the COX-2 enzyme is blocked to down regulate the CD36 expression present in the cellular membrane.

It must be noted that throughout this investigation standard errors are quoted for the median positional plots. Deeper insight is needed into the margins of errors and their significance associated with median positional plots.

4.4 Invasion Assay

An invasion assay was carried out investigating the effect of COX-2 inhibition on invasive potential for the invasive prostate cancer cell line PC-3. The same experimental protocols and time scales were followed as outlined in section 3.4, with the COX-2 inhibited invasion assay compared to the COX-2 active invasion assay in chapter 3. For the COX-2 inhibition invasion assay, the cells were serum starved over night, followed with a 10 μ M treatment of NS398 prior to AA exposure. The invasion assay was scratched and washed with PBS before treating with AA. The cells were treated with 20 μ M AA in cyclodextrin for 14 hours. The scratches in the invasion assay were imaged at $t=0$ hours and $t=14$ hours which can be seen in Figure 56a and b respectively.

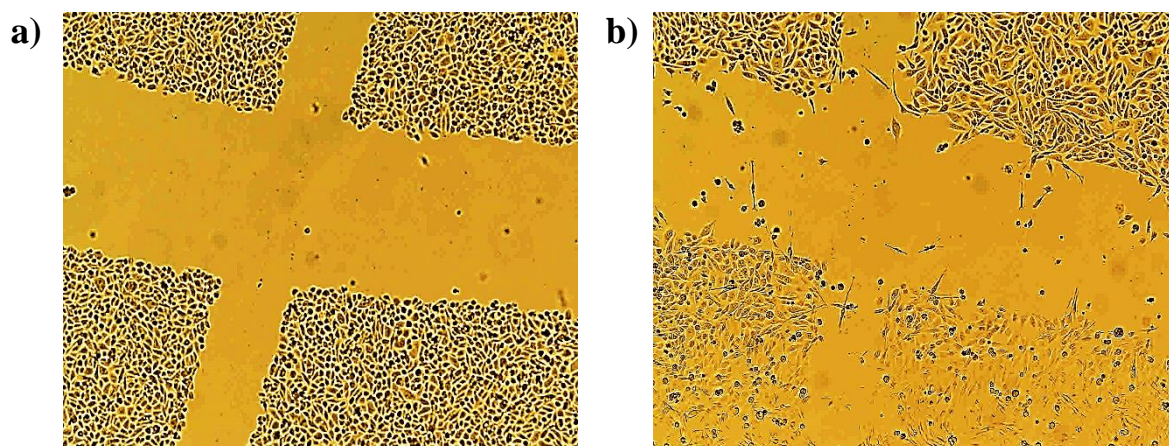


Figure 56 – Scratch invasion assay for PC-3 cells COX-2 inhibited and treated with AA for (a) 0 hours and (b) 14 hours imaged at x5 magnification 960 μm x 960 μm

At $t=0$ hours, the wound is well defined with little cellular debris remaining in the open wound. After 14 hours treatment the wound remains well defined and open. The COX-2 inhibition has suppressed the PC-3 cells invasive ability when exposed to AA. The scratch assay data can be seen in Table 5. The migration index and percentage wound closure has been calculated for COX-2 inhibited PC-3 cells treated with AA.

PC-3 COX-2 Inhibited Treated with AA				
Scratch	Average Width Before Treatment	Average Width After Treatment	Migration Index	Percentage Closure (%)
1	359.9	332.1	27.8	7.7
2	186.7	171.8	14.8	7.9
3	365.6	334.5	31.1	8.5
4	186.5	164.2	22.2	11.9

Table 5 – Invasion assay data for PC-3 cells COX-2 inhibited treated with AA for 0 hours (before treatment) and 14 hours (after treatment) for all 4 scratches and 4 data points per scratch averaged.

It was seen previous in section 3.4 than when the COX-2 enzyme is active, PC-3 cells readily invade the scratch, showing substantial wound closure over 14 hours. The percentage wound closure for both COX-2 active and inhibited is compared and plotted in Figure 57. There is a significant difference in percentage wound closure between PC-3 cells when blocking the COX-2 enzyme compared to the COX-2 active invasion assay. The difference in percentage wound closure is over 40%. Blocking the COX-2 severely limits the PC-3 cells ability to invade the surrounding environment.

A study carried out by Patel *et al.* was suggestive that COX-2 inhibition supresses tumour invasion and growth in both PC-3 and LNCaP prostate cancer cell lines (6). This study concludes that the COX-2 inhibits tumour growth in both cell lines by inducing a G₁ cell cycle block. The study could be questioned regarding the investigation surrounding tumour growth. The doubling time for PC-3 and LNCaP cell lines are 33 hours and up to 68 hours respectively (7,8). It is questionable to compare the two cell lines when PC-3 cells double roughly twice as fast as LNCaP cells, introducing experimental variability. The study also treats cell lines with a broad-spectrum antibiotics Penicillin–Streptomycin, further introducing biological uncertainty. A study carried out by Ryu *et al* highlights the importance of antibiotic free studies showing Penicillin-Streptomycin exposure to cells lines introduces changes in gene expression and regulation (9). Brown *et al.* agrees with the findings of Patel *et al.* Showing COX-2 inhibition limits prostate cancer invasion (10). Brown further suggests that AA is responsible for invasion.

Nithipatikom *et al.* use a Boyden chamber assay to assess the migration in PC-3 low and high invasive cell lines (11). The study investigated the correlation between migratory potential COX-2 expression and PGE2 synthesis. It was found that both high

and low invasive PC-3 cell lines lost their invasive potential when COX-2 was inhibited with the selective inhibitor NS398, with no indication of AA membrane release or PGE2 synthesis. Attiga *et al.* also carried out the same investigation on the invasive prostate cancer cell lines PC-3 and DU145 with the same result seen as the study carried out by Nithipatikom *et al.* (12). All studies agree with the findings seen in the PC-3 invasion assays and demonstrate that COX-2 inhibition prevents the invasion of prostate cancer cell lines.

The PCA analysis revealed that when blocking the COX-2 enzyme in PC-3 cells, the uptake mechanism failed to initiate, suggesting the invasive potential is directly linked to a cells ability to uptake and metabolise AA. The consiquence of PC-3 cell failing to uptake AA results in a reduced potential to undergo morphological and biochemical changes, from the lack of lipid resources, fundimental building blocks for cellular structures. For a cell to be highly motile and induce a change in cellular phenotype, there needs to be morphological and biochemical changes. Without the excess cellular AA, the cell motility is severly reduced, as AA is known to cause increased prostate cancer motility and proliferation. This is potentially why there is a significant difference in the invasion assays between COX-2 inhibited and COX-2 active studies. Supressing the COX-2 enzyme induces a cellular block on the uptake of AA, and therefore hinders the motility, as expressed by a very low percentage wound closure compared to the COX-2 active study. The lack of AA uptake when the cellular COX-2 enzyme is inhibited will also have a direct ability for the PC-3 cell to change membrane fluidity, a key step in the change from an mesenchymal to amoeboid structure. This structural change is required to penetrate tight cell junctions of endothelial vascular cells as prostate cancer breaks free of the primary site. This finding could be used as a

therapeutic target for the management of prostate cancer. If it is known that AA is a key inducer of prostate cancer invasion, then by blocking the COX-2 enzyme limits the PC-3 cells ability uptake AA and shift to an amoeboid phenotype, hence increasing the time the disease is localised. It must be noted that further biochemical evaluation needs to be carried out, with a hypothesis set for future work.

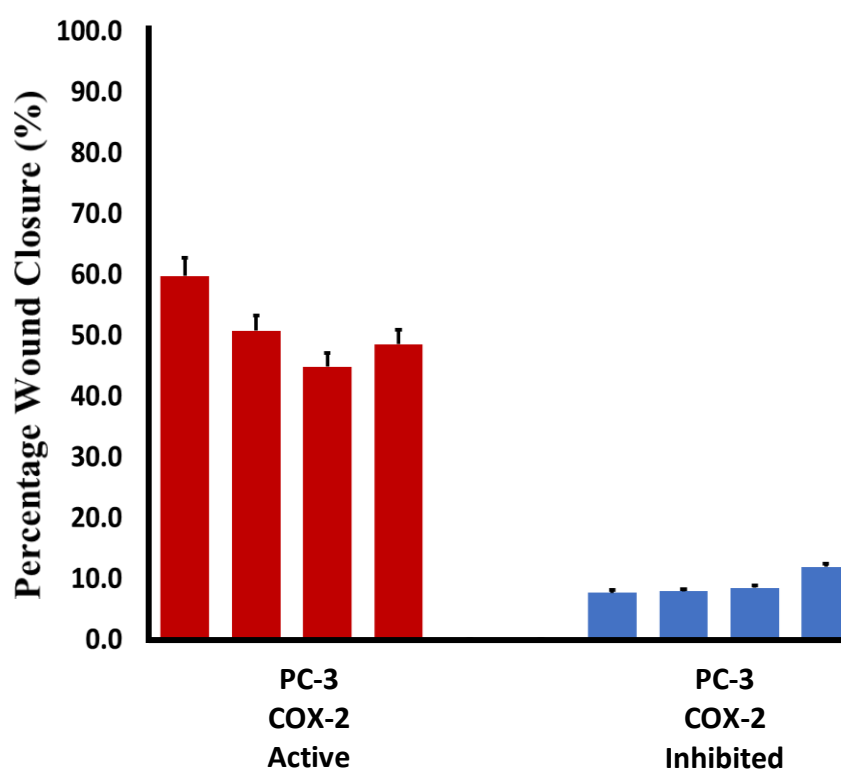


Figure 57 – Bar plot of the percentage wound closure of PC-3 cells after 14 hours exposure to AA for COX-2 active (red) and COX-2 inhibited (blue)

4.5 A Control Study Analysing the Biochemical Effect of Cyclodextrin and NS398 on the Global Lipid Chemistry

The effect of both cyclodextrin and NS398 were analysed with respect to changes in chemistry associated with the C=O carbonyl chemistry between 1720 cm^{-1} – 1750 cm^{-1} . This analysis is to check that the chemical behaviour observed with AA treatment is a

result of the fatty acids interaction with the cell, rather than a cellular reaction mechanism from been exposed to cyclodextrin or NS398.

First derivative PCA analysis was carried out on PC-3 cells treated with cyclodextrin and also PC-3 cells treated with NS398 30 minutes prior to cyclodextrin exposure. The PCA analysis was represented in the form of a median positional plot taking the median values of PC1 for each time point and PCA separation was plotted as a function of time. The median positional plots for PC-3 cells treated with cyclodextrin only (blue) and NS398 and cyclodextrin (red) can be seen in Figure 58. Cyclodextrin appears to have little effect on the global lipid chemistry. It is well documented that cyclodextrin disrupts cellular lipid structures, but this is beyond the sensitivity of FT-IR microscopy. FT-IR microscopy analyses the global chemical change, noticing an increase or decrease in a particular cellular component. As cyclodextrin causes reorganisations of lipid rafts, the nett lipid content in the cell we remain the same, therefore appearing as no change within the FT-IR analysis. The key result is that cyclodextrin causes no nett change in cellular lipids as seen with exposure to AA. There is no separation in the PCA throughout the entire 60-minute time course, represented by insignificant shifts within the median positional plot.

When treating the PC-3 cells with NS398 and then exposing the cells to cyclodextrin, the same result is observed. The NS398 and cyclodextrin have no effect on the nett global cellular lipid content throughout the 60-minute time course. This can be seen by the PCA experiencing no biochemical change represented by all the time points overlapping, illustrated by no noticable changes in the median positional plot.

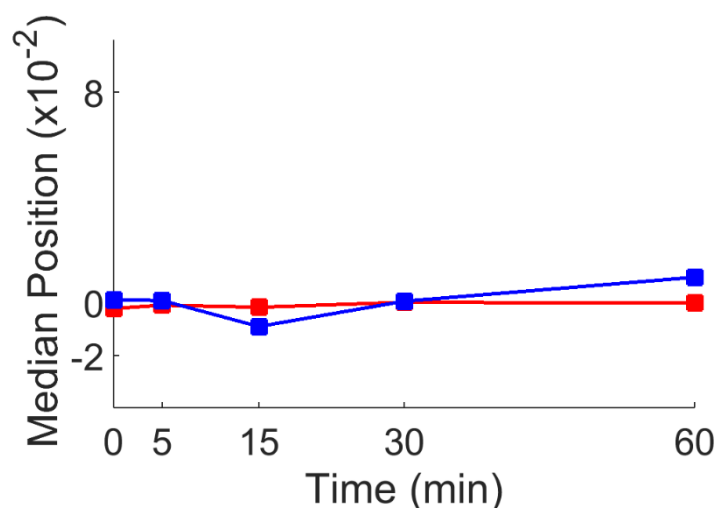


Figure 58— PCA scores median cluster position plots of FTIR spectra, examining the C=O stretch between 1720 cm^{-1} – 1750 cm^{-1} treated with cyclodextrin only (blue) and COX-2 inhibited treated

4.6 Seeded PCA Investigating the Effect of COX-2 Inhibition on AA uptake and Prostaglandin E2 Synthesis

Seeded PCA was used to investigate the effect of COX-2 inhibition on uptake of AA and synthesis of PGE₂ throughout the 60-minute time course for the invasive cell line PC-3 and non-invasive cell line PNT2 treated with AA, between the spectral range 1720 cm^{-1} – 1750 cm^{-1} . The outlined methodology of seeded PCA is available in chapter 2. Spectra of AA and PGE₂ were taken, multiplied by $\times 10^5$ and added to both datasets for COX-2 active and inhibited PC-3 and PNT2 cells. PCA was finally carried out on the AA and PGE₂ spiked data sets, forcing PC1 in the PCA to be the spectra of AA and PGE₂ for the given data sets. This gives the advantage of adding specificity to the separation in the PCA score space. Forcing PC1 to be a specific lipid spectral profile to match either AA or PGE₂ means that the biochemical variance within the data set can

be biased to investigate the effect of a given molecule, allowing spectral molecular profiles to be tracked throughout the time course in both PC-3 and PNT2 cell lines.

4.7 AA Seeded PCA

The median positional plots for the AA seeded PCA with COX-2 active (blue) and COX-2 inhibited (red) for cell lines PC-3 and PNT2 can be seen in Figure 59a and b respectively.

The median positional plots for the AA seeded PCA of the COX-2 active PC-3 cells treated with AA shows a significant shift throughout the 60-minute time course. At $t=5$ min median positional plot shows a shift in the positive direction away from the initial $t=0$ min zero value signifying a change in cellular chemistry specific to the spectral features of AA. At $t=15$ min there is a substantially larger shift in the positive direction to a maximum positional displacement. This maximum displacement suggests the greatest uptake of cellular AA with the spectral chemistry most representative of the AA spectrum in the PC1 loading. By $t=30$ min, the biochemical variance returns almost to the initial $t=0$ zero value with the $t=60$ min time point displaying no difference between the median positional value. The chemistry at $t=30$ and $t=60$ min is chemically similar to the initial $t=0$ min from the cell losing the spectral features of AA, probably due to AA metabolism and the ejection of PGE_2 from the cell. The PC1 loading plot can be seen in Figure 60. The peak occurs around 1730 cm^{-1} specific to the C=O carbonyl stretch in AA molecules.

When the COX-2 enzyme is blocked, no such separation is seen in the PCA, represented by changes or displacements in the median positional plots. This result matches what

was seen previously with the unseeded PCA median positional plot in Figure 50, confirming the change in lipid chemistry is specific to the AA molecule.

When looking at the AA seeded median positional plot for the non-invasive cell line PNT2, there appears to be no change in median positional value when treating the cells with for both COX-2 active and inhibited. This shows that the non-invasive PNT2 cells lack the fundamental ability to uptake AA as no chemical separation is seen in the seeded PCA. This result is supportive of the result obtained in the unseeded PCA median positional plot in Figure 54.

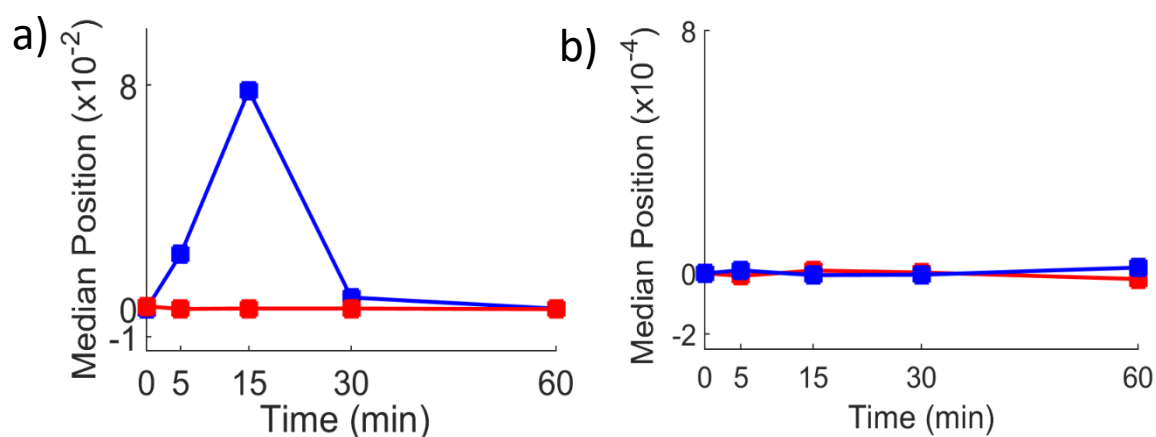


Figure 59 a) AA seeded PCA median positional plot for PC-3 cells treated with AA COX-2 active (blue) and COX-2 inhibited (red) and b) AA seeded PCA median positional plot for PNT2 cells treated with AA COX-2 active (blue) and COX-2 inhibited (red) treated for 0, 5, 15, 30 and 60 minutes.

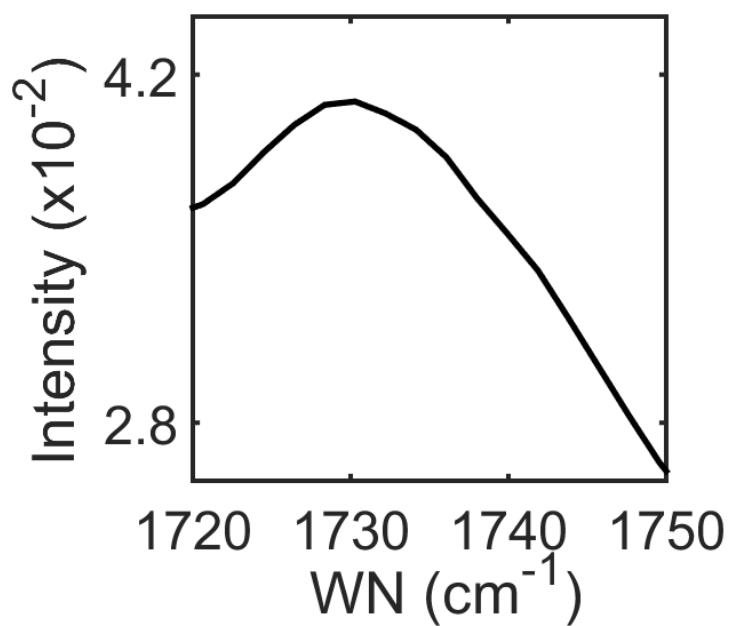


Figure 60 – AA seeded PC1 Loading

4.8 PGE₂ Seeded PCA

A FT-IR spectrum of PGE₂ was collected for the spiked PGE₂ PCA, which can be seen between the ranges 1000 cm⁻¹ – 1800 cm⁻¹ and 2600 cm⁻¹ – 3500 cm⁻¹ in Figure 61a and b respectively.

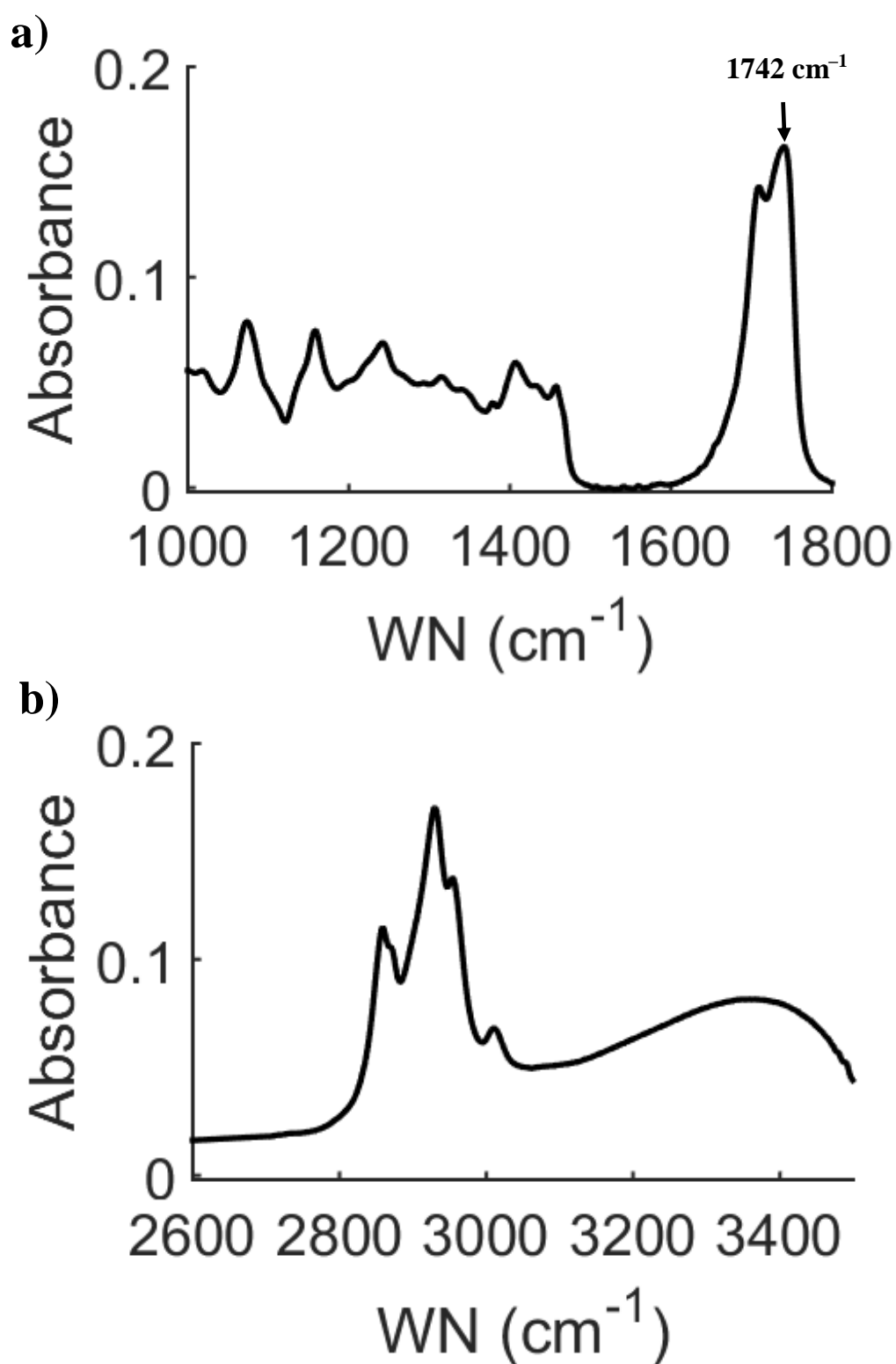


Figure 61 – PGE₂ spectrum between the spectral ranges (a) 1000 cm^{-1} – 1800 cm^{-1} and (b) 2600 cm^{-1} – 3500 cm^{-1} .

The median positional plots for the PGE₂ seeded PCA with COX-2 active (blue) and COX-2 inhibited (red) for cell lines PC-3 and PNT2 can be seen in Figure 62a and b respectively.

When the COX-2 enzyme is active in the PC-3 cell line there appears to be a significant change in the PGE₂ seeded PCA positional plot. Any change in positional plot signifies a change in the cellular biochemical makeup specific to PGE₂. As early as $t=5$ minutes, there is already large displacement of the positional median value, this is suggestive that there is PGE₂ synthesis almost instantly when AA uptake occurs. The PC1 loading plot can be seen in Figure 63. The loading plot shows that the spectrum differs from the AA seeded loading plot in Figure 63. The PGE₂ PC1 loading displays a peak at 1740 cm^{-1} very specific to the ketone C=O stretch incorporated within the 5-carbon cyclic ring in the PGE₂ molecule whereas the AA PC1 loading in Figure 60 had a peak at 1730 cm^{-1} which is the C=O carbonyl stretch within the AA molecule. By $t=15$ min there is a maximum displacement within the median positional plot indicating a maximum PGE₂ cellular concentration as the cellular chemistry is the most similar to the PGE₂ spectrum in PC1. At $t=30$ min there is a shift in the negative direction in the median positional plot, with the positional value becoming less positive highlighting the cells are losing spectral features of the PGE₂. This suggests that the cell is ejecting the PGE₂ from the cell, as a high concentration of PGE₂ is cytotoxic. By $t=60$ min, there median positional value has returned to a similar value of the initial $t=0$ min, which shows there is no difference in chemistry between the two time points. It has been shown that by $t=60$ min there is no excess intracellular AA present within the cell which can be detected by FT-IR spectroscopy. If there is no excess cellular AA then there will be no

PGE₂ production hence why the chemistry in the seeded PGE₂ positional plot mimics the initial $t=0$ min.

When the COX-2 enzyme is inhibited, there appears to be no such changes in the median positional value plots representing the seeded PGE₂ PCA plots. The small fluctuations seen in positional values are insignificant compared to that seen with the COX-2 enzyme active. It was already shown that blocking the COX-2 enzyme, prevents or inhibits the PC-3 cells ability to uptake AA. If the cell cannot uptake AA, there cannot be PGE₂ production, as this requires the catalysis of AA. Also, if the COX-2 enzyme is inhibited, this blocks the pathway which is needed to produce PGE₂.

When looking at the median positional plot for the non-invasive cell line PNT2, there appears to be no change in median positional value when treating the cells with for both COX-2 active and inhibited. This indicates that PNT2 cells fail to produce PGE₂ with both COX-2 active and inhibited investigations. This agrees with the results shown previously that PNT2 cells fail to uptake AA and by blocking the COX-2 enzyme has no effect on AA uptake. If the PNT2 cells fail to uptake AA when the COX-2 enzyme is both active and inhibited, there will be no PGE₂ production. This is reflected by the results seen in the seeded PGE₂ PCA.

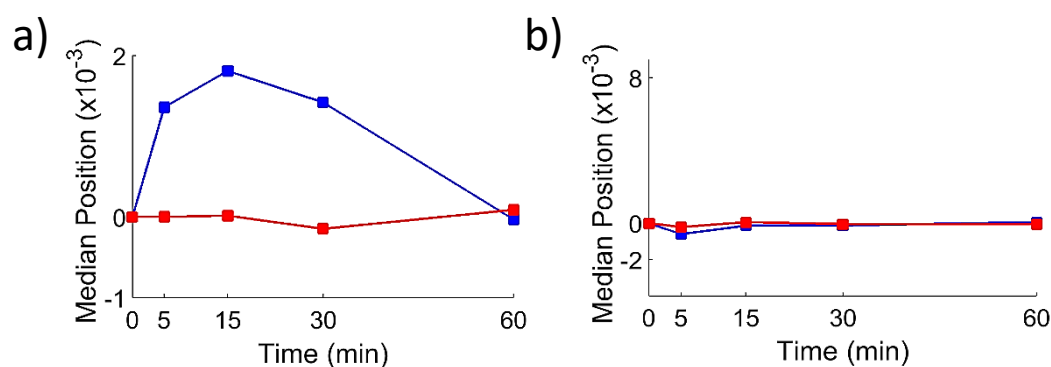


Figure 62 a) PGE₂ seeded PCA median positional plot for PC-3 cells treated with AA COX-2 active (blue) and COX-2 inhibited (red) and b) PGE₂ seeded PCA median positional plot for PNT2 cells treated with AA COX-2 active (blue) and COX-2 inhibited (red) treated for 0, 5, 15, 30 and 60 minutes.

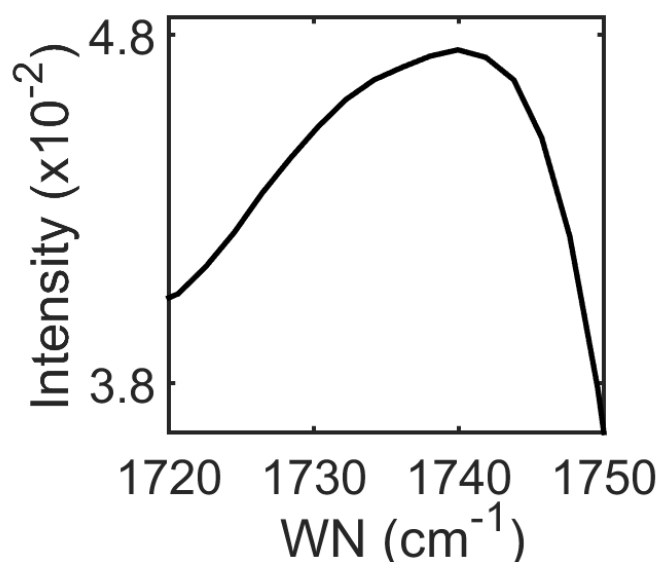


Figure 63 – PGE₂ seeded PC1 Loading

4.8 Conclusion

In the invasive cell lines PC-3M, PC-3, LNCaP C4-2B, LNCaP C4-2 and DU145 it is apparent that the COX-2 enzyme plays a critical role in the cellular uptake mechanisms of AA uptake and metabolism. When the COX-2 enzyme is active, the invasive cell lines readily uptake AA. When the COX-2 enzyme is inhibited, there appears to be a cellular block of AA uptake. It is hypothesised that there is an initial upstream

mechanism which is responsible for the cellular response preventing AA uptake. Invasive cells appear to be highly selective in what they uptake into their intracellular environment, when the COX-2 enzyme is blocked then the cell recognises that there is an inability to metabolise AA, therefore simply does not uptake AA. The non-invasive cell lines showed no indication to AA uptake for both COX-2 active and inhibited studies. Further highlighting that a key difference between an invasive and non-invasive prostate cancer phenotype is the cells ability to uptake AA. When biasing the PCA with the specific spectral seeds of AA and PGE₂, the same result was found with greater specificity showing AA uptake and PGE₂ synthesis.

The invasion assays revealed that the inhibition of cellular COX-2 greatly reduced the invasive potential and motility of invasive PC-3 cells. This suggests that AA plays a critical role in the initiation of a metastatic disease. Overall it appears that AA directly influences both AA uptake and invasion which could be a direct effect of one another. The specifics to the upstream signalling mechanism are yet to be elucidated. Limiting the invasiveness of prostate cancer is highly promising. Preventing AA uptake in prostate cancer cell lines is valuable as AA is known to increase prostate cancer proliferation. AA is needed for motility and therefore metastasis. This therefore could potentially act as a therapeutic target for localised stages of the disease. If the invasive ability of the disease is suppressed then monitoring the disease becomes easier.

References

-
- ¹ C. J. Hawkey. COX-2 Inhibitors. *The Lancet*. 353 (1999) 307-314.
 - ² C. J. Hawkey. COX-2 Chronology. *Gut*. 54 (2005) 1509-1514.
 - ³ U. Satyanarayana, D. S. Rao, Y. R. Kumar, J. M. Babu, P. R. Kumar, J. T. Reddy. Isolation, Synthesis and Characterization of Impurities in Celecoxib, a COX-2 Inhibitor. *J Pharm Biomed Anal*. 35 (2004) 951-957.
 - ⁴ C. A. Rouzer, L. J. Marnett. Cyclooxygenases: Structural and Functional Insights. *J Lipid Res*. 50 (2009) 29-34.
 - ⁵ Pepino MY, Kuda O, Samivski D, Abumrad NA (2014) Structure-Function of CD36 and Importance of Fatty Acid Signal Transduction in Fat Metabolism *Annu Rev Nutr* 288(22):281-303.
 - ⁶ M. I. Patel, K. Subbaramaiah, B. Du, M. Chang, P. Yang, R. A. Newman, C. C. Cardo, H. T. Thaler, A. J. Dannenberg. Celecoxib Inhibits Prostate Cancer Growth: Evidence of a Cyclooxygenase-2-Independent Mechanism. *Clin Can Res*. 11 (2005) 1999-2007.
 - ⁷ M. E. Kaighn, K. S. Narayan, Y. Ohnuki, J. F. Lechner, L. W. Jones. Establishment and Characterization of a Human Prostatic Carcinoma Cell Line (PC-3). *Invest Urol*. 17 (1979) 16-23.
 - ⁸ J. S. Horoszewicz, S. S. Leong, T. M. Chu, Z. L. Wajzman, M. Friedman, L. Papsideo, U. Kim, L. S. Chai, S. Kakati, S. K. Arya, A. A. Sandberg. The LNCaP Cell Line – A New Model for Studies on Human Prostate Carcinoma. *Prog Clin Biol Res*. 37 (1980) 115-132.
 - ⁹ H. Ryu, W. L. Eckalbar, A. Kreimer, N. Yosef, N. Ahituv. Use Antibiotics in Cell Culture with Caution: Genome-Wide Identification of Antibiotic-Induced Changes in Gene Expression and Regulation. *Sci Rep*. 7 (2017) 1-9.
 - ¹⁰ M. D. Brown, C. A. Hart, E. Gazi, S. Bagley, N. W. Clarke. Promotion of Prostatic Metastatic Migration Towards Human Bone Marrow Stroma by Omega 6 and its Inhibition by Omega 3 PUFA. *Br J Cancer*. 94 (2006) 842-853.
 - ¹¹ K. Nithipatikom, M. A. Isbell, P. F. Lindholm, A. K. Balla, S. Kaul, W. B. Campell. Requirement of Cyclooxygenase-2 Expression and Prostaglandins for Human Prostate Cancer Cell Invasion. *Clin Exp Metastasis*. 19 (2002) 593-601.
 - ¹² F. A. Attiga, P. M. Fernandex, A. T. Weeraratna, M. J. Manyak, S. R. Patierno. Inhibitors of Prostaglandin Synthesis Inhibit Human Prostate Tumour Cell Invasiveness and Reduce the Release of Matrix Metalloproteinases. *Cancer Res*. 15 (2000) 4629-4637.

Chapter 5

The Analysis of Prostate Cancer Cell Lines Treated with Isotopically Labelled Arachidonic Acid Using FT-IRM

It was previously seen in chapters 3 and 4 that there was a noticeable difference between invasive and non-invasive prostate cancer phenotypes. Invasive prostate cancer cell lines readily uptake AA whereas non-invasive cell lines appear to lack the ability to intracellularly facilitate the fatty acid. When the COX-2 enzyme is blocked in invasive cell lines, the cells fail to uptake AA. PCA and seeded PCA were used to investigate the biochemical lipid changes within each cell line, investigating the C=O carbonyl stretch at 1732 cm^{-1} and the C=O ketone stretch in PGE₂ at 1740 cm^{-1} .

This Chapter further investigates the uptake mechanism of AA using FT-IRM and PCA to track isotopically labelled intracellular AA. AA was replaced with a deuterated form arachidonic-5,6,8,9,11,12,14,15-d₈ acid (d₈-AA). The added molecular C-D stretches introduces a highly unique spectral vibration which adds specificity to the molecular tracking of AA. Furthering the COX-2 investigation, DHA was used as a substitute to inhibiting the COX-2 pathway by competing with AA for COX-2 active sites.

5.1 Molecular d₈-AA and Spectral Vibration

The isotopically labelled AA used throughout investigations is d₈-AA, commercially available deuterated AA. Hydrogen was substituted for deuterium in the 5th, 6th, 8th, 9th, 11th, 12th, 14th and 15th positions along the carbon backbone within the AA molecule with 2 hydrogens replaced for deuterium across each double bond, the skeletal representation of d₈-AA can be seen in Figure 64.

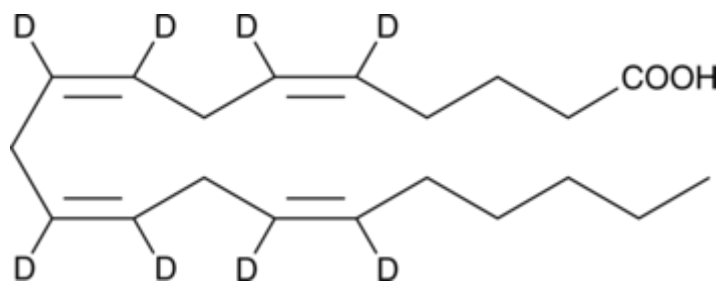


Figure 64 – Skeletal chemical structure of d₈-AA

By replacing 8 molecular hydrogen atoms for deuterium atoms, the bonds vibrational frequency is reduced due to the difference in atomic mass between a hydrogen and deuterium. The shift in vibrational frequency means the C-D stretch is in a region of the IR spectrum with no other biological spectral vibrations at 2251 cm⁻¹. This enables the deuterium tagged AA to be uniquely identified within the cell. With this distinctive C-D vibration, it is possible to produce a spectral profile following the path of AA throughout the time course.

5.2 Investigating the Effect of d₈-AA Uptake and COX-2 Inhibition on Prostate Cancer Cell Lines Using FT-IRM and Seeded PCA

The same set of experiments were carried out as in Chapter 4, investigating AA uptake and COX-2 inhibition on the invasive cell line PC-3 and non-invasive cell line PNT2. AA was replaced with d₈-AA with the aim of providing spectral specificity to track the d₈-AA with the unique C-D stretch at 2251 cm⁻¹.

As the concentration of intracellular d₈-AA is very low, the resulting spectral absorbance of the C-D stretches of the d₈-AA will be very low. This poses the problem of spectral detection, distinguishing the C-D stretch peak at 2251 cm⁻¹ from the spectral noise proves

challenging. Hence, a good signal to noise ratio is essential throughout this study in order to detect spectral absorbances from the C-D stretches. To tackle this issue, the FT-IRM collection parameters were changed throughout the studies in this chapter. The number of background scans were changed to 1000 and number of scans were altered to 500 to increase the spectral signal to noise ratio. Increasing the number of scans roughly 4-fold has the disadvantage of increasing the spectral acquisition time linearly. Increasing the acquisition time also creates issues regarding the stability of the instrument and the temperature of the detector. The FT-IRM encountered issues when scanning for a lengthy amount of time with either the loss of inlet pressure for the bearings controlling the moving mirror causing the spectrometer to crash or loss of communication between the sample stage and the software. The detector temperature would sometime increase rapidly due to the poor vacuum seal within the detector, meaning the detectors liquid nitrogen would have to be replaced more frequently, making long spectral acquisitions problematic.

Issues relating to this lengthy acquisition time was solved by increasing the spectral wavenumber resolution to 5 cm^{-1} from 4 cm^{-1} . The speed of the data readout at 4 cm^{-1} is very slow for a large number of scans. The switch from 4 cm^{-1} to 5 cm^{-1} offers almost the speed of 8 cm^{-1} wavenumber resolution with almost the resolution of 4 cm^{-1} . The increase in wavenumber resolution also smooths the spectra, as fewer data points are taken for a given spectral range, allowing some spectral noise to be smoothed and reduced.

Otherwise, the same experimental protocols were followed as in chapters 3 and 4. The fatty acid d_8 -AA was delivered at a concentration of $20\text{ }\mu\text{M}$ in cyclodextrin. When blocking the COX-2 enzyme, the cells were treated with $10\text{ }\mu\text{M}$ NS398 30-minutes prior to d_8 -AA exposure. When the treatment was finished, cells were washed in PBS, formalin fixed for 20-minutes and finally washed with deionised water and air dried.

5.2.1 Seeded PCA of d₈-AA Treated Prostate Cancer Cell Lines

A FT-IR spectrum of d₈-AA was taken with the spectral range cut to 2220 cm⁻¹ – 2280 cm⁻¹ focusing on the C-D stretch at 2251 cm⁻¹ which can be seen in Figure 65. This well-defined C-D peak was used as the seed in seeded PCA with the spectrum of d₈-AA added to both invasive and non-invasive cell lines data sets. The d₈-AA spectrum was multiplied by 10⁵ to bias the PCA analysis to influence the majority of the chemical variance in the data set to be a result of the C-D peak at 2251 cm⁻¹. In the seeded PCA analysis of d₈-AA treated cell lines, the spectrum in Figure 65 became the PC1 loading, and any changes in the positive PC1 direction are characteristic of accumulating chemical features of d₈-AA.

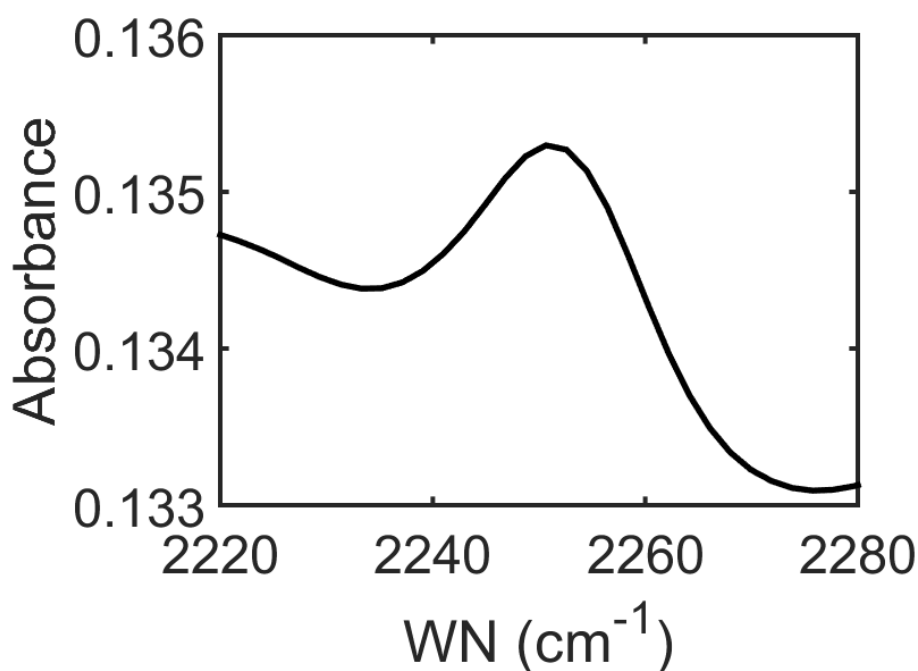


Figure 65 – FT-IR spectrum of d₈-AA over the spectral range 2220 cm⁻¹ – 2280 cm⁻¹ highlighting the C-D stretch around 2251 cm⁻¹

The seeded PCA was carried out over the spectral range $2220\text{ cm}^{-1} - 2280\text{ cm}^{-1}$ looking for any chemical changes solely relating to the C-D stretch, a signature of the d_8 -AA fatty acid.

A median positional plot was used to describe the separation in the seeded PCA score spaces for both PC-3 (blue) and PNT2 (red) treated with d_8 -AA for $t=0, 5, 15, 30$ and 60 min shown in Figure 66. There is a significant change in the cellular chemistry of PC-3 throughout the 60-minute time course when exposed to exogenous d_8 -AA. There appears to be a small change throughout the first 5-minutes. Comparing this to the previous results seen in section 3.1 and 3.2, there is a much smaller initial shift in the PCA score space. This is probably down to the sensitivity of the FT-IR instrument. The C-D stretch is weak compared to that of the C=O carbonyl stretch at 1732 cm^{-1} which was assessed in chapters 3 and 4. There will be a smaller spectral absorbance attained for the C-D stretch compared that that of the C=O carbonyl stretch, resulting in a smaller change within the PCA score space. By $t=15$ min, there appears to be maximum displacement in the median positional plot, indicating maximum chemical variance compared the initial $t=0$ min time point. This maximum variance is specific to the C-D stretches within the cell, indicating cellular d_8 -AA uptake. At $t=30$ min, there is a directional transition within the median positional plot demonstrating the cells are losing chemical features associated with the deuterated tag. Finally, at $t=60$ min, the cell returns to the initial $t=0$ value showing that the cells have returned to their initial state, highlighting the cells have lost all spectral features associated with d_8 -AA. The loss of the spectral deuterium tag suggests that there is metabolic catalysis of the d_8 -AA and cellular rejection of the bioactive metabolites, matching the well documented metabolic events associated with the AA cascade. This result agrees with the studies investigating PC-3 cells treated with AA in chapters 3 and 4, with all studies

suggesting maximum fatty acid uptake at $t=15$ min and loss of chemical features associated with the fatty acids by $t=60$ min. This demonstrates that the chemical cellular changes are specifically down to the uptake and ejection of d_8 -AA and AA in complimentary studies.

The PNT2 cells appear to show no indication of C-D spectral features. The median positional values show no significant changes in both positive or negative directions, indicating no separation in the seeded PCA score space between any time points. This directly relates to the lack of biochemical variation seen throughout the 60-minute time course. This deuterated experiment matches the studies previously carried out looking at AA uptake in the non-invasive PNT2 cell line in chapters 3 and 4. The specificity of the d_8 -AA further strengthens the conclusion that there is no d_8 -AA uptake in the PNT2 cell lines.

The isotopic label has provided validation on the chemistry previously witnessed in chapters 3 and 4. The unique C-D stretch has provided the molecular specificity required to tracking the cellular uptake of AA. This demonstrates that FT-IRM can be used to investigate metabolism with the technique proving sensitive enough to be able to probe and map specific vibrational signatures.

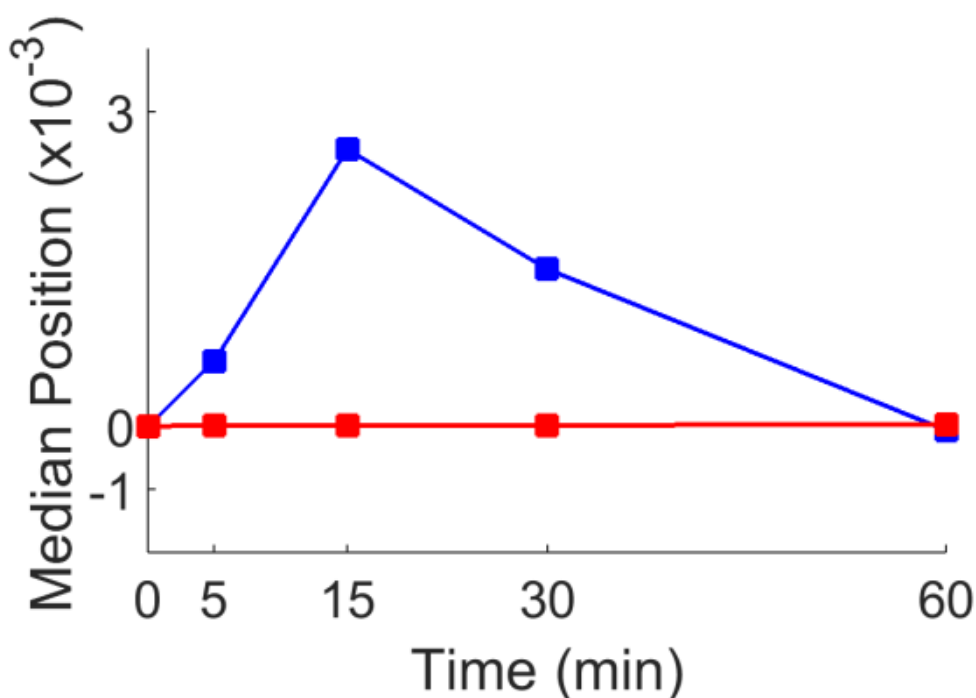


Figure 66 – Seeded PCA scores relative median positional plots of FTIR spectra, examining the C-D stretch between 2220 cm⁻¹ – 2280 cm⁻¹ for invasive cell line PC-3 (blue) and non-invasive cell line PNT2 (red) treated with d₈-AA for 0, 5, 15, 30 and 60 min.

4.2.2 Seeded PCA of d₈-AA Treated Prostate Cancer Cell Lines COX-2 inhibited

The effect of COX-2 inhibition of the cellular uptake and metabolism of AA was investigated using d₈-AA. The median positional plot for invasive cell line PC-3 (blue) and non-invasive cell line PNT2 (red) treated with d₈-AA and COX-2 inhibited at $t=0$, 5, 15, 30 and 60 min can be seen in Figure 67. The PC-3 and PNT2 cells appear to show no chemical change associated with the uptake of d₈-AA, when blocking the COX-2 pathway. There are no significant changes in directionality within the median positional plot for both invasive and non-invasive cell lines throughout the 60-minute time course.

This result confirms that blocking the COX-2 enzyme in invasive cell lines inhibits the cells ability to uptake AA. The isotopically labelled AA matches the results previously seen in

chapter 4. Confidence can be drawn with the added specificity with the deuterated tag applied to the seeded PCA that no AA is entering the cell when the COX-2 enzyme is blocked. This further strengthens the hypothesis that there must be an upstream signalling mechanism preventing AA entering the cell when the active site of the cellular COX-2 enzyme is compromised.

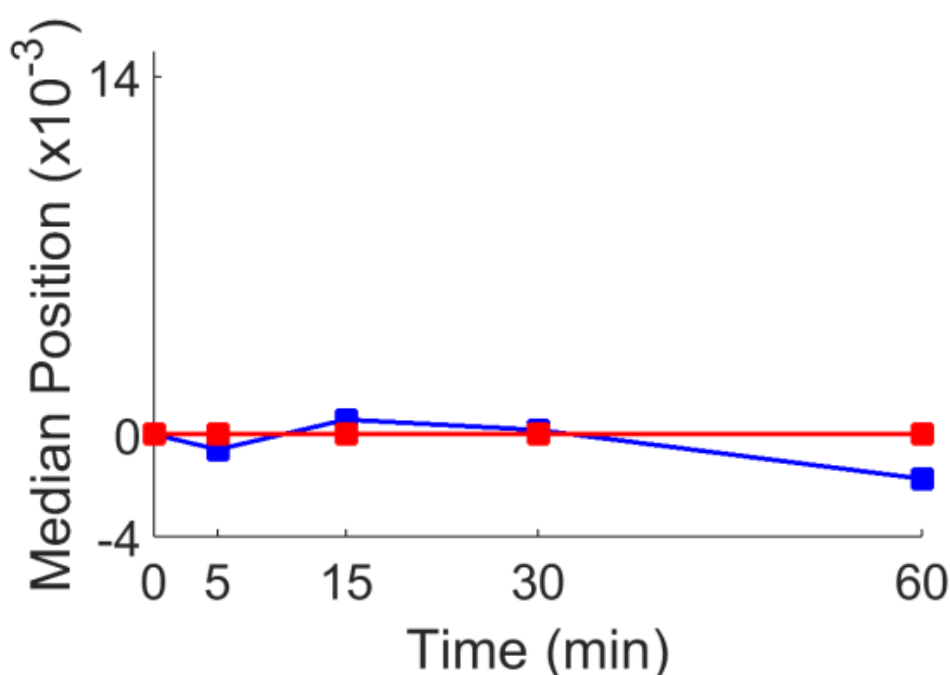


Figure 67 – Seeded PCA scores relative median positional plots of FTIR spectra, examining the C-D stretch between 2220 cm^{-1} – 2280 cm^{-1} for invasive cell line PC-3 (blue) and non-invasive cell line PNT2 (red) treated with d_8 -AA and COX-2 inhibited for 0, 5, 15, 30 and 60 min.

5.3 Investigating COX-2 Inhibition via DHA and AA Competition

An investigation was carried out examining the effect of DHA on AA uptake. We have shown in previous data that COX-2 has a suppressive effect on the chemistry associated with fatty acid uptake in figure 2. To confirm that the chemistry seen is a direct effect of NS398 on COX-2, we replaced NS398 with DHA, as this competes with AA for COX-2 sites. DHA has a greater Michaelis constant (K_m) for the reaction than AA, meaning DHA

will out compete AA for the COX-2 enzymatic sites due to a greater binding affinity, effectively suppressing the COX-2 enzyme for AA metabolism.

5.3.1 PCA of Prostate Cancer Cell Lines Treated With DHA

A study was carried out examining the effect of DHA on the invasive cell line PC-3 and non-invasive cell line PNT2. Cell lines were treated with 20 μ M DHA in cyclodextrin for $t=0, 5, 15, 30$ and 60 min. PCA was carried out over the spectral range $1720\text{ cm}^{-1} - 1750\text{ cm}^{-1}$ studying the chemical cellular changes regarding the C=O carbonyl stretch specific to fatty acids at 1732 cm^{-1} .

A median positional plot was used to describe the separation in the PCA score space for both PC-3 (blue) and PNT2 (red) cell lines treated with DHA over a 60-minute time course which can be seen in Figure 68.

The PC-3 cells experienced a change in intracellular lipid chemistry when exposed to the exogenous supply of DHA. There appears to be a large positive displacement in the median positional plot as early as $t=5$ min with respect to the initial $t=0$ min time point. This suggests the PC-3 cell line are showing characteristics of the C=O carbonyl stretch specific to fatty acids, suggesting there is cellular DHA uptake, just as was seen using AA. There is a maximum displacement seen at $t=15$ min highlighting the greatest separation in the PCA score space. At $t=30$ min, there is a large decrease in median positional value showing a directional change in the PCA score space and indicating that the cellular chemistry is becoming more representative of the initial $t=0$ min. Finally, by $t=60$ min, there is a further decrease in biochemical variance within the data set shown by a decrease in median positional value. It appears that after $t=15$ min the cells are losing the spectral features of the C=O carbonyl stretch implying cellular metabolism.

The PNT2 cell line demonstrated no change in chemical variance throughout the 60-minute time course. The non-invasive cell line appeared to show no indication of DHA uptake reflected by no significant directional changes in the median positional plot. The results are suggestive that there are similar fundamental cellular mechanisms which prevent AA and DHA uptake in non-invasive cell lines.

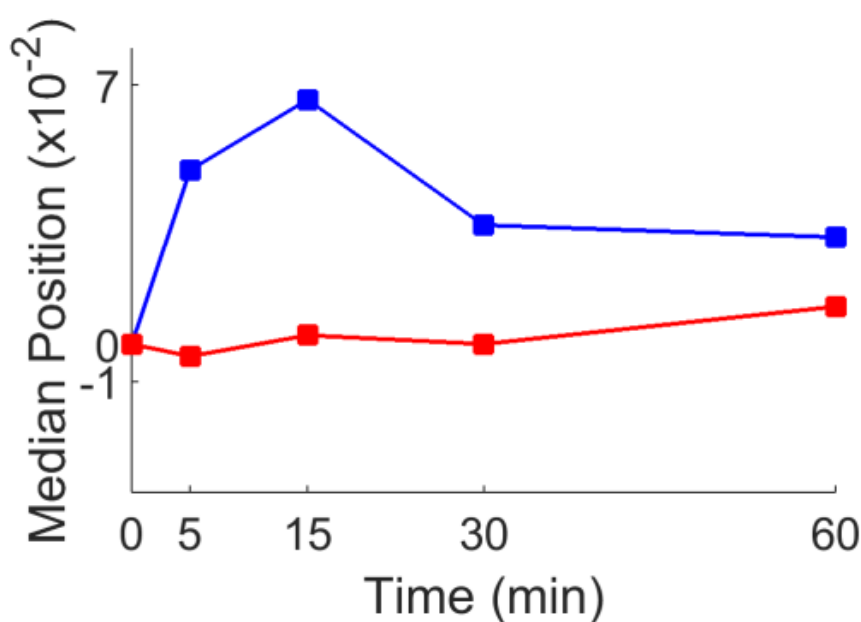


Figure 68 – PCA relative median positional plots of FTIR spectra, examining the C=O stretch between $1720 - 1750 \text{ cm}^{-1}$ for PC-3 (blue) and PNT2 (red) cells treated with DHA for 0, 5, 15, 30 and 60 min.

5.3.2 Seeded PCA of Prostate Cancer Cell Lines Treated with DHA and AA

The cell lines PC-3 and PNT2 were treated with equal concentrations of $20 \mu\text{M}$ $\text{d}_8\text{-AA}$ and DHA and exposed for $t=0, 5, 15, 30$ and 60 minutes. The same protocol was used for the $\text{d}_8\text{-AA}$ seeded PCA as previously described in this chapter. Seeded PCA was carried out over the spectral range $2220 \text{ cm}^{-1} - 2280 \text{ cm}^{-1}$ solely investigating the chemical changes associated with deuterium uptake through the C-D stretch at 2251 cm^{-1} .

The seeded PCA median positional plot of PC-3 (blue) and PNT2 (red) cell lines treated with d₈-AA and DHA can be seen in Figure 69. The PC-3 cells treated with both d₈-AA and DHA showed an interesting result. It appears that there are no chemical changes associated with the C-D stretch at 2251 cm⁻¹ and therefore no evidence of d₈-AA uptake. There are no significant changes in the median positional plot and hence the seeded PCA score throughout the 60-minute time course. It was shown that PC-3 cells readily uptake and metabolise d₈-AA in the seeded PCA in Figure 66. When DHA is added, there appears to be a block on the d₈-AA uptake, the same result as when blocking the COX-2 enzyme with NS398. PC-3 cells readily uptake DHA, as indicated by the result in Figure 68, when introduced into a cellular system with d₈-AA. It is suggested that the cell does not allow intracellular access to d₈-AA over DHA. The DHA acts as a COX-2 inhibitor just like the NS398 due to its substantially greater COX-2 affinity and *k_m* value. There is no indication of any deuterium within the cells which is conclusive of no d₈-AA uptake. This implies the cell selectively chooses DHA over d₈-AA. This ties in with the two hypotheses made in chapters 3 and 4 that cells are more selective than initially thought and when inhibiting the COX-2 pathway the cells initiate an upstream signalling mechanism to prevent cellular uptake of AA. This finding demonstrates that the results seen blocking AA uptake with NS398 and DHA is a genuine chemical effect rather than a cellular response to NS398.

The PNT2 cells display no changes in chemistry when treated with both DHA and d₈-AA. There are no significant changes in median positional value showing no change within the seeded PCA score. It is shown that PNT2 cells neither uptake DHA or d₈-AA. This would be expected, as PNT2 cells shown no indication of d₈-AA or DHA uptake when treated individually.

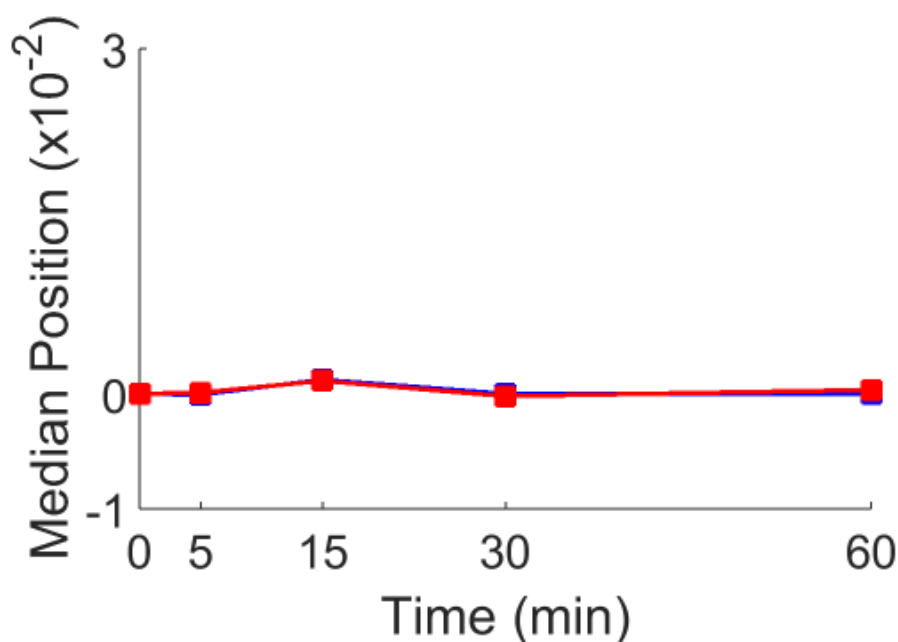


Figure 69 – PCA relative median positional plots of FTIR spectra, examining the C–D stretch between 2200 – 2300 cm⁻¹ for PC-3 (blue) and PNT2 (red) cells treated with both DHA and d₈-AA for 0, 5, 15, 30 and 60 min.

5.4 Conclusion

The deuteration of AA proved a valuable study in the validation of AA uptake in invasive and non-invasive cell lines. It was apparent that there were deuterated spectral signatures in the invasive cell lines, whereas no such species were detected within non-invasive cell lines. This further indicates that non-invasive cell lines lack the fundamental ability to uptake cancer fuelling fatty acids such as AA and d₈-AA. The ability to uptake AA appears to be a key difference between an invasive and non-invasive phenotype, and potentially a pivotal driver in the progression of the disease.

When the COX-2 enzyme was inhibited, there appeared to be no deuterated spectral signatures indicative of d₈-AA uptake for both invasive and non-invasive cell lines. This

further supports the hypothesis that there must be an upstream signalling mechanism preventing AA to enter the invasive cell lines.

DHA appears to have the same effect as AA on invasive and non-invasive cell lines. Invasive cells showed spectral chemistry associated with the C=O carbonyl stretch at 1732 cm^{-1} with no such behaviour witnessed for non-invasive cell lines. When using DHA as a COX-2 inhibitor, the same result is seen as when using NS398. The invasive and non-invasive cell lines showed no change in C-D spectral features within the cell throughout the 60-minute time course. The chemistry appears genuine, the cells initiate an AA block from muting the activity of the COX-2 enzyme. Invasive cell lines readily uptake both AA and DHA in individual separate studies. When combined in equal concentrations, the cell accepts DHA and rejects the d_8 -AA. This further implies that cells are highly selective, with an ability to reject a fatty acid species on the recognition of a double bond position. Why this happens is currently unknown.

Chapter 6

The Analysis of Arachidonic Acid Uptake and Cellular Distribution in PC-3 Cells with Active and inhibited COX-2 Using Fluorescence Microscopy and FT-IRM imaging

In chapters 3-5, it has been shown that PC-3 cells readily uptake AA, the uptake mechanism arresting when inhibited by COX-2. The specific cellular lipid distribution has not yet been defined. Therefore, in this chapter, fluorescence microscopy (FM) will be coupled with FT-IRM imaging to show the intracellular structure and distribution of AA. The FT-IRM imaging will be used at both low and high-magnification, using a pixel size of $5.5\mu\text{m} \times 5.5\mu\text{m}$ and $0.7\mu\text{m} \times 0.7\mu\text{m}$ respectively.

6.1 Studying the Effect of AA on PC-3 Cells through Fluorescence Microscopy

Invasive PC-3 cells were treated with AA and formalin fixed at $t=0, 5, 15, 30$ and 60 minutes. Standard culture protocols were used throughout this investigation with the experimental methodology defined in chapter 2. For the FM investigation, cells were treated with Nile-red 30-minutes prior to AA exposure. The images were taken with a Nikon Eclipse 90i. The exposure time was set to 6 s , which was chosen on a trial and error basis. This parameter was optimised purely looking for the maximum signal without saturating the image. Nile red fluorescence was imaged using a $465 - 495\text{ nm}$ excitation / $515 - 555\text{ nm}$ emission channel resulting in a green fluorescent image. The green fluorescence of Nile red is highly sensitive and specific towards lipid droplets (1), making the green filter ideal for tracking AA uptake.

The FM images of replicate 1 and 2 treating PC-3 cells with AA at $t=0, 5, 15, 30$ and 60 can be seen in Figure 70 and Figure 71. For replicate 1 in Figure 70, the cellular fluorescence is minimal at $t=0\text{ min}$, masking and defining the overall shape of the PC-3 cells. As early as $t=5\text{ min}$, there appears to be a change in cellular fluorescence. The outlines of the cells appear sharp and defined, with an increase in cellular fluorescence.

This could potentially be uptake and incorporation of AA within the cell membrane, but $\times 10$ magnification is too low to be conclusive of membrane incorporation. At $t=15\text{min}$, there appears to be an even greater increase in the overall cellular fluorescence, indicating further AA uptake. By $t=30\text{min}$, there appears to be intracellular pooling of the AA, with defined lipid droplets within the cells. Finally, at $t=60\text{min}$, the cellular fluorescence has significantly decreased, with noticeably reduced intracellular stores of AA. The sudden drop in cellular fluorescence could be further indication of AA metabolism and cellular ejection. The trend and time scale observed in this fluorescence study is similar to the time scale and is consistent with the chemical changes observed previously with the PCA of lipid uptake in PC-3 cells seen in section 3.1.

Replicate 2 in Figure 71 mimics the same trend as seen in replicate 1. At $t=0$ the cellular fluorescence is minimal, representing the basic lipid makeup of the PC-3 cells. By $t=5$ and 15 min, there is an increase in cellular fluorescence, with lipid droplets present within the cell. At $t=30$ min there appears to be maximum cellular fluorescence with time $t=60\text{min}$ losing significant cellular fluorescence, implying AA uptake, metabolism and cellular rejection.

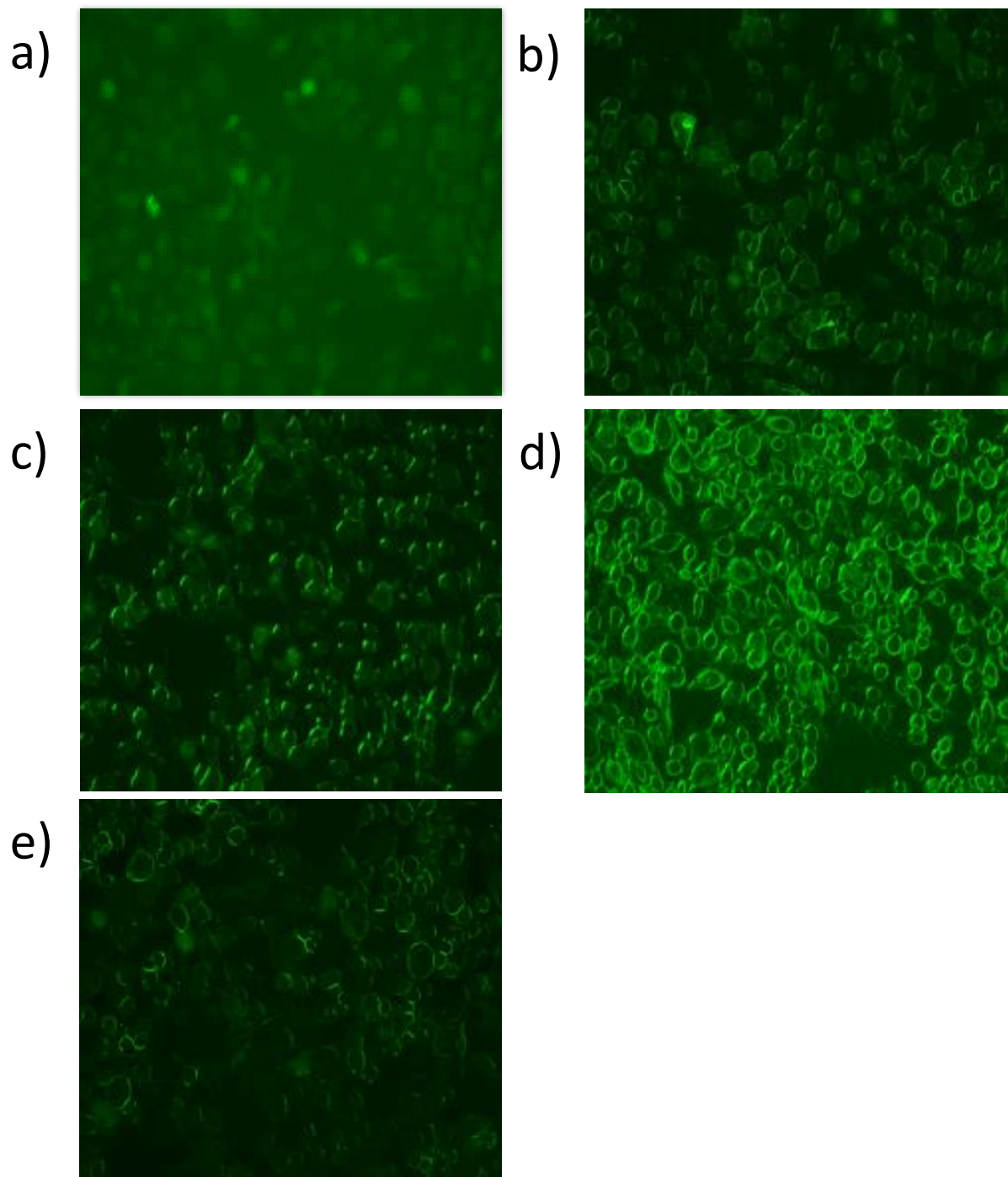


Figure 70 – COX-2 active PC-3 cells treated with AA investigated by FM images tracking the uptake and distribution of AA for (a) $t=0$ min, (b) $t=5$ min, (c) $t=15$ min, (d) $t=30$ min and (e) $t=60$ min (replicate 1) imaged at x10 magnification $750\ \mu\text{m} \times 750\ \mu\text{m}$

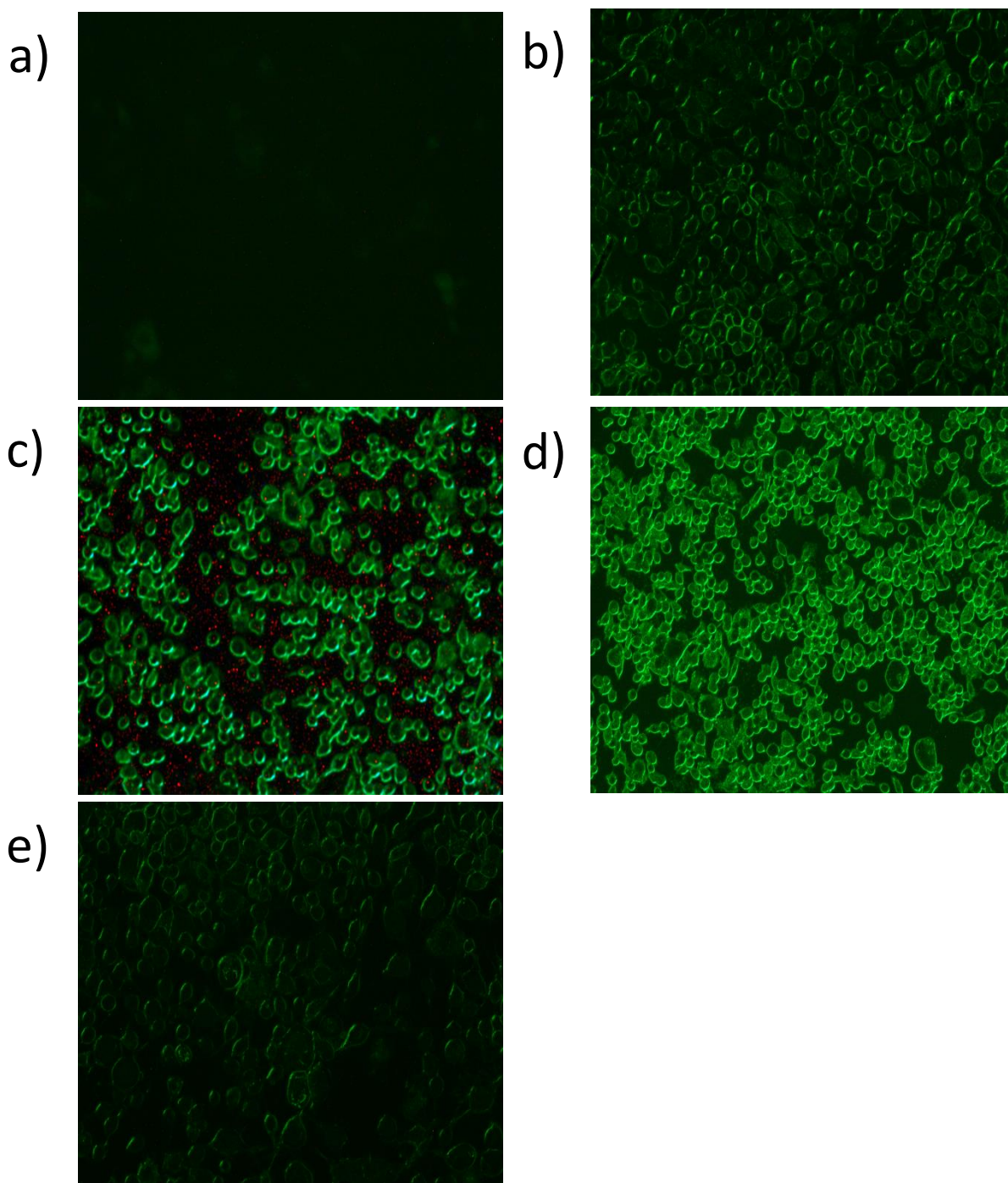


Figure 71 – COX-2 active PC-3 cells treated with AA investigated by FM images tracking the uptake and distribution of AA for (a) $t=0$ min, (b) $t=5$ min, (c) $t=15$ min, (d) $t=30$ min and (e) $t=60$ min (replicate 2) imaged at x10 magnification $750\ \mu\text{m} \times 750\ \mu\text{m}$.

Fluorescent quantification has been carried out using ImageJ, a free licence image analysis software. This software enables the intensity of cellular fluorescence within the image to be quantified by measuring pixel intensity. The raw intensity of each cell was taken and divided by the cell area to normalise the intensity value. This was carried out as raw cellular fluorescent is a function of cell size. A larger cell will naturally have a greater raw intensity than a smaller one, so if the cellular intensity is divided by its area, then a like-for-like comparison between individual cell intensities can be drawn. The image background was then subtracted from the normalised cell intensity, providing the absolute intensity value. The mean cellular intensity for each time point was then plotted as a function of time. The normalised intensity plots for replicate 1 and 2 investigating PC-3 cells treated with AA at $t=0, 5, 15, 30$ and 60 min can be seen in Figure 72a and Figure 72b respectively.

The same conclusion can be drawn from the quantification of cellular fluorescent intensity. In both instances, there is an increase in fluorescent intensity up to $t=30$ min, highlighting an increase in intracellular concentration of AA followed by a decrease in fluorescent intensity at $t= 60$ minutes, representing a decrease in intracellular stores of AA indicating metabolism and cellular rejection.

Interestingly, when comparing $t=5$ min for replicate 1 and 2 in Figure 72a and Figure 72b respectively, there is a significant difference in cellular fluorescent intensity, with replicate 1 displaying an increase by almost 10 units. This could simply be natural variation between replicates, as it shows the overall same trend in cellular fluorescence. Cellular temperature could have also played a role in the difference of fluorescent intensity between replicates 1 and 2. When initially treating the cells with AA, the cells need to be removed from the incubator, where they were kept at 37°C with an atmosphere at $5\% \text{ CO}_2$ v/v. The medium is removed and replaced with a medium containing $20 \mu\text{M}$ AA and the cells are placed back

into the incubator until a specific time point, in this case 5 minutes, when they are formalin fixed. During this process, there are potential sources to create experimental variance in culture temperature. Replicate 2 could have been slightly longer outside of the incubator, resulting in a lower media temperature. As metabolism is temperature dependant, a small change in medium temperature could result in a slower initial uptake of AA. Also, the temperature of the AA rich medium which was added needs to be considered. If the AA rich media of replicate 2 was again slightly cooler than replicate 1, the consequence would be the same. A slower uptake would result in a reduced initial fluorescent intensity. When comparing the remaining time points between replicate 1 and 2, the fluorescence appears on a similar scale.

Interestingly, the overall trend and shape of the normalised fluorescence plots for AA uptake in PC-3 cells matches the shape of the median positional plots chapter 4. This further highlights that the lipid uptake monitored through PCA agrees with the FM.

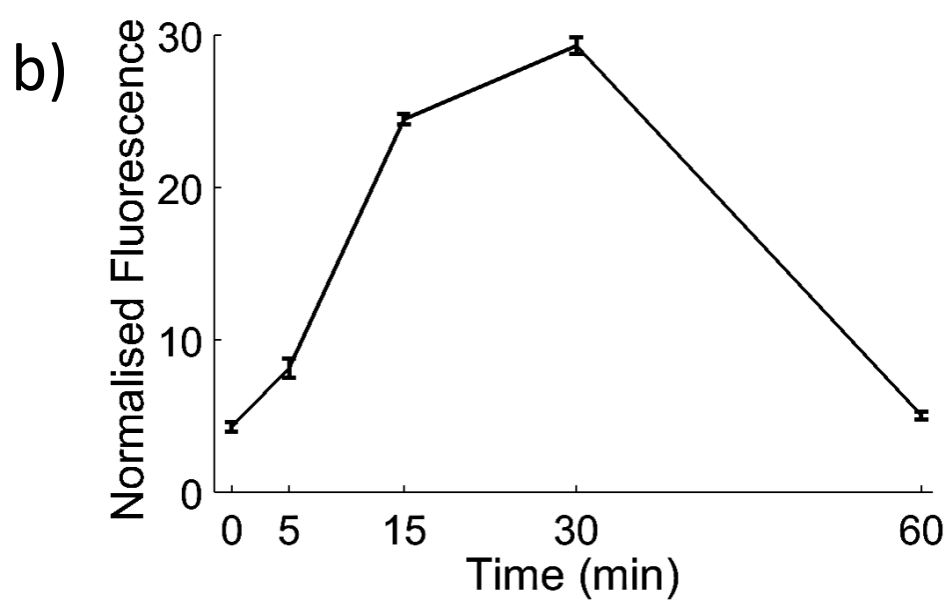
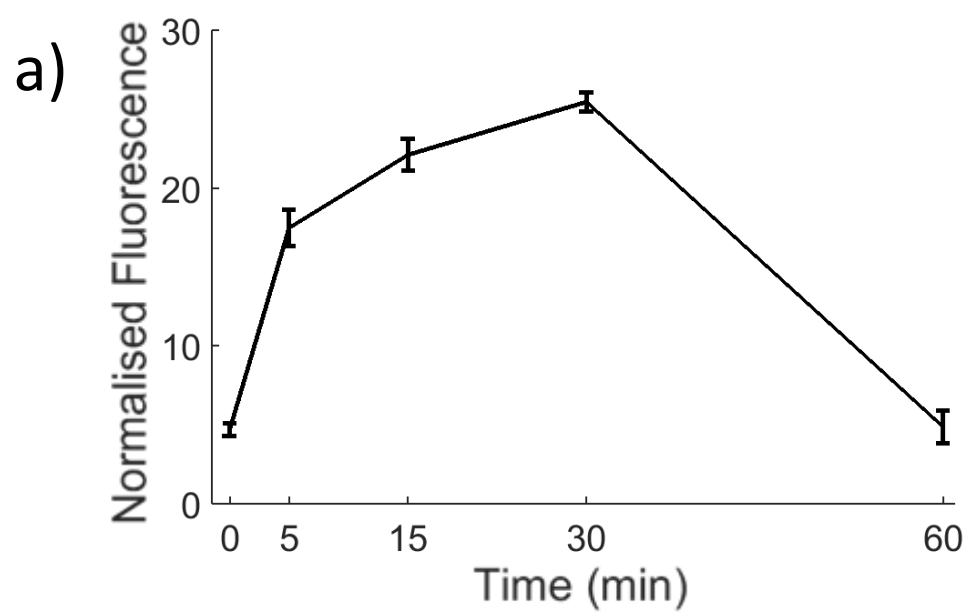


Figure 72 – Normalised fluorescent intensity for FM Nile red analysis of AA uptake in COX-2 active PC-3 cells for $t=0, 5, 15, 30$ and 60 min for (a) replicate 1 and (b) replicate 2.

6.2 Studying the Effect COX-2 inhibition on AA Uptake in PC-3 Cells through Fluorescence Microscopy

PC-3 cells were COX-2 inhibited with NS398 30-minutes prior to AA exposure and then treated with Arachidonic acid and finally formalin fixed at $t=0$, 5, 15, 30 and 60 minutes. Replicates 1 and 2 can be seen in Figure 73 and Figure 74 respectively.

Replicate 1 appears to remain uniform in fluorescence throughout the 60-minute time course. When comparing time points, the very uniform fluorescence indicates no change in lipid content. Replicate 2 displays the same behaviour again when looking at the overall trend between time points. There appears to be no AA uptake throughout the 60-minutes time course.

When comparing replicate 1 and 2, there appears to be a difference in background fluorescence. The fluorescence throughout replicate 2 remains uniform but when compared to replicate 1, appears to have a higher fluorescence at all time points. Experimental variability could have been introduced that may have increased the background fluorescence of replicate 2. An excess of unbound Nile-red may have been present in the culture media from insufficient washing of the cells before treatment, in turn increasing the fluorescence from the background and culture media. The culture dish may co-add to the fluorescence background. If the culture substrate was slightly different, this may result in an increased background fluorescence.

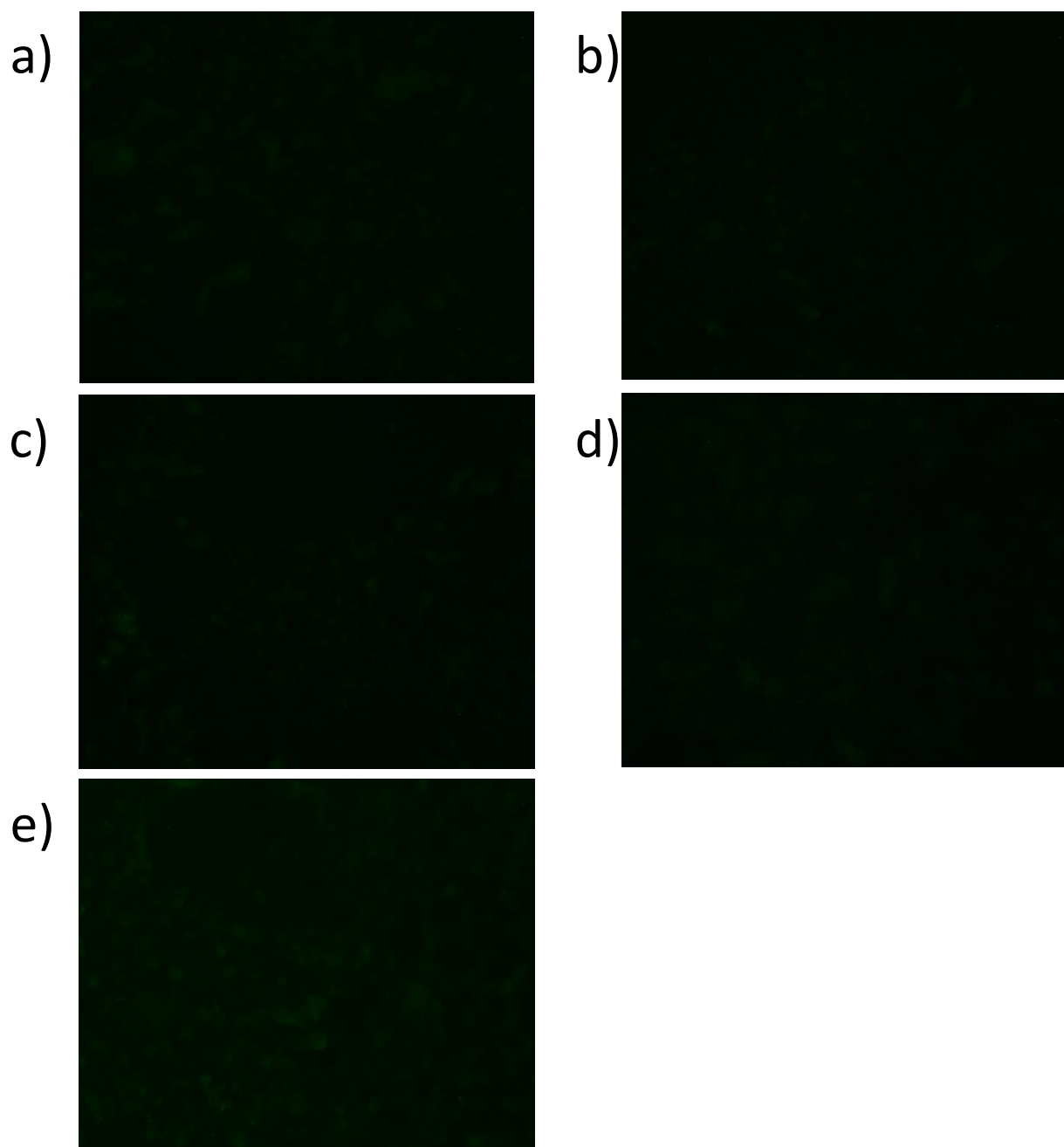


Figure 73 – COX-2 inhibited PC-3 cells treated with AA investigated by FM images tracking the uptake and distribution of AA for (a) $t=0$ min, (b) $t=5$ min, (c) $t=15$ min, (d) $t=30$ min and (e) $t=60$ min (replicate 1) imaged at x10 magnification $750\ \mu\text{m} \times 750\ \mu\text{m}$.

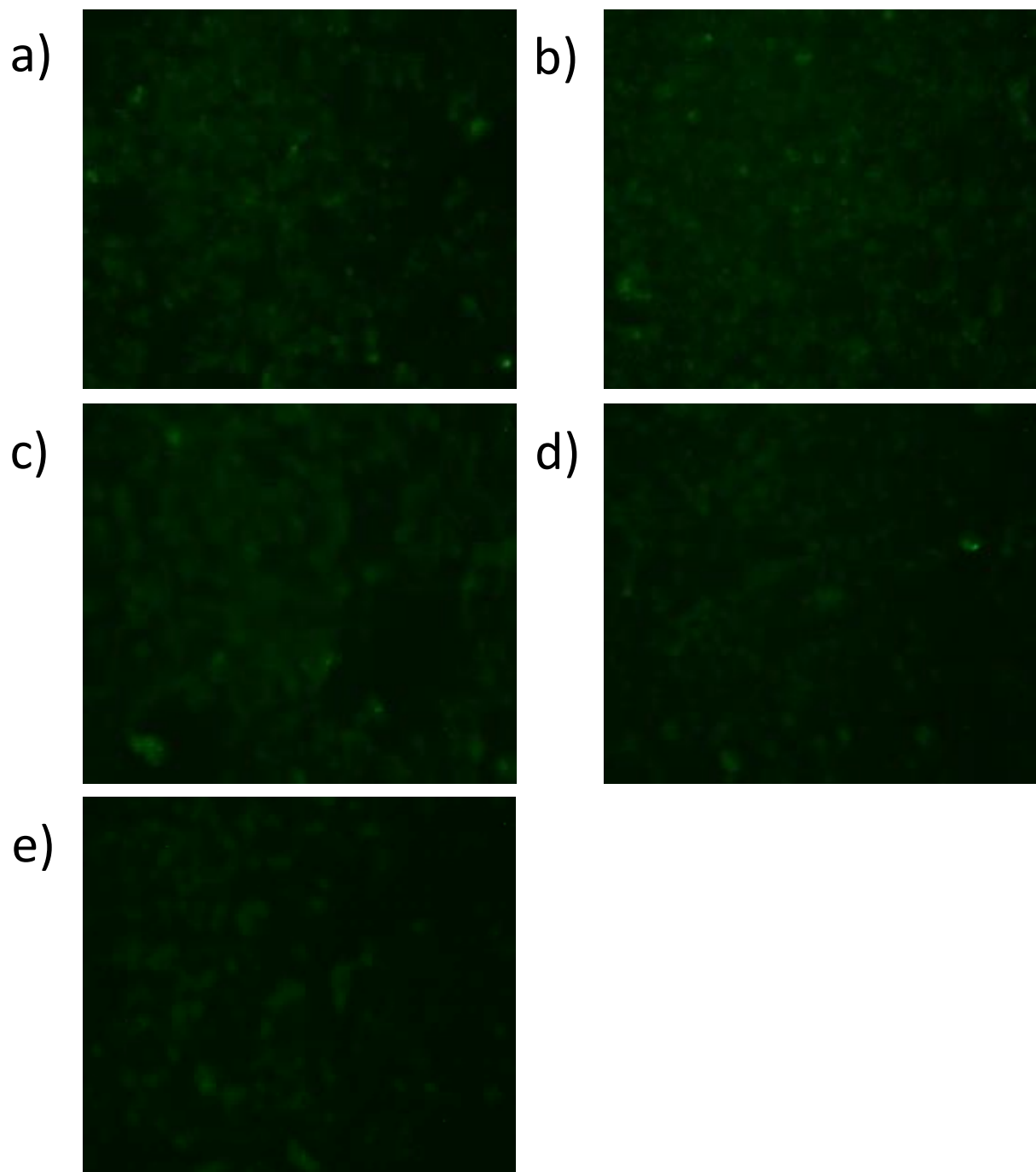


Figure 74 – COX-2 inhibited PC-3 cells treated with AA investigated by FM images tracking the uptake and distribution of AA for (a) $t=0$ min, (b) $t=5$ min, (c) $t=15$ min, (d) $t=30$ min and (e) $t=60$ min (replicate 2) imaged at x10 magnification $750\ \mu\text{m} \times 750\ \mu\text{m}$.

Quantitative analysis has been carried out comparing the absolute cellular fluorescence examining the effect of COX-2 inhibition on AA uptake. The intensity plots for replicates 1 and 2 can be seen in Figure 75a and Figure 75b respectively.

For replicate 1, the cellular fluorescence remains relatively constant throughout the 60-minute time course with no significant changes in fluorescent intensity. Replicate 2 appears to have a slight increase in absolute fluorescence throughout the whole-time course when comparing it to replicate 1. Replicate 2 also has a significantly higher starting fluorescence for both $t=0$ and 5 min than replicate 1. A potential reason for a difference in fluorescence at $t=0$ min could be temperature. As the fluorescence microscope does not have stage heating, replicate 2 could have had a greater starting temperature. Changes in temperature affect the viscosity of the medium, in turn directly effecting the collisions between lipid molecules and the fluorophore. Fluorescence is highly sensitive to changes in temperature with many fluorophores showing fluorescence is temperature dependant (2).

Overall, the trends of replicate 1 and 2 agree with the same conclusion drawn. COX-2 appears to have a significant effect on the cell's ability to uptake AA. When COX-2 is inhibited, there were no significant changes in the absolute cellular fluorescence. No change in cellular fluorescence is conclusive evidence that the overall net cellular lipid content remained unchanged throughout the time course for both replicate 1 and 2. This agrees with the results obtained in chapters 4 and 5, further strengthening and validating the hypothesis that there must be an upstream signalling mechanism which prevents the uptake of AA when the COX-2 enzyme is suppressed.

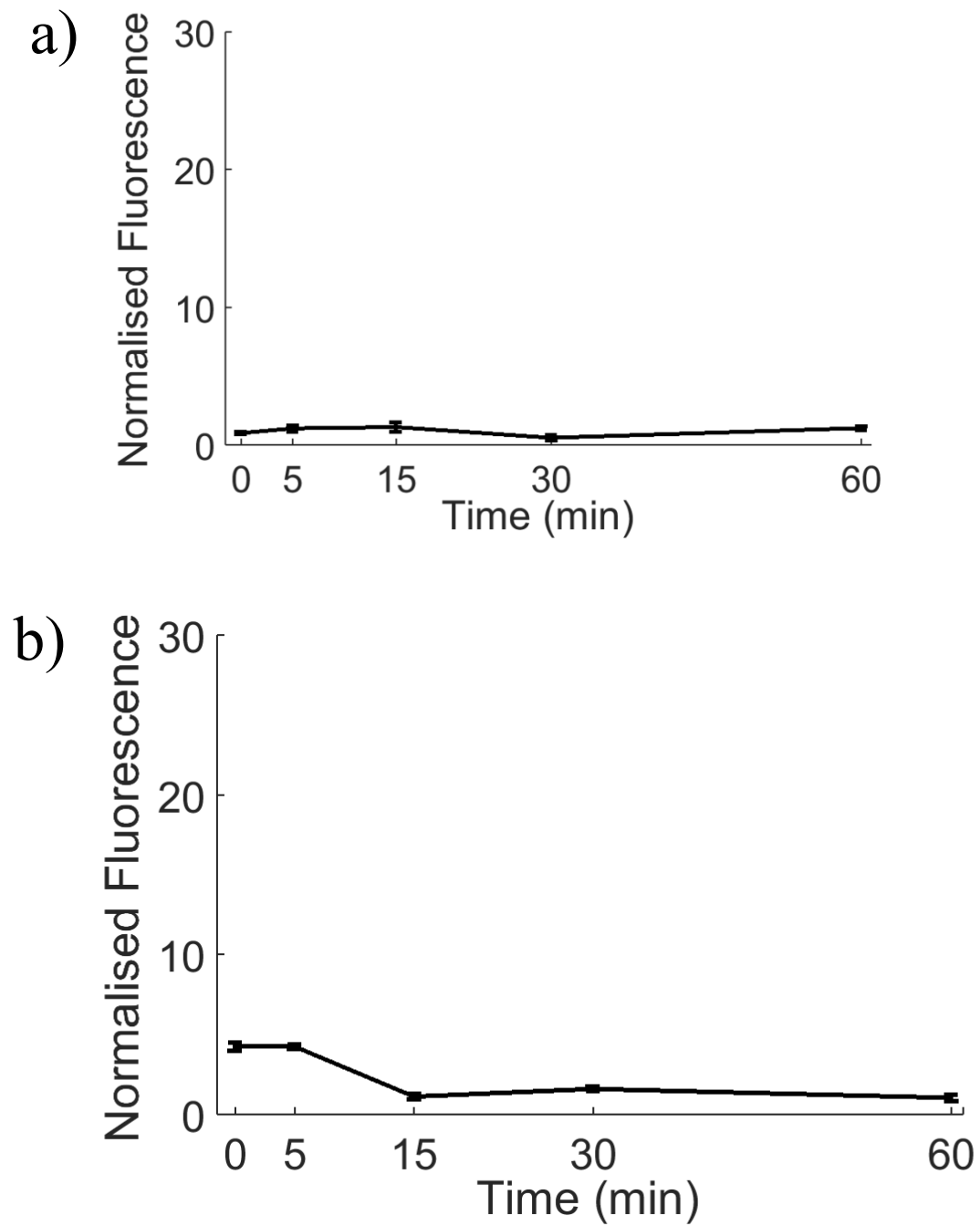


Figure 75 – Normalised fluorescent intensity for FM Nile red analysis of AA uptake in COX-2 inhibited PC-3 cells for $t=0, 5, 15, 30$ and 60 min for (a) replicate 1 and (b) replicate 2.

6.3 Investigating the Cellular Distribution of AA Using Low Magnification FT-IRM Imaging For COX-2 Active and Inactive PC-3 Cells Treated with AA.

There is a need to investigate the chemical distribution of AA within the cell. From the x10 magnification FM study, AA appears to free pool in the form of droplets within the cellular cytosol.

To investigate the cellular distribution of AA, FT-IRM images were collected of PC-3 cells treated with AA with COX-2 both active and inhibited at $t=0, 5, 15, 30$ and 60 min. The C=O carbonyl stretch between $1720\text{ cm}^{-1} - 1750\text{ cm}^{-1}$ specific to fatty acids will be used to track the uptake and metabolism of AA. Mapping this peak should in turn produce FT-IR chemical images that are relatable to the FM investigations carried out. The area under the curve between $1720 - 1750\text{ cm}^{-1}$ will be used as a function of time to map AA. The area under the peak was used as to peak intensity as peak area is more representative of the complex cellular environment with molecules experiencing many different interactions, particularly lipids. As a carbonyl C=O bond is polar, it will experience different extents of molecular hydrogen bonding, meaning vibrational frequencies will shift, taking the area under the curve between $1720 - 1750\text{ cm}^{-1}$ will account for various frequencies associated with AA.

When treating the cells with AA, the only molecular change to the exogenous cellular environment is the concentration of AA. Therefore, the assumption was made that the cellular protein content remains constant. Making this assumption allows the area under the amide I and II to act as a normalising factor. The ratio of the peak C=O carbonyl stretch area and the combined amide I and II peaks area was taken creating a heat map for both COX-2 active and inhibited studies treating PC-3 cells, with AA at $t=0, 5, 15, 30$ and 60

minutes, shown in Figure 76a – Figure 76e and Figure 77a and Figure 77e respectively. Regions of high lipid vibrations appear white, with low concentrations appearing darker in colour.

Firstly, looking at the COX-2 active FT-IR chemical heat maps for PC-3 cells treated with AA in Figure 76; at $t=0$ min, the intensity of the C=O carbonyl stretch is minimal appearing dark in colour throughout the chemical image. By $t=5$ min, there appears to be a sizable increase in intensity, appearing to show huge increases in lipid content around the cell membranes. There appears to be a maximum intensity at $t=15$ min, showing the greatest AA uptake. At $t=30$ and 60 min, the intensity appears to have reduced. This is suggestive that the cell has lost AA molecules by cellular metabolism and rejection. The chemical FT-IR mapping is consistent to what was seen in the FM imaging of PC-3 cells treated with AA. The overall intensity pattern matches the FM, with the cellular distributions also appearing around the membrane and within the cell's cytosol.

When looking at the COX-2 inhibited FT-IR chemical lipid heat map for PC-3 cells treated with AA in Figure 77, there are no differences in heat map intensity throughout the 60-minute time course. The overall C=O carbonyl stretch intensity remains uniform across all time points. These chemical images match the FM investigations and show no AA uptake through COX-2 inhibition.

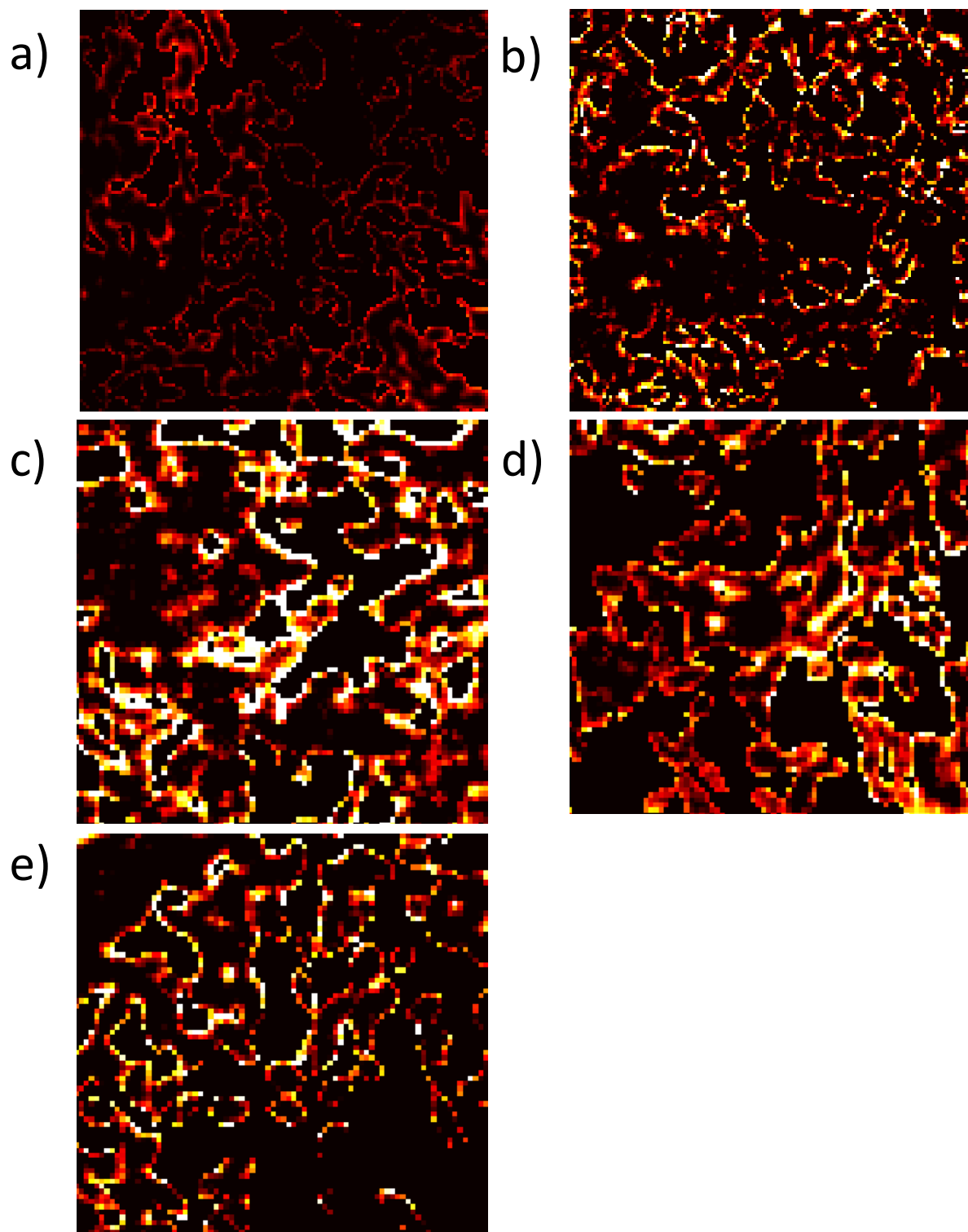


Figure 76 – COX-2 active PC-3 cells treated with AA investigated by FT-IR lipid heat map of the C=O carbonyl stretch between 1720 cm^{-1} – 1750 cm^{-1} with an image size of $704\text{ }\mu\text{m}$ x $704\text{ }\mu\text{m}$ for (a) $t=0\text{ min}$, (b) $t=5\text{ min}$, (c) $t=15\text{ min}$, (d) $t=30\text{ min}$ and (e) $t=60\text{ min}$.

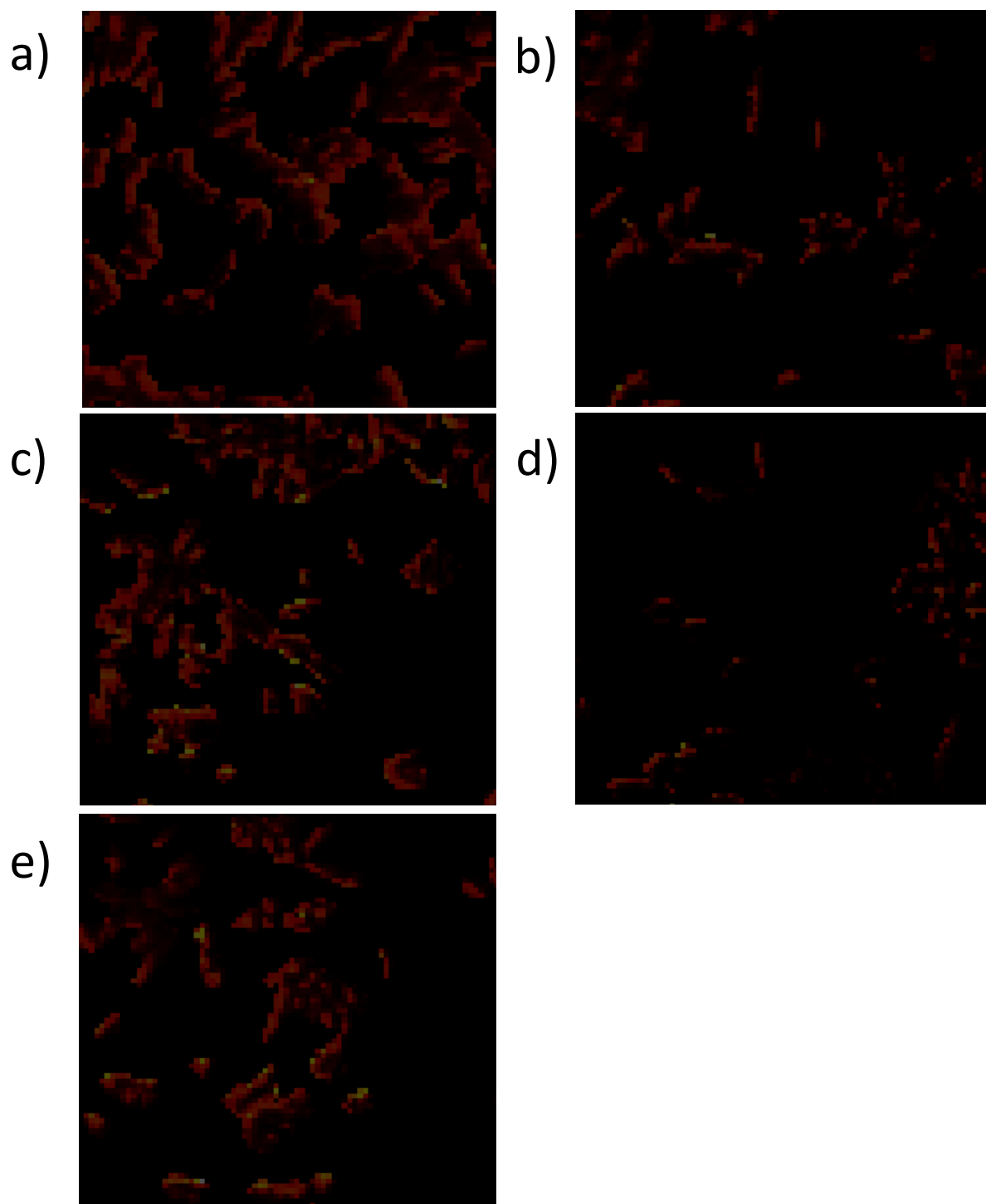


Figure 77 – COX-2 inhibited PC-3 cells treated with AA investigated by FT-IR lipid heat map of the C=O carbonyl stretch between 1720 cm^{-1} – 1750 cm^{-1} with an image size of $704\text{ }\mu\text{m}$ x $704\text{ }\mu\text{m}$ for (a) $t=0\text{ min}$, (b) $t=5\text{ min}$, (c) $t=15\text{ min}$, (d) $t=30\text{ min}$ and (e) $t=60\text{ min}$.

PC-3 cells were exposed to AA for 15 minutes and imaged using the imaging setting brightfield by a Nikon Eclipse 90i microscope at x20 magnification which is shown in Figure 78. The cells were exposed to AA for 15 minutes because all previous studies have suggested that PC-3 cells show maximum AA uptake at this time point.

There are distinctly different cell phenotypes on display within the image. AA has induced morphological changes within the culture of PC-3 cells. Both mesenchymal and amoeboid phenotypes can be seen, key morphological changes required in cellular motility and invasion. Within the diagram key structures are labelled. Firstly, (A) shows the formation of lipid droplets close to the cell membrane in the cell cytosol. This agrees with the result obtained in the Nile red study in Figure 71c, where lipid droplets were observed through FM. Secondly, (B) represents amoeboid protrusions or lamellipodia, these protrusions apply a large force to tight cell junctions in the endothelial vascular lining during intra/extravasation during metastasis, as well as a key organelle in cell motility. Finally, C represents a mesenchymal structure; PC-3 cells in their native state possess this morphology. Interestingly, most of the lipid droplets occur within amoeboid structures. A key morphological structure prostate cancer cells must have in order to undertake intravasation. AA increases prostate cancer proliferation, a possible indication that AA stimulated amoeboid transitions play a role in the progression of the disease.

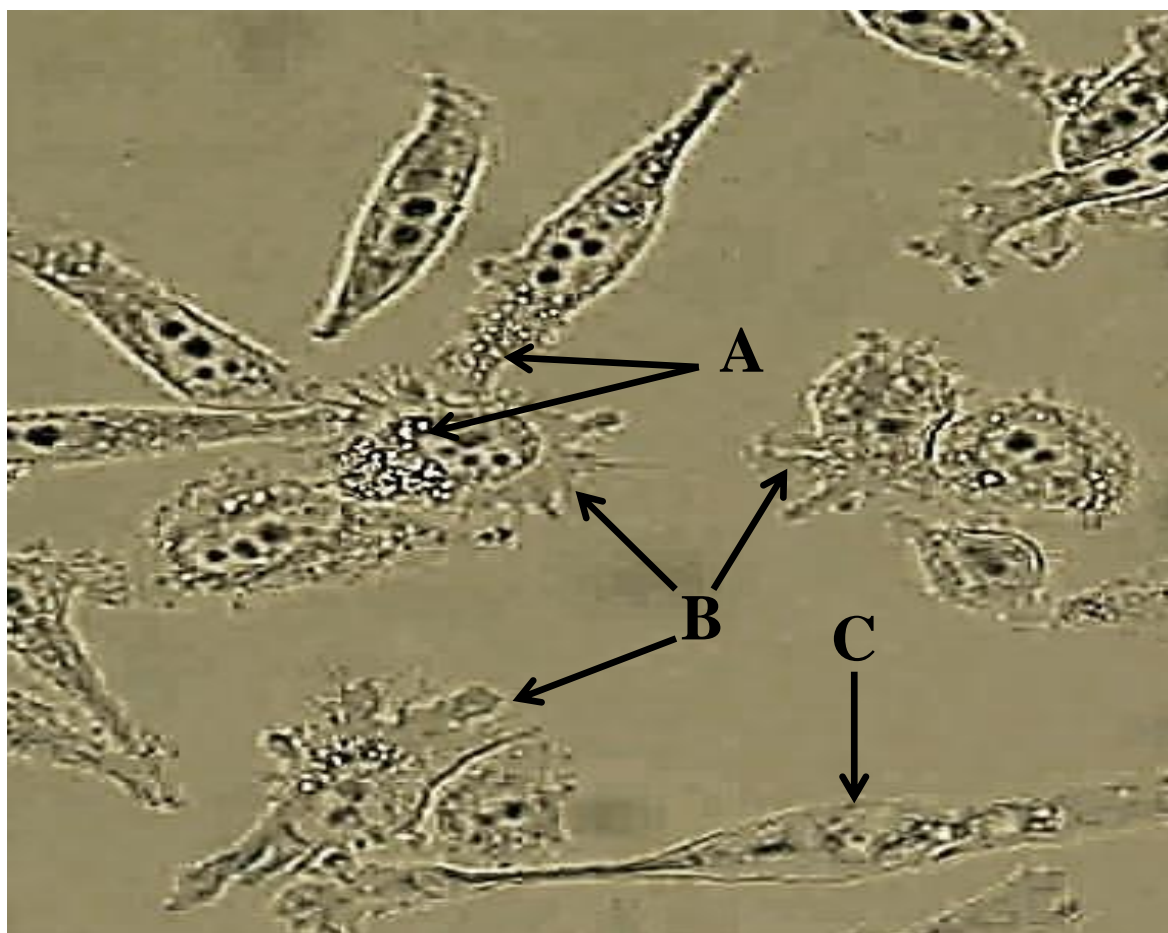


Figure 78 PC-3 cells treated with AA and formalin fixed imaged at x20 magnification with an image size of 480 μm x 480 μm displaying (A) Lipid droplets formed inside amoeboid phenotypes and (B) amoeboid protrusion typical of invasive phenotypes and (C) – Mesenchymal phenotype

6.4 Investigating AA Distribution within PC-3 Cells Using High Magnification FT-IRM

High magnification FT-IRM was used to attempt to chemically define through FT-IRM and locate intracellular structures, something which has rarely been applied. The deuterated form of AA, $\text{d}_8\text{-AA}$ was used throughout this investigation, with the attempt to isolate lipid pools and droplets through the highly unique and distinct C-D stretch at 2251 cm^{-1} specific to $\text{d}_8\text{-AA}$.

All cells analysed were treated for 15 minutes (the length of time maximum uptake occurs) and formalin fixed. Collecting high magnification FT-IR spectra of high enough quality to map C-D vibrations over a given hyperspectral image is both complex and problematic. Instrument optimisation proved pivotal for spectral acquisition when using the high magnification setup. The FT-IR collection parameters that have been optimised are the number of scans and background scans, spectral resolution, condenser alignment, power of IR source, and the number of out of range (OOR) pixels of the FPA detector.

6.4.1 Condenser Alignment

Initially, problems arose when collecting FT-IRM high magnification images. Spectra with very low absorbances with oscillatory features were acquired when collecting a FT-IR background with uneven intensity displayed in the spectral chemical image, seen in Figure 79.

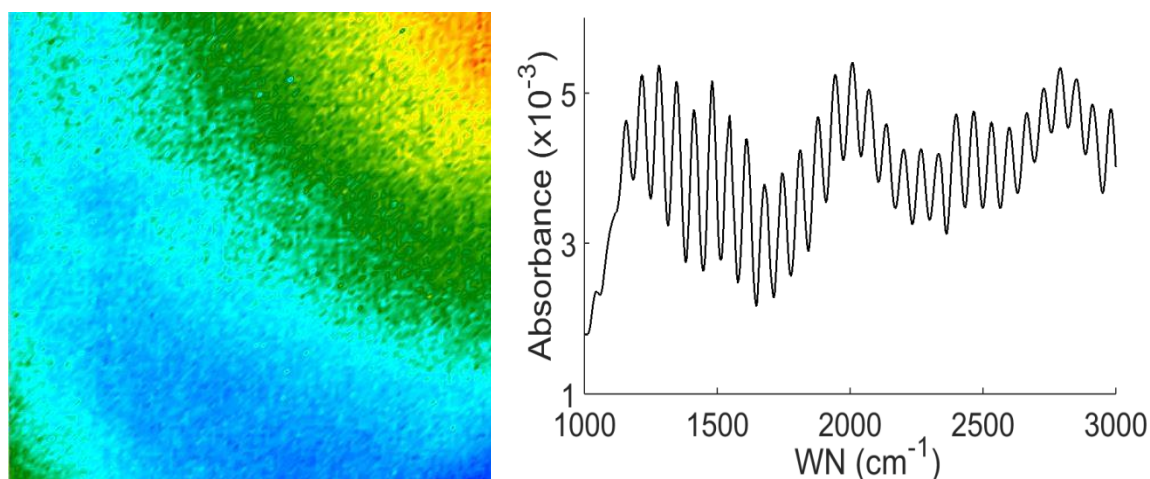


Figure 79 (Left) FT-IR high magnification background chemical image 90 μm x 90 μm and (Right) high magnification mean background spectrum with poor condenser alignment.

The very low intensity distribution appeared to be heading to a maximum in the top right of the image, when ideally the maximum intensity would be seen in the centre of the spectral image. This is a good indication that the condenser was poorly aligned.

The condenser alignment was changed manually via tightening and loosening screw threads in the condenser itself. The background was recollected after a trial and error process optimising the condenser alignment with the resulting spectrum displayed in Figure 80.

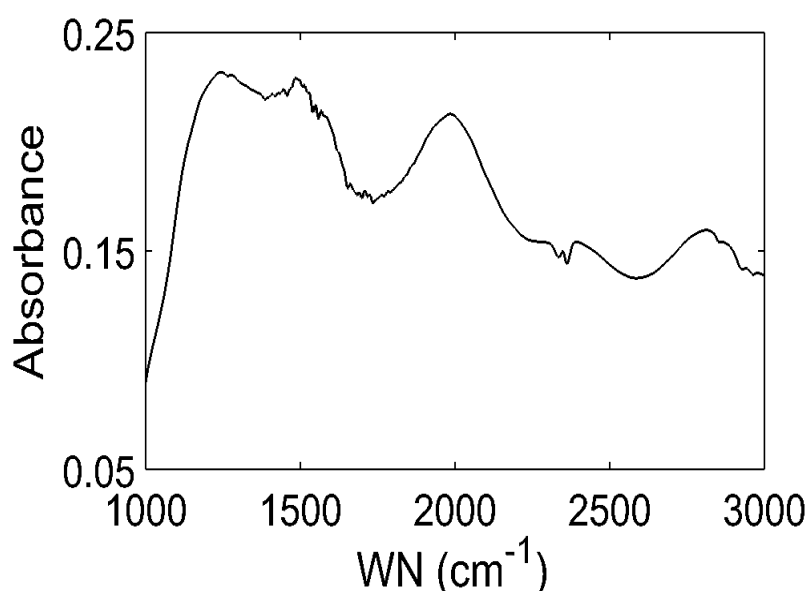


Figure 80 – High magnification FT-IR mean background spectrum with good condenser alignment

The background spectrum absorbance is at a value which can be used in image acquisition. The spectrum noise is substantially better with chemical features of calcium fluoride well defined. It must be noted that the condenser alignment was highly sensitive and easily strayed off line. Each day, the condenser was realigned to obtain optimum spectral absorbance.

6.4.2 High Magnification FT-IR Parameter Optimisation

The main problems faced were the detector signal intensity and the spectral SNR, as the number of photons hitting the detector is considerably lower in a high magnification setup. Initially, the aperture was fully opened to increase the amount of IR on the sample, with the source set to boost (increasing the intensity of IR produced by the source), increasing the intensity of IR hitting the sample, combatting the low signal and number of photons reaching the detector. The number of scans and background scans were taken in a ratio of 1:1. This was assessed stepwise in 1000 steps up to 4000 scans. The instrument stability significantly decreased beyond this point and the spectrometer encountered errors. The spectral resolution was set at 10 cm^{-1} to increase acquisition speed. The integration time was adjusted so the number of OOR pixels was $<1\%$ to again further increase the signal intensity. The FT-IR collection parameters have been outlined in

Table 6.

Collection Parameters	
Integration Time	0.182 ms
Spectral Resolution	10 cm^{-1}
Number of Scans	4000
Number of Background Scans	4000
OOR pixels	$< 1\%$

Table 6 – High magnification FT-IR optimised collection parameters.

After parameter optimisation, the average spectrum of a cell was taken to assess the quality, which can be seen in Figure 81. The Overall SNR is good with DNA bands around 1000 –

1250 cm^{-1} , amide I and II at 1680 cm^{-1} and 1540 cm^{-1} respectively and the lipid CH_2 and CH_3 stretches between 2800 cm^{-1} – 3000 cm^{-1} appearing clear and well defined, the signal intensity albeit lower than usual but to be expected with the high magnification setup.

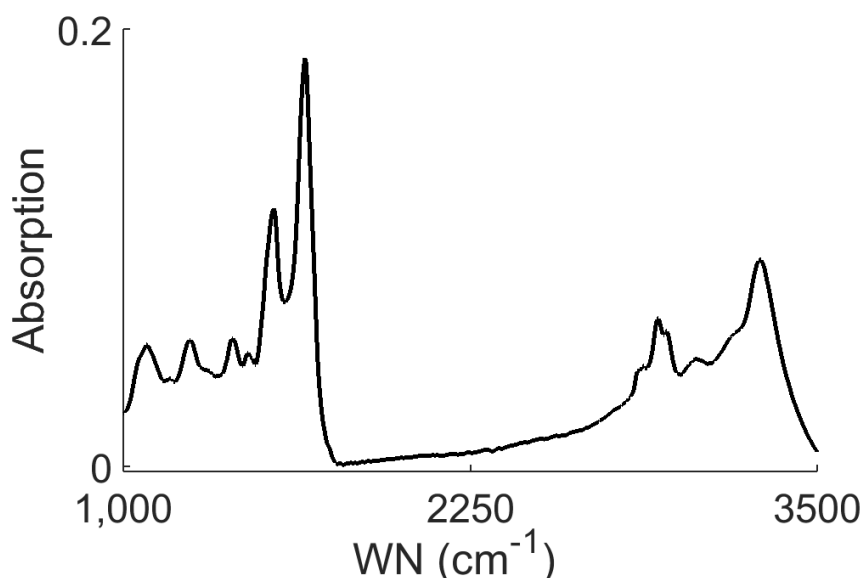


Figure 81 – An example of a good cellular average spectrum using high magnification FT-IRM

6.4.3 High Magnification FT-IR False Colour Images

False colour images were generated from high magnification FT-IR spectra. The fundamental chemical constituents of each cellular structure were analysed. The nucleoli are condensed structures of DNA, therefore containing strong PO_4^- phosphate stretches at 1080 cm^{-1} . Mapping the area under the phosphate stretch at 1080 cm^{-1} should provide the cellular location of nucleoli. The nucleoplasm contains chromatin, a chemical combination of histone which is a protein and DNA. By combining the areas under the amide I and II peaks with the area under the phosphate stretch at 1080 cm^{-1} and setting a sharp contrast filter should provide the location of the nucleoplasm. This in turn should differentiate between regions of solely high DNA content from areas of high DNA and protein content,

distinguishing between the nucleoli and the nucleoplasm. Finally, lipid droplets will be located by mapping the area under the highly specific C-D stretch at 2251 cm^{-1} .

Cells with an amoeboid phenotype were investigated. These amoeboid phenotypes are regarded as a key structure in driving metastasis and invasion. Therefore, it is of interest to identify intracellular structures and distribution of AA within the cell.

Cell 1

The high magnification FT-IR chemical images for cell 1 can be seen in Figure 82 – (a) microscopic image x25 magnification, (b) false colour image of nucleoplasm, (c) false colour image of the nucleoli and (d) chemical heat map of d_8 -AA. Overall, the high magnification FT-IR chemical images have defined the outline of the cell and its structures in reasonable detail. The cell contains fine amoeboid protrusions around the outside of the cell which can be seen in microscopic image (a). These fine details have not been captured within the high magnification FT-IR chemical images, demonstrating the sensitivity of the instrument and the signal to noise ratio was unable to mask these small architectural structures. The cell's nucleoplasm is well defined when comparing the microscopic image (a) and nucleoplasm chemical image (b). Combining the phosphate and protein stretches has displayed the histone and protein within the nucleoplasm. Within the nucleoplasm there is a defined hole. This hole is the region of condensed DNA in the nucleoli. The chemical heat map was sensitive enough to separate DNA and protein peak areas from solely DNA peak areas of the nucleoli. The chemical image map of the nucleoli can be seen in (c). If chemical images (b) and (c) were superimposed, the DNA location in image (c) would fit into the hole in the nucleoplasm in image (b). Finally, the false colour image for d_8 -AA in (d) reveals that the majority of the fatty acid is pooled around the membrane of the cell with

regions of intracellular supplies. The heat map is isn't defined enough to be definitive of the presence of lipid droplets.

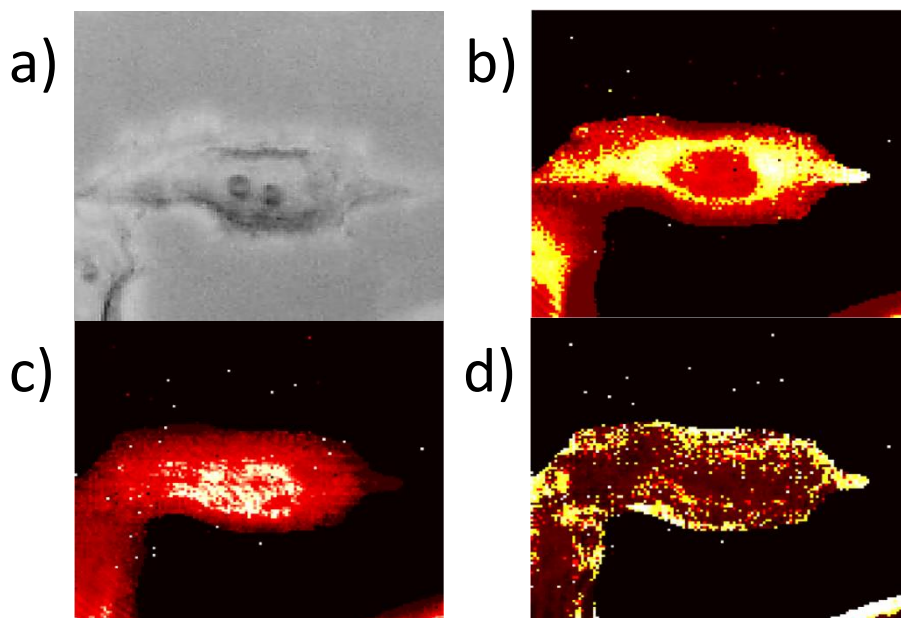


Figure 82 – (a) microscopic image x25 magnification and chemical heat maps of high magnification FT-IR images identifying the structures (b) nucleoplasm, (c) nucleoli and (d) lipid droplets. Image size 90 μm x 90 μm .

A spectrum was collected for both the most intense and least intense pixel within the C-D d_8 -AA chemical image (d) which are displayed in Figure 83a and Figure 83b respectively. The spectral range displayed is between 2240 cm^{-1} and 2260 cm^{-1} to specifically highlight the C-D peak differences at roughly 2251 cm^{-1} . The regions of high intensity within the d_8 -AA chemical images clearly display the presence of d_8 -AA within the cell, whereas low intensity regions express no such spectral features.

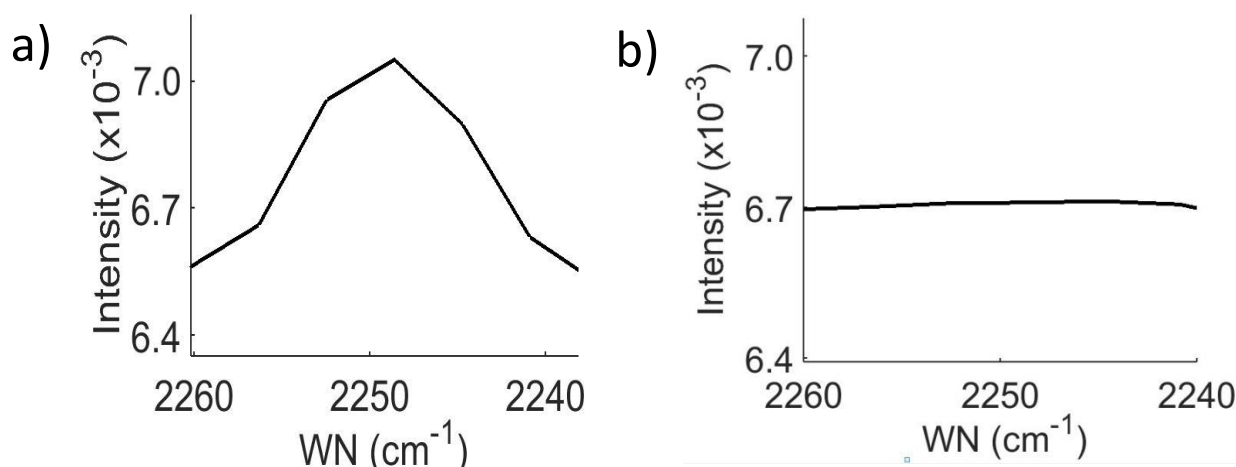


Figure 83 – High magnification FT-IR spectra of the C-D peak at 2251 cm^{-1} for the (a) highest chemical map pixel intensity and (b) lowest chemical map pixel intensity.

Cell 2

The high magnification FT-IR chemical images for cell 2 can be seen in Figure 84 – (a) microscopic image x25 magnification, (b) false colour image of nucleoplasm, (c) false colour image of the nucleoli and (d) chemical heat map of d_8 -AA. Comparing the microscopic image (a) with the nucleoplasm chemical heat map (b), it appears that the false colour image highlights the nucleoplasm in the microscopic image well. Again, there appears to be well defined holes in the nucleoplasm which is the nucleoli displayed in the nucleoli heat map (c). Finally, there appears to be d_8 -AA present around the edges of the cell, with significant accumulation of the fatty acid pooling in the cell cytosol close to the cell membrane. These regions of accumulation are likely to be lipid droplets

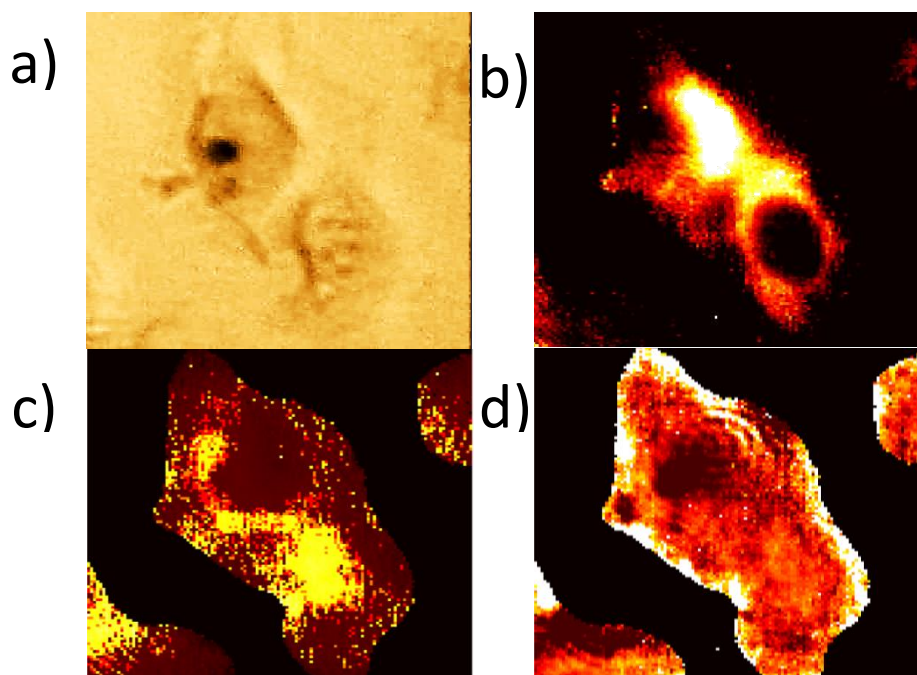


Figure 84 – (a) microscopic image x25 magnification and chemical heat maps of high magnification FT-IR images identifying the structures (b) nucleoplasm, (c) nucleoli and (d) lipid droplets. Image size 90 μm x 90 μm .

It appears that high magnification FT-IRM has the ability to define sub cellular structures. The optimisation of the instrument has played a key role in been able to identify key spectral characteristics relating to the chemical makeup of specific organelles. Issues with the signal to noise ratio was overcome, with defined C-D stretches outside spectral noise. The intracellular distribution of $\text{d}_8\text{-AA}$ was found to be incorporated or pooled around the cellular membrane.

Further high magnification FT-IR images were taken to identify lipid droplets. The area of the C-D peaks at 2251 cm^{-1} were mapped with a cosine smoothing filter applied. The heat map was set to black and white, with regions of white relating to regions of C-D absorbance, providing a sharper contrast. The microscopic images at x25 magnification coupled with its respective C-D heat map can be seen in Figure 85 – cell 3, Figure 86 – cell 4 and Figure 87 – cell 5.

Cells 3, 4 and 5 all appear conclusive in the uptake of d₈-AA. All chemical images are positive of spectral signatures of d₈-AA. There are large pools of d₈-AA in cells 3, 4 and 5, with bead like droplets present in the intracellular cytosol. The C-D heat maps clearly define the areas of condensed DNA in the nucleoli, regions that are without lipid species.

The study by Jamin *et al.* was able to map specific functional groups throughout a cell, specifically investigating the proteins, lipids and nucleic acids with synchrotron FT-IRM and FM (3). Another study carried out by Gazi *et al.* looked directly at motile PC-3 cells using synchrotron FT-IRM (4). Gazi specifically looked at lipid distributions of the CH₂ and CH₃ stretches and cellular protein distributions of the amide I and II vibrations. The study was able to use lipid false colour images to map cellular organelles. In this study, no cellular organelles were identified using the CH₂ and CH₃ lipid stretches. The increased specificity was needed to identify lipid droplets using a deuterated tag mapping the C-D stretch at 2251 cm⁻¹. It could be questioned that the study conducted by Gazi *et al.* had spectral distortions from Mie scattering as the RMieS correction algorithm was not available. Mie scattering distortions could directly affect the lipid vibrations between 2800 cm⁻¹ – 3000 cm⁻¹ adding variability between studies.

FT-IRM has demonstrated the ability to locate intracellular lipids through isotopic labelling. The deuterium has given specific spectral markers which can be used to locate the deuterated species d₈-AA. The lipid droplets appeared to accumulate mainly around the cellular membrane, which would be the primary location through the uptake mechanisms. Uptake mechanisms incorporate AA within the membrane through esterification, followed by PLA₂ enzyme cleavage into the intracellular cytosol, exactly where the majority of the d₈-AA is located.

Cell 3

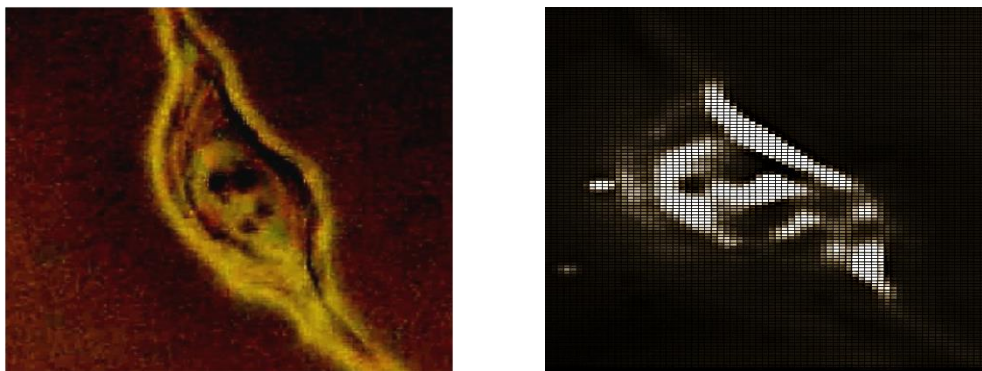


Figure 85 – (a) microscopic image x25 magnification and chemical heat map of high magnification FT-IR image identifying (b) d₈-AA lipid pools. Image size 90 μ m x 90 μ m.

Cell 4

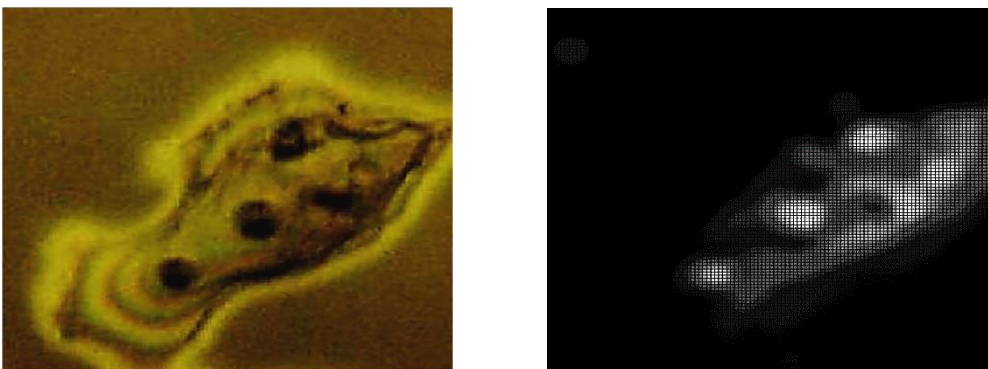


Figure 86 – (a) microscopic image x25 magnification and chemical heat map of high magnification FT-IR image identifying (b) d₈-AA lipid pools. Image size 90 μ m x 90 μ m.

Cell 5

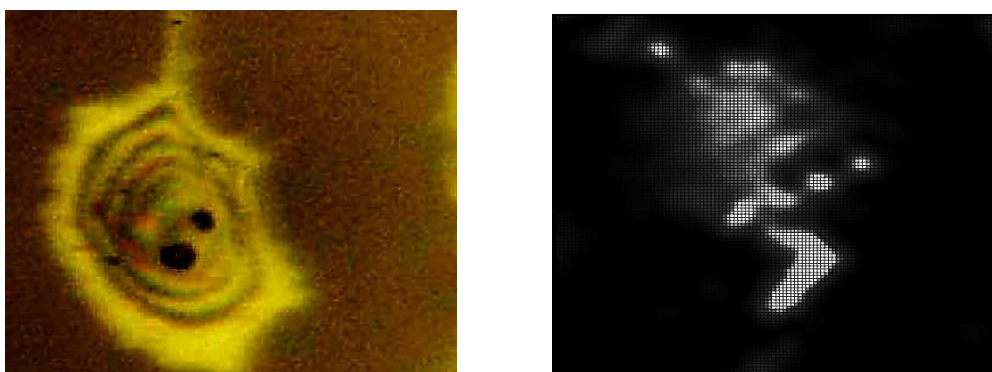


Figure 87 – (a) microscopic image x25 magnification and chemical heat map of high magnification FT-IR image identifying (b) d₈-AA lipid pools. Image size 90 μ m x 90 μ m.

6.5 PC-3 Motility and Morphological Cellular Changes

Prostate cancer metastasis is dependent on the cell's motility. Cellular structure and morphology both change massively when a cell is in the process of migrating (5). When a cell gears up to move, flat cellular protrusions are formed at the periphery of the motile cell (6). This protrusion is known as lamellipodia, which is the fundamental organelle for cellular movement (7). The cell body is positioned behind the lamellipodium extension, where the retracting tail is situated at the back end of the motile cell. There is an abundance of actin filaments just below the cell's plasma membrane. This structure is typically known as the actin cortex.

The formation of lamellipodia requires a change in the cellular distribution of the actin cytoskeleton (8). When a lamellipodia forms, actin polymerisation produces and arranges fibrous actin within the protrusion.

The orientation of myosin II minifilaments is seen to play a critical role in the cytoskeletal function, with the ability to apply force to move actin filaments in the direction required (9). Myosin II is predominantly located around the body of the cell and co-localises with actin filaments, these link the structures of cell body and the sides of the lamellipodium extension (10). When the cell is moving forward, the width of the lamellipodium remains similar, as the cell's motility is underway. In order to maintain motility, there must be constant polymerisation of actin filaments at the forefront of the lamellipodium. The actin that is towards the cell body is depolymerised, where these subunits of actin will be reused again in polymerisation at the forefront of the lamellipodium. This process is known as treadmilling. The actin bundles which form with the sides of the lamellipodium form arc structures with the cell body as well as stress fibres along to cope with the increased

structural tension. The growing protrusion forms new adhesion sites with the substrate called focal contacts giving the cell an anchor to generate the force needed to move the cell forward. Whilst ongoing actin polymerisation propels the cell forward, translocation of the cells body follows, accomplished through the contraction of actin and myosin bundles are the forefront of the cell body. Finally, the rear of the cell loses its adhesive capabilities, releasing the contracting tail for the process to then repeat itself. The steps described are highlighted in Figure 88.

Such a change in cellular protein content and orientation within the lamellipodium protrusions with treadmilling, actin arcs and stress fibres should be detectible with high magnification FT-IRM by mapping the area of the amide I between $1590\text{ cm}^{-1} - 1700\text{ cm}^{-1}$. The main cellular body should have the maximum protein intensity with regions of increased protein noticeable at certain morphological positions of interest associated with lamellipodium.

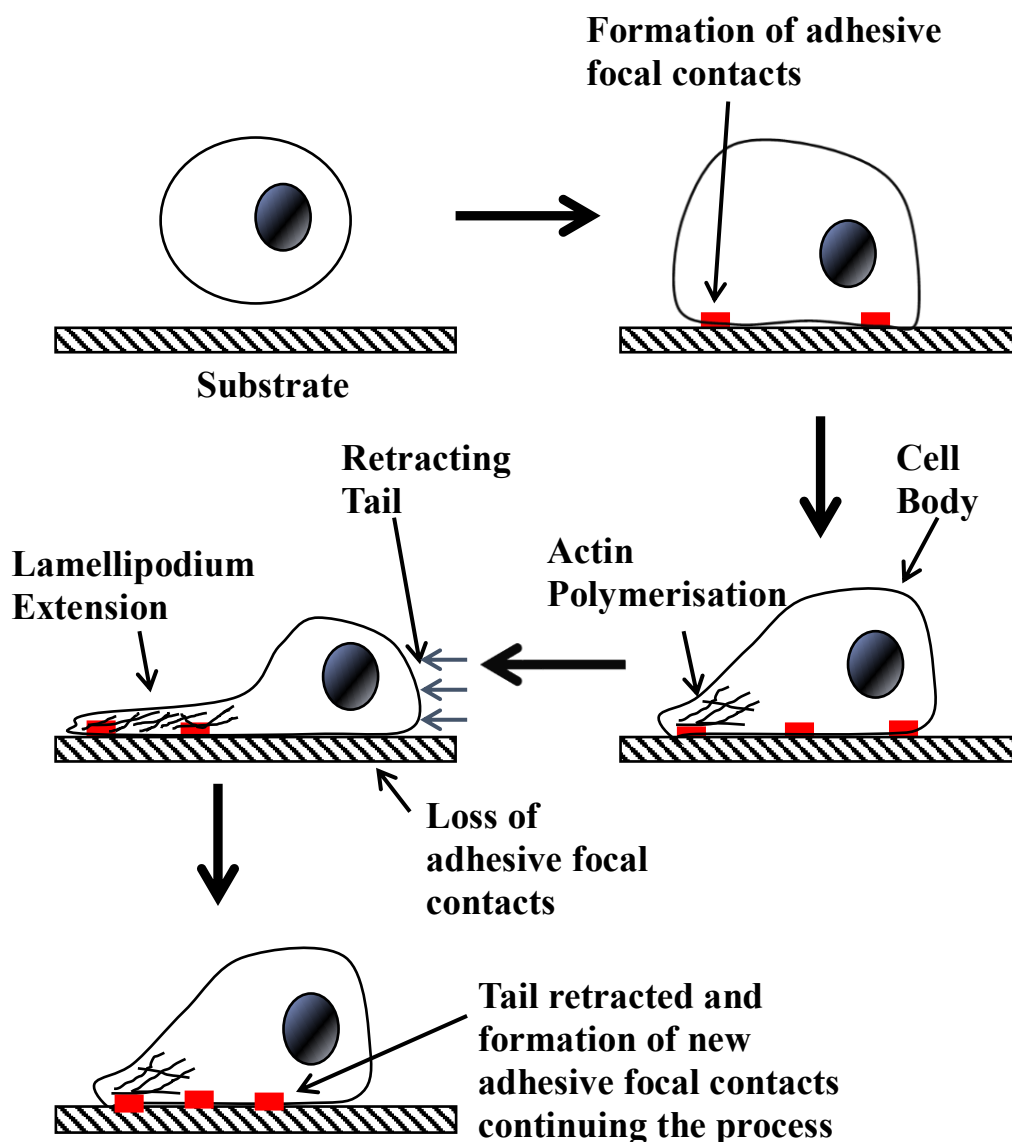


Figure 88 – A diagram of the lamellipodium extension process in cellular motility.

The amide I peak area has been mapped for a cell expressing an amoeboid phenotype with its microscopic and protein chemical image displayed in Figure 89. The protein chemical image is a 3D representation of the cells landscape. Higher landscapes therefore contain stronger protein absorbances. The lamellipodia of interest have been marked A, B and C in both the microscopic and protein chemical image. The retracting tail has also been highlighted by a black box in the microscopic image and a white box in the protein chemical

image. All lamellipodia contain significant levels of protein, represented by the raised landscapes in the 3D protein chemical image compared to the retracting tail. The retracting tail contains very low protein absorbances, which would be physiologically expected. The majority of the actin filaments are located at the forefront of forming lamellipodia, hence the large difference in protein absorbance between the lamellipodia and the retracting tail. The forefront of the driving lamellipodium C contains higher protein absorbances than the lamellipodia A and B. This is because the actin filaments are concentrating at the edge in which the direction of the cell is moving, resulting in stronger absorbances from a greater actin content. A study conducted by Gazi *et al.* was able to highlight intense protein regions representing the cell body and lamellipodium which is consistent with the findings in this study (4).

Brown *et al.* stated that motility and the ability to induce amoeboid characteristics is prerequisite for metastasis (11), whereby AA stimulates morphological change. Studies have also placed great importance on morphological transitions, with the reorganisation of actin frameworks in the cell's cytoskeleton (12,13,14). It has been shown that invasive cell lines readily uptake AA with non-invasive cell lines displaying no such behaviour in sections 3.1 and 3.2. It could be thought that the difference between the two phenotypes is their ability to be induced by AA to undergo a morphological change. The non-invasive cell lines may have a limited ability to undergo cytoskeleton reorganisation suppressing the emergence of an amoeboid phenotype, a critical step needed in metastasis.

It is evident that high magnification FT-IRM is capable of defining fine architectural structures when specifically targeting strong vibrational signatures such as the amide I. It is likely that the lamellipodia would not have been defined if a weaker vibration was used.

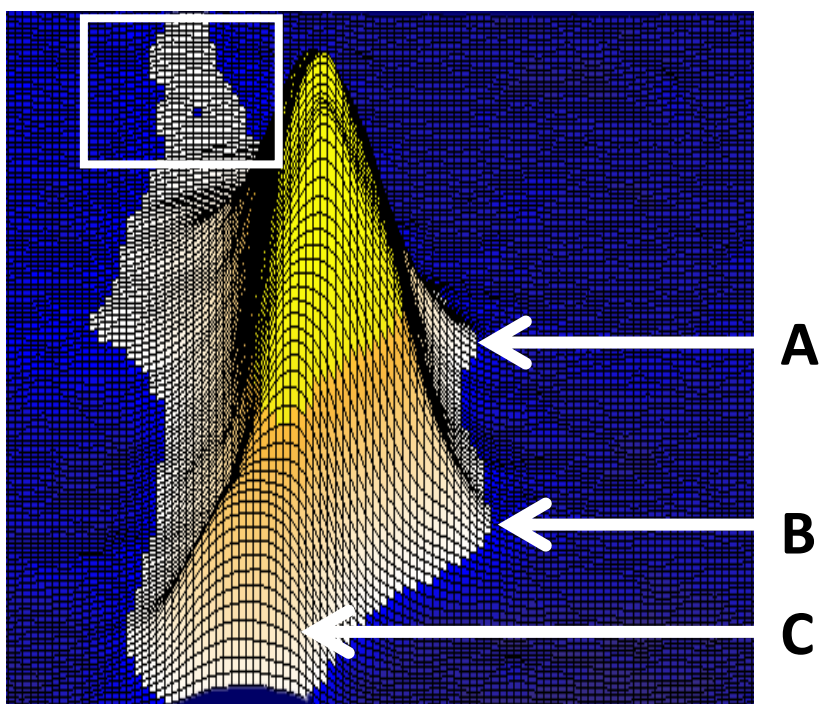
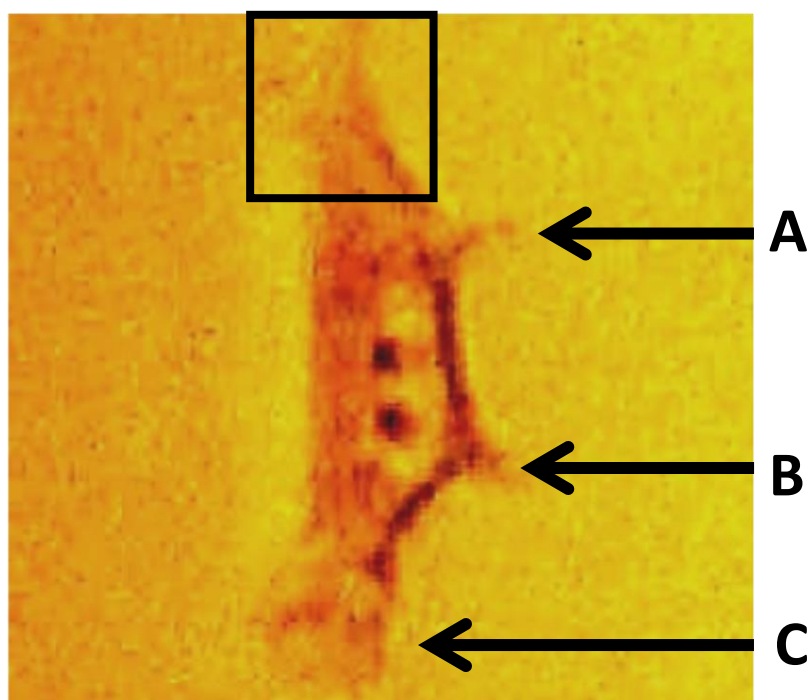


Figure 89 (a) Microscopic image of PC-3 cell at x25 magnification and (b) 3d chemical heat map of amide I peak. Image size 90 μm x 90 μm .

6.6 Conclusion

FM proved a valuable technique in tracking the uptake and metabolism in PC-3 cells. There appeared to be maximum uptake by 15 – 30 minutes matching the chemistry and time scales of previous investigations in chapters 3 and 4 using PCA. When the COX-2 enzyme was blocked, there was no change in cellular fluorescence indicating no AA uptake validating previous PCA FT-IRM studies. This provided further evidence that there must be an initial upstream signalling mechanism effecting the fundamental uptake of AA.

FT-IR chemical images resulted in mirror images of the FM analysis. Mapping the C=O carbonyl stretch, a spectral marker of AA enabled regions rich in AA to be located. When high magnification FT-IR was used to analyse PC-3 cells treated with d₈-AA for 15 minutes, it was possible to define large cellular structures such as nucleoli and the nucleoplasm. The highly unique C-D stretch identified d₈-AA pooling within the cell membrane in the cell cytosol, with clear spherical lipid droplets recognised. When investigating the protein distribution within the cell, it was possible to see fine architectural structures such as lamellipodium. AA induces proliferation (15) and motility resulting in the formation of lamellipodia type structures which can be seen using high magnification FT-IRM. Lamellipodia drive the motility process, a key development needed for the disease to progress. This is additional evidence that AA increases the invasive potential of PC-3 cells. High magnification FT-IRM coupled with FM proves a highly valuable tool supplying further validation to previous studies.

References

-
- ¹ L. L. Listenberger, D. G. Brown. Fluorescent Detection of Lipid Droplets and Associated Proteins. *Current Protocols in Cell Bio Supp.* 35 (2007) 1-24.
- ² W.T. Liu, J. H. Wu, E. S. Y. Li, E. S. Selamat. Emission Characteristics of Fluorescent Labels with Respect to Temperature Changes and Subsequent Effects on DNA microchip Studies. *Appl Environ Microbiol.* 71 (2005) 6453-6457.
- ³ N. Jamin, P. Dumas, J. Moncuit, W. Fridman, J. Teillaud, G. L. Carr, G. P. Williams. Highly Resolved Chemical Imaging of Living Cells by Using Synchrotron Infrared Microspectrometry. *Proc Natl Acad Sci USA.* 95 (1998) 4840.
- ⁴ E. Gazi, J. Dwyer, N. P. Lockyer, J. Miyan, P. Gardner, C. A. Hart, M. D. Brown, N. W. Clarke. A Study of Cytokinetic and Motile Prostate Cancer Cells Using Synchrotron-Based FIR Microspectroscopic Imaging. *Vib Spec.* 38 (2005) 193-201.
- ⁵ B. Geiger, J. P. Spatz, A.D. Bershadsky. Environmental Sensing Through Focal Adhesions. *Nat Rev of Mol Cell Biol.* 10 (2009) 21-33.
- ⁶ Y. Rikitake, Y. Takai. Chapter Three – Directional Cell Migration, Regulation by Small F Proteins, Nectin-Like Molecule-5, and Afadin. *Int Rev of Cell and Mol Biol.* 287 (2011) 97-143.
- ⁷ E. Atilgan, D. Wirtz, S. X. Sun. Morphology of the Lamellipodium and Organization of Actin Filamenta at the Leading Edge of Crawling Cells. *J. of Biophys.* 89 (2005) 3589-3602.
- ⁸ H. Lodish, A. Berk, S. L. Zipursky, et al. *Molecular Cell Biology.* 4th edition. New York: W. H. Freeman: 2000.
- ⁹ G. Laevsky, D. A. Knecht. Cross-Linking of Actin Filaments by Myosin II is a Major Contributor to Cortical Integrity and Cell Motility in Restrictive Environments. *J. of Cell Sci.* 116 (2003) 3761-3770.
- ¹⁰ O. Reis, R. Winter, T. W. Zerda. The Effects of High External Pressure on DPPC-Cholesterol Multilamellar Vesicles: A Pressure-Tuning Fourier Transform Infrared Spectroscopy Study. *Biochimica et. Biophysica Acta.* 1279 (1996) 5-16.
- ¹¹ M. Brown, J. A. Roulson, C. A. Hart, T. Tawadros, N. W. Clarke. Arachidonic Acid Induction of Rho-Mediated Transendothelial Migration in Prostate Cancer. *Br J Can.* 110 (2014) 2099-2108.
- ¹² P. Friedl, D. Gilmour. Collective Cell Migration in Morphogenesis, Regeneration and Cancer. *Nat Rev Mol Cell Biol.* 10 (2009) 445-457.
- ¹³ T. Lammermann, M. Sixt. Mechanical Modes of ‘Amoeboid’ Cell Migration. *Curr Opin Cell Biol.* 21 (2009) 636-644.
- ¹⁴ V. Sanz-Moreno, C. J. Marshall. Rho-GTPase Signalling Drives Melanoma Cell Plasticity. *Cell Cycle.* 8 (2009) 1484-1487.
- ¹⁵ P. Yang, C. A. Cartwright, J. Li, S. Wen, I. N. Prokhorova, I. Shureiqi, P. Troncoso, N. M. Navone, R. A. Newman, J. Kim. Arachidonic Acid Metabolism in Human Prostate Cancer. *Int J Oncol.* 41 (2012) 1495-1503.

Chapter 7

Conclusion and Future Work

7.1 Conclusion

Overall, it is evident that invasive prostate cancer cell lines readily uptake and metabolise AA with no such indication seen for non-invasive cell lines. It is hypothesised that a key factor influencing the cellular metastatic phenotype is the cells ability to uptake and metabolise AA. Chemical mapping of the C=O carbonyl stretch around 1732 cm^{-1} provides deeper insight to the cellular distribution of AA, again suggesting that AA is initially incorporated in the cell membrane, disperses into the cell cytoplasm, accumulates in the form of lipid droplets and finally is metabolised into its bioactive downstream metabolites validated with both low and high magnification FT-IRM. It was possible to track the downstream metabolite PGE₂ through seeded PCA, again confirming that AA is initially up taken by invasive cell lines and then metabolised. This result is consistent with study carried out by Brown *et al.* whereby PC-3 cells were shown to readily uptake AA (1). Brown *et al.* showed maximum lipid uptake at 30-minutes through FM and FT-IRM, similar timings that were shown in all invasive cell lines throughout this study. The work carried out in the study has built on the work carried out by Brown *et al.* further exploring the AA uptake and metabolism in a variety of different invasive and non-invasive prostate cancer cell lines. From this, it can now be seen that there is potentially a distinct difference in metabolic processes in invasive and non-invasive cell lines.

When the COX-2 enzyme is blocked, no such cellular spectral features are seen with the invasive cell lines. It is theorised that there is upstream signalling preventing the incorporation and transport of AA into the cellular cytoplasm. A potential target for the upstream signalling could be the CD36 protein expressions within the cell membrane since these are responsible for fatty acid transport. Applying a deuterated tag reinforced the

information already drawn from the initial experiments and allowed specific molecular identity from the C-D stretch at roughly 2251 cm^{-1} . This specificity means confidence can be drawn that the global cellular chemistry changes seen are a result of the specific $\text{d}_8\text{-AA}$. When PC-3 cells with COX-2 blocked enzymes were exposed to both DHA and $\text{d}_8\text{-AA}$ the results suggested that DHA blocked the uptake of $\text{d}_8\text{-AA}$. Fluorescence microscopy supports the hypotheses made showing definite AA uptake, with clear lipid droplets forming within the cell, also seen in the low and high magnification FT-IRM chemical mapping.

High magnification FT-IRM was able to track intracellular stores of $\text{d}_8\text{-AA}$. This defined the droplets around the outside of the cell membrane and within the cell cytosol, with no deuterated stretches appearing within the cell nucleus. This allowed the AA distribution to be identified throughout the cell, showing pooling in physiologically realistic positions within the cell.

Overall it appears that COX-2 readily inhibits the uptake of AA. A new up-stream signalling pathway is suggested and if elucidated could alter the way lipid chemistry could be viewed in the progression and proliferation of prostate cancer. The AA uptake and metabolic mechanism involves diffusion or transport of AA across the cell membrane, catalysis of AA to PGE_2 around the nuclear envelope and rough endoplasmic reticulum by the COX-2 enzyme, with the PGE_2 finally ejected from the cell shown in Figure 90. It could be hypothesised that when COX-2 is inhibited, there is an upstream signalling mechanism which prevents the uptake of AA, down-regulating the CD36 expression preventing active uptake of AA displayed in Figure 91.

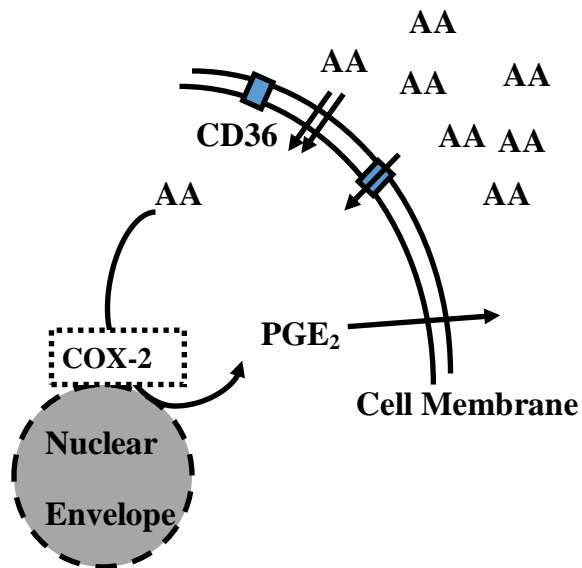


Figure 90 – AA cascade mechanism for uptake and metabolism

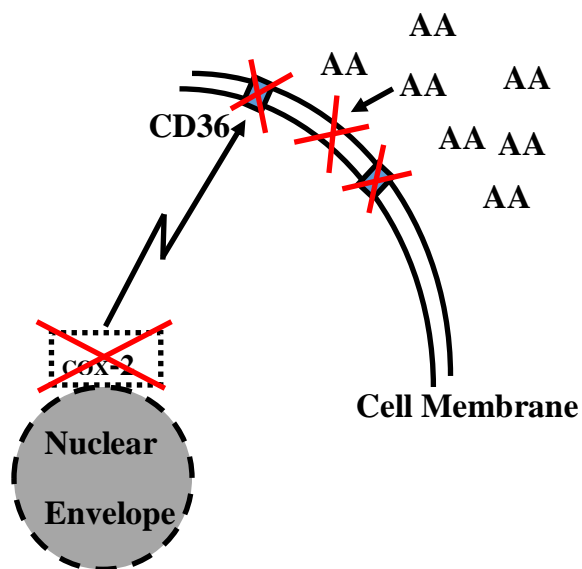


Figure 91 – Hypothesised COX-2 inhibited AA block signal pathway

The results suggest that cells are more selective than once thought, with an ability to prevent AA uptake when limited in its metabolic processes in COX-2 inhibition (AA cascade). It appears that FT-IRM has the sensitivity and ability to track uptake and metabolism in

cellular systems giving a new insight into the value of FT-IRM in metabolomics and upstream signalling mechanisms in the lipid cascade.

Literature already demonstrates the role of COX-2 in prostate cancer progression and development. This study furthers the understanding of AA metabolism via the COX-2 pathways in invasive and non-invasive cell lines. This has contributed to the void in literature as to why potentially COX-2 inhibits the progression and development of prostate cancer. If the prostate cancer cell is unable to uptake AA, then this limits an essential fuel required in the proliferation of prostate cancer. This is a possible indication that COX-2 inhibition could be a potential therapeutic target in the suppression of prostate cancer development, with the mechanism surrounding COX-2 inhibition and the blocking of AA uptake to be elucidated.

7.2 Future Work

Throughout this study, a number of findings has left several unanswered questions which need to be further investigated.

Studies state that the COX-2 expression is increased in cancerous tissues such as gastrointestinal, pancreatic, lung, prostate and colon malignant tissues (2). Dietary fats are said to be one of the main risk factors in developing breast, colorectal and prostate cancer (3,4,5). Furthering this, high dietary intake of ω -6 polyunsaturated fatty acids such as AA are linked with the development of breast, colorectal and prostate cancer (6,7,8,9). Investigating the effect of endogenous AA exposure to invasive and non-invasive breast and colorectal cell lines could prove beneficial. Investigating the effect of AA uptake and COX-2 inhibition on both invasive and non-invasive cell lines for breast and colorectal types of the disease could give indication whether the findings throughout this study for

invasive and non-invasive prostate cancer cell lines are universal across multiple types of cancer. It was hypothesised that there must be upstream signalling preventing AA uptake when COX-2 inhibition was induced for prostate cancer cell lines. Does the same hypothesis apply for breast and colorectal cancers?

The fatty acid uptake mechanisms are currently unclear. There are multiple ways AA could enter the invasive prostate cancer cells, including free diffusion across the membrane or membrane incorporation through esterification, followed by PLA2 cleavage into the cell cytosol (10,11). CD36 facilitates a major proportion of fatty acid uptake in cellular systems (12). It was shown that COX-2 inhibition prevents AA uptake in invasive prostate cancer cell lines. Does the CD36 expression influence this? A possible hypothesis could be that the cell down regulates CD36 expressions when COX-2 suppression is achieved, preventing AA uptake. The CD36 up and down regulation needs to be further investigated to identify whether this is the primary cause for a block on cellular AA uptake.

Further analysis could be done with mass spectrometry (MS), investigating the uptake of AA when COX-2 is both active and inhibited. Mass spectrometry could provide valuable information on lipid species composition and orientation within the cellular membrane. MS could probe in depth changes to cellular membranes, looking into potential signal mechanisms preventing AA uptake. Membrane fluidity could also be monitored through MS by investigating the lipid chain lengths present in the cellular membrane when prostate cancer cells are exposed to AA.

Further investigation needs to be carried out looking at the error and its significance in the seeded PCA and median positional plot techniques used throughout this study.

Actin filament orientation could be examined when exposing invasive prostate cancer cell lines to AA with COX-2 active and inhibited. An interesting potential study could use high magnification FT-IR with a polarising filter. Specific organisation of protein actin filaments would lead to a change in amide I and II bands as the polarising filter is turned through 180 degrees, revealing the orientation and structure of the cellular actin filaments. A complementary study could be carried out whereby AA treated prostate cancer cells at different time points could be stained with phalloidin, a fluorescent stain used to investigate actin filaments. FM could then be carried out showing the orientation of cellular actin filaments. High magnification FT-IRM and the FM images could then be compared investigating the chemical protein changes expressed when undergoing morphological changes when exposed to AA, a key step in the invasion process. Then when blocking the COX-2 enzyme are the same changes seen?

Ultimately, the investigation of AA in invasive prostate cancer cell lines would be carried out in an environment similar to the body *in vivo* rather than *in vitro*. Therefore, it would be beneficial to investigate the effect of AA uptake and COX-2 inhibition on a more complex prostate cancer model. This could potentially be achieved through 3D printing, a novel and relatively new technique that is being applied to the formation of biological structures. If the cellular environment around the prostate was mimicked with specific cellular structures, then this may act as a more representative environment for prostate cancer to progress, allowing a true indication as to what initiates prostate cancer in its native environment. If the architecture of an endothelial blood vessel is printed in the region of the prostate cancer colony with a distant bone marrow site, then it may be possible to get a very different insight into prostate cancer progression.

References

-
- ¹ M. D. Brown, C. A. Hart, E. Gazi, S. Bagley, N. W. Clarke. Promotion of Prostatic Metastatic Migration Towards Human Bone Marrow Stroma by Omega 6 and its Inhibition by Omega 3 PUFAs. *Br J Cancer*. 94 (2006) 842-853.
- ² A. Kirschenbaum, X. H. Liu, P. Adam, R. Lee, P. Unger, A. C. Levine, S. Yao. NS398, A Selective Cyclooxygenase-2 Inhibitor, Induces Apoptosis and Downregulates bcl-2 Expression in LNCaP cells. *Cancer Res*. 58 (1998) 4245–4249.
- ³ T. Key. Risk Factors for Prostate Cancer. *Can Surv*. 23 (1995) 7-30.
- ⁴ L. Lipworth. Epidemiology of Breast Cancer. *J. Can Prev*. 4 (1995) 1033-1038.
- ⁵ J. D. Potter. Risk Factors for Colon Neoplasia: Epidemiology and Biology. *Eur. J. Can*. 31 (1995) 1033-1038.
- ⁶ D. P. Rose. Effects of Dietary Fatty Acids on Breast and Prostate Cancer: Evidence from *in Vitro* Experiments and Animal Studies. *Am. J. Clin. Nutr*. 66 (1997) 1513-1522.
- ⁷ P. K. Pandalai, M. J. Pilat, K. Yamazaki, H. Naik, K. J. Pienta. The Effects of Omega-3 and Omega-6 Fatty Acids on *in vitro* Prostate Cancer Growth. *Anticancer Res*. 16 (1996) 815-820.
- ⁸ J. Ghosh, C. E. Myers. Arachidonic Acid Stimulates Prostate Cancer Cell Growth: Critical Role of 5-Lipoxygenase. *Biochem Biophys Res Commun*. 235 (1997) 418–423.
- ⁹ D. P. Rose, J. M. Connolly. Effects of Fatty Acids and Eicosanoid Synthesis Inhibitors on the Growth of Two Human Prostate Cancer Cell Lines. *Prostate*. 18 (1991) 243–254.
- ¹⁰ A. R. Brash. Arachidonic Acid as a Bioactive Molecule. *J. Clin Invest*. 107 (2001) 1339-1345.
- ¹¹ M. Hughes-Fulford, R. R. Tjandrawinata, C. F. Li, S. Sayyah. Arachidonic Acid, An Omega-6 Fatty Acid, Induces Cytoplasmic Phospholipase A2 in Prostate Carcinoma Cells. *Carcinogenesis*. 26 (2005) 1520-1526.
- ¹² X. Su, N. A. Abumrad. Cellular Fatty Acid Uptake: A Pathway Under Construction. *Trends Endocrinol Metab*. 20 (2010) 72-77.